# Elaboration and transfer of tensile strained thin films

Laurent Michaud

Université Grenoble Alpes

# THÈSE

Pour obtenir le grade de

**DOCTEUR DE L'UNIVERSITE GRENOBLE ALPES**

Spécialité : **Physique des matériaux**

Arrêté ministériel : 25 mai 2016

Présentée par


## Laurent MICHAUD

Thèse dirigée par **François RIEUTORD**
et codirigée par **Pierre MONTMEAT** et **Samuel TARDIF**

préparée au sein du **Laboratoire d'Electronique et de Technologie de l'Information (LETI - CEA)**
dans **l'École Doctorale Physique**


# Elaboration et transfert de films ultra-contraints

# Elaboration and transfer of tensile strained thin film

Thèse soutenue publiquement le **23/06/2021**
devant le jury composé de :

**M Philippe GOUDEAU**
Directeur de recherche CNRS, Institut P' Université de Poitiers, Membre
**Mme Anne TALNEAU**
Directrice de recherche CNRS, C2N Université Paris-Saclay, Rapporteur/présidente
**Mme Stéphanie ESCOUBAS**
MCF-HDR, IM2NP Université Aix-Marseille, Rapporteur,
**M Guillaume PARRY**
MCF-HDR, SIMAP Université Grenoble Alpes, Membre
**M Frank FOURNEL**
Expert scientifique, CEA Leti Grenoble, Encadrant
**M François RIEUTORD**
Directeur de recherche, CEA IRIG Grenoble, Directeur de thèse
**M Pierre MONTMEAT**
Ingénieur de recherche, CEA Leti Grenoble, Encadrant
**M Samuel TARDIF**
Ingénieur de recherche, CEA IRIG Grenoble, Encadrant

# Remerciements

Avant de rentrer dans le vif du sujet c'est le moment pour moi de remercier toutes les personnes qui m'ont permis de mener à bien cette thèse. Tout d'abord un grand merci aux membres du jury, Guillaume Parry, Anne Talneau, Stéphanie Escoubas et Philippe Goudeau. J'ai beaucoup apprécié nos échanges et je suis très reconnaissant du temps que vous avez consacré à l'évaluation de mes travaux de recherche.

Ensuite je tiens à adresser de chaleureux remerciements à mes encadrants : Pierre Montméat et Samuel Tardif ainsi qu'à François Rieutord, mon directeur de thèse. C'était un plaisir de travailler et apprendre à vos côtés. Je souhaite à tous les doctorants d'être aussi bien entourés, grâce à vous j'ai pu aller au bout de ce que j'étais venu chercher en me lançant dans une thèse, tant sur le plan humain que professionnel. Merci Pierre pour ton incroyable efficacité et ton soutien énorme dans mes travaux. Merci Sam de m'avoir fait découvrir le monde passionnant des synchrotrons et de m'avoir converti à ce formidable langage qu'est python. François c'était un honneur de pouvoir bénéficier de ton expérience et de tes conseils. Et merci à Frank Fournel qui est devenu mon encadrant de fait après avoir donné beaucoup de son temps pour m'aiguiller dans mes recherches et me faire partager ses connaissances dans le domaine du collage.

Un grand merci à tout le personnel du SSURF à commencer par Véronique Carron et Sylvain Maitrejean qui se sont succédés en temps que chefs de service et m'ont permis de mener mes recherches dans des conditions optimales. Merci à Cécile Moulin qui a pris la direction du laboratoire LSJ au début de la crise du covid, bravo pour ta gestion et ton soutien qui nous ont permis de traverser un peu plus sereinement ces mois compliqués. C'était un plaisir de travailler au sein du 41.26 dont les qualités des occupants sont inversement proportionnelles à la solidité de ses murs. Merci à Floch, Thierry, Greg, Gaëlle, Véronique, Pierre, Marc, Alain, Mommo, Christophe, Laurent, Loïc, Karine, Jérome, Brigitte, Vincent, Pascal, Alain, à tous les habitués du coin café et à tout ceux qui ont pu m'ont aidé en salle blanche ou au bureau. J'en oublie forcément en écrivant ces lignes. Un grand merci à la joyeuse bande de jeunes plus ou moins précaires du SSURF pour la super ambiance et les afterworks : Lucas, Quentin, Océane, Mrad, Mayara, Maxence, Valentin, Clément, Caroline, Marvin et tous les stagiaires, alternants ou doctorants du service. Merci à mes voisins de bureau qui m'ont supporté pendant que je codais. Merci Joël de m'avoir tenu compagnie pendant toutes ces soirées de rédaction. Merci Edy, c'était un plaisir de pouvoir travailler avec toi. Merci à tous les amis que je me suis fait au SSURF, Léa, Antoine, Baptiste et Laura pour tous ces super moments passés au bureau, en montagne ou autour d'un verre. Votre soutien a énormément compté. Merci Quentin de ne pas avoir "scrapé" tout mes plaques et pour toutes ces belles courses passées et à venir.

Plus largement je veux remercier tous les employés du Leti qui ont joué un rôle essentiel dans ma thèse que ce soit pour faire avancer les lots en salle blanche, caractériser mes échantillons, me former sur des équipements ou voler à mon secours sur eyelit.

Je tiens à remercier tout ceux qui m'ont permis d'élargir mon horizon scientifique, tout particulièrement Laurent Gonon et Vincent Mareau pour m'avoir apporté leur confiance et leurs conseils pour mes mesures Raman. Un grand merci à Joël Eymeri pour tout ses conseils avisés. Merci Nikita pour les données obtenues au plus chaud de l'été grenoblois. Merci Claire de m'avoir intégré aux jeunes du C5 et pour toutes les soirées escalades, jeux de plateau ou MK. Merci à toute l'équipe de BM32 et tout particulièrement Jean-Sébastien Micha pour son travail sur Lauetools. Merci Dominique Thiaudière, Thibault Chommaux et Pierre-Olivier Renault pour votre aide et votre implication sur les mesures faites à SOLEIL.

Merci également à tous les amis de Grenoble, Culoz et alentour, Dijon, Lausanne. On s'est moins vu ces derniers temps à cause des restrictions et du travail mais votre amitié a beaucoup compté pour traverser ces années de thèses.

Et enfin je ne peux pas finir ces remerciements sans mentionner ceux qui sont là depuis le début et à qui je dois énormément : ma famille. Je pense tout particulièrement à mes parents qui m'ont toujours soutenu tout au long de mes études, ça n'a pas toujours été facile. Merci à mes frères de m'avoir montrer la voie et d'avoir toujours été là pour des conseils ou juste s'aérer les week-ends. Et bien-sûr merci à mes grand-parents pour tout leur soutien et m'avoir transmis l'envie d'apprendre. J'aurais tellement aimé pouvoir fêter ce diplôme avec vous tous.

## Résumé

Cette thèse est consacrée à l'étude d'une méthode alternative et originale pour élaborer un film mince de silicium monocristallin ultra-contraint dans le but de développer une plateforme d'ingénierie de la déformation ("strain engineering") pour les semi-conducteurs monocristallins. Les contraintes sont largement utilisées pour améliorer les performances des transistors à base de silicium et offrent des possibilités exceptionnelles, notamment pour l'utilisation de semi-conducteurs compatibles Complementary metal–oxide–semiconductor (CMOS) dans des applications optoélectroniques. Les méthodes habituelles utilisées pour fabriquer des semi-conducteurs contraints sont limitées en termes de valeur de déformation, d'orientation de la contrainte, de surface déformée et de qualité cristalline. Notre objectif est de proposer un procédé permettant de contrôler précisément l'état de déformation (c'est-à-dire le tenseur de déformation) dans un monocristal. Ce procédé est applicable à différents semi-conducteurs et matériaux et est compatible avec un environnement industriel. Le procédé étudié ici repose sur le collage polymère temporaire, l'abrasion mécanique, la gravure humide et le collage direct pour transférer un film mince de silicium monocristallin d'un substrat de type silicium sur isolant à un polymère flexible. Puis le cristal est déformé en appliquant une contrainte externe et est enfin recollé sur un substrat rigide. Les structures silicium sur polymère (SOP) ont été obtenues avec des films minces de silicium monocristallin d'une épaisseur allant de 20 à 205 nm. Des films d'un diamètre total de 200 mm ont été transférés ainsi que des motifs. Une étude approfondie du comportement mécanique des structures SOP est fournie en utilisant des platines d'essai de traction biaxiale et uniaxiale combinées à la spectroscopie Raman, de la corrélation d'images numériques, la diffraction des rayons X et à la micro diffraction de Laue (µLaue). Ces résultats ont été utilisés pour valider un banc d'essai mécanique adapté aux structures silicium sur polymère flexibles. Des stratégies d'acquisition et d'analyse de données ont également été developpées. L'utilisation d'une membrane sous pression (bulge test) a permis le collage direct entre un film de silicium déformé et un substrat de silicium oxidé. La diffraction des rayons X offre une analyse détaillée du cristal transféré. Le processus de transfert a également été adapté à des dispositifs fonctionnels et à des films minces de nitrure d'aluminium polycristallin. Notre banc d'essai mécanique a permis d'extraire le coefficient de déformation ou de contrainte Raman de l'AlN dans différentes configurations. Ces résultats prometteurs ont montré que le collage direct est une méthode appropriée pour maintenir un film mince de silicium monocristallin dans un état de contrainte après son retrait d'un substrat de polymère flexible étiré. Cela peut conduire à un développement sans précédent dans l'ingénierie de la déformation. Des travaux ultérieurs peuvent permettre la production de films minces déformés de différentes natures, orientations et niveaux de déformation.



**Mots Clefs :** *semi-conducteur, contraint, films, collage, rayon X, Raman*

## Abstract

This thesis is dedicated to the study of an alternative and original method to produce strained single-crystal silicon thin film in an effort to develop a strain engineering platform for single crystal semi-conductor. Strain engineering is widely used to boost Si based transistor performance and offers outstanding possibility for the use of Complementary metal–oxide–semiconductor (CMOS) compatible semi-conductor in interesting optoelectronic applications. Usual methods used to fabricate strained semi-conductors are limited in terms of achievable strain value, strain orientation, strained surface and crystalline quality. We aim at proposing a process allowing to tune precisely deformation state (*i.e.*, strain tensor) in a single-crystal. This process is applicable for different semi-conductors and materials and compatible with an industrial environment. The process studied here relies on temporary polymer wafer bonding, mechanical grinding, wet etching and direct bonding to transfer a single crystal silicon thin film from a Silicon On Insulator substrate to a flexible polymer, strain the crystal and bond it back on a rigid substrate. Silicon On Polymer structure were obtained with single crystal silicon thin film with a thickness ranging from 20 to 205 nm. Up to full diameter 200 mm films were transferred as well as patterned wafers. An extensive study of mechanical behavior of Silicon On Polymer (SOP) structures is provided using biaxial and uniaxial tensile test stages combined with Raman spectroscopy, digital image correlation, X-ray diffraction and Micro Laue X-ray Diffraction (µLaue). These results were used to validate a custom mechanical bench test for flexible SOP structures. Corresponding data acquisition and analysis strategies were also developed. The understanding of SOP mechanical behavior enabled the use of a bulge test apparatus to perform a direct bonding between a strained SOP and a silicon oxide die. µLaue allowed for a detailed analysis of the reported crystal. The transfer process was also adapted to functional devices and poly-crystal aluminum nitride thin films. Our custom mechanical bench test allowed the extraction of AlN Raman strain or stress coefficient in different configurations. Promising results showed that direct bonding is a suitable method to maintain a single crystal silicon thin film in a strained state after removal from a stretched flexible polymer substrate. This can lead to some unprecedented development in strain engineering. Further work can enable the production of strained thin film of different nature, stress orientation and strain level.



**Keywords:** *semiconductor, strain, films, wafer bonding, X-ray, Raman*

# Contents

# List of figures

# List of Tables

# Liste of acronyms

**AFM** Atomic Force Microscopy. ix, 2, 9, 18, 57, 66, 67, 74, 162

**AOP** AlN On Polymer. xi, 162, 164, 166, 167, 171

**AS** Anti Stiction. viii, xi, 43, 44, 63, 67, 73, 76, 78, 80–84, 86, 89, 143, 147, 148, 164

**BCB** Benzocyclobutene. vii, 17, 22–24

**BOX** Buried Oxide. viii, 22–24, 37, 40, 41, 45, 57, 61, 66, 70, 73, 76, 79, 82, 83, 86

**BSI** Brewer Science Inc.. 43, 50, 54, 63, 64, 66

**CCD** Charge-coupled device. 101

**CD** Critical Dimension. 40, 136

**CMOS** Complementary metal–oxide–semiconductor. ii, iii, 10, 12, 17, 18, 22, 142

**CMP** Chemical-mechanical Polishing. 18, 142

**CTE** Coefficient of Thermal Expansion. 11, 67, 68, 171

**DC** Double Confocal. 65, 72

**DCB** Double Cantilever Beam. 14, 52, 54, 63

**DIC** Digital Image Correlation. x, xi, 98, 101, 102, 111, 122–126, 136, 175, I, VI, VII

**ESRF** European Synchrotron Radiation Facility. x, xi, 107, 108, IV, V

**FCC** Face Centered Cubic. 4, 5, IV

**FWHM** Full Width at Half Maximum. x, 105, 106, 111, 129, 130, 132, 164

**HRXRD** High Resolution X-Ray Diffraction. ix, 55, 83, 84

**ICs** Integrated Circuits. 13, 16, 17

**IPA** isopropyl alcohol. viii, 41, 63

**IR** Infrared. 20, 52–54, 64, 65, 72, 145

**μLaue** Micro Laue X-ray Diffraction. ii, iii, x, xi, 2, 93, 99, 107–110, 112–121, 129–131, 136, 137, 142, 145, 146, 153, 170, 175, I, IV, V

**MEMS** Microelectromechanical Systems. xi, 9, 13, 16, 17, 162, 166, 171

**MOSFETs** metal–oxide–semiconductor field-effect transistor. vii, 6, 10

**PDMS** Polydimethylsiloxane. vii, ix, 23–25, 37, 46, 47, 81, 88, 175

**PEN** Polyethylene naphthalate. 24

**PL** Photoluminescence. 8

**PVD** Physical Vapor Deposition. xi, 164, 171

**RMS** Root mean square. 18, 142, 162

**ROI** Region Of Interest. xi, 109, VI, VII

**RT** Room Temperature. 6, 13, 14, 18–20, 67, 68, 147, 149, 152, 156

**SAM** Scanning Acoustic Microscopy. viii, ix, xi, 2, 43, 45, 49–52, 64, 70–72, 145, 147, 148, 164, 165

**sc-Si** single-crystal Silicon. vii–xi, xiii, 1, 2, 11, 21–24, 35, 37, 39, 40, 43, 46, 47, 55, 63, 64, 66–89, 94, 96–99, 103, 105, 111, 112, 115–126, 128–133, 135–137, 142–152, 154–156, 162, 164, 167, 175

**SEM** Scanning Electron Microscope. vii–ix, xi, 2, 9, 10, 17, 25, 42, 48, 59–61, 66, 70, 78, 103, 135, 162, 163

**SLSM** Standard Linear Solid Model. ix, 97, 109, 110

**SNR** Signal to Noise Ratio. 104, 109, 133

**SOI** Silicon on Insulator. vii–ix, xiii, 1, 3, 6, 11, 12, 17, 21–24, 37–46, 50, 57–59, 62, 64, 65, 69–73, 76, 78–84, 86, 87, 89, 112, 113, 156, 167, 175

**SOP** Silicon On Polymer. iii, vii–xi, xiii, 2, 3, 22–24, 39, 47, 48, 67, 74, 84–86, 88, 94, 97–100, 103, 104, 108–112, 114, 115, 120, 122, 123, 126–129, 136, 137, 142–145, 147–149, 152, 167, 175, IV

**TMAH** TetraMethylAmmonium Hydroxide. viii, 23, 41, 42, 60–62, 86, 135

**TTV** Total Thickness Variation. 54, 64, 72

**UV** Ultra-Violet. ix, xi, xiii, 19, 38, 74–78, 147–149, 156

**XRD** X-ray Diffraction. 2, 93, 98, 107, 111, 120, 122–124, 136, 137, 156, 171, 175, I, III

**XRR** X-Ray Reflectivity. 2, 20, 55, 83, 84

**ZOI** Zone Of Interest. xi, VI, VII

# Introduction

Transistors and devices based on semi-conductors have been following a trend of constant miniaturization in order to increase their performances. Many issues have to be overcome to decrease the dimensions of transistors and achieve satisfying performances. One of the challenge is the control of strain in micro and nanostructures. Fabrication processes or temperature changes can induce strain leading to failure or loss of performance. Hence, great care has to be taken to control and monitor strain in semi-conductors. Nevertheless strain or stress can also have a positive effect on performances, power consumption and material properties for certain applications. Since 2000, strain engineering has been a key point in the architecture of modern transistors and microelectronic devices. Different methods have been investigated to produce strained micro or nanostructure with the use of stressor layer, epitaxial growth or stress concentration. A significant amount of effort has been also made to produce strained substrates. In this case, strained structure can be designed without adding complexity to the device fabrication.

This thesis is dedicated to the study of an alternative and original fabrication process to obtain strained thin films with macroscopic surface areas. The goal is to obtain a strained semi-conductor thin film on a rigid substrate. The workflow is divided in three steps: transferring a thin film on a flexible and stretchable substrate, applying a strain to the flexible structure and finally transferring the strain thin film to a rigid substrate. The process is based on silicon single-crystal layer transfer using temporary polymer wafer bonding, application of external stress on a flexible semi-conductor on polymer and direct bonding. The first challenge is to be able to transfer a single-crystal semi-conductor film of controlled dimensions and quality on a suitable flexible substrate from a commercial Silicon on Insulator (SOI). The different mechanisms limiting the maximum achievable strain in the thin film are also to be determined. And finally the problematic is to determine if a strained single crystal can be transferred from a flexible substrate to a rigid one without strain relaxation. The whole process developed here is compatible with industrial tools and can be performed for samples with dimension ranging from micrometer to full size 200 mm wafers. Compared to what can be found in the literature, it allows to control strain both in amplitude and crystal orientation. Silicon thin films are used for proof of concept, as the material is easily available and is a suitable choice for many strain engineering applications. However the technological developments presented in this thesis are easily applicable to other crystalline materials.

The first chapter is dedicated to the study of the state-of-the-art in strain engineering, bonding and thin film transfer for semiconductors. The effect of strain on material properties will be presented, as well as different approaches used to achieve strained structures in the literature. An overview of adhesive and direct wafer bonding is also given to introduce the techniques used for the transfer process. It is essential to understand the mechanisms involved in wafer bonding with or without the used of adhesive layers in order to identify the difficulties of a single-crystal thin film transfer between organic and inorganic substrates.

The second chapter presents in detail a transfer process for single-crystal Silicon (sc-Si) thin films of various geometries and thicknesses on various polymer substrates. The different fabrication techniques are described (wafer bonding, lithography, wet etching, dry etching and mechanical grinding) along with

the different wafers and polymers and process variations. The silicon films thickness ranges from 20 nm to 205 nm while the substrates thickness ranges from 40 µm to 230 µm. A focus will be made on the influence of the bonding interface quality and localization on the quality of transferred films. Extended characterizations of the bonded stack and transferred films will be presented at different steps of the process (Scanning Acoustic Microscopy, ellipsometry, X-Ray Reflectivity, Atomic Force Microscopy, Raman spectroscopy, defectivity, Scanning Electron Microscope and adherence energy measurement using blade insertion technique).

Then in a third chapter, the mechanical study of resulting Silicon On Polymer (SOP) structure will be exposed in order to determine limiting factors in maximum strain. Raman spectroscopy and X-ray diffraction techniques (monochromatic X-ray Diffraction and Micro Laue X-ray Diffraction) were used in combination with tensile test apparatus to build a custom-made test bench. In particular, the experimental procedure will be detailed as well as the data processing. Both uniaxial stress and biaxial stress effect on the structure will be evaluated. The goal is also to provide a platform for the study of the mechanical behavior of crystalline materials on flexible substrates.

This leads to a fourth chapter dedicated to the transfer of a permanently strained silicon film from a flexible polymer substrate to a rigid substrate compatible with industrial fabrication processes. Adjustment to standard surface preparation methods will be needed to accommodate the used of flexible polymer substrates. The experimental bulge test set-up used to strain and transfer single-crystal Silicon films on a rigid substrate will be presented. Strain characterization of the resulting samples will be exposed using Micro Laue X-ray Diffraction and Raman spectroscopy.

Finally a collaborative work on the transfer of poly-crystalline aluminum nitride-based devices and thin films with a Post-Doctoral researcher in our group (Edy Azrak) is presented to illustrate the versatility of the transfer and characterization processes initially developed for silicon thin films. Aluminum nitride is a piezoelectric material commonly used in telecommunication or radio-frequency applications. Similarly to silicon the transfer process to a flexible will be evaluated for different film thicknesses (200 nm to 1600 nm) with extended characterizations at different process steps. The mechanical characterization initially developed with silicon will be also used for these piezoelectric films.

# Chapter 1

# State of the art

## Contents

# Introduction

This first chapter aims at giving some insights on what motivated this thesis and how this work is positioned relative to the literature, along with the relevant theoretical framework and recent developments. First the principle of strain engineering in semi-conductors will be exposed along with some examples. The main approaches used in this field and corresponding research teams will also be detailed. Then an overview on adhesive and direct wafer bonding mechanism and techniques will be provided in order to give a better understanding of the transfer process proposed in this thesis. As part of this thesis is dedicated to a transfer process partially based on transfer of crystalline Si film on polymer substrate, we will review different transfer methods and how they can be used for strain engineering.

## 1.1 Elastic strain engineering in crystalline materials

### 1.1.1 Principle and motivation of strain engineering

#### 1.1.1.1 Crystal lattice and electronic band structure

Before we described the effect of strain on a single-crystal material, we quickly review the basic definition and properties of crystalline materials, in particular the electronic band structure from which most properties can be derived. In crystalline materials, atoms are arranged in a periodic structure. This structure is defined by a unit cell, which is the smallest atom arrangement repeated in a three dimensional space to form a perfect crystal structure. The number of atoms, their nature and their relative positions characterize the unit cell. In the case of silicon crystal, the unit cell is formed by two atoms of coordinates (0, 0, 0) and (1/4, 1/4, 1/4) in the crystal referential system ( $x = [100], y = [010], z = [001]$). The resulting lattice is a Face Centered Cubic (FCC) with half of the tetrahedral interstitial sites filled, also called a diamond structure, as seen in figure 1.1(a). The inter-atomic distance is defined by the equilibrium between interatomic attractive and repulsive forces. For silicon, the cubic lattice parameter $a_{Si}$ is equal to 5.431 Å at room temperature. The application of an external stress on a crystal changes the inter-atomic distances, depending on the elastic modulus corresponding to the stress direction. By changing the inter-atomic distances, this applied stress and resulting strain will affect the interactions between the electrons of different atoms. The energy levels of electrons are quantified and according to the Pauli exclusion principle, two electrons can not be in the same quantum state. For a single atom, the quantum energy levels are well defined. When a second atom is brought nearby, the respective electrons start to interact and the energy levels start to hybridize. In a crystal, a very large number of atoms are brought together and share many electrons in covalent bonds. Thus, a degenerescence in the electron energy levels is observed, and the Pauli exclusion principle is still respected. In periodic crystals, band diagrams are used to represent the energy levels occupied by electrons as seen in figure 1.1(b) for silicon.

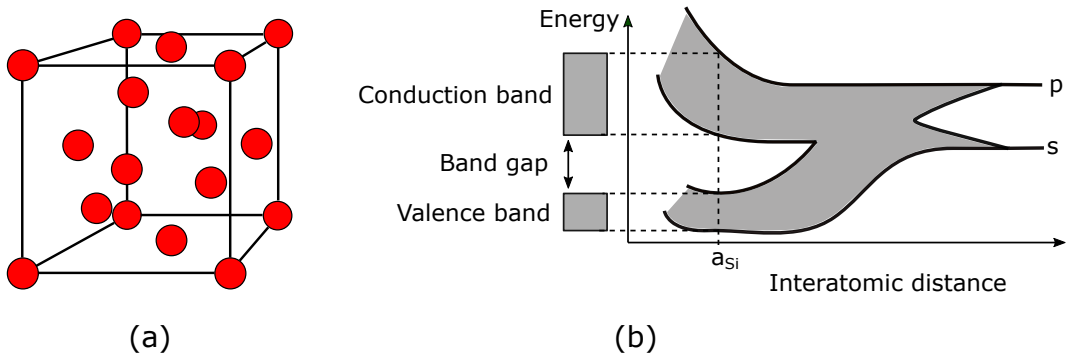


Figure 1.1: (a) Diamond crystal structure, the black lines define the cubic unit cell and the red circles indicate the atomic positions. (b) Schematic band diagram of silicon as a function of the inter-atomic distance

For a more accurate representation of the electronic band structure, one needs to introduce the concept of Brillouin zone. The Brillouin zone is a unique primitive cell represented in the reciprocal space, where the energy or frequency of vibrations of the crystal structure are represented as a function of the wave vector $q$ which characterize the propagation of a studied wave (vibrational or electronic). $q = 0$ at the origin of the Brillouin zone, is a center of symmetry and several axes of symmetry can be defined ($\Delta$ = [110] and $\Lambda$ = [111]). For FCC or Diamond-structure crystals such as silicon, it is a truncated octaedron as represented in figure 1.2(a) [Setyawan and Curtarolo, 2010]. The electronic band structure of a crystal can be represented in terms of energy level as a function of wave vectors ($k$) [Kittel, 2004], see figure 1.2(b). The electronic band structure allows one to predict conductivity, light interaction and many more properties of solid crystals. The band gap is defined as the difference in between the lowest point of the conduction band and the highest point of a valence band. If the two extrema are obtained for the same value of $k$, the band gap is said to be **direct** else it is called **indirect**. These properties have consequences on the optoelectronic properties of the crystal. For direct absorption process a photon is absorbed by the crystal with the creation of an electron/hole pair. For indirect absorption process, electrons and holes are separated by a substantial wave vector $k_c$. Photon wave vector amplitudes are negligible, which prevents a direct photon transition at the energy of the minimum band gap. A phonon of wave vector $k_c$ is needed for the transition, which will present an energy threshold larger than the true band gap. This type of transition is facilitated at higher temperatures where phonons are thermally excited. For optoelectronic application such as laser or photodiode, a direct band gap semiconductor is needed [Vogl et al., 1993]. Strain in the crystal structure will change the interatomic distances, crystal symmetry and thus can be used to tailor the band structure.

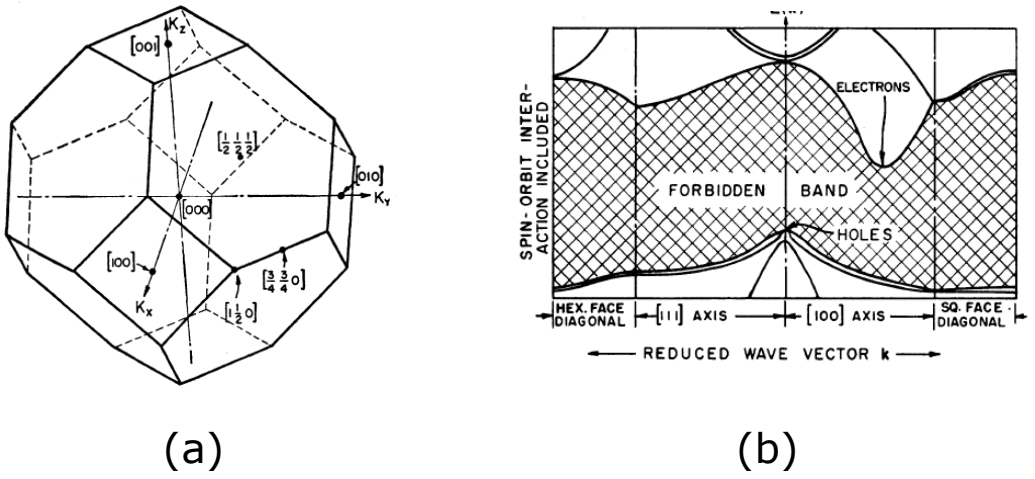


Figure 1.2: (a) Brillouin zone of silicon, a $2\pi/a_{Si}$ is omitted in the different points label for clarity [Herman, 1955]. (b) Schematic diagram the electronic band structure of silicon along axis of high symmetry

#### 1.1.1.2 Strain in semi-conductors

Strain can sometimes be an unwanted byproduct of semi-conductors manufacturing processes. As devices performances increased and transistor sizes decreased, it has become an important metric to monitor in transistors. It can sometimes lead to performance loss and worse, material or device failures. Though it appeared that by tuning the strain nature and level one could also improve transistor performances and modify material properties, following the modification of the electronic band structure [Li et al., 2014]. The strain can modify the electronic, magnetic, optical, plasmonic, ionic, photonic, thermoelectric or catalytic properties, *e.g.*, strain engineering is widely used to boost the performances of Si transistors[Ghani et al., 2003]. Strain engineering became a topic of interest in the nineties as it requires relevant fabrication processes for micro and nanostructures as well as methods to induces and probe elastic strain at microscopic or nanoscopic scales[Bedell et al., 2014; Manasevit et al., 1982; Rim et al., 1995; Welser et al., 1994].

Strain engineering is widely used in the semi conductor industry for silicon based devices. Strain is a common way of tuning carrier's mobility. Depending on the doping, different strain configuration are targeted in devices. Silicon hole and electron mobilities are represented as a function of strain in figure 1.3. This calls for a good control of strain amplitude and direction to optimize mobility and thus device performances.

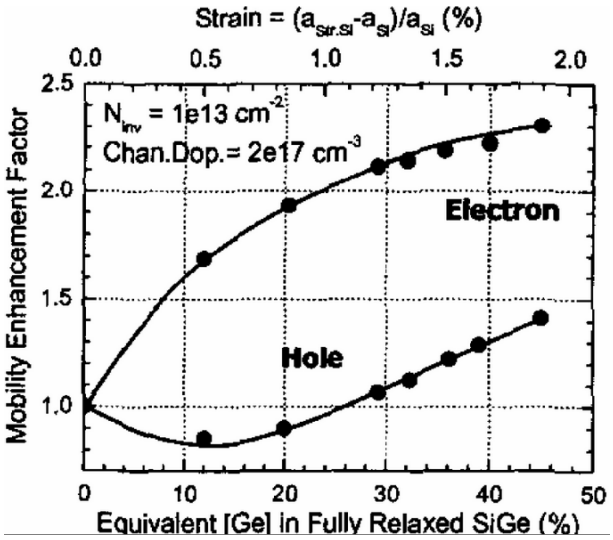


Figure 1.3: Mobility enhancement vs. Strain and Ge % at in strained Si/relaxed SiGe MOSFETs at $1 \times 10^{13}$ cm$^{-1}$ carrier concentration. Hole mobility enhancement requires large amount of strain [Rim et al., 2003]

In the case of metal–oxide–semiconductor field-effect transistor (MOSFETs) transistor on Silicon on Insulator (SOI), the channel can be strained. In the case of a channel oriented along <110> on a (100) substrate, for a nMOS a uniaxial tensile stress along <110> or a biaxial tensile stress is beneficial to the carriers mobility. Whereas in pMOS, a compressive uniaxial stress along <110> or biaxial stress is beneficial [Usuda et al., 2005]. To obtain a strain transistor on SOI, either the active silicon layer can be strained or the channel can be locally strained by the growth or deposition of a stressor layer. Local strain induced during the fabrication process is highly dependent on the transistor dimensions [Madan et al., 2008].

Moreover group IV semiconductor such as silicon and germanium display a strong piezoresistance effect, regardless on their type of doping, *i.e.* their resistivity changes under the application of strain [Smith, 1954; Richter et al., 2006]. Using this properties strain gauges [Yang and Lu, 2013] and flexible sensor can be manufactured using silicon [Won et al., 2019]. This application does not require to achieve high strain but a perfect knowledge of the material behavior under the application of strain is needed.

Another striking example of band gap strain engineering is the indirect to direct band gap transition at high tensile strain that can be observed for some group IV semiconductors such as germanium. This opens up the possibility to use CMOS compatible materials for monolithic optoelectronic applications. Alloying germanium with tin is an alternative way to obtain a band-gap with no strain or lower strain values than for pure Ge. To obtain a direct band gap, either 4.9% uniaxial strain along [100] [Guilloy et al., 2015], 1.9% biaxial strain [Gassenq et al., 2015] or $8\%_{at}$ of tin are necessary. The general principle is detailed in figure 1.4. Other models have been proposed to study the indirect to direct transition band gap in germanium, notably [Guilloy et al., 2016] made a prediction that the transition will occur at 5.6% uniaxial strain along [100] direction by taking into account non-linear effects. Atomistic simulations were also performed for biaxial tensile strain, showing a transition at 3% biaxial strain in a (001) plane at Room Temperature (RT) [Sakata et al., 2016].

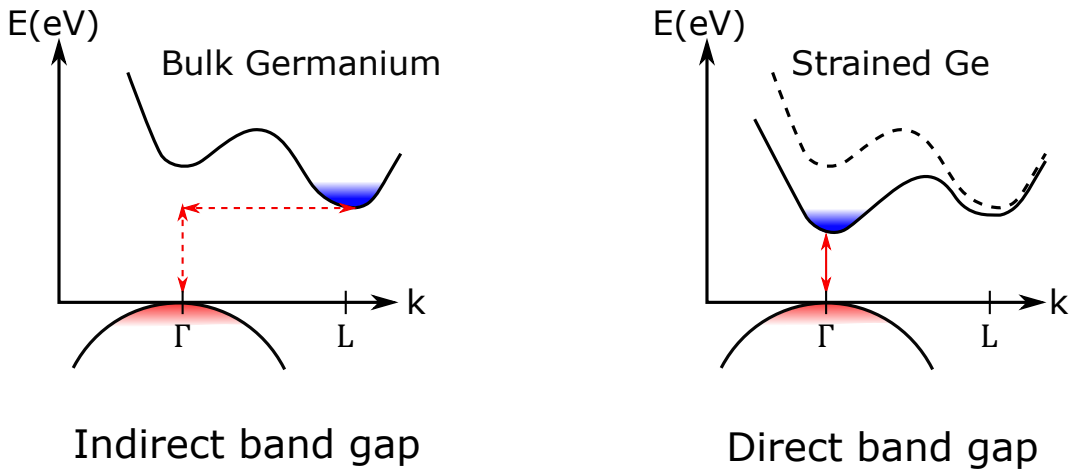


Figure 1.4: Schematic diagram of the effect of tensile strain or tin alloying on the germanium electronic band structure and band gap.

Numerous groups have been developing strained Ge microstructures as exposed in table 1.1 to obtain experimentally a direct band-gap. Noticeably Sánchez-Pérez et al. and Geiger et al. have obtained a direct band gap in germanium nanomembranes and microbridges respectively.

| Type of structure | Stress orientation | Strain (%) | Observations | Reference |
|---|---|---|---|---|
| Ge microbridge from 0,16 % strained GeOI (2 µm × 2 µm) | Biaxial | 1,9 | Thick layers for photonic applications | [Gassenq et al., 2015] |
| GeOI microbridge (250 nm/1 µm) | Unaxial < 100 > biaxial | 0.98<br>0.57 | Photoluminescence (PL) measurements $Si_3N_4$ $Si_3N_4$ stressor layer | [Hryciw et al., 2012] |
| Ge microbridge, circular membrane | Biaxial | 1.1 | PL red shift | [Sukhdeo et al., 2015] |
| Ge wire | Uniaxial < 100 > | 5.7 | PL and direct band gap at 3% strain, Raman measurement | [Sukhdeo et al., 2014] |
| Ge nanomembrane under pressure(24 nm to 84 nm) | biaxial | 2 | PL/direct band gap | [Sánchez-Pérez et al., 2011] |
| Ge microbridge | Unaxial < 100 > | 3.3 | band gap measurement | [Guilloy et al., 2016] |
| Ge thin film | Uniaxial < 100 > | 4 | Epitaxially grown SiGe stressor | [Bollani et al., 2015] |
| Ge grown via molecular beam epixtaxy on InGaAs | Biaxial | 2.33 | Strong increase in PL | [Huo et al., 2011] |
| Ge microbridge | Biaxial<br>Uniaxial | 1.8<br>4.8 < 100 ><br>3.8 < 110 | Characterization of Raman strain/shift coefficients | [Gassenq et al., 2017] |
| Ge microbridge (1 µm) | Uniaxial < 100 > | 3.6 to 5.4 | Direct band gap above 4% Low temperature (20 K | [Geiger et al., 2015] |
| Ge microbridge | Uniaxial < 100<br>Biaxial | 3.5<br>~1.3 | full strain tensor mapping | [Tardif et al., 2016] |

Table 1.1: Experimentally strained germanium structures structure in the literature

### 1.1.2 Producing strained semi-conductors

Two different kind of approaches have emerged to produce strained semiconductors (*i.e.*, at different scales). First, local approaches, where strain is only applied to a micro or nano structure. They can rely on process-induced strain, usually obtained during the manufacturing of transistors. Other local approaches based on the mechanical loading of nano and micro object will be presented, those approaches aim at studying strain engineering and mechanical properties of micro and nano scale object without any device oriented applications. On the other hand, global approaches which aim at producing strained materials at the wafer scale can also be considered. This enables the use of standard fabrication techniques with strained materials.

#### 1.1.2.1 Local strain: Nano and micro object

Several teams have studied the mechanical properties of silicon at nano and micro-scale. The silicon object can be static and subject to permanent strain. The sacrificial etching of an interfacial layer between a stressed semiconductor film and a substrate can be used to concentrate the stress in a small area of the semiconductor layer, thus applying a local permanent loading that depends on the process and on the geometry. Various geometries and materials have been studied with this approach.

Alternatively, Microelectromechanical Systems (MEMS) or other external loading can be produced to strain locally a semi-conductor in a tunable way. Devices where a compressive force is applied for example with an Atomic Force Microscopy (AFM) or nano-indenter tip are used to put silicon nano-wire under tensile strain Zhang et al. [2016].

At Catholic University of Louvain (UCL), a group has proposed different lab-on-chip devices for *in situ* mechanical characterization of semi-conductor thin films [Passi et al., 2012; Kumar Bhaskar et al., 2013]. The proposed structure can either be a static using residual stress concentration thanks to under etching of a sacrificial oxide layer or a MEMS where the stress or strain is finely controlled. It allows local observation of strained structure under the application of stress (*e.g.* with a SEM). An example is given in figure 1.5. A nitride layer is used as a stressor layer and different strain level are obtained by varying the microstructure dimensions. Recent development allowed one to observe crack propagation [Jaddi et al., 2019].

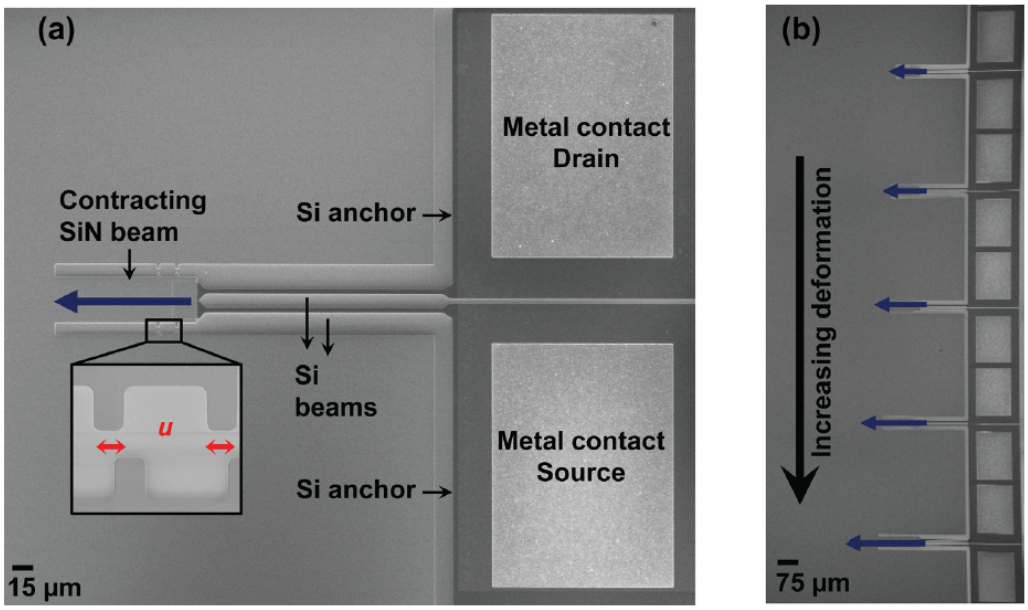


Figure 1.5: (a) SEM image of an elementary test structure for electro-mechanical characterisation of Si nano-beams. (b) SEM image of an array of test structures with increasing tensile deformation [Kumar Bhaskar et al., 2013]

Values approaching to the theoretical maximum have been achieved in nano objects such as nanowires.

The strain limits in silicon were evaluated to 23% (< 100> uniaxial tension) and 20% (<110> uniaxial tension) in an *ab initio* study [Dubois et al., 2006]. For example, Zhang et al. fabricated a push-to-pull device achieving a fully elastic strain of 13% (loading-unloading tests) and up to 16% before sample fracture [Zhang et al., 2016] (figure 1.6(a)).

Walavalkar et al. proposed a method to strain a nanopillar up to 24 % in flexion by reticulating a light sensitive matrices around the pillar[Walavalkar et al., 2010]. Figure 1.6 (c) shows a Scanning Electron Microscope (SEM) image of the structure. Strained silicon microbridge can also be fabricated by concentration of residual tensile stress present in a thin film. The thin film is situated on top of an oxide layer. First a lithography step is performed to obtain a thin strip of silicon. Then the oxide is etched under the silicon structure to obtain a suspended strip or silicon microbridge. With this method, 4.5 % uniaxial tensile strain was obtained a 30 nm silicon nanowire [Minamisawa et al., 2012]. The structure is illustrated in figure 1.6(b).

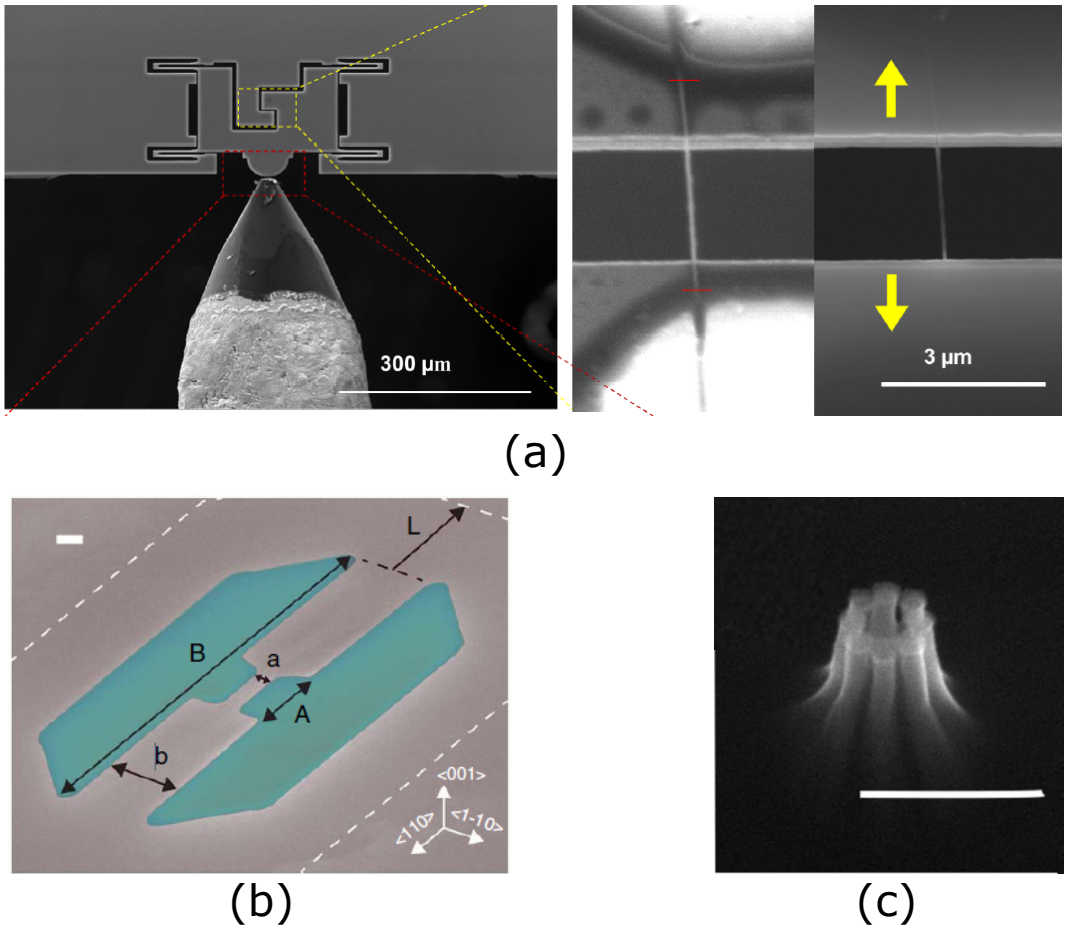


Figure 1.6: SEM observation of different strained silicon nanowires structures present in the literature (a) Push-to-pull structure for a nanowire with a diameter of100 nm [Zhang et al., 2016] (b) Strained silicon microbridge, scale bar is 300 nm [Minamisawa et al., 2012] (c) Strained silicon nanopillar after contraction of an electron activated polymer matrix, scale bar is 500 nm [Walavalkar et al., 2010]

As stated earlier, strained microstructure are also implemented in active devices. Strain induced mobility enhancement has been introduced for MOSFETs at the 90 nm node [Thompson et al., 2004]. Hole mobility increases under compression and even more under tensile strain whereas the mobility of conduction band electrons decreases under compression and increases with tensile strain. Proportionally, the mobility increase for electrons is higher [Haugerud et al., 2003]. For performance enhancing in silicon, biaxial stress is not favored for complexity and cost reasons. Uniaxial stress can be applied in easier ways by using extrinsinc stressor layer (*e.g.*, silicon nitride in CMOS transistors produced by Intel [Ghani et al., 2003]) or in packaging steps [Thompson et al., 2004]. For example, a reconfigurable field effect transistor

based on a strained silicon nanowire can be obtained [Baldauf et al., 2016].

#### 1.1.2.2 At the wafer scale

Different methods to obtain strain silicon micro or nanostrocture were presented in the previous section. However, full size strained wafer can be desirable for the fabrication of devices with a strained layer without using specific architecture or for further stress concentration. Several methods for achieving wafer scale strained films will be presented, with various strain level and silicon crystal quality.

A simple way to induce uniaxial stress in a full size wafer proposed by Himcinschi et al. is the bonding of two wafers while imposing a radius of curvature to the the bonded stack. It offers a good control over the induced strain, however the maximum values achievable are low and the process is not compatible with industrial bonding tools. An extremely low uniaxial strain of 0.077 % for 0.5 m radius of curvature was reported [Himcinschi et al., 2007]. It is worth mentioning as it is the only method reported allowing one to obtain a uniaxially strained layer on a full sheet wafer.

On the other hand numerous works have been published on the production of biaxially strained full sheet wafer. A first example would be biaxial strain induced by bonding two wafers with a temperature gradient. If the two wafers have a different Coefficient of Thermal Expansion (CTE) (*i.e.,* for heterostructures) or present a temperature difference before surface contact, a strain will be present once the assembly is cooled down [Abadie et al., 2020].

Porous silicon layers were also employed as a mean to strain sc-Si layers. Under oxidation, the porous layers expand and induce a significant biaxial strain. 1.2% biaxial strains were achieved in a 60 nm thick pristine silicon layer, after crack apparition up to 2.2% strain were reported [Boucherif et al., 2010; Marty et al., 2006].

Several teams have developed methods to produce strain silicon using epitaxial growth on virtual substrate (*i.e.* SiGe buffer layer with a controlled lattice parameter). The biaxial strain in the silicon layer stems from the lattice mismatch with the substrate. Usually silicon-germanium alloys are used [Drake et al., 2003; Daval et al., 2011]. This method was even used for the industrial production of strained SOI. The maximum stress was reported by Hartmann et al.. Si grown on $Si_{1-x}Ge_x$ with x equal to 20, 30, 40 or 50% with a maximum tensile stress reported of 3.15 GPa for x = 48 %. It corresponds to 1.75 % biaxial strain. Defect densities from $10 \times 10^5$ cm$^{-1}$ to 3 cm$^{-1} \times 10 \times 10^5$ cm$^{-1}$ were reported as the layer thickness increases from 5 to 35 nm [Hartmann et al., 2008]. After epitaxial growth on virtual substrates, the strained silicon layer can be transferred on a carrier silicon wafer using e.g. ion implantation, wafer bonding and fracture during thermal annealing (*i.e.,* based on the SmartCut ™process). This process is illustrated in figure 1.7.

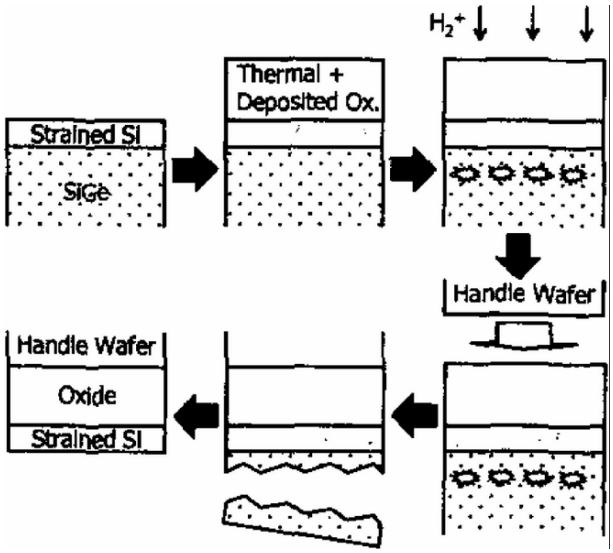


Figure 1.7: Fabrication of strained SOI by layer transfer and selective SiGe etch.[Rim et al., 2003]

## 1.2 Wafer bonding

As discussed in the previous section, wafer bonding is a valuable technique to prepare strained films at the wafer scale. Wafer bonding consist in assembling two wafers with or without the use of an additional adhesive layer. It is used in the microelectronic industry at various stages of the fabrication process of transistors. Its use ranges from handling to making electrical contacts or transistor packaging. Depending on the application, materials properties, CMOS compatibility and thermal budget, different techniques are used to assemble wafers. They are presented in table 1.2 along with the typical bonding conditions and applications.

Going in details over all these techniques is beyond the scope of this work. The objectives here are to study and combine two types of wafer bonding (direct and adhesive bonding), in order to transfer and permanently strain a thin semi-conductor film on a rigid substrate. A detailed review of these two techniques is given below.

| Wafer bonding technique | Typical bonding condition | Advantages and disadvantages | Applications areas |
|---|---|---|---|
| Direct bonding | 600-1200 °C<br>RT in some cases<br>Small or no bond pressure | + high bond strength<br>+ hermetic<br>+ resistant to high temperatures<br>- high surface flatness required<br>- high bond temperature not always compatible with electronic wafers | SOI wafer fabrication |
| Anodic bonding | 150 °C to 500 °C<br>200 V to 1500 V<br>no bond pressure | + high bound strength<br>+ hermetic<br>+ resistant to high temperature<br>- bond temperature in combination with high voltage not always compatible with electronic wafers | sensor packaging |
| Solder bonding | 150 °C to 450 °C<br>Low bond pressure | + high bond strength<br>+ hermetic<br>+ compatible with electronic<br>- solder flux | Bump and flip chip bonding |
| Eutectic bonding | 200 °C to 400 °C<br>Low to moderate bond pressure | + high bond strength<br>+ hermetic<br>+ compatible with electronic wafers<br>- sensitive to native oxides at surfaces | Hermetic packaging<br>Bump and flip-chip bonding, MEMS |
| Thermocompression bonding and direct metal-to-metal bonding | 350 °C to 600 °C<br>100 MPa to 800 MPa (high bond pressure) | + high bond strength<br>+ compatible with electronic wafers - very high net forces for full wafer bonding required<br>- high surface flatness required | Wire bonding<br>Bump and flip-chip bonding *e.g.,* 3D ICs |
| Ultrasonic bonding | RT up to 250 °C<br>High bond pressure | + compatible with electronic wafers<br>- only demonstrated for small bond areas | Wire bonding |
| Low-temperature melting glass bonding | 400 °C to 1100 °C<br>Low to moderate bond pressure | + high bond strength<br>+ hermetic<br>- bond temperatures not always compatible with electronic wafers | sensor packaging |
| Adhesive bonding | RT up to 400 °C<br>Low to moderate bond pressure | + high bond strength<br>+ low bond temperature<br>+ works practically with any substrate material including electronic wafers<br>- no hermetic bond<br>limited temperature stability | MEMS, Sensor packaging, 3D Integrated Circuits (ICs), temporary bonds |

Table 1.2: Presentation of the different types of wafer bonding in microelectronic [Niklaus et al., 2006]

#### 1.2.0.1 Adhesion

The principle of wafer bonding and adhesion in general is that two materials will adhere to each other if they are sufficiently close to each other. The bonding can be of different nature and energy. Table 1.3 presents the order of magnitude of dissociation energy and interatomic distance for different types of bonds. For van der Waals interactions to be significant, the inter-atomic distance needs to be in the 0.3 nm to 0.5 nm range. For direct wafer bonding, as van der Waals forces are always present even at room temperature, it implies that the surface nano-roughness, macro-roughness and curvature must be extremely low for bonding at RT without any external force. The use of an adhesive layer such as a liquid or a low viscosity polymer and thermo compression widely facilitates the creation of a bonding interface between two solid state wafers.

| Type of bonds | Dissociation energy (kJ/mol) | Interatomic distance (nm) |
|---|---|---|
| Van der Waals | 2 to 8 | 0.3 to 0.5 |
| Hydrogen bond | 10 to 30 | 0.2 to 0.3 |
| Dipolar interaction | 5 to 12 | 0.2 to 0.3 |
| Ionic bond | 40 to 80 | 0.2 to 0.3 |
| Covalent bond | 200 to 800 | 0.1 to 0.2 |

Table 1.3: Order of magnitude of bond dissociation energy and interatomic distance for different types of interatomic bonds [Étienne and David, 2012; Platzer, 1969; Miller, 1966].

The bonding interface can then be characterized by its adhesion and adherence. Adhesion is the energy needed to create a bonding interface between two substrates and adherence is the energy needed to separate them. The value of these energies depends on the nature of the bonds at the interface between the different surfaces.

Adhesion would be typically measured by inserting a force sensor between two wafers during bonding. Adherence is more widely used as a metric to evaluate the nature and quality of a bonding interface. Different destructive control techniques have been proposed to evaluated adherence or bonding energy [Vallin et al., 2005] such as blister tests [Forsberg et al., 2013], tensile test [Muller and Stoffel, 1991], or four points bending [Dauskardt et al., 1998; Argoud, 2012].

For two surfaces, the Dupré work of adhesion is defined by:

$$W_{adhesion} = \gamma_1 + \gamma_2 - \gamma_{12} \tag{1.1}$$

where $\gamma_1$, $\gamma_2$ are surface energies and $\gamma_{12}$ is the interface energy.

In the case of wafer bonding, the adherence can be measured by a blade or wedge insertion between two bonded beams. The measurement relies on the balance between elastic energy and surface energy at equilibrium. The work of adhesion is the work required to form two new surfaces with a crack formation from the bonded assembly [Lawn, 1993]. Here the method used is a blade insertion using the Double Cantilever Beam (DCB) model [Maszara et al., 1988].

This method allows for simple, reproducible measurements without any specific sample preparations steps. In the case of Double Cantilever Beam model and wedge insertion, the critical energy release rate $G_{IC}$ (i.e. the elastic energy change upon a variation of bonded area) is equal to the work of adhesion.

$$W_{AB} = G_{IC} = \frac{3Eh^2d^3}{4c^4} \tag{1.2}$$

With $d$ the thickness of the beam, $h$ half the blade thickness, $c$ the crack length and E the Young's modulus in the direction of the crack propagation. The measurement of the crack length allows the determination of $W_{AB}$. A more detailed review of the experimental setup used in this study is presented in subsection 2.1.7.2.

### 1.2.1 Polymer or adhesive bonding

#### 1.2.1.1 Polymers

Alternatively to direct bonding, adhesive bonding can be performed using polymers layers. It alleviates the strict requirements of direct bonding, but comes with its own limitations, as described hereafter. To better appreciate these differences, some elements of the physics and chemistry of polymers are recalled. Polymers are materials formed by macro-molecules, themselves composed by repeating small chemical moieties. These repeating elements are called monomers as illustrated in figure 1.8. Polymer chains can also be organized at a supramolecular level (*e.g.* aligned ) depending on fabrication process parameters. A polymer is defined by the nature of the monomers, the length (or molecular weight) of the chains and the interaction between those chains. The interactions can either be chemical (reticulation) or physical. They are illustrated in figure 1.9

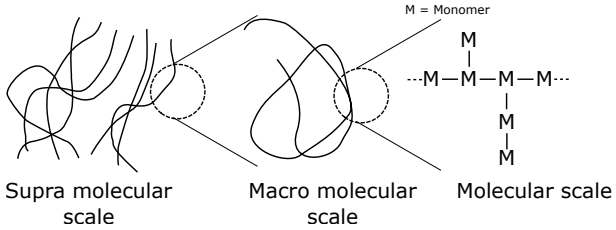


Figure 1.8: Schematic of polymer structure at different scales.

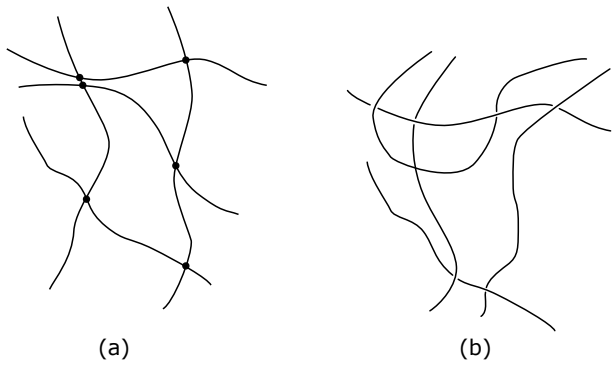


Figure 1.9: Different polymer organic chains organizations: (a) reticulated chains, (b) entangled chains

Depending of the nature of the polymer, they can be initially present in the form of monomers in a solvent, solid to be melted or preformed sheets. Historically, the first polymers used for wafer bonding were photoresist used in photolithography. They are spin coated on the wafer surface and it is still the case for many polymer adhesive. This method yields smooth and homogeneous surface with a microscopic control of the film thickness.

Glass transition temperature is an important metric as it has a strong influence on polymers properties. It characterizes the range of temperature at which an amorphous or semi-crystalline polymer changes from a vitreous to a rubbery material displaying a visco-elastic mechanical behavior. This transition can be reversible for some polymers. The glass transition has a strong influence on certain material properties, such as the Young modulus. A significant drop is observed at $T_g$ as seen in figure 1.10, after the transition a so-called rubber plateau is observed.

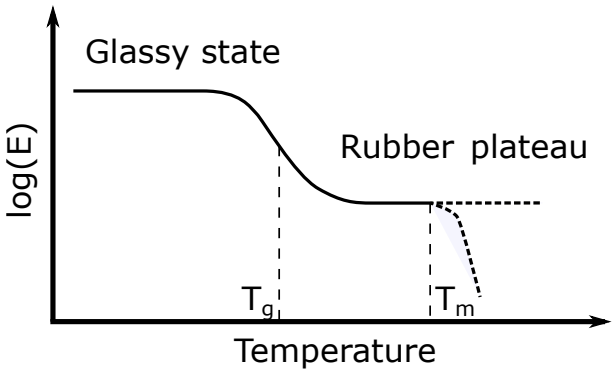


Figure 1.10: Young modulus as a function of temperature for a polymer. $T_g$ can vary from −150 to 150 °C depending on the polymer and heating rate.

#### 1.2.1.2 Polymer bonding in microelectronics

As stated above, bonding requires bringing two surfaces into sufficiently close contact. A polymer layer can be used as an adhesive to bond two wafers as illustrated in figure 1.11 Polymers offer a way to create an adequate surface for bonding various material with relatively low roughness requirement and contained cost. Surface preparation and roughness acceptance are less challenging compared to other techniques such as direct bonding. The compliant nature of polymer adhesive diminishes the effects of wafer surface defects or inhomogeneities. Either thermoplastic or thermosettings polymers are used in microelectronic devices fabrications. A polymer layer is first formed on a wafer surface by drying, solidification of a melted polymer or curing of a precursor (*e.g.,* via mixing, heating, light exposition). The two wafers are then put in contact in a vacuum chamber. In order to properly seal the bonding interface, different parameters are used: temperature, force applied on the bonding stack and bonding chuck nature (*e.g.,* hardness). Alignment procedure can be necessary in some applications [Lee et al., 2011]. This parameters, combined to the nature of the adhesive layer allows for a high tolerance to surface roughness variations compared to other wafer bonding techniques. Thermal budget is an obvious limitation of adhesive wafer bonding, though some glues can sustain up to 400 °C. The adherence energy can be tailored by changing the nature of the polymer and bonding parameter (*i.e.,* temperature, force and gas pressure). Some applications requires temporary wafer bonding such as thinning down using mechanical grinding [Abadie et al., 2019]. Adherence can be increased by using surface preparation on the polymer (*e.g.,* plasma).

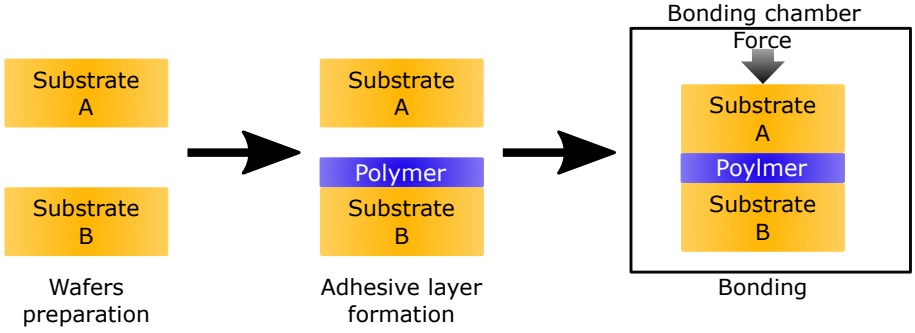


Figure 1.11: Schematic of adhesive wafer bonding. The pressure and temperature of the bonding chamber are controlled.

Polymer or adhesive wafer bonding can be used for various application such as fabrication of 3D ICs[Lee et al., 2011],film and devices transfer for MEMS fabrication [Dragoi et al., 2003], transfer of thin films and thin devices using wafer handling [Montméat et al., 2018; Abadie et al., 2019], wafer level packaging [Linz et al., 2010; Jin et al., 2003].

Here is an example of polymer wafer bonding application for MEMS fabrication proposed by Li et al..

Figure 1.12 presents an example of a fabrication process based on adhesive wafer bonding to obtain a MEMS. Here two wafers are bonded with BCB layers, one of which is patterned. This allows the fabrication of silicon membranes on cavities. The thermal budget of the process (250 °C) is compatible with standard CMOS technology, the fabrication of metallic contacts is possible after the bonding step.

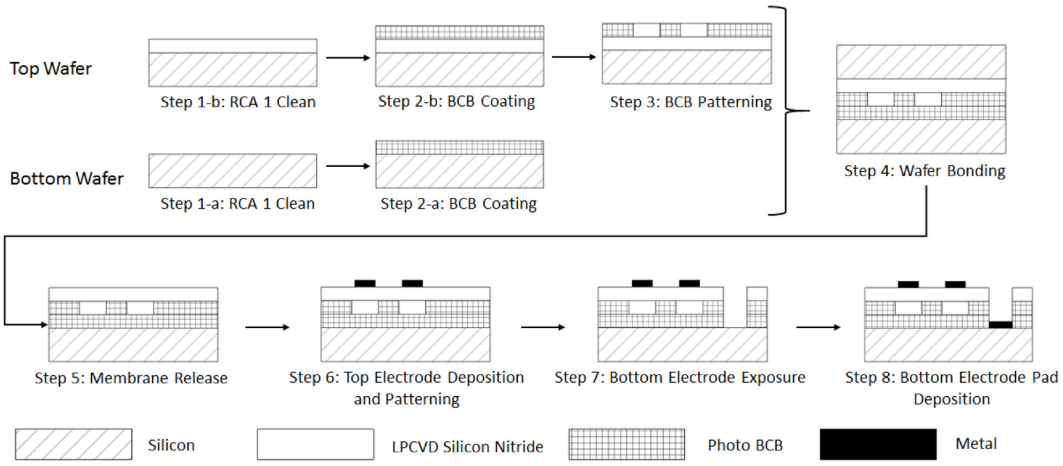


Figure 1.12: Fabrication process of a capacitive micromachined ultrasonic transducers using adhesive wafer with BCB, from [Li et al., 2016].

A SEM images of a transverse cut of the resulting structure can be observed in figure 1.13. The use of adhesive wafer bonding allowed for the fabrication of a MEMS without strict surface finish requirements.

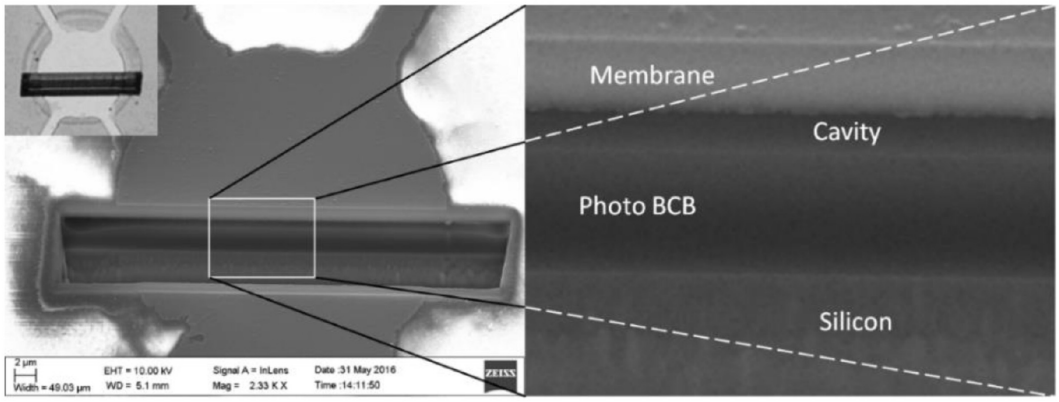


Figure 1.13: SEM image of a capacitive micromachined ultrasonic transducer using adhesive wafer with BCB, from [Li et al., 2016].

## 1.2.2 Direct bonding

### 1.2.2.1 General principle

Direct bonding can be described as the bonding of two materials simply by joining their surfaces without the use of any adhesive layer. This phenomenon has been observed and studied well before its application to semiconductors wafers. Namely as early as 1230-1240, when a Franciscan friar described the importance of cleanliness when joining gold and silver [Anglicus, 1609]. The first industrial application of direct bonding was developed and patented at Philips Research Laboratories for the fabrication of He-Ne laser cavities with a limited thermal budget [Haisma, 1995]. The optical flats bearing and the highly reflective mirrors were direct-bonded to the fused-silica body of the laser. Nowadays, direct bonding is a widespread method in the microelectronic industry, it is used for the fabrication of SOI substrate with the SmartCut™ technology [Bruel, 1995] as well as in the fabrication of MEMS and three dimensional Integrated Circuits (ICs)

[Moriceau et al., 2011]. Among the advantages of direct bonding we can cite the fact that no additional layer is needed on the wafer surfaces, the capability of withstanding high thermal budgets for the the bonding interface and the compatibility of the bonded stack with front-end CMOS technologies [Moriceau et al., 2011]. Front-end is a term referring to the first steps of transistor fabrication in industrial clean room, as opposed to the back-end operations which mostly include the fabrication of metallic contacts. Direct bonding can be performed at RT simply by the contact of two sufficiently clean, smooth and flat wafers. Initially, Van der Waals forces are sufficient to create a bonding interface but yield low bonding energies of about $20\,mJ/m^2$. Further thermal annealing allows the formation of covalent bonds and increase the bonding energy up to $6\,J/m^2$ in the case of silicon. As detailed below, the bonding energy depends mainly on surface state and annealing temperature. Silicon and silicon oxide bonding will be mainly discussed after, although direct bonding can be performed with other materials such as germanium [Akatsu et al., 2006], III-V semiconductors [Sanchez et al., 2018], glass [Bedjaoui and Poulet, 2017] or piezoelectric materials [Ballandras et al., 2019].

#### 1.2.2.2 Surface requirement in microelectronic

The criteria for successful bonding can be understood considering that bonding results from a balance between attractive forces (van der Waals, capillary, etc..) and repulsive forces due to solid-solid contact. The bonding energy results from the difference between the work of adhesive and repulsive forces when the surfaces are brought in contact.

At equilibrium, the two forces balance each other. The equilibrium distance depends on how both forces depend on distance. For contact forces, that can be either attractive (e.g. formation of covalent bonds) or repulsive (compression of asperities), this balance strongly depend on the topography of surfaces.

Thus, although direct bonding presents many advantages, it comes at the cost of strict requirements for the processed wafers.

The first one is of topological order. The curvature of two wafers needs to be low enough and/or similar, because of the elastic energy cost necessary to have the two surface curvatures matching each other. This parameter is usually quantified with a metric called the bow, obtained using an optical profilometer as described in chapter 2. For standard substrate in larger diameter (*i.e.,* 200 or 300 mm) this is not an issue as long as they don't undergo deposition or extensive mechanical grinding steps. At lower scale, the surface nano-roughness needs to be minimized in order to increase the initial contact surface area between the two wafers and allow an approach of the two solids at low distances where attractive forces are large enough. It is typically smaller than 0.6 nm Root mean square (RMS) in a $1\,\mu m \times 1\,\mu m$ area probed with an Atomic Force Microscopy (AFM) [Moriceau et al., 2003]. Again using commercial silicon wafers, this is usually not a concern. In the case of an increase of surface roughness due to process steps, Chemical-mechanical Polishing (CMP) allows achieving a suitable surface state.

Then, particle contamination has to be strongly monitored. Indeed, given the rigidity of a silicon wafer and the lower surface roughness, if a particle of $1\,\mu m$ is present at the interface during bonding, it will result in a 5 mm diameter defect [Tong and Goesele, 1999]. Below a certain particle size, as detailed in figure 1.14, the ratio between the bonding defect and particle size becomes much lower due to a shift from a global bending of the wafers to a local compression [Tong and Goesele, 1999; Maszara et al., 1988; Wan et al., 1993; Stengl et al., 1989]. Bonding processes are carried out in clean rooms where the tolerance for particle contamination is the lowest possible. Prior to bonding, the wafers undergo a particle removal step with wet cleaning using ammonia based solutions.

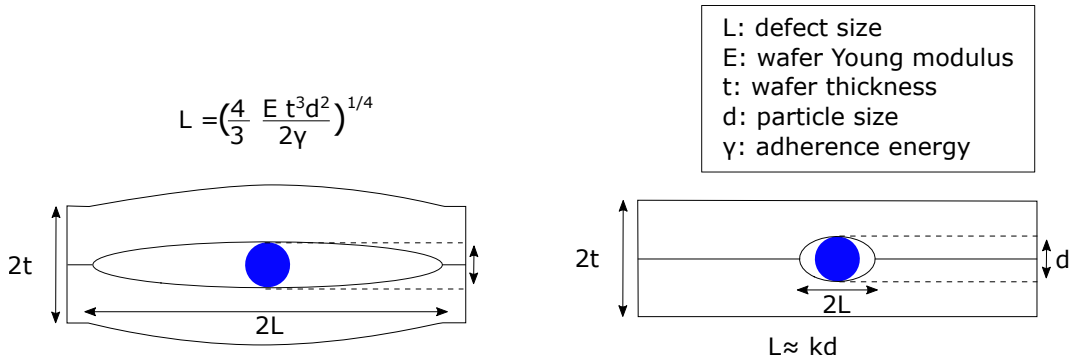


Figure 1.14: Influence of the presence of a particle on the bonding interface. [Wan et al., 1993; Maszara et al., 1988; Qin-Yi Tong et al., 1994]

Organic contaminants are also removed from the surface prior to bonding as even in a clean room environment some organic compounds are present in the atmosphere. Wet techniques based on acidic solutions are typically used or Ultra-Violet (UV) ozone treatment, with the aim of oxidizing these compounds.

The final preparation step for direct bonding consist in tuning the surface chemistry. The silicon surface can either be hydrophobic or hydrophilic. The first case is achieved with a short HF etching step which leaves the surface terminated by hydrogen atoms (Si-H bonds ). In the second case, oxidizing chemistries are used in order to have silanol groups (Si-OH) at the surface. For the bonding of two hydrophilic silicon wafers, the number of silanol groups on the surfaces has a strong influence on the bonding mechanism. This implies that interfacial water be present at the wafer surface during bonding. Only this type of direct bonding will be discussed in this work. The mechanism remains the same for a Si/Si hydrophilic bonding or a $SiO_2$/Si bonding when the silicon dioxide layer is thermally grown and has a thickness smaller than 20 nm. In both cases, a hydrolized thin oxide is present on surfaces. Above this thickness some differences can be observed for higher post-bonding temperature [Ventosa et al., 2008] due the different capability of these oxides to absorb hydrogen produced at higher temperatures.

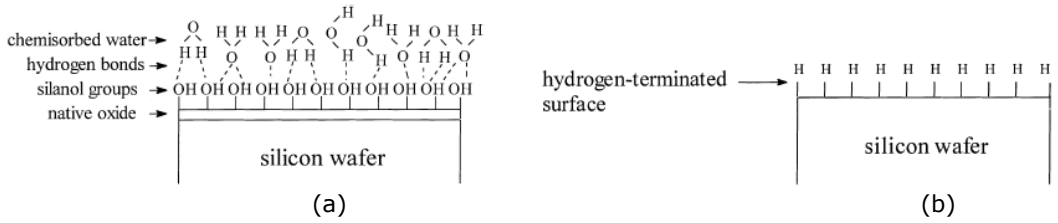


Figure 1.15: Schematic of the surface chemistry of silicon wafer prior to direct bonding (a)Hydrophilic surface (b) Hydrophobic surface [Plößl and Kräuter, 1999]

#### 1.2.2.3 Mechanisms

Direct wafer bonding is usually performed at RT and the resulting stack is then annealed to strengthen the bonding interface. For an hydrophilic wafer bonding, the evolution of bonding energy as a function of annealing temperature is presented in figure 1.16. The different steps in the increase of adhesion energy correspond to several mechanisms taking place.

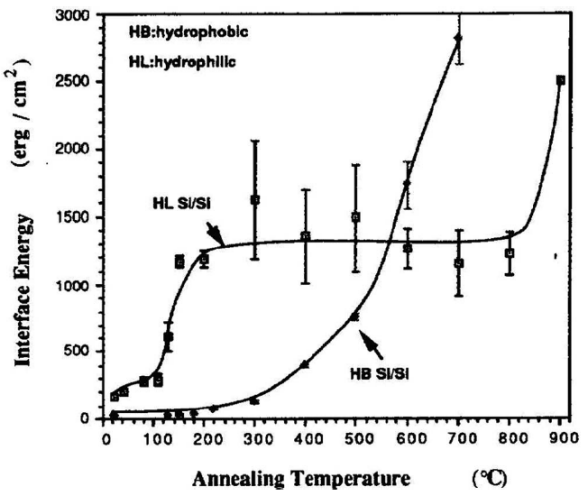


Figure 1.16: Bonding energy as a function of annealing temperature in an hydrophilic and hydrophobic silicon silicon wafer bonding [Qin-Yi Tong et al., 1994]

The first driving force of direct bonding are Van Der Waals interactions that have to overcome the contact forces between the two wafers associated with curvature and surface roughness of the bonded pair, in order to create a sufficient contact area. This way a bonding can be performed at RT. The bonding is either manually initiated by applying a slight pressure at a wafer edges or using a "bond pin" in automatic bonders. From there, a propagating bonding front can be observed using Infrared (IR) imaging. The order of magnitude for the velocity of this bonding front is 2 cm/s. The bonding front dynamics has been explained by Rieutord et al. who linked the bonding front velocity (U) to the adhesion energy $2\gamma$ and other parameters such as the atmosphere gas viscosity $\eta$ or the rigidity of the bonded wafers $\frac{Et^3}{1-\nu^2}$ [Rieutord et al., 2005]:

$$U = \frac{(2\gamma)^{5/4}}{\eta t^{3/4}} \frac{\Lambda^{1/2}}{\left(\frac{E}{1-\nu^2}\right)^{1/4}} \left(1/9A^{3/4}\right) \tag{1.3}$$

With $A \approx 0.95$, $\Lambda$ is the mean free path, $t$ the wafer thickness, E the wafer Young modulus, $\nu$ the Poisson ratio. It shows that the wafers thickness and rigidity have a strong importance on the kinetic of the bonding interface formation.

Initially, direct wafer bonding has been described mainly from a purely chemical point of view by the evolution of the interfacial bonds. Stengl et al. proposed a reaction to explain the transformation of silanol ending to covalent bonds between the wafers : $Si{-}OH + Si{-}OH \longrightarrow Si{-}O{-}Si + H_2O$

Rieutord et al. pointed out the importance of considering properly the repulsive contact part in the interaction and proposed a model based on rough surface contact to describe adhesion mechanism [Rieutord et al., 2006]. This model, which predicts for example the existence of a small gap at the interface, fits experimental observations of the bonding interface during thermal annealing. Figure 1.17 present a schematic of this model. As temperature increases, new interfacial bonds are created and adhesive energy increases resulting in a contact area increase due to local elasticity or plasticity (asperity compression). The formation of the covalent bonds between the two wafers increases the local adhesion energy, and contact points tend to spread, closing the interface in analogy to a ziplock mechanism. [Ventosa et al., 2009]. Ventosa et al. studied this mechanism using high energy X-Ray Reflectivity (XRR) to measure the electron density at the bonding interface as seen in figure 1.17. Extensive use of this technique, complemented by other techniques like FTIR-MIR spectroscopy, TEM, acoustic wave reflection, allowed a full description of the bonding interface and the sealing mechanisms, from RT to 1200°C annealing temperatures.

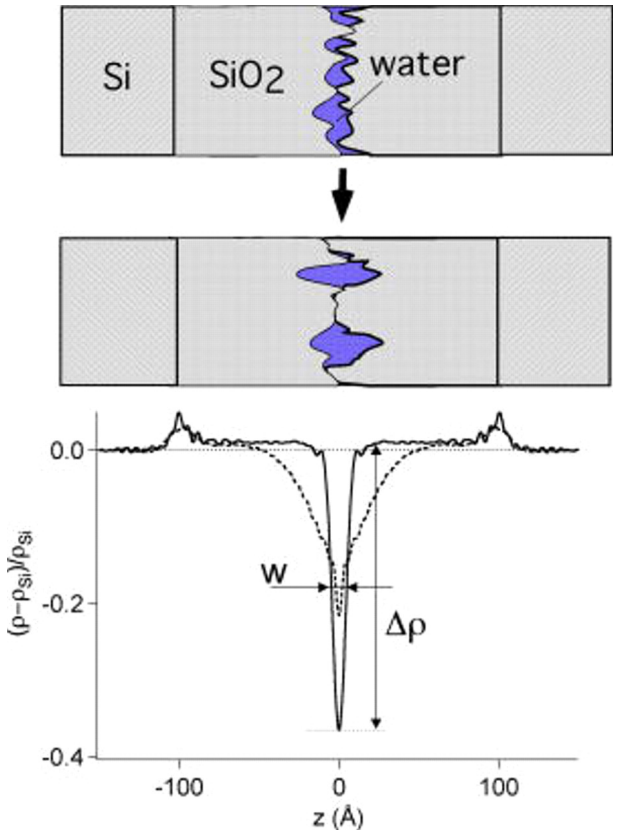


Figure 1.17: Sealing mechanism of the oxide–oxide bonding (top). The electron density profiles are shown on the bottom curve, at room temperature (solid line) and after annealing at 400 °C for 2 h (dashed line). [Ventosa et al., 2009]

## 1.3 Transfer techniques for semi-conductor thin film

Having discussed in the previous sections the interest of applying strain to single crystal material and how to bond such a material to another one, we now turn to the transfer a semi-conductor thin film. In this work, we use a route where we apply strain with an external load on a thin film, thus there is a need to obtain and transfer a crystalline semi-conductor thin film, such as silicon, on a flexible polymer substrate than can be more conveniently handled. The use of an external force offers more flexibility and range in the study of strain engineering and has been an historically relevant choice [Jayaraman, 1983]. This approach is also widely used for the study of mechanical properties of metallic films. These films can be directly formed on organic materials and present a poly-crystalline structure [Djaziri et al., 2011; He et al., 2016; Renault et al., 2003]. A similar procedure could be considered for silicon using low temperature deposition on polymer substrates but it would be limited to poly-crystalline silicon [Fortunato et al., 2012]. Here the goal is to separate the fabrication of a single crystal semi-conductor material and the application of strain. This way the quality and dimension of the materials are finely controlled (*i.e.,* a sc-Si film with a diameter of 200 mm). Then the use of external stress allows tuning the strain applied on the thin film in orientation and absolute value. To achieve these, the fabrication and transfer of sc-Si must be studied.

### 1.3.1 Silicon on Insulator fabrication using SmartCut™technology

A widespread technique used for the transfer of single-crystal Silicon (sc-Si) thin film is based on wafer direct bonding and splitting by annealing after ion implantation. This is the basis of the SmartCut™technology. In this study, in order not to also cope with the implantation and fracture problems, the implantation and fracture steps can be avoided starting from a Silicon on Insulator (SOI)-substrate already manufactured. This type of substrate is composed of three layers :

- A thin top sc-Si layer. The SOI used in this study are oriented such that the (001) planes are parallel to the surface, within a miscut tolerance of 1°, and the (110) planes are parallel to a line joining the wafer center and the notch. Its thickness ranges from tens of nanometers to several micrometers.
- A Buried Oxide (BOX) layer composed of thermal silicon oxide. Its thickness ranges from tens of nanometers to several micrometers.
- A thick bulk (100) silicon substrate.

The motivation for SOI use in microelectronic applications is the vertical separation of the active silicon layer from the bulk silicon by an insulating oxide layer. It greatly limits parasitic effects, such as leakage currents or radiation-induced photocurrents. Moreover, it enables the elaboration of more power effective CMOS transistors [Celler and Cristoloveanu, 2003]. Here the SOI are produced by Soitec using the Smart-Cut ™ process [Bruel, 1993, 1995]. It relies on direct wafer bonding and ion implantation in order to fracture a donor wafer as presented in figure 1.18. Smart Cut™ is now the most common method to manufacture SOI substrate as it can be used to produce a wide range of thicknesses for the BOX and top silicon layer while maintaining a low defect density and excellent crystalline quality. The thickness of the top Si layer and of the BOX can be tailored to the desired application (*e.g.*, RF, power or photonic applications). Using wafers produced this way ensures to obtain a perfect single crystal layers with low defect density, homogeneous thickness and well defined orientation.

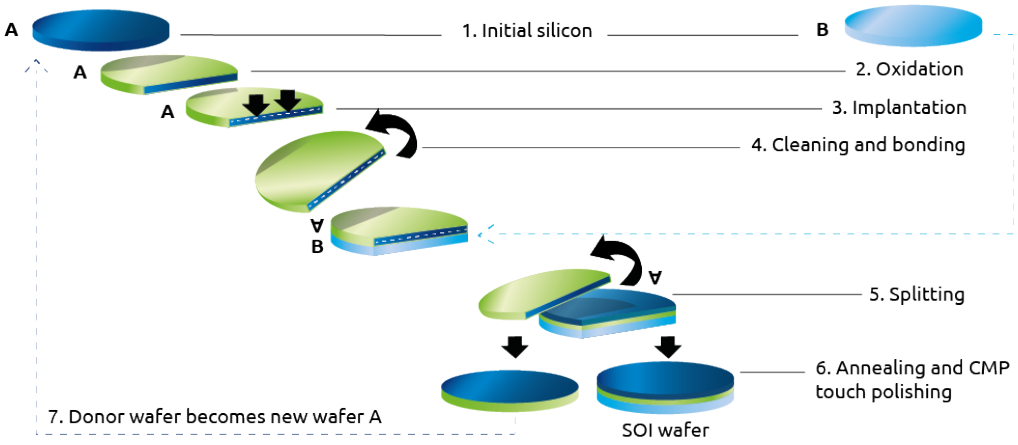


Figure 1.18: Schematic of the SmartCut™ process [Soitec, 2020]

### 1.3.2 Rigid Silicon On Polymer structures

As showed earlier, polymers are commonly used in semiconductor processing. And many of them have already been used to elaborate heterostructures with semi-conductors : polyethylene naphtalate [Guan et al., 2016], polyepoxy [Liu et al., 1998], polypyrrole [Chida et al., 2011], or polyimide [Sánchez-Pérez et al., 2011]. Argoud et al. also developed a process to transfer an sc-Si films on a Benzocyclobutene (BCB) layer using an approach derived from SmartCut™. A donor wafer is bonded with a BCB layer to a carrier wafer after ion implantation. Given the compliant nature of the adhesive layer, a minimal thickness was found in order to obtain a suitable quality transfer after fracture of the implanted silicon layer. Figure 1.19 presents the different options, in order to have a total transfer, the presence of a stiffener or polymer thickness lower than 200 nm are required.

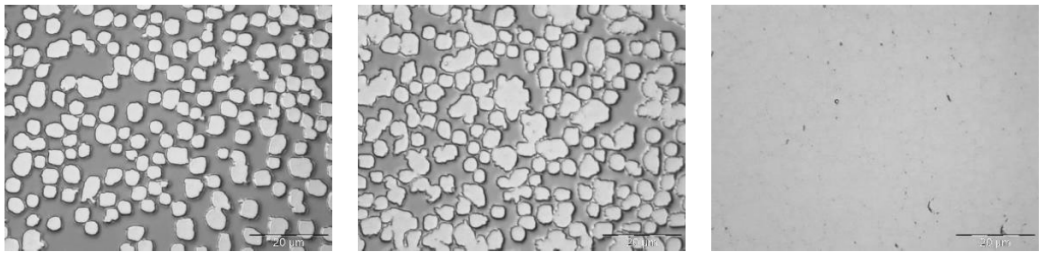


Figure 1.19: Experimental configuration for the transfer of a sc-Si thin film on a BCB layer using ionic implantation and fracture.[Argoud et al., 2010]

A Taiko process developed by Disco was also used to obtained SOP structure. Two wafers are temporary bonded. The backside of the donor wafer is first mechanically ground down to 40 µm only in a central disk. A chemical etching decreases the thickness of the central film down to 5 µm. The imprint left by the grinding is filled with PDMS and the carrier is dismounted, leaving a structure as the one visible in figure 1.20. The frontside can undergo further chemical etching to achieve a 5 µm silicon thickness layer. This process allows for a simple handling of the transferred film.

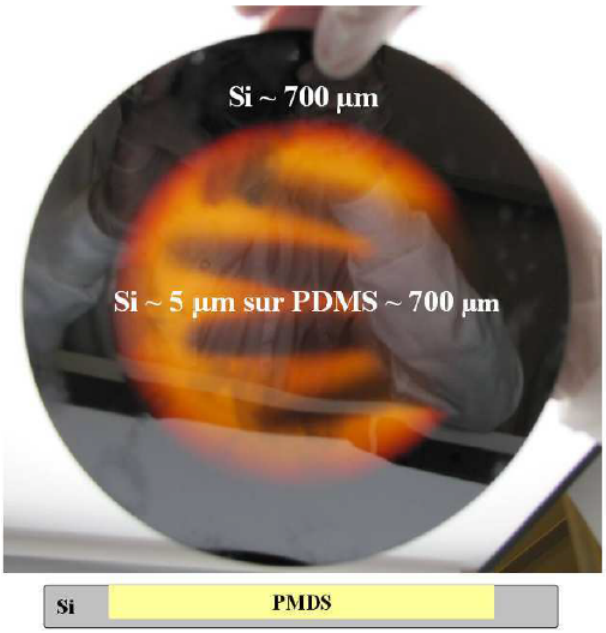


Figure 1.20: Snapshot of a 5 µm silicon thin on PDMS transferred using a Taiko process developed by Disco company [Argoud, 2012].

A common idea found in the literature is to transfer the top silicon layer of a SOI onto a polymer layer. They presence of a BOX maintains the good quality of the silicon thin film during the transfer. The general idea is illustrated in figure 1.21. Mechanical grinding is commonly used to remove thick layers of silicon (*e.g.*., from one to several hundred µm). However it is not suitable for ultra-thin film as the silicon layer presents some defects as deep as 1 µm even with a fine grinding [Haapalinna et al., 2004]. Chemical mechanical polishing (CMP) methods can achieve a defect free surface with a low surface roughness but can only be applied to remove thin silicon layers. Chemical etching (e.g with TMAH or KOH) is suitable to reduce thick layers, though the resulting layers thickness can display some inhomogeneity [Biswas and Kal, 2006]. Several of these methods are often combined to obtain the desired thickness with a suitable quality on the right substrate.

Argoud studied the transfer of silicon thin films (14 nm and 100 nm thick) on polymer substrates: BCB and Polydimethylsiloxane (PDMS). A SOI is bonded to a rigid carrier using an adhesive polymer layer and the backside of the SOI is removed successively by mechanical grinding and chemical etching. In the case of PDMS layers, undulation and fractures were present in the silicon layer [Argoud, 2012]. Similarly a transfer of a SOI top silicon layer(70-220 nm thick) was performed on a 200 nm thick thermosetting nano-imprint resist [Bleiker et al., 2017]. A rigid carrier wafer is often needed for handling the silicon thin film. Interface engineering to further separate the carrier can be difficult, however it is required for the fabrication of a flexible structure.

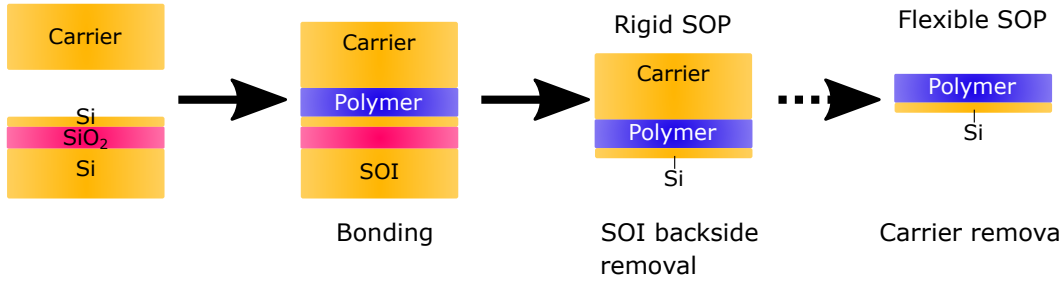


Figure 1.21: General schematic of SOI dismounting on a polymer layer to produce rigid or flexible SOP structures.

Other groups have proposed transfer process based on polymer bonding and mechanical grinding [Byun et al., 2010]. At low thicknesses (*i.e.,* under 100 µm), a significant portion of the silicon becomes defective and a high bow is observed due to the mechanical stress induced by the mechanical grinding [Haapalinna et al., 2004].

### 1.3.3 Flexible and stretchable SOP

As shown earlier, the transfer of silicon layers on polymer layers is well studied. However, obtaining a stand-alone polymer substrate for a transferred silicon layer requires more development to control the different interfaces. More complex flows based on ion implantation are possible with a double transfer, first one on a glass substrate via hydrogen implantation and fracture then a second onto a polymer substrate [Senawiratne and Usenko, 2011].

Using the SOI dismounting approach (figure 1.21), previous development in our group allowed the transfer of a 200 nm sc-Si on flexible polymer substrate [Montméat et al., 2016]. Byun et al. also obtained an oxide/silicon on BCB/PEN with a 1.5 µm thick silicon layer, though the presence of an oxide layer on top of the structure limits the possible applications. More recently, the transfer of a sc-Si layer from an SOI to a PDMS substrate was demonstrated simply by etching the BOX with HF and stamping the weakly attached silicon layer [Ochoa and Li, 2021]. However, the crack-free areas reported are an order of magnitude smaller than other works presented here (*i.e.,* 100 µm × 100 µm).

The previous works presented were based on the transfer of full-sheet wafers (*i.e.,* without any pattern). The J.A. Roger's group also took a similar approach but with patterned SOI. Ribbons are manufactured from the top silicon layer. After a polymer bonding step, a selective chemical etching step is performed to partially etched the BOX. The silicon ribbons can then be transferred on the polymer substrate thanks to the mechanical rupture of the remaining oxide pad . Some examples of the resulting structure and devices are displayed in figure 1.22.

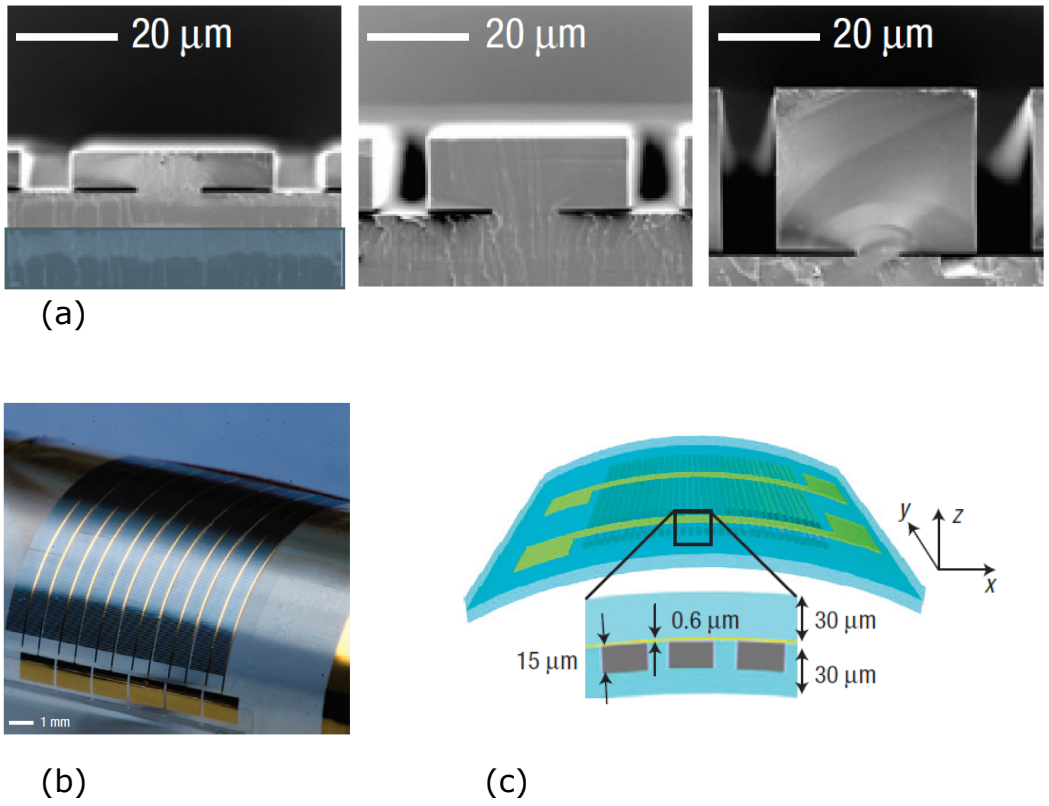


Figure 1.22: Illustration of a flexible silicon on polymer produced in J.A. Rogers' group (a) SEM images of underetched silicon ribbons prior to their transfer on PDMS substrate. (b) Snapshot of a resulting flexible solar microcells and (c) corresponding schematic.

## Conclusion

This chapter exposed the importance and effects of strain in semi-conductors. Controlling strain can increase performances of existing devices and also open new applications for existing materials and structure. For more than two decades, strain engineering has been at the heart of transistor fabrication. Several methods to induce strain in micro-structures have been presented. They can either be performed during transistor fabrication or on stand-alone structures for more fundamentals studies. Other approaches aims at producing strained layers at the wafer scale, they are mainly based on epitaxial growth and thus limited in crystal quality, strain level and strain nature (*i.e.*, biaxial). In the next chapter, we propose an approach for large scale production of strained semi-conductor thin films. This method is based on layer transfer using wafer bonding and external mechanical loading. To introduce the problematic of the thesis, an overview of wafer bonding techniques and mechanism has been given. Polymer wafer bonding offers a versatile method for layer transfer and can be applied to different materials and configuration. Direct wafer bonding allows the creation of covalent bonds in between two surface at the price of strict surface roughness and contamination requirements. A literature review of different silicon layer transfer methods is given in order to position the work presented here.

## References

Abadie, K., Fournel, F., Morales, C., Vignoud, L., Colona, J.-P. and Widiez, J. [2020]. Manufacturing of Optimized Ge Substrates Using a Covalent Bonding Process, ECS.
**URL:** *https://ecs.confex.com/ecs/prime2020/meetingapp.cgi/Paper/139169* 11

Abadie, K., Montméat, P., Enot, T., Fournel, F. and Wimplinger, M. [2019]. Application of temporary adherence to improve the manufacturing of 3D thin silicon wafers, *International Journal of Adhesion and Adhesives* **91**: 123–130.
**URL:** *http://www.sciencedirect.com/science/article/pii/S0143749619300739* 16

Akatsu, T., Deguet, C., Sanchez, L., Allibert, F., Rouchon, D., Signamarcheix, T., Richtarch, C., Boussagol, A., Loup, V., Mazen, F., Hartmann, J.-M., Campidelli, Y., Clavelier, L., Letertre, F., Kernevez, N. and Mazure, C. [2006]. Germanium-on-insulator (GeOI) substrates—A novel engineered substrate for future high performance devices, *Materials Science in Semiconductor Processing* **9**(4): 444–448. Number: 4.
**URL:** *http://www.sciencedirect.com/science/article/pii/S1369800106001818* 18

Anglicus, B. [1609]. *De genuinis rerum coelestium, terrestrium at inferarum proprietatibus rerum (Book 16, Chap. 4, p. 718, Wolfgang Richter, Frankfurt, 1601).*, Vol. 16. 17

Argoud, M. [2012]. *Mécanismes de collage et de transfert de films monocristallins dans des structures à couches de polymères*, PhD Thesis, Université de Grenoble. vii, 14, 23, 24

Argoud, M., Moriceau, H., Fretigny, C., Rieutord, F., Morales, C. and Clavelier, L. [2010]. Single Crystal Silicon Film Transfer onto Polymer, *ECS Trans.* **33**(4): 217–224. Number: 4.
**URL:** *http://ecst.ecsdl.org/content/33/4/217* vii, 22, 23

Baldauf, T., Heinzig, A., Mikolajick, T., Weber, W. and Trommer, J. [2016]. Strain-engineering for improved tunneling in reconfigurable silicon nanowire transistors, pp. 1–4. 11

Ballandras, S., Courjon, E., Bernard, F., Laroche, T., Clairet, A., Radu, I., Huyet, I., Drouin, A. and Butaud, E. [2019]. New generation of SAW devices on advanced engineered substrates combining piezoelectric single crystals and Silicon, *2019 Joint Conference of the IEEE International Frequency Control Symposium and European Frequency and Time Forum (EFTF/IFC)*, pp. 1–6. ISSN: 2327-1949. 18

Bedell, S., Khakifirooz, A. and Sadana, D. [2014]. Strain scaling for CMOS, *MRS Bull.* **39**(2): 131–137.
**URL:** *http://link.springer.com/10.1557/mrs.2014.5* 5

Bedjaoui, M. and Poulet, S. [2017]. Direct Bonding and Debonding Approach of Ultrathin Glass Substrates for High Temperature Devices, *2017 IEEE 67th Electronic Components and Technology Conference (ECTC)*, pp. 725–732. 18

Biswas, K. and Kal, S. [2006]. Etch characteristics of KOH, TMAH and dual doped TMAH for bulk micromachining of silicon, *Microelectronics Journal* **37**(6): 519–525. Number: 6. 23

Bleiker, S. J., Dubois, V., Schröder, S., Stemme, G. and Niklaus, F. [2017]. Adhesive wafer bonding with ultrathin intermediate polymer layers, *Sensors and Actuators A: Physical* **260**: 16–23.
**URL:** *https://www.sciencedirect.com/science/article/pii/S0924424717301292* 24

Bollani, M., Chrastina, D., Gagliano, L., Rossetto, L., Scopece, D., Barget, M., Mondiali, V., Frigerio, J., Lodari, M., Pezzoli, F., Montalenti, F. and Bonera, E. [2015]. Local uniaxial tensile strain in germanium of up to 4% induced by SiGe epitaxial nanostructures, *Applied Physics Letters* **107**(8): 083101. Number: 8.
**URL:** *http://aip.scitation.org/doi/10.1063/1.4928981* 8

Boucherif, A., Blanchard, N. P., Regreny, P., Marty, O., Guillot, G., Grenet, G. and Lysenko, V. [2010]. Tensile strain engineering of Si thin films using porous Si substrates, *Thin Solid Films* **518**(9): 2466–2469. Number: 9.
**URL:** *http://www.sciencedirect.com/science/article/pii/S0040609009016320* 11

Bruel, M. [1993]. PROCEDE DE FABRICATION DE FILMS MINCES DE MATERIAU SEMICONDUCTEUR. Inventors: _:n3097 Issue: FR9111491. 22

Bruel, M. [1995]. Silicon on insulator material technology, *Electronics Letters* **31**(14): 1201–1202. Number: 14 Conference Name: Electronics Letters. 17, 22

Byun, K. Y., Ferain, I., Song, S., Holl, S. and Colinge, C. [2010]. Single-Crystalline Silicon Layer Transfer to a Flexible Substrate Using Wafer Bonding, *Journal of Elec Materi* **39**(10): 2233–2236. Number: 10. 24

Celler, G. K. and Cristoloveanu, S. [2003]. Frontiers of silicon-on-insulator, *Journal of Applied Physics* **93**(9): 4955–4978. Number: 9.
**URL:** *http://aip.scitation.org/doi/10.1063/1.1558223* 22

Chida, Y., Katsumata, H., Fujiya, T., Kaihatsu, S., Morita, T., Hoshino, D. and Nishioka, Y. [2011]. Silicon linear actuator driven by electrochemomechanical strain of polypyrrole film, *Sensors and Actuators A: Physical* **169**(2): 367–372. Number: 2.
**URL:** *http://www.sciencedirect.com/science/article/pii/S0924424710005078* 22

Dauskardt, R. H., Lane, M., Ma, Q. and Krishna, N. [1998]. Adhesion and debonding of multi-layer thin film structures, *Engineering Fracture Mechanics* **61**(1): 141–162.
**URL:** *https://www.sciencedirect.com/science/article/pii/S0013794498000526* 14

Daval, N., Figuet, C., Aulnette, C., Landru, D., Drazek, C., Bourdelle, K. K., Guiot, E., Letertre, F., Nguyen, B.-Y. and Mazure, C. [2011]. SiGe and Ge on Insulator Wafers, pp. 29–38.
**URL:** *http://ecst.ecsdl.org/cgi/doi/10.1149/1.3570773* 11

Djaziri, S., Renault, P.-O., Hild, F., Le Bourhis, E., Goudeau, P., Thiaudière, D. and Faurie, D. [2011]. Combined synchrotron X-ray and image-correlation analyses of biaxially deformed W/Cu nanocomposite thin films on Kapton, *J Appl Crystallogr* **44**(5): 1071–1079. Number: 5. 21

Dragoi, V., Glinsner, T., Mittendorfer, G., Wieder, B. and Lindner, P. [2003]. Adhesive wafer bonding for MEMS applications, Maspalomas, Gran Canaria, Canary Islands, Spain, p. 160. 16

Drake, T. S., Chléirigh, C. N., Lee, M. L., Pitera, A. J., Fitzgerald, E. A., Antoniadis, D. A., Anjum, D. H., Li, J., Hull, R., Klymko, N. and Hoyt, J. L. [2003]. Fabrication of ultra-thin strained silicon on insulator, *Journal of Elec Materi* **32**(9): 972–975. Number: 9.
**URL:** *https://link.springer.com/article/10.1007/s11664-003-0232-x* 11

Dubois, S. M.-M., Rignanese, G.-M., Pardoen, T. and Charlier, J.-C. [2006]. Ideal strength of silicon: An ab initio study, *Phys. Rev. B* **74**(23): 235203. Number: 23.
**URL:** *https://link.aps.org/doi/10.1103/PhysRevB.74.235203* 10

Forsberg, F., Saharil, F., Haraldsson, T., Roxhed, N., Stemme, G., Wijngaart, W. v. d. and Niklaus, F. [2013]. A comparative study of the bonding energy in adhesive wafer bonding, *J. Micromech. Microeng.* **23**(8): 085019. Number: 8 Publisher: IOP Publishing. 14

Fortunato, G., Pecora, A. and Maiolo, L. [2012]. Polysilicon thin-film transistors on polymer substrates, *Materials Science in Semiconductor Processing* **15**(6): 627–641.
**URL:** *https://www.sciencedirect.com/science/article/pii/S1369800112001059* 21

Gassenq, A., Guilloy, K., Osvaldo Dias, G., Pauc, N., Rouchon, D., Hartmann, J.-M., Widiez, J., Tardif, S., Rieutord, F., Escalante, J., Duchemin, I., Niquet, Y.-M., Geiger, R., Zabel, T., Sigg, H., Faist, J., Chelnokov, A., Reboud, V. and Calvo, V. [2015]. 1.9% bi-axial tensile strain in thick germanium suspended membranes fabricated in optical germanium-on-insulator substrates for laser applications, *Appl. Phys. Lett.* **107**(19): 191904. Number: 19.
**URL:** *https://aip.scitation.org/doi/10.1063/1.4935590* 6, 8

Gassenq, A., Tardif, S., Guilloy, K., Duchemin, I., Pauc, N., Hartmann, J. M., Rouchon, D., Widiez, J., Niquet, Y. M., Milord, L., Zabel, T., Sigg, H., Faist, J., Chelnokov, A., Rieutord, F., Reboud, V. and Calvo, V. [2017]. Raman-strain relations in highly strained Ge: Uniaxial ⟨100⟩, ⟨110⟩ and biaxial (001) stress, *Journal of Applied Physics* **121**(5): 055702. Number: 5.
**URL:** *http://aip.scitation.org/doi/10.1063/1.4974202* 8

Geiger, R., Zabel, T., Marin, E., Gassenq, A., Hartmann, J.-M., Widiez, J., Escalante, J., Guilloy, K., Pauc, N. and Rouchon, D. [2015]. Uniaxially stressed germanium with fundamental direct band gap. 7, 8

Ghani, T., Armstrong, M., Auth, C., Bost, M., Charvat, P., Glass, G., Hoffmann, T., Johnson, K., Kenyon, C. and Klaus, J. [2003]. A 90nm high volume manufacturing logic technology featuring novel 45nm gate length strained silicon CMOS transistors, *IEEE International Electron Devices Meeting 2003*, IEEE, pp. 11–6. 5, 10

Guan, Q., Laven, J., Bouten, P. C. and de With, G. [2016]. Mechanical failure of brittle thin films on polymers during bending by two-point rotation, *Thin Solid Films* **611**: 107–116.
**URL:** *https://linkinghub.elsevier.com/retrieve/pii/S0040609016301766* 22

Guilloy, K., Pauc, N., Gassenq, A., Gentile, P., Tardif, S., Rieutord, F. and Calvo, V. [2015]. Tensile Strained Germanium Nanowires Measured by Photocurrent Spectroscopy and X-ray Microdiffraction, *Nano Lett.* **15**(4): 2429–2433. Number: 4.
**URL:** *http://dx.doi.org/10.1021/nl5048219* 6

Guilloy, K., Pauc, N., Gassenq, A., Niquet, Y.-M., Escalante, J.-M., Duchemin, I., Tardif, S., Osvaldo Dias, G., Rouchon, D., Widiez, J., Hartmann, J.-M., Geiger, R., Zabel, T., Sigg, H., Faist, J., Chelnokov, A., Reboud, V. and Calvo, V. [2016]. Germanium under High Tensile Stress: Nonlinear Dependence of Direct Band Gap vs Strain, *ACS Photonics* **3**(10): 1907–1911. Number: 10.
**URL:** *http://pubs.acs.org/doi/10.1021/acsphotonics.6b00429* 6, 8

Haapalinna, A., Nevas, S. and Pähler, D. [2004]. Rotational grinding of silicon wafers—sub-surface damage inspection, *Materials Science and Engineering: B* **107**(3): 321–331. Number: 3.
**URL:** *http://www.sciencedirect.com/science/article/pii/S0921510703006858* 23, 24

Haisma, J. [1995]. Direct bonding in patent literature, *Philips Journal of Research* **49**(1): 165–170. Number: 1.
**URL:** *http://www.sciencedirect.com/science/article/pii/0165581795820094* 17

Hartmann, J. M., Abbadie, A., Rouchon, D., Barnes, J. P., Mermoux, M. and Billon, T. [2008]. Structural properties of tensile-strained Si layers grown on Si1-xGex virtual substrates (x=0.2, 0.3, 0.4 and 0.5), *Thin Solid Films* **516**(12): 4238–4246. Number: 12.
**URL:** *http://www.sciencedirect.com/science/article/pii/S0040609008000084* 11

Haugerud, B. M., Bosworth, L. A. and Belford, R. E. [2003]. Mechanically induced strain enhancement of metal–oxide–semiconductor field effect transistors, *Journal of Applied Physics* **94**(6): 4102–4107. Number: 6.
**URL:** *http://aip.scitation.org/doi/abs/10.1063/1.1602562* 10

He, W., Goudeau, P., Le Bourhis, E., Renault, P.-O., Dupré, J. C., Doumalin, P. and Wang, S. [2016]. Study on Young's modulus of thin films on Kapton by microtensile testing combined with dual DIC system, *Surface and Coatings Technology* **308**: 273–279.
**URL:** *http://www.sciencedirect.com/science/article/pii/S0257897216309197* 21

Herman, F. [1955]. The Electronic Energy Band Structure of Silicon and Germanium, *Proceedings of the IRE* **43**(12): 1703–1732. Conference Name: Proceedings of the IRE. vii, 5

Himcinschi, C., Radu, I., Muster, F., Singh, R., Reiche, M., Petzold, M., Gösele, U. and Christiansen, S. [2007]. Uniaxially strained silicon by wafer bonding and layer transfer, *Solid-State Electronics* **51**(2): 226–230. Number: 2.
**URL:** *http://linkinghub.elsevier.com/retrieve/pii/S0038110107000081* 11

Hryciw, A., Miller, D. A. B., Jain, J. R., Brongersma, M. L., Howe, R. T. and Baer, T. M. [2012]. A micromachining-based technology for enhancing germanium light emission via tensile strain, *Nature Photonics* **6**(6): 398. Number: 6. 8

Huo, Y., Lin, H., Chen, R., Makarova, M., Rong, Y., Li, M., Kamins, T. I., Vuckovic, J. and Harris, J. S. [2011]. Strong enhancement of direct transition photoluminescence with highly tensile-strained Ge grown by molecular beam epitaxy, *Appl. Phys. Lett.* **98**(1): 011111. Number: 1.
**URL:** *https://aip.scitation.org/doi/10.1063/1.3534785* 8

Jaddi, S., Coulombier, M., Raskin, J.-P. and Pardoen, T. [2019]. Crack on a chip test method for thin free-standing films, *Journal of the Mechanics and Physics of Solids* **123**: 267–291.
**URL:** *https://linkinghub.elsevier.com/retrieve/pii/S0022509618305659* 9

Jayaraman, A. [1983]. Diamond anvil cell and high-pressure physical investigations, *Rev. Mod. Phys.* **55**(1): 65–108. Publisher: American Physical Society.
**URL:** *https://link.aps.org/doi/10.1103/RevModPhys.55.65* 21

Jin, Y., Wang, Z. F., Lim, P. C., Pan, D. Y., Wei, J. and Wong, C. K. [2003]. MEMS vacuum packaging technology and applications, *Proceedings of the 5th Electronics Packaging Technology Conference (EPTC 2003)*, pp. 301–306. 16

Kittel, C. [2004]. *Introduction to Solid State Physics*, 8th edn, Wiley. 5

Kumar Bhaskar, U., Pardoen, T., Passi, V. and Raskin, J.-P. [2013]. Piezoresistance of nano-scale silicon up to 2 GPa in tension, *Appl. Phys. Lett.* **102**(3): 031911. Number: 3.
**URL:** *http://aip.scitation.org/doi/10.1063/1.4788919* vii, 9

Lawn, B. [1993]. *Fracture of Brittle Solids*, Cambridge Solid State Science Series, 2 edn, Cambridge University Press, Cambridge. 14

Lee, S. H., Chen, K. and Lu, J. J. [2011]. Wafer-to-Wafer Alignment for Three-Dimensional Integration: A Review, *Journal of Microelectromechanical Systems* **20**(4): 885–898. Conference Name: Journal of Microelectromechanical Systems. 16

Li, J., Shan, Z. and Ma, E. [2014]. Elastic strain engineering for unprecedented materials properties, *MRS Bulletin* **39**(2): 108–114. Number: 2. 5

Li, Z., Wong, L. L. P., Chen, A. I. H., Na, S., Sun, J. and Yeow, J. T. W. [2016]. Fabrication of capacitive micromachined ultrasonic transducers based on adhesive wafer bonding technique, *J. Micromech. Microeng.* **26**(11): 115019. vii, 16, 17

Linz, T., Krshiwoblozki, M. v. and Walter, H. [2010]. Novel Packaging Technology for Body Sensor Networks Based on Adhesive Bonding A Low Cost, Mass Producible and High Reliability Solution, *2010 International Conference on Body Sensor Networks*, pp. 308–314. ISSN: 2376-8894. 16

Liu, X. H., Suo, Z. and Ma, Q. [1998]. Split singularities: stress field near the edge of a silicon die on a polymer substrate, *Acta Materialia* **47**(1): 67–76. Number: 1.
**URL:** *http://www.sciencedirect.com/science/article/pii/S1359645498003450* 22

Madan, A., Samudra, G. and Yeo, Y.-C. [2008]. Strain optimization in ultrathin body transistors with silicon-germanium source and drain stressors, *Journal of Applied Physics* **104**: 084505–084505–5. 6

Manasevit, H. M., Gergis, I. S. and Jones, A. B. [1982]. Electron mobility enhancement in epitaxial multilayer Si-Si1-xGex alloy films on (100) Si, *Appl. Phys. Lett.* **41**(5): 464–466. Publisher: American Institute of Physics.
**URL:** *https://aip.scitation.org/doi/abs/10.1063/1.93533* 5

Marty, O., Nychyporuk, T., de la Torre, J., Lysenko, V., Bremond, G. and Barbier, D. [2006]. Straining of monocrystalline silicon thin films with the use of porous silicon as stress generating nanomaterial, *Applied Physics Letters* **88**: 101909–101909. 11

Maszara, W. P., Goetz, G., Caviglia, A. and McKitterick, J. B. [1988]. Bonding of silicon wafers for silicon-on-insulator, *Journal of Applied Physics* **64**(10): 4943–4950. Number: 10.
**URL:** *https://aip.scitation.org/doi/abs/10.1063/1.342443* vii, 14, 18, 19

Miller, M. L. [1966]. Persistent polarization in polymers. I. Relationship between the structure of polymers and their ability to become electrically polarized, *Journal of Polymer Science Part A-2: Polymer Physics* **4**(5): 685–695. _eprint: https://onlinelibrary.wiley.com/doi/pdf/10.1002/pol.1966.160040502.
**URL:** *https://onlinelibrary.wiley.com/doi/abs/10.1002/pol.1966.160040502* xiii, 14

Minamisawa, R. A., Süess, M. J., Spolenak, R., Faist, J., David, C., Gobrecht, J., Bourdelle, K. K. and Sigg, H. [2012]. Top-down fabricated silicon nanowires under tensile elastic strain up to 4.5%, *Nature Communications* **3**(1): 1096. Number: 1 Publisher: Nature Publishing Group.
**URL:** *https://www.nature.com/articles/ncomms2102* 10

Montméat, P., Brandolisi, I. D. N., Tardif, S., Enot, T., Enyedi, G., Kachtouli, R., Besson, P., Rieutord, F. and Fournel, F. [2016]. Transfer of Ultra-Thin Semi-Conductor Films onto Flexible Substrates, *ECS Trans.* **75**(9): 247–252. Number: 9.
**URL:** *http://ecst.ecsdl.org/content/75/9/247* 24

Montméat, P., Enot, T., Enyedi, G., Pellat, M., Thooris, J. and Fournel, F. [2018]. Development and adhesion characterization of a silicon wafer for temporary bonding, *International Journal of Adhesion and Adhesives* **82**: 100–107.
**URL:** *http://www.sciencedirect.com/science/article/pii/S0143749618300095* 16

Moriceau, H., Rayssac, O., Aspar, B. and Ghyelen, B. [2003]. The bonding energy control: an original way to debondable substrates, *Semiconductor Wafer Bonding VII: Science, Technology, and Applications: Proceedings of the International Symposium* **2003**: 49. 18

Moriceau, H., Rieutord, F., Fournel, F., Le Tiec, Y., Di Cioccio, L., Morales, C., Charvet, A. M. and Deguet, C. [2011]. Overview of recent direct wafer bonding advances and applications, *Advances in Natural Sciences: Nanoscience and Nanotechnology* **1**(4): 043004. Number: 4. 18

Muller, B. and Stoffel, A. [1991]. Tensile strength characterization of low-temperature fusion-bonded silicon wafers, *J. Micromech. Microeng.* **1**(3): 161–166. Publisher: IOP Publishing.
**URL:** *https://doi.org/10.1088/0960-1317/1/3/006* 14

Niklaus, F., Stemme, G., Lu, J. Q. and Gutmann, R. J. [2006]. Adhesive wafer bonding, *Journal of Applied Physics* **99**(3): 031101. Number: 3 Publisher: American Institute of Physics.
**URL:** *https://aip.scitation.org/doi/full/10.1063/1.2168512* xiii, 13

Ochoa, M. A. and Li, Y. S. [2021]. A lithography-free approach to create Si nanomembranes on flexible substrates, *Solid State Communications* **325**: 114154.
**URL:** *http://www.sciencedirect.com/science/article/pii/S0038109820306499* 24

Passi, V., Bhaskar, U., Pardoen, T., Sodervall, U., Nilsson, B., Petersson, G., Hagberg, M. and Raskin, J.-P. [2012]. High-Throughput On-Chip Large Deformation of Silicon Nanoribbons and Nanowires, *J. Microelectromech. Syst.* **21**(4): 822–829. Number: 4.
**URL:** *http://ieeexplore.ieee.org/document/6179958/* 9

Platzer, N. [1969]. PROGRESS IN POLYMER ENGINEERING, *Ind. Eng. Chem.* **61**(5): 10–30.
**URL:** *https://pubs.acs.org/doi/abs/10.1021/ie50713a003* xiii, 14

Plößl, A. and Kräuter, G. [1999]. Wafer direct bonding: tailoring adhesion between brittle materials, *Materials Science and Engineering: R: Reports* **25**(1): 1–88. Number: 1.
**URL:** *http://www.sciencedirect.com/science/article/pii/S0927796X98000175* vii, 19

Qin-Yi Tong, Cha, G., Gafiteanu, R. and Gosele, U. [1994]. Low temperature wafer direct bonding, *Journal of Microelectromechanical Systems* **3**(1): 29–35. Number: 1 Conference Name: Journal of Microelectromechanical Systems. vii, 19, 20

Renault, P.-O., Le Bourhis, E., Villain, P., Goudeau, P., Badawi, K. F. and Faurie, D. [2003]. Measurement of the elastic constants of textured anisotropic thin films from x-ray diffraction data, *Appl. Phys. Lett.* **83**(3): 473–475.
**URL:** *http://aip.scitation.org/doi/10.1063/1.1594280* 21

Richter, J., Arnoldus, M. B., Hansen, J. L., Larsen, A. N., Hansen, O. and Thomsen, E. V. [2006]. Piezoresistance in Strained Silicon and Strained Silicon Germanium, *MRS Online Proceedings Library Archive* **958**. 6

Rieutord, F., Bataillou, B. and Moriceau, H. [2005]. Dynamics of a Bonding Front, *Phys. Rev. Lett.* **94**(23): 236101. Number: 23 Publisher: American Physical Society.
**URL:** *https://link.aps.org/doi/10.1103/PhysRevLett.94.236101* 20

Rieutord, F., Moriceau, H., Beneyton, R., Capello, L., Morales, C. and Charvet, A.-M. [2006]. Rough Surface Adhesion Mechanisms for Wafer Bonding, *ECS Trans.* **3**(6): 205–215. Number: 6.
**URL:** *https://iopscience.iop.org/article/10.1149/1.2357071* 20

Rim, K., Chan, K., Shi, L., Boyd, D., Ott, J., Klymko, N., Cardone, F., Tai, L., Koester, S., Cobb, M., Canaperi, D., To, B., Duch, E., Babich, I., Carruthers, R., Saunders, P., Walker, G., Zhang, Y., Steen, M. and Ieong, M. [2003]. Fabrication and mobility characteristics of ultra-thin strained Si directly on insulator (SSDOI) MOSFETs, *IEEE International Electron Devices Meeting 2003*, pp. 3.1.1–3.1.4. vii, 6, 12

Rim, K., Welser, J., Hoyt, J. and Gibbons, J. [1995]. Enhanced hole mobilities in surface-channel strained-Si p-MOSFETs, *Proceedings of International Electron Devices Meeting*, pp. 517–520. ISSN: 0163-1918. 5

Sakata, K., Magyari-Köpe, B., Gupta, S., Nishi, Y., Blom, A. and Deák, P. [2016]. The effects of uniaxial and biaxial strain on the electronic structure of germanium, *Computational Materials Science* **112**(Part A): 263–268. Number: Part A.
**URL:** *http://www.sciencedirect.com/science/article/pii/S0927025615006709* 6

Sanchez, L., Fournel, F., Montmayeul, B., Bally, L., Szelag, B. and Adelmini, L. [2018]. Collective Die Direct Bonding for Photonic on Silicon, *ECS Trans.* **86**(5): 223. Number: 5 Publisher: IOP Publishing.
**URL:** *https://iopscience.iop.org/article/10.1149/08605.0223ecst/meta* 18

Senawiratne, J. and Usenko, A. [2011]. Single Crystal Silicon Thin Film on Polymer Substrate by Double Layer Transfer Method, pp. 123–128.
**URL:** *http://ecst.ecsdl.org/cgi/doi/10.1149/1.3570786* 24

Setyawan, W. and Curtarolo, S. [2010]. High-throughput electronic band structure calculations: challenges and tools, *Computational Materials Science* **49**(2): 299–312. Number: 2 arXiv: 1004.2974.
**URL:** *http://arxiv.org/abs/1004.2974* 5

Smith, C. S. [1954]. Piezoresistance Effect in Germanium and Silicon, *Phys. Rev.* **94**(1): 42–49. Number: 1.
**URL:** *https://link.aps.org/doi/10.1103/PhysRev.94.42* 6

Soitec [2020]. Soitec's website.
**URL:** *https://www.soitec.com* vii, 22

Stengl, R., Mitani, K., Lehmann, V. and Gosele, U. [1989]. Silicon wafer bonding: chemistry, elastomechanics, and manufacturing, *IEEE SOS/SOI Technology Conference*, pp. 123–124. 18, 20

Sukhdeo, D. S., Nam, D., Kang, J.-H., Brongersma, M. L. and Saraswat, K. C. [2014]. Direct bandgap germanium-on-silicon inferred from 5.7% uniaxial tensile strain [Invited], *Photon. Res., PRJ* **2**(3): A8–A13. Number: 3. 8

Sukhdeo, D. S., Nam, D., Kang, J.-H., Brongersma, M. L. and Saraswat, K. C. [2015]. Bandgap-customizable germanium using lithographically determined biaxial tensile strain for silicon-compatible optoelectronics, *Opt. Express, OE* **23**(13): 16740–16749. Number: 13. 8

Sánchez-Pérez, J. R., Boztug, C., Chen, F., Sudradjat, F. F., Paskiewicz, D. M., Jacobson, R., Lagally, M. G. and Paiella, R. [2011]. Direct-bandgap light-emitting germanium in tensilely strained nanomembranes, *Proc Natl Acad Sci U S A* **108**(47): 18893–18898. Number: 47.
**URL:** *https://www.ncbi.nlm.nih.gov/pmc/articles/PMC3223450/* 7, 8, 22

Tardif, S., Gassenq, A., Guilloy, K., Pauc, N., Dias, G. O., Hartmann, J.-M., Widiez, J., Zabel, T., Marin, E., Sigg, H., Faist, J., Chelnokov, A., Reboud, V., Calvo, V., Micha, J.-S., Robach, O. and Rieutord, F. [2016]. Lattice strain and tilt mapping in stressed Ge microstructures using X-ray Laue micro-diffraction and rainbow filtering, *Journal of Applied Crystallography* **49**(5): 1402–1411. Number: 5.
**URL:** *https://onlinelibrary.wiley.com/doi/abs/10.1107/S1600576716010347* 8

Thompson, S. E., Armstrong, M., Auth, C., Alavi, M., Buehler, M., Chau, R., Cea, S., Ghani, T., Glass, G., Hoffman, T., Jan, C., Kenyon, C., Klaus, J., Kuhn, K., Zhiyong Ma, Mcintyre, B., Mistry, K., Murthy, A., Obradovic, B., Nagisetty, R., Phi Nguyen, Sivakumar, S., Shaheed, R., Shifren, L., Tufts, B., Tyagi, S., Bohr, M. and El-Mansy, Y. [2004]. A 90-nm logic technology featuring strained-silicon, *IEEE Transactions on Electron Devices* **51**(11): 1790–1797. Number: 11 Conference Name: IEEE Transactions on Electron Devices. 10

Tong, Q.-Y. and Goesele, U. [1999]. *Semiconductor wafer bonding: science and technology*, john wiley edn. 18

Usuda, K., Numata, T., Irisawa, T., Hirashita, N. and Takagi, S. [2005]. Strain characterization in SOI and strained-Si on SGOI MOSFET channel using nano-beam electron diffraction (NBD), *Materials Science and Engineering: B* **124-125**: 143–147.
**URL:** *https://www.sciencedirect.com/science/article/pii/S0921510705005404* 6

Vallin, O., Jonsson, K. and Lindberg, U. [2005]. Adhesion quantification methods for wafer bonding, *Materials Science and Engineering: R: Reports* **50**(4): 109–165. Number: 4. 14

Ventosa, C., Morales, C., Libralesso, L., Fournel, F., Papon, A. M., Lafond, D., Moriceau, H., Penot, J. D. and Rieutord, F. [2009]. Mechanism of Thermal Silicon Oxide Direct Wafer Bonding, *Electrochem. Solid-State Lett.* **12**(10): H373. Number: 10 Publisher: IOP Publishing.
**URL:** *https://iopscience.iop.org/article/10.1149/1.3193533/meta* vii, 20, 21

Ventosa, C., Rieutord, F., Libralesso, L., Morales, C., Fournel, F. and Moriceau, H. [2008]. Hydrophilic low-temperature direct wafer bonding, *Journal of Applied Physics* **104**(12): 123524. Number: 12 Publisher: American Institute of Physics.
**URL:** *https://aip.scitation.org/doi/full/10.1063/1.3040701* 19

Vogl, P., Rieger, M. M., Majewski, J. A. and Abstreiter, G. [1993]. How to convert group-IV semiconductors into light emitters, *Phys. Scr.* **1993**(T49B): 476. Number: T49B. 5

Walavalkar, S. S., Homyk, A. P., Henry, M. D. and Scherer, A. [2010]. Controllable deformation of silicon nanowires with strain up to 24%, *Journal of Applied Physics* **107**(12): 124314. Number: 12.
**URL:** *http://aip.scitation.org/doi/10.1063/1.3436589* 10

Wan, K.-T., Horn, R. G., Courmont, S. and Lawn, B. R. [1993]. Pressurized internal lenticular cracks at healed mica interfaces, *Journal of Materials Research* **8**(5): 1128–1136. Number: 5.
**URL:** *https://doi.org/10.1557/JMR.1993.1128* vii, 18, 19

Welser, J., Hoyt, J. and Gibbons, J. [1994]. Electron mobility enhancement in strained-Si n-type metal-oxide-semiconductor field-effect transistors, *IEEE Electron Device Letters* **15**(3): 100–102. Conference Name: IEEE Electron Device Letters. 5

Won, S. M., Wang, H., Kim, B. H., Lee, K., Jang, H., Kwon, K., Han, M., Crawford, K. E., Li, H., Lee, Y., Yuan, X., Kim, S. B., Oh, Y. S., Jang, W. J., Lee, J. Y., Han, S., Kim, J., Wang, X., Xie, Z., Zhang, Y., Huang, Y. and Rogers, J. A. [2019]. Multimodal Sensing with a Three-Dimensional Piezoresistive Structure, *ACS Nano* **13**(10): 10972–10979. Publisher: American Chemical Society.
**URL:** *https://doi.org/10.1021/acsnano.9b02030* 6

Yang, S. and Lu, N. [2013]. Gauge Factor and Stretchability of Silicon-on-Polymer Strain Gauges, *Sensors* **13**(7): 8577–8594. Number: 7. 6

Zhang, H., Tersoff, J., Xu, S., Chen, H., Zhang, Q., Zhang, K., Yang, Y., Lee, C.-S., Tu, K.-N., Li, J. and Lu, Y. [2016]. Approaching the ideal elastic strain limit in silicon nanowires, *Science Advances* **2**(8): e1501382. Number: 8.
**URL:** *http://advances.sciencemag.org/content/2/8/e1501382* 9, 10

Étienne, S. and David, L. [2012]. *Introduction à la physique des polymères: cours et exercices*, Dunod, Paris. OCLC: 816673920. xiii, 14

# Chapter 2

# Transfer of a single crystal silicon thin film onto a flexible polymer substrate

## Contents

# Introduction

This chapter will detail the development of a process aiming at transferring a single-crystal Silicon (sc-Si) film from a Silicon on Insulator (SOI) onto a flexible polymer substrate. This process must be fully compatible with 200 mm diameter wafers, industrial tools and a clean room environment. It relies mostly on polymer wafer bonding, mechanical grinding and selective chemical etching. This enables the use of this process for different materials even if this chapter is dedicated to the transfer of sc-Si thin films. In a first part, the specific materials and methods used for this process will be presented. The transfer process will be detailed as well as the different characterization techniques used to monitor the quality of samples during fabrication. Then a precise study of the influence of fabrication parameters on the final product will be presented. Precise characterization of the thin film during the transfer process will be provided to evaluate different parameters influence such as the position of the bonding interface during transfer, nature of the adhesive layer, silicon thickness and pattern morphology. The transfer of macroscopic silicon pattern with thickness ranging from 20 to 205 nm will be presented.

## 2.1 Material and methods

### 2.1.1 Description of materials

For sc-Si films transfer , the process starting point is a Silicon on Insulator (SOI) substrate. A description of this type of wafer and their fabrication process is given in section 1.3.1.

Here, two types of 200 mm SOI are used, as detailed in table 2.1. Other substrates needed in the study are also presented in this table.

| Name | Supplier | Thickness |
|---|---|---|
| SOI | Soitec™ | 725 µm (400 nm BOX and 205 nm top Si layer) |
| SOI | Soitec™ | 725 µm (1000 nm BOX and 400 nm top Si layer) |
| Bulk Si Carrier | Taisi Electronic Materials Corp. | 725 µm |
| Borosilicate glass | Plan Optik AG | 700 µm |

Table 2.1: Reference and properties of commercial wafers used in this work. Only wafers with a diameter of 200 mm were used. Silicon substrates present a (001) orientation

The table 2.2 gives a description of the different polymer based materials used in this work. Most of them are commercial materials as they are required to be fully compatible with a clean room environment as well as with industrial tools and fabrication processes. For example Polydimethylsiloxane (PDMS) could not be used and especially cured inside the CEA-Leti clean room as it is associated with highly volatile monomers.

| Name | Supplier | Type | Composition | Tg (°C) |
|---|---|---|---|---|
| BrewerBOND®305-30 (BSI) | Brewer Science, Inc. | commercial spin-on glue | polyolefin | 70 |
| SPIS 21 | Shin-Etsu | commercial dry film glue | silicon based polymer | 90 |
| SP-537T-230 | Furukawa™ | 300 mm dicing tape | Acrylic adhesive and polyolefin backing film | - |
| Revalpha | Nitto Denko™ | Double sided thermal release dicing tape | - | |
| SYLGARD®184 | Dow corning™ | Silicone Elastomer | PDMS | -120 |
| Novec™2702 | 3M™ | anti-stiction coating | Fluoropolymer | -63 |
| Novec™7200 | 3M™ | Sovlent | Ethoxy-nanofluorobutane | - |

Table 2.2: Polymers used in this work and their properties

As detailed in the previous table, two different models of commercial dicing tapes are present in this study. Dicing tapes are used for handling of thin wafers, holding dice on a cutting tool or surface encapsulation during a grinding step. Both tape structures are represented in figure 2.1. The SP-537T-230 from Furukawa (simply denoted Furukawa tape hereafter) presents a single adhesive layer. This layer is sensitive to Ultra-Violet (UV) light and its adhesion will decrease under exposure, due to reticulation of the polymers chains composing the acrylic adhesive. It will also cause an increase in the tape rigidity. Alternatively, a Revalpha tape from Nitto Denko could be used. This tape is double sided with a pressure sensitive layer on one side and a thermal release layer on the other. The thermal release layer adherence will drop down drastically above a given temperature (120 °C to 170 °C depending on the reference used here)[Soejima et al., 2013].

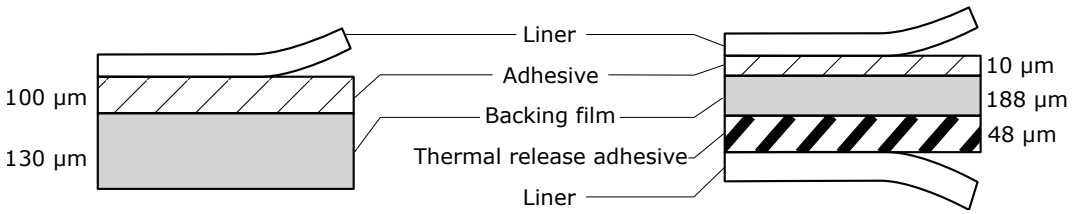


Figure 2.1: Structure of dicing tape (left) Single sided pressure sensitive (right) Double sided tape with a thermal release layer

### 2.1.2 Process overview

To obtain the desired material with adequate dimensions and properties, several process flows were studied. The complete process is presented in figure 2.2, including its variants. It is mainly based on a temporary bonding process using a rigid carrier for handling purposes. It allows a complete removal of the SOI backside and to transfer the top silicon layer onto a flexible polymer substrate. The materials and methods used to perform the process steps will be described in this section. Process variations and their consequences on final material properties will be discussed later in this chapter.

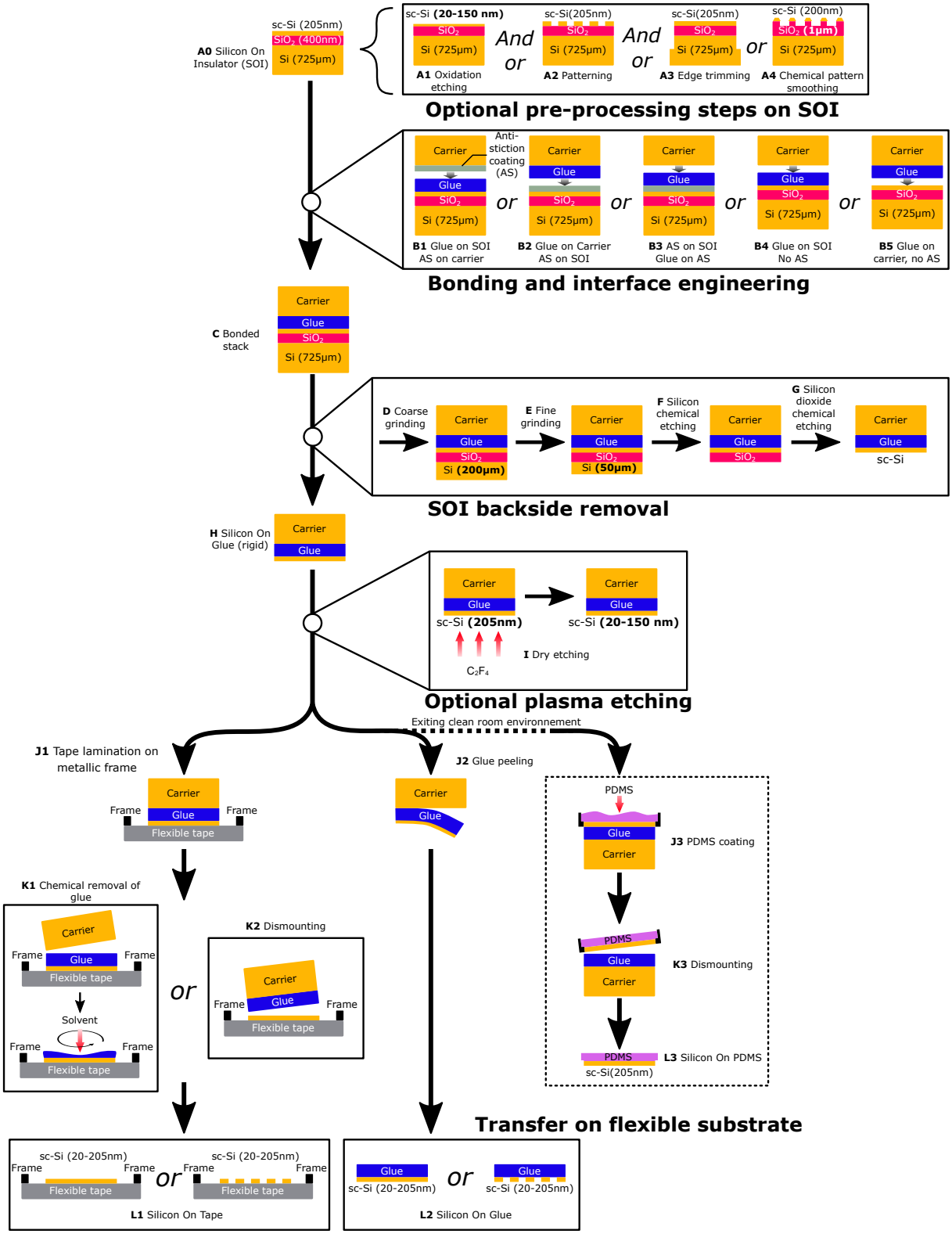


Figure 2.2: Detailed schematic of transfer processes of a sc-Si thin film from a SOI to a flexible polymer substrate. Each bold letter corresponds to a process step or a specific stack. Process splits are associated with a number. The processes are fully compatible with 200 mm wafers, clean room environment and industrial tools. The final result of these processes are a flexible and stretchable SOP with a silicon thickness ranging from 20 nm to 205 nm and with different polymers substrates. Full 200 mm films can be transferred as well as patterned ones.

### 2.1.3 Optional pre-processing steps on SOI

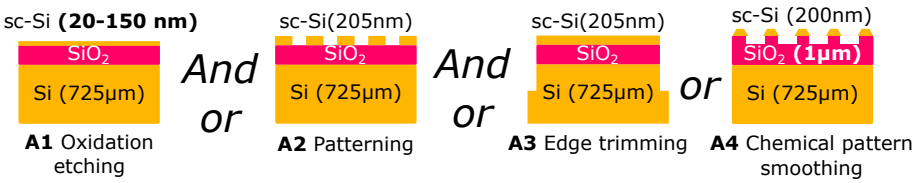


Figure 2.3: Different processing options for SOI substrates used in the transfer process. Any combination of the first three options is possible while the last one ask for a different substrate.

For the transfer of a sc-Si thin film, a SOI is the starting point of the process detailed in figure 2.2. Different treatments can be applied to the SOI before going throughout the transfer process as presented in figure 2.3. All the combination between **A1** (oxidation/etching), **A2** (patterning) and **A3** (edge trimming) steps are possible. Only the chemical pattern smoothing presented in step **A4** asks for a different SOI, as thicker BOX and silicon top layer are needed for the additional oxidation and etching steps. The different pre-processing steps are detailed below.

#### 2.1.3.1 A1: sc-Si sacrificial etching

Oxidation and etching (**A1**) of the SOI aims at decreasing the top silicon thickness. The wafer is first oxidized in a microelectronics oven (VT412 from ASM )at 950 °C under steam atmosphere. The targeted thermal oxide thickness is calculated using equation 2.1 where $t_{si}$ is the oxidized silicon thickness and $t_{siO_2}$ the grown oxide thickness.

$$t_{SiO_2} = 2.27\, t_{si} \tag{2.1}$$

After obtaining the desired oxide thickness, this last layer is then etched using a 49 wt% HF aqueous solution in a single wafer etching tool from SEZ. The silicon film acts as an etch stop layer. The silicon and oxide thicknesses are monitored using a an ellipsometer (Nanometrics Atlas XP+, see subsection 2.1.7).

#### 2.1.3.2 A2: Si film patterning

Depending on the intended use, the SOI top silicon layer could be patterned to define devices, such as ribbons or disks for mechanical tests. Standard photolithography process with JSR IX420H photoresist material were used to that end. Different types of masks were tested: soft masks (*i.e.* ink on a polymer backing film), which are cost-effective and easy to prototype but have less defined edges, and hard masks (*i.e.* chromium on glass), which are more expensive but with much better defined edges and lower Critical Dimension (CD) value. A final design used for a 1X chromium mask is shown in figure 2.4. Three different kinds of patterns are defined: [110] and [100] oriented $2 \times 24\,mm^2$ ribbon and 20 mm diameter disks. Tensile tests performed on samples using patterned SOI will be detailed in chapter 3.

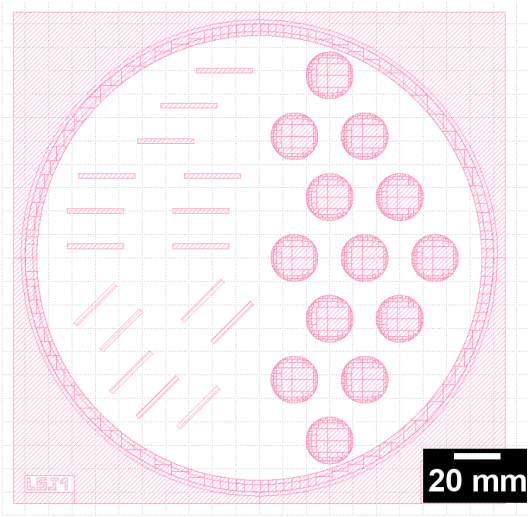


Figure 2.4: Positive 1X chromium mask used for the photolithography of patterns used in the fabrication of tensile test samples.

#### 2.1.3.3 A3: Edge trimming

A 250 µm thick and 1.5 mm wide strip on the edge of the starting wafer could be removed using a dicing tool from DISCO. It prevents edge fragility during mechanical grinding of the SOI backside after the bonding step (steps **D** an **E**). Figure 2.5 illustrates the origin of edge fragility without trimming step. One of the edge trimming drawbacks is the associated particle contamination. A mega-sonic cleaning in isopropyl alcohol (IPA) is performed after to limit this contamination.

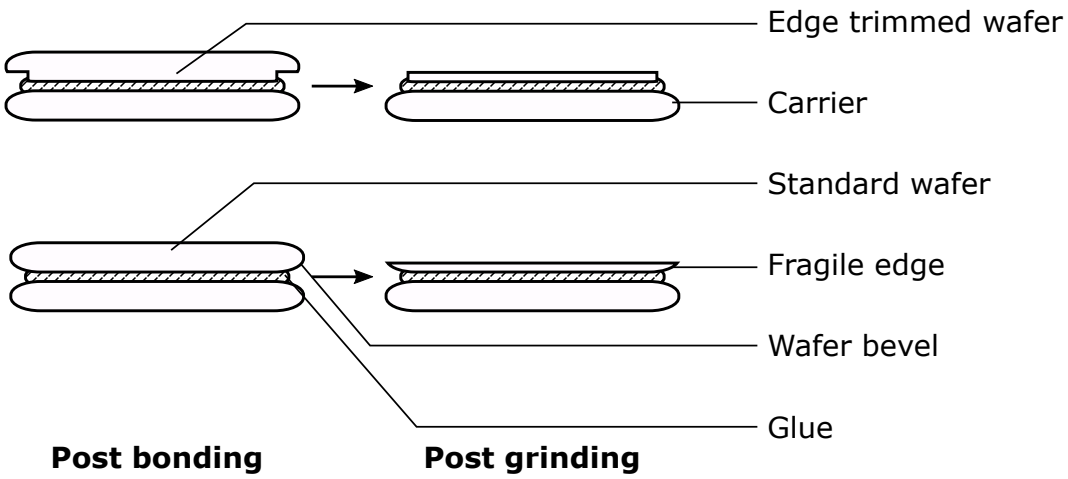


Figure 2.5: Edge trimming effect on bevel fragility after mechanical grinding of a wafer backside.

#### 2.1.3.4 A4: Pattern sidewall chemical smoothing

Additionally, an anisotropic etching process was tested on silicon pattern edges to smooth out any remaining roughness after lithography and etching (step **A4**). For standard lithography process, isotropic etching processes are used, all crystalline planes are etched at the same rate. For WET etching with strongly aqueous alkaline media such as KOH or TetraMethylAmmonium Hydroxide (TMAH), the etch rate depends on the activation energy of the silicon atomic planes. The etch rate of (110) and (100) planes is higher than the one of more stable (111) planes [Tabata et al., 1992]. Figure 2.6 (a) presents (100) and (111) silicon surfaces after TMAH etching at different concentration in aqueous solution from the work of Tabata et al.. For the process used here, the different steps are detailed in figure 2.6(b). A SOI with a 1 µm BOX and a 400 nm

top silicon layer is used. The top silicon layer was first thermally oxidized to form a 400 nm thick silicon oxide layer. Then the 1X chromium mask presented in figure 2.4 was used to pattern a photoresist layer. The top silicon dioxide layer was etched, then the remaining 200 nm of the silicon thin film, according to the patterns defined earlier. After photoresist removal, a chemical smoothing of the silicon pattern edges was performed. The silicon oxide acts as an etch mask for the top silicon surface. A 25 wt% TMAH aqueous solution was used for 75 min at 80 °C. An isotropic WET etching step is then used to remove at least 400 nm of silicon oxide, revealing the patterns top silicon surface.

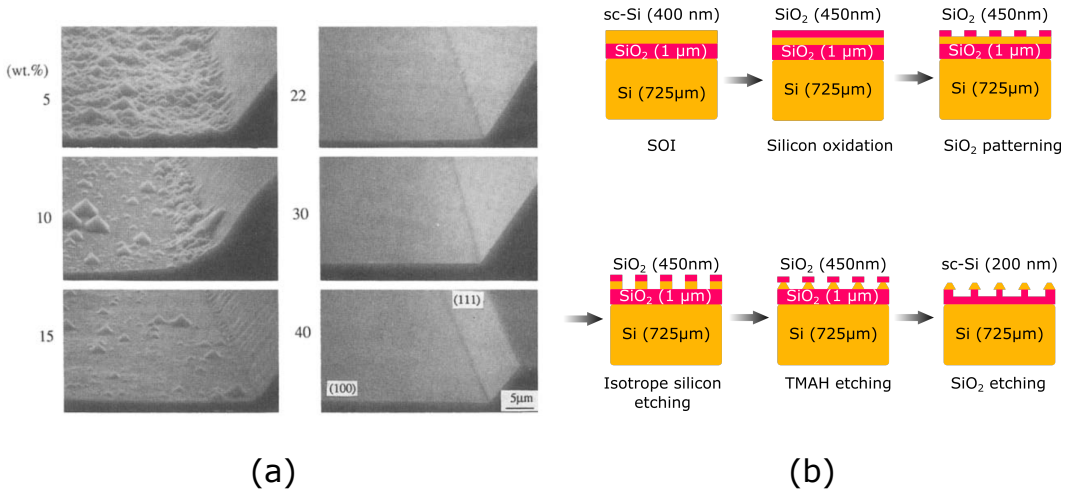


Figure 2.6: (a)SEM images of (100) and (111) silicon surfaces etched in solutions with concentration between 5 and 40 wt% at 70 °C for 90 min [Tabata et al., 1992] (b) Process flow for the smoothing of silicon patterns sidewalls (**A4**). A SOI is oxidized, the top oxide and silicon layer are patterned, then the wafer is etched in a TMAH solution and finally the top oxide layer is fully etched with an isotropic WET etching step.

### 2.1.4 Bonding and interface engineering

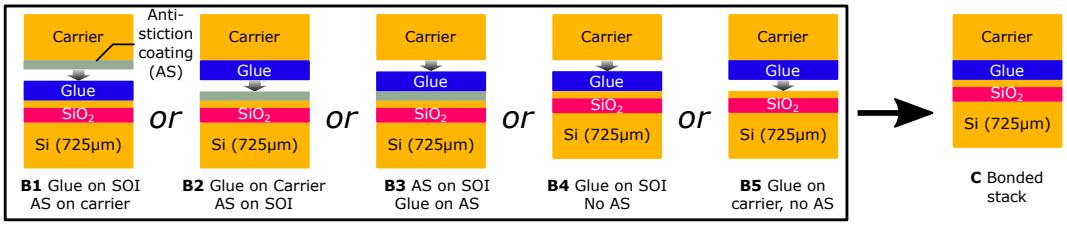


Figure 2.7: The different bonded stacks studied for the thin film transfer process.

Once the SOI film was prepared for the transfer (*e.g.* with desired thickness and patterns), it was bonded to a carrier in order to safely remove the backside of the SOI wafer. As the objective was to obtain a flexible structure, the bonding to a rigid carrier is temporary. Different bonding stacks and glues were evaluated to control the adherence between the layers and the position of the weakest interface which drove the dismounting process of the temporary bonded stack. These options are presented in figure 2.7. The bonding was performed in a 200 mm EVG 520 bonder tool. A schematic of the bonding chamber is visible in figure 2.8. The two wafers are placed and aligned manually on the bonding chuck and are separated by metallic flags. Prior to the bonding step, they are held together by metallic clamps, to maintain the initial alignment. The wafer coated with glue (either SOI or carrier) is placed at the bottom, on the bonding chuck. The bonding recipe is the following :

- The bonding chamber is filled with $N_2$ and evacuated down to $10 \times 10^{-4}$ mbar
- The temperature of the piston and bonding chuck is raised to the set-point and maintained for 3 min

- Metallic flags are removed and the piston applied a force of 6 kN for 3 min
- The piston is lifted up and the chamber is purged back to atmospheric pressure
- Bonded structure is cooled down to room temperature, bonding quality was then monitored using Scanning Acoustic Microscopy (SAM) as described in subsection 2.1.7.2

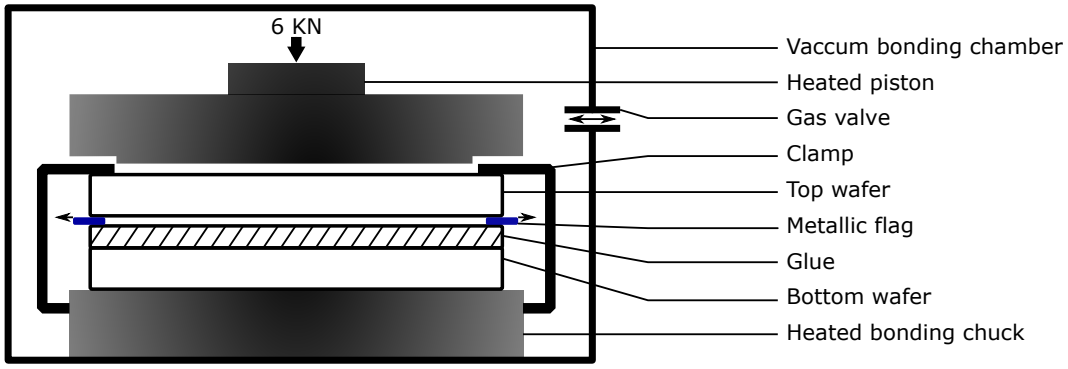


Figure 2.8: Schematic of a bonding tool for polymer bonding

#### 2.1.4.1 Spin coating the glue

Two different interfacial glues have been evaluated for our process. The first one is the BrewerBOND®305-30 from Brewer Science Inc, referred as BSI. It is a thermoplastic polymer commonly used for the processing of ultra-thin wafer up to 300 °C. Here the BSI was spin coated at 700 RPM for 30 s to obtain a layer of 40 ± 1 µm using an EVG 101 spin coating tool (see figure 2.9). The layer is then baked at 120 °C for 11 min and at 220 °C for 11 min. Specifications of the BSI are given in the table 2.2. The BSI bonding is performed at 210 °C.

To decrease the adherence energy, an Anti Stiction (AS) coating composed of a fluoropolymer (3M Novec 2702, table 2.2) is used in addition to BSI. The AS is spin coated on the desired surface at 1000 RPM for 30 s. The corresponding solvent (3M Novec 7200) is then applied two times at the same rotation speed and duration. To remove excess solvent, the coating is cured at 150 °C for 30 min. The resulting layer is around 5 nm thick [Montméat et al., 2018]. The presence of the AS can be controlled with a water contact angle measurement (DIGIDROP DSA 100 tool from Küss). Initially a bulk silicon wafer presents a contact angle lower than 15° (hydrophilic). After AS coating, the angle is 108°, showing the enhanced hydrophobic behavior of the surface [Montméat et al., 2018] as illustrated by figure 2.10. Considering the BSI and AS, different bonding stacks can be proposed (see figure 2.7) :

- **B1**: AS on the carrier and Brewer Science Inc. (BSI) on the SOI. This enabled peeling of the glue from the carrier (**K2**) or dismounting of the carrier (**L1**).
- **B2**: AS on the SOI and BSI on the carrier. This enable the dismounting of the sc-Si film from both the glue and the carrier (**L2**).
- **B3**: AS and BSI on the SOI. This resulted in a stack similar to **B2** and also enabled the dismounting of the sc-Si film from both the glue and the carrier (**L2**), but the AS is not placed at the bonding interface, the BSI is spin-coated on it.
- A last stack can be considered : AS and BSI on the carrier. This would result in a stack similar to **B1** and also enables the dismounting of the carrier (**L2**), but the AS is not placed at the bonding interface, since, similarly to **B3**, BSI is spin coated on it. This stack was not tested since the coating of the AS on BSI is challenging due to the possible dissolution of the BSI by the AS during the spin-coating of the AS.

During dismounting, the separation always occurred at the weakest interface that is AS/BSI in these stacks.

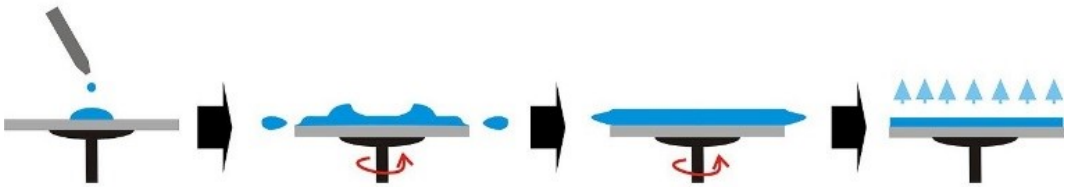

Figure 2.9: Spin coating technique used for bonding polymer or AS materials, the thickness is a function of rotation speed and polymer viscosity First, the solution is placed at the wafer center. A quick acceleration disperses the material excesses. Then the rotation is speed is kept constant to obtain a good thickness homogeneity. Finally the layer is annealed

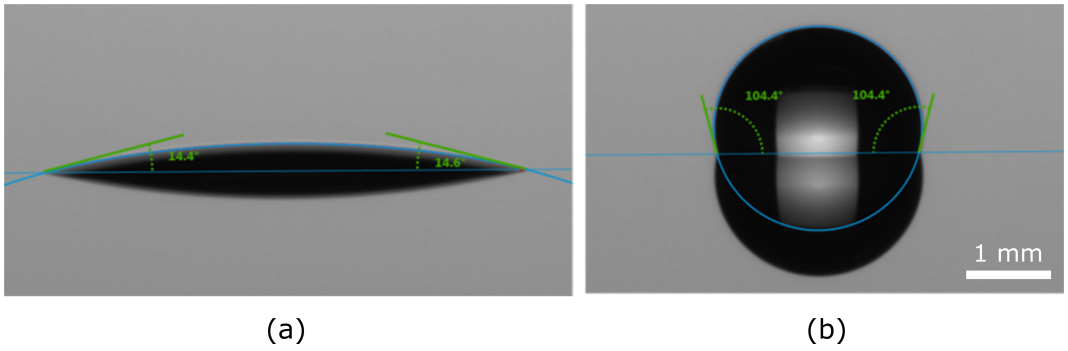


Figure 2.10: Water contact angle observed on a DIGIDROP DSA 100 tool
(a) Bulk Silicon wafer (b) Silicon wafer coated with 3M novec 2702 AS material

#### 2.1.4.2 Laminating the glue

For lower temperature applications and lower adherences without the use of AS coating, a dry film can be directly laminated on the substrate. The reference used in this study is SPIS 21 from Shin-Etsu and was bonded at 100 °C. The polymer is purchased on the form of rolls with a face made to be laminated and another one for thermo-compressive bonding, protected by a cover-sheet. The adhesive properties and composition are symmetric though. The dry film was laminated under vacuum using a heated roll (120 °C). No AS coating was needed for this adhesive. Two bonding stacks were evaluated:

- **B4**: glue laminated on SOI. This enables the separation of the stack at the interface between the glue and the carrier.
- **B5**: Alternatively the glue was laminated on the carrier. It allowed the separation of the interface between the glue and the SOI

### 2.1.5 SOI backside removal

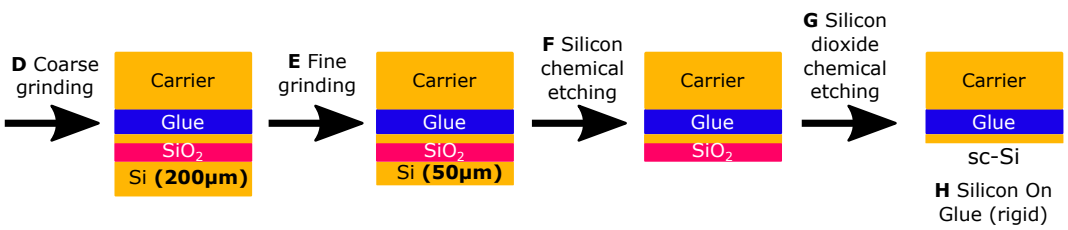


Figure 2.11: Removal of the SOI backside from the bonded stack using mechanical grinding and chemical etching

After bonding, a first mechanical grinding is performed. Grinding is commonly used in microelectronics to remove thick layers of materials (*i.e.,* from tens to hundred of µm). Grinding wheel coated by diamond abrasives removes layers of material as illustrated by the schematic in figure 2.12. The speed of material removal depends on the diamond abrasives granularity. A coarser grain results in a faster grinding but with higher subsurface damages concentration [Haapalinna et al., 2004; Pei et al., 2008] (figure 2.12). DISCO tools have been used for these steps.

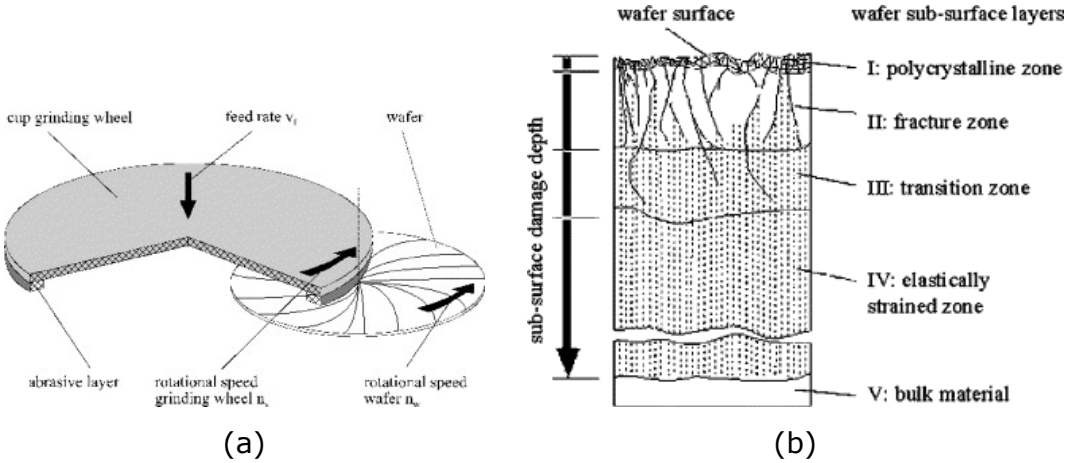


Figure 2.12: (a) Schematic of a grinding tool (b) Schematic of the different subsurface damages caused by mechanical grinding in a silicon wafer [Hadamovsky, 1990]

The grinding takes place in two steps :

- A first coarse grinding that removes 525 µm of the SOI substrate backside (**D**), leaving 200 µm of the initial bulk silicon substrate above the SOI buried oxide layer.

- A final grinding with a much finer wheel granularity in order to remove another 150 µm, leaving 50 µm of the initial bulk silicon substrate (**E**)

Grinding in two successive steps is needed to have a fast enough removal rate while keeping a good control of the final thickness and surface state to prevent inhomogeneity during chemical etching.[Haapalinna et al., 2004]. The second fine grinding step leaves a damaged layer of roughly 1 µm in the 50 µm layer[Pei et al., 2008]. This is suitable to further chemical etching.

Another advantage to proceed in two separate grinding steps is that the bonding interface can be monitored in between the two steps. Mechanical grinding induces high mechanical stress at the bonding interface. A small bonding defect (i.e. a few µm) can produce a much larger defect after a grinding step and can even results in a catastrophic fracture of the stack. A first grinding step with a 200 µm set-point allowed to monitor the evolution of defect with Scanning Acoustic Microscopy (SAM) imaging while greatly decreasing the risk of fracture in the thinned down layer. Fracture usually happens at lower thickness or with defect that would have been flagged after the bonding step. Annealing a thinned defective bonded stack can reduce the defect size and allows one to continue the process flow, else the stack is discarded.

Selective chemical etching is used to remove the remaining SOI backside after mechanical grinding steps. A single wafer etching tool from SEZ is used. Again, the process is divided in two steps:

- Etching of the remaining 50 µm silicon layer with $HF/HNO_3$ aqueous solution. The BOX was used as an etch stop layer as the solution presents a strong $Si/SiO_2$ selectivity [Schwartz and Robbins, 1976].

- Etching of the BOX with a 50 wt% HF aqueous solution. This time, the silicon layers acted as an etch stop layer with a very high selectivity.

At this point, an optional plasma etching step can be performed (step **I**, figure 2.13). A $C_2F_4$ plasma is used in a P500E tool from Applied Materials®. This step was only performed on sc-Si layer with an initial thickness of 205 nm as it is meant to replace the initial oxidation/etching preparation step (**A1**).

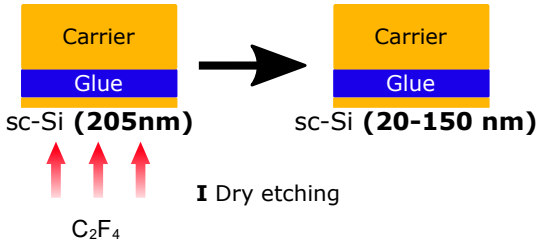


Figure 2.13: Plasma etching of a sc-Si film after transfer on a polymer layer on a silicon carrier

A technical challenge at this stage is the measurement of the sc-Si film thickness. More details will be given in subsection 2.1.7. This optional process split was used to decrease the sc-Si thickness after the first transfer on polymer and not before (*i.e.,* oxidation and etching of the top silicon layer **A1**). This allowed keeping a standard thickness value for the first transfer while the final thickness can be finely tuned to the desired value here after. Any possible issues caused by a low thickness during the transfer process can thus be avoided.

### 2.1.6 Transfer on flexible substrate

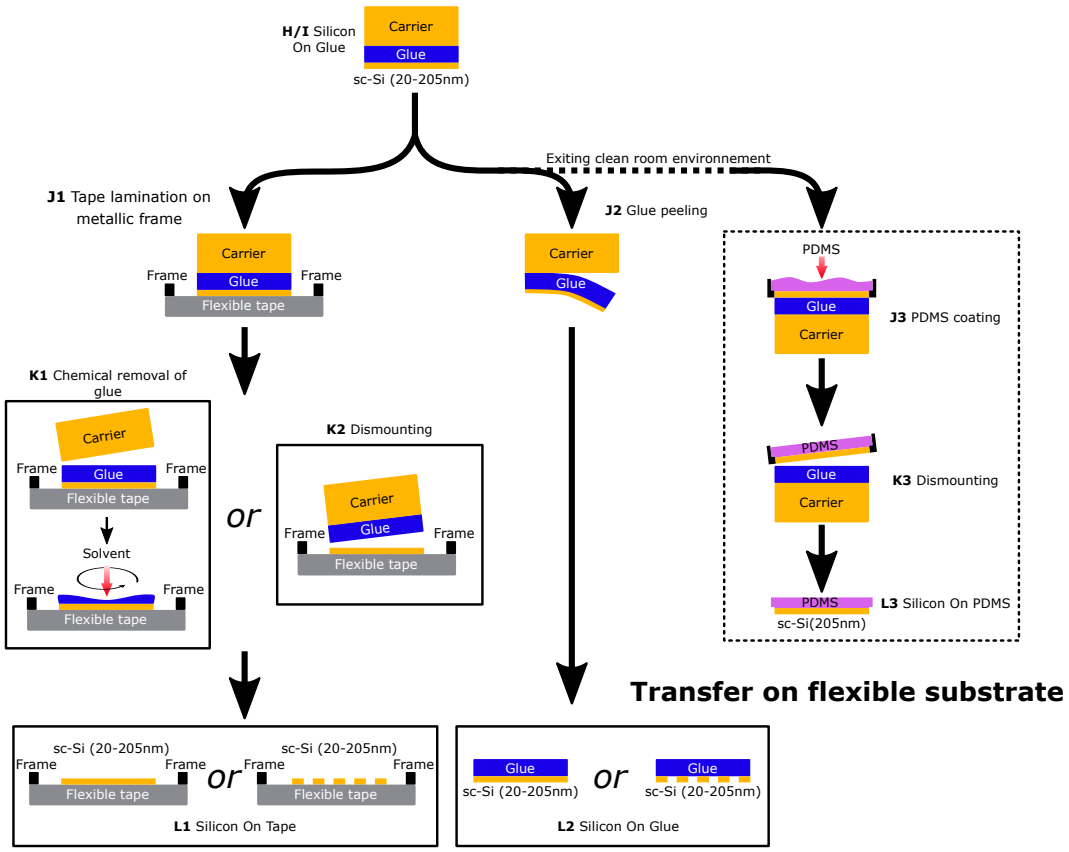


Figure 2.14: The different transfer options to obtain a sc-Si film on flexible polymer substrates. Step **K1** and **K2** are used to obtain silicon on tape whereas step **J2** results in a silicon on glue stack. An additional step performed outside of a clean room environment allows to transfer a sc-Si layer on PDMS layer (**J3-L3**)

After the two steps of selective chemical etching, only the top silicon film of the SOI is left on the glue used in the temporary bonding step (stack **H** or **I**). The sc-Si film needs now to be dismounted from the rigid

silicon carrier to obtain a flexible and stretchable structure. Depending on the chosen bonding process, there are different options to obtain a sc-Si film on a flexible polymer substrate, as illustrated in figure 2.14:

- For bonded stack **B1** or **B4**, the weak interface is situated between the glue and carrier, the glue could be peeled off from the rigid carrier (step **J2**). The resulting structure is a SOP. The glue acting as a flexible substrate (stack **L2**).

- Alternatively, a flexible tape could be laminated on the stack **H** or **I**. A metallic disc frame was placed around the wafer for handling purposes (illustrated in figure 2.15). This step could be either performed manually or with an automated tool (850DB from EVG). The two different tapes used are presented in table 2.2. Then the carrier and glue are removed. The process depends on the position of the weakest interface. In the case of bonding stacks **B1** and **B4**, the carrier is first dismounted and the glue remains on the sc-Si thin film. Then the glue layer can be removed using a megasonic cleaning under a d-Limonene flow in an EVG 850DB tool(**L1**). For bonding stacks **B2**, **B3** and **B5** the glue layer is dismounted with the rigid carrier (**L2**) thanks to the presence of a weak interface between the sc-Si thin film and the glue (AS/Glue or low temperature bonding interface). Both this process options yielded a SOP with an adhesive tape acting as a substrate and held by a metallic frame.

- A last option, allowed to transfer the sc-Si thin film on a thick PDMS layer. A 1 to 10 mix of Sylgard®184 Silicone Elastomer (PDMS) is poured on the stack **B2** and cured at room temperature for at least 48 h. The 5 mm thick PDMS layer was peeled off with the sc-Si film.

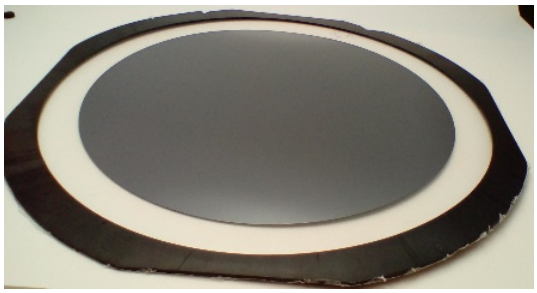

Figure 2.15: Snapshot of a dicing tape laminated on a 200 mm wafer and a DISCO metallic frame

Transfer of silicon pattern is performed the same way as for full sheet films. Once the silicon patterns are transferred on a chosen flexible substrate, they could be separated to be individually characterized. An automatic cutting tool (Graphtec CE6000) is used to cut the polymer substrate. Optical marks allowed to cut homogeneous samples with the silicon film centered and aligned. The preparation of a batch of uniaxial tensile test sample on Furukawa is illustrated in figure 2.16. In this case, a single orientation soft mask was used but the method remain the same for different masks

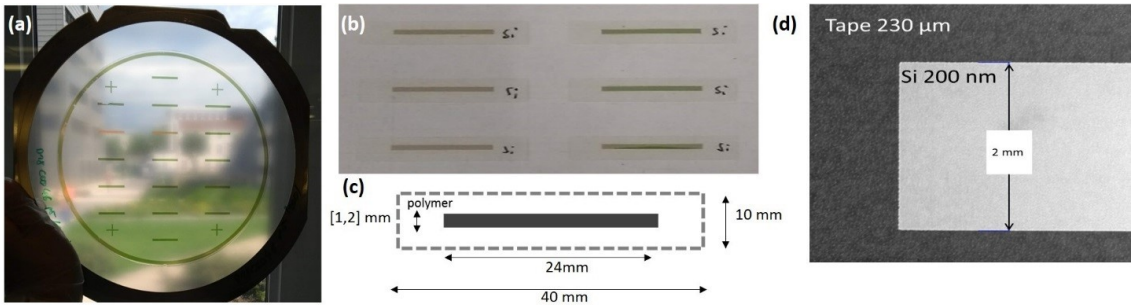


Figure 2.16: Tensile test sample fabrication process. (a) Patterns transferred on flexible tape. (b) Uniaxial tensile test samples after cutting (c) Uniaxial tensile test sample dimension (d) Micrograph of a ribbon pattern.

A method to obtain a single pattern on a polymer substrate up to 300 mm diameter using a Kapton mask was also developed. This process is used to prepare samples for tensile apparatus needing large polymer substrate without sacrificing patterns surrounding the studied one . The different step are detailed in figure 2.17. A 25 µm thick Kapton sheet is placed on the patterned SOP prior to tape lamination with a cut-out around the desired pattern or patterns. Then the transfer process was carried on, only to transfer the pattern placed in the Kapton cut-out.

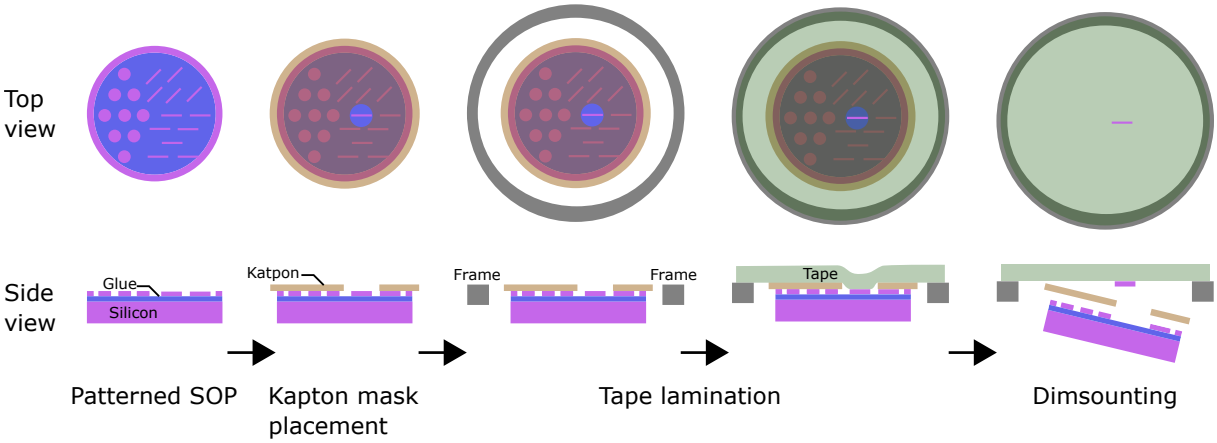


Figure 2.17: Process for the transfer of a single pattern from a SOP onto a Furukawa tape using a Kapton mask

This process can also be used to isolate a single pattern on a tape held by a metallic frame for handling purposes. This way, different transfer parameters and process splits could be tested on patterns using a single patterned wafer.

### 2.1.7 Characterization

Metrology steps are necessary during the process to control key parameters in the transfer process. Concerning the bonding interface, bonding defects and bonding energy are monitored. After bonding, bonding stack morphology and stress should also be controlled. Finally the defectivtiy, stress, thickness and surface roughness of the silicon thin film are observed at different stage of the transfer process.

#### 2.1.7.1 Defectivity

First, if a trimming step is performed, the particle contamination of the surface prior to bonding is quantified using an KLA tencor surfscan SP1 tool. This tool, based on laser diffraction, detects particles and surface defects with a size threshold set between 0.09 and a few micrometers. For this study the recipe threshold is set between 0.2 and 1 µm. The coordinates of the defects are also saved by this tool. A morphological analysis can then be performed with a Scanning Electron Microscope (SEM).

SEM observations presented in this work are obtained with secondary electron detectors on different tools:

- FIB G3 from Applied Materials. It is used for defect inspection after defectivity measurement.
- Zeiss MERLIN
- Hitachi S5000

For further defectivity measurements, a KLA tencor surfscan SP2 was used. Metal and particle contamination concerns prevent the use of this tool earlier in the process.

#### 2.1.7.2 Bonding interface metrology

Bonding interface are evaluated using Scanning Acoustic Microscopy (SAM). A megasonic transducer produces acoustic waves (230, 140 or 30 MHz frequency) that travel through the stack. The lateral resolution varies as the inverse of the transducer frequency and is here ranging from 10 µm to 50 µm. Each interface will reflect a fraction of the incident signal. Mapping of the whole stacks surface reflected signal allows to extract the percentage of unbonded areas and to observe defects morphology and position. The transducer records the reflected signal intensity as a function of time. The time at which the reflected signal is received by the transducer is function of the interface depth in the stack and the different materials of the stack. The degree of ultrasonic reflection from an interface is governed by equation 2.2.

$$R = \frac{Z_1 - Z_2}{Z_1 + Z_2} \tag{2.2}$$

Where R is the fraction of reflection, $Z_1$ and $Z_2$ are the acoustic impedance of the two materials analogous to refractive index in light propagation. The propagation speed $c$ of an acoustic wave in a material of stiffness C and density ρ is presented in equation 2.3.

$$c = \sqrt{\left(\frac{C}{\rho}\right)} \tag{2.3}$$

Schematic of a SAM is presented in figure 2.18. The reflected signal is collected while the transducer scans the stack surface. For a given point, the amplitude is collected as a function of time (*i.e.*, an "a-scan"). An image of the bonding interface is then reconstructed from the part of the signal that corresponds to the interface depth (and time of flight of the acoustic wave). Images presented in this work are called "c-scan" and correspond to the mapping of a signal gate placed at a fixed time and with a certain time width for the whole stack surface. In the case of direct bonding with a defect-free bonding interface between two identical materials, no signal should be reflected by the bonding interface. The convention in direct bonding is to show a black pixel when no defect is detected and *(i.e.*, no reflected signal in the corresponding time range) whereas a white or bright pixel will indicate the presence of an interface (*i.e.*, air bubble). An example is given in figure 2.18

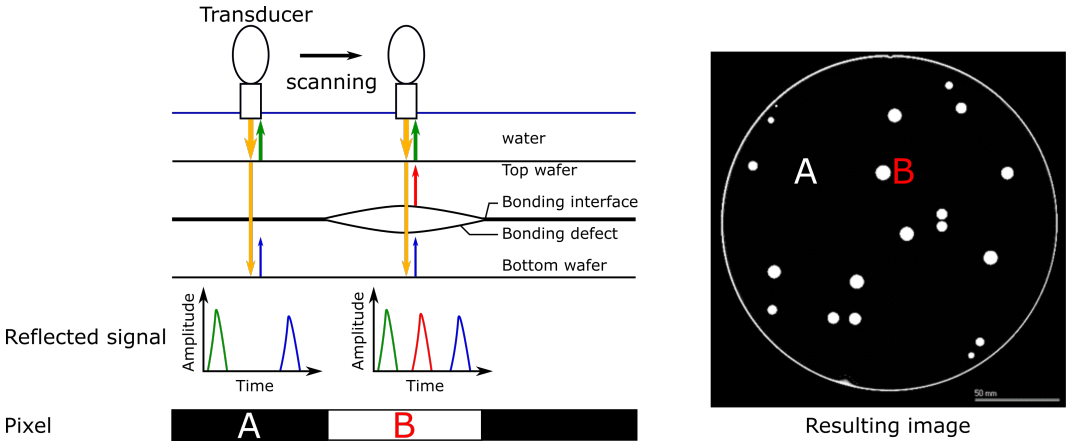


Figure 2.18: Schematic of a SAM with an example of a signal reflected by a defect in a covalent bonding stack

In the case of polymer bonding, the signal is more complex to analyze. First of all, even without any delamination, the different ceramic/polymer interface will give a quite important acoustic reflected signal as the acoustic impedance difference is quite important (the polymer thickness is also not negligible compare to the acoustic wavelength). This constant reflection implies to reduce the acoustic amplitude in order to optimize the difference between a delamination detection and this continuous signal. A polymer bonding SAM image will then also be mainly “grey” as shown on figure 2.19. As the acoustic wave propagates

through the polymer layer, the acoustic amplitude will also be impacted by the material attenuation and the thickness variation will then impact the recorded acoustic signal amplitude. It is then possible to see the signature of the polymer thickness non-homogeneity.

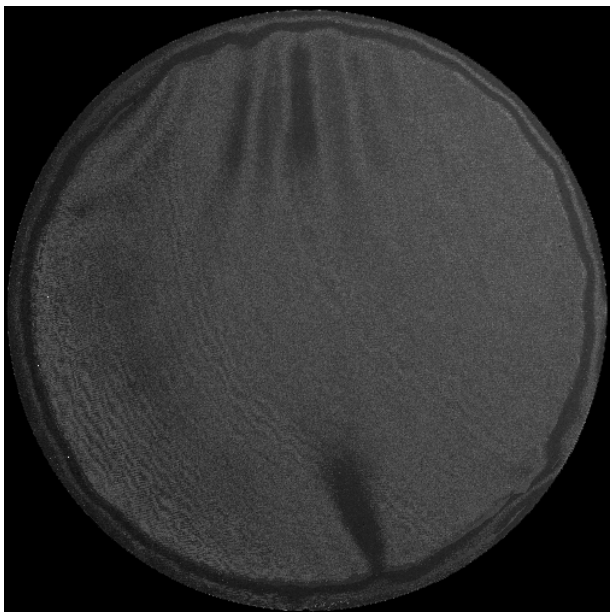

Figure 2.19: SAM c-scan image the bonding interface between two silicon wafer bonded with a an adhesive polymer layer.

Moreover as several interfaces are present and close to each other the signal is even more complex to analyze in the case of two wafers bonded with a 40 µm layer of BSI:

- A first interface **I** between the water and the SOI backside. The carrier wafer is always placed at the bottom so that the height of the bonding interface remained constant along the different grinding and etching steps.
- A second interface **II** between the SOI Si thin film and the glue.
- A third interface **III** between the glue and the carrier wafer. The reflected of this interface is typically mapped during a c-scan to probe the quality of the bonding interface.
- A last interface **IV** is present between the carrier and the chuck of the tool.

Figures 2.20(b-d) display examples of SAM a-scan and c-scan for different thicknesses of the SOI backside. At 725 µm, the analysis of the a-scan is straight forward with an entry and exit peak of the SOI separated by 162 ns. Using equation 2.3 with $C_{si}$ =165.6 GPa (Silicon stiffness along the normal to the surface for a (001) wafer [Hopcroft et al., 2010]) and $\rho_{si}$ =2330 kg/m$^3$, a corresponding length of 1364 ± 15 µm is calculated. It corresponds to about twice the thickness of the SOI (back and forth). The peak corresponding to the bonding interface is close to the SOI exit peak ( 25 ± 3 ns ). At lower backside thicknesses, more peaks appeared on a-scans.

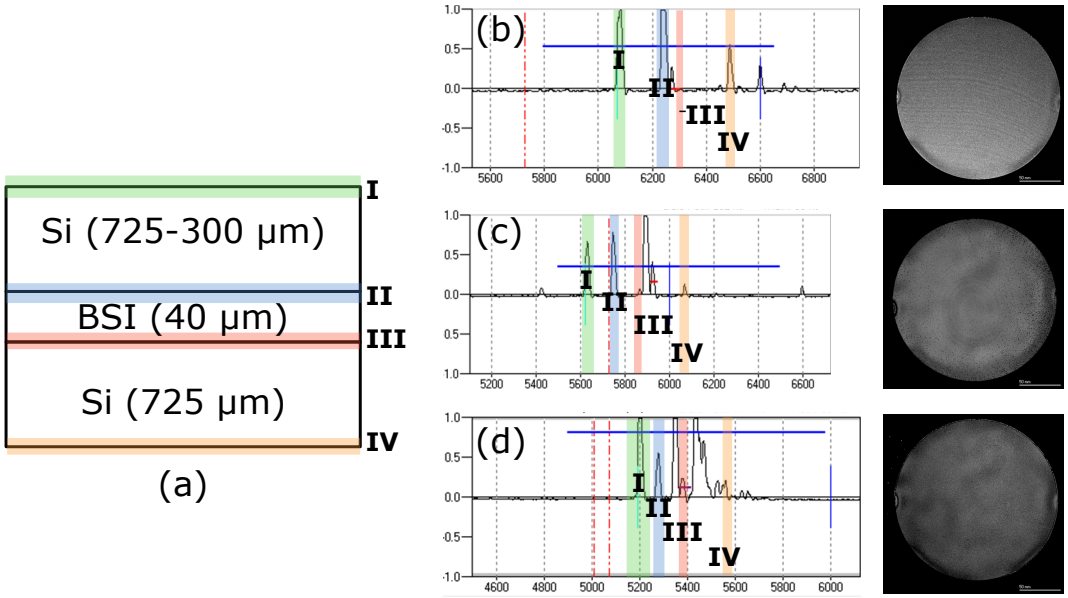


Figure 2.20: SAM analysis of adhesive bonding stack with a top wafer of different thicknesses (a) Analyzed stack, colored area corresponds to the matching time frame in a-scan (b-d) A-scans and c-scans from the red gate. (b) 725 µm (c) 500 µm (d) 300 µm

The first two still corresponded to the entry and exit peak of the top wafer, as presented in table 2.3. The position of the peak corresponding to the bonding interface is empirically determined but it is always a satellite peak, separated by (25 ± 3) ns from its nearest neighbor, which is likely an echo from the SI/BSI reflected signal.

| Top silicon thickness µm | Δt (ns) | Half of the acoustic travel length (µm ) |
|---|---|---|
| 725 | 162 | 682 |
| 500 | 114 | 480 |
| 300 | 72 | 303 |
| 200 | 47 | 198 |
| 150 | 35 | 147 |

Table 2.3: Time delays obtained on a-scans between peaks **I** and **II** and the calculated distance for different top wafer thicknesses

Figure 2.21 presents some examples of SAM c-scans of polymer bonded stacks. The image (a) shows some slight contrast variations but overall there is no sharp change in the collected signal indicating a defect. Scan (b) shows a significant defect on the right side. It corresponds to the location of the metallic clamp holding the stack in place before bonding. An annealing step might be able to cure this defect. The bonding interface imaged in scan (c) presents significant defects all over the bonding interface. Air bubbles were trapped at the interface due to dewetting of the glue layer. This kind of defects leads to the discarding of the stacks as it will not be able to sustain mechanical grinding steps.

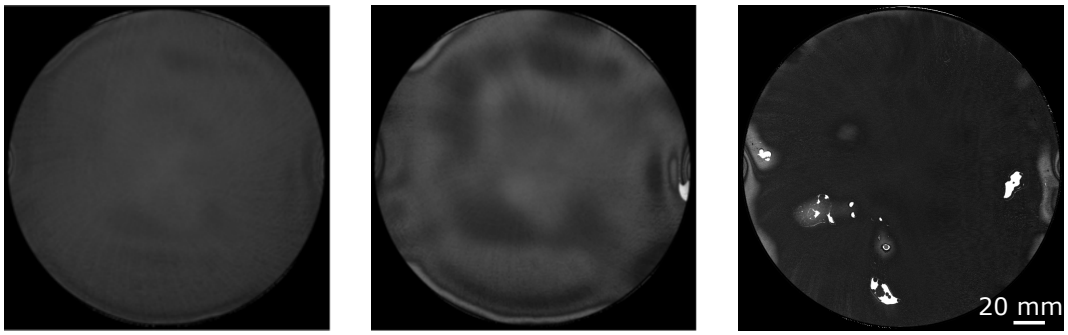


Figure 2.21: Examples of SAM c-scan images of 200 mm polymer bonded stacks. (a) Defect free bonding interface (b) Edge defects at the clamp location (c) Major defects due to the dewetting of the glue layer

After controlling the quality of the bonding interface, quantifying the adherence energy is a key issue for a temporary bonding process. During the different dismounting and transfer steps (Steps **K** and **L**) a qualitative information on the position of the weakest interface is obtained since it is the one that yields when separating the film from the carrier. To quantify more accurately the adherence energy, the Double Cantilever Beam (DCB) method proposed for wafer bonding by Maszara *et al.* was used [Maszara et al., 1988]. A blade is inserted in between the bonded wafer as illustrated in figure 2.22. The adherence is calculated using El Zein formula for anisotropic materials [El-Zein and Reifsnider, 1988], simplified for the present geometry in equation 2.4.

$$G = \frac{3}{16}\frac{E\delta^2 t^3}{(1-\nu^2)\,a^4}, \tag{2.4}$$

where G is the adherence energy ($J/m^2$), E is the silicon Young modulus in the beam direction (169 GPa, $\nu$ the Poisson ratio between the beam and the crack front propagation direction (0.06), $\delta$ the blade thickness, $t$ the wafer thickness and $a$ the crack length described in figure 2.22. While E and $\nu$ are tabulated, and $t$ and $\delta$ can be measured prior to the experiment, some experimental uncertainty can arise from the measurement of $a$. $a$ can be decomposed in three component : $a_{blade}$, $a_{measured}$ and $a_{\mathrm{IR}}$. $a_{blade}$ is the length between the blade edge and the contact point between the wafer and the razor blade, it is measured with an optical microscope prior to the blade insertion. $a_{measured}$ is obtained by Infrared (IR) observation and corresponds to the debonded distance between the razor blade tip and the first optical interference. $a_{\mathrm{IR}}$ is the remaining debonded length, not included in $a_{measured}$ due to optical interference. Knowing the beam deformation equation, it can be calculated [Fournel et al., 2012, 2013].

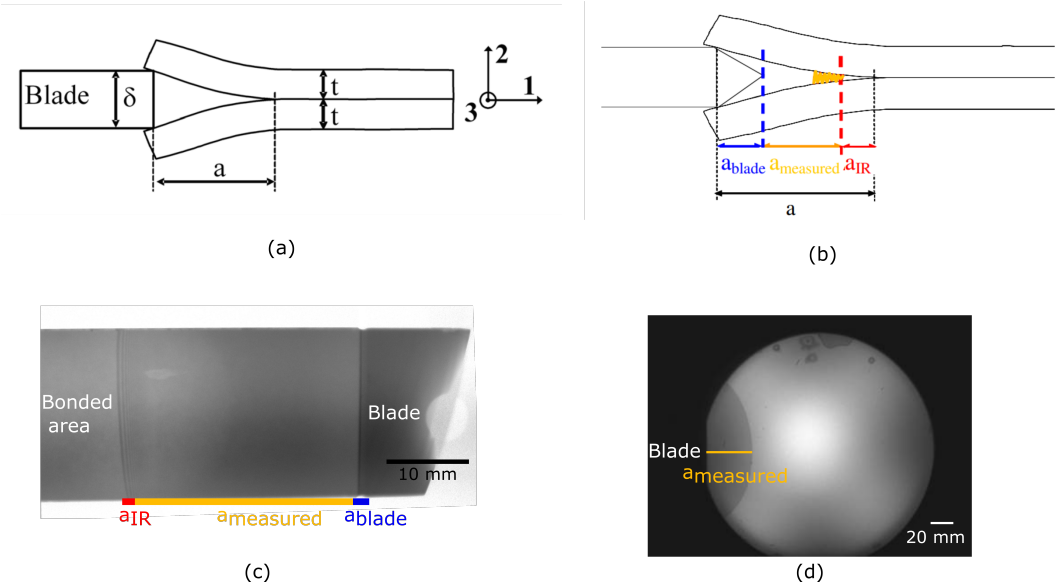


Figure 2.22: Blade insertion for adherence measurement in wafer bonding. (a) Schematic of a blade insertion (b) Detail of the different parameters used in the determination of $a$ used in equation 2.4 (c) IR image of a razor blade inserted between two bonded silicon beams. Measured parameter for adherence energy are highlighted. (d) IR Snapshot of a bonded stack during a blade insertion measurement

This method is widely used in direct bonding but its validity needs to be evaluated for polymer bonding. The presence of an adhesive polymer at the bonding interface can be taken into account with a closed formed solution proposed by [Penado, 1993]. This method was also used by [Argoud, 2012] and [Guillemenet and Bistac, 2001]. The equation 2.4 is modified with a second term. Adherent (here silicon) and adhesive (here a polymer) are assumed to act as springs in series with individual contribution $K_{Si}$ and $K_{Pol}$. The total contribution is expressed as :

$$K = \frac{1}{1/K_{Si} + 1/K_{Pol}} \tag{2.5}$$

where

$$K_{Si} = \frac{2Eb}{t} \tag{2.6}$$

and

$$K_{Pol} = \frac{E_{Pol} b}{t_{pol}} \tag{2.7}$$

With b as the sample width.

The resulting expression for G is :

$$G_{pol} = \frac{3}{16} \frac{E\delta^2 t^3}{(1-\nu^2) a^4} \frac{1}{(1+(\lambda_{Si}/\lambda)(0.64t/a))^4} \tag{2.8}$$

With

$$\lambda = \left(\frac{3K}{Ebt^3}\right)^{1/4} \tag{2.9}$$

and

$$\lambda_{Si} = \left(\frac{3K_{Si}}{Ebt^3}\right)^{1/4} = \frac{6^{1/4}}{t} \tag{2.10}$$

Using equation 2.4, 2.5, 2.6, 2.7, 2.9, 2.10 and 2.8 the adherence energy for a bonded stack with a polymer

adhesive $G_{pol}$ can be expressed as :

$$G_{pol} = G\frac{1}{(1+(\frac{tE_{pol}+2t_{pol}E}{tE_{pol}})^{1/4}0.64\frac{t}{a})^4} = G*\zeta_{pol} \tag{2.11}$$

Where $\zeta_{pol}$ is a correction coefficient for the standard DCB adherence energy value. For two 725 µm thick (100) silicon wafer bonded with a 40 µm BSI layer ($E_{pol}$ = 2.1 GPa) $\zeta_{pol} \approx 0.9$. Neglecting the polymer effect in a polymer bonded stack can lead up to a 10% overestimation in the case of BSI. As this is still within the margin of error of the measurement, and as the blade insertion purpose is a comparison between the different interface and the value reported in the literature, the standard El zein equation was used here. Combined with the underestimation of debonded length, a significant uncertainty can arise from DCB measurements. Absolute values need to be taken into account with great care but it remains a powerful, cost effective and fast method for assessing the bonding energy in polymer bonded stack.

#### 2.1.7.3 Wafer Morphology

During the grinding step, thickness of the different layers are monitored, as well as the morphology of the stack. A rough estimation of the stack thickness is usually performed with a mechanical comparator but for a better overview of stack morphology, a FRT MICROPROF tool is used. Three types of characterization are performed with this tool :

- Evaluation of the full stack height in two full diameters. The method used is a double confocal measurement (DC measurement). Two confocal microscopes monitor each face of the stack, their height difference gives the full stack thickness in a given point. From these thickness profiles the Total Thickness Variation TTV can be extracted as seen in figure 2.23(a). This metric gives a rough estimation of the thickness homogeneity and a maximum value is often specified for industrial tools or processes.
- An Infrared (IR) sensor was also used to evaluate the thickness profile and TTV of the top silicon layer during grinding steps.
- The bow, the convention used here is the bow-semi, the formula used is equation 2.12 where $f_{\mathrm{FAV}}$ and $b_{\mathrm{FAR}}$ are the surface to sensor distance with the wafer front-side up and backside up respectively [ASTM and SEMI, 2015]. The two measurements are necessary to avoid the influence of gravity on the bow. Curvature radius can also be calculated from these values as shown in equation 2.13. The convention is that a negative bow indicates a concave wafer and a positive bow is obtained for a convex wafer.

$$B = \frac{f_{\mathrm{FAV}} - b_{\mathrm{FAR}}}{2} \tag{2.12}$$

$$R = (\frac{D^2}{8B} + \frac{B}{2}) \tag{2.13}$$

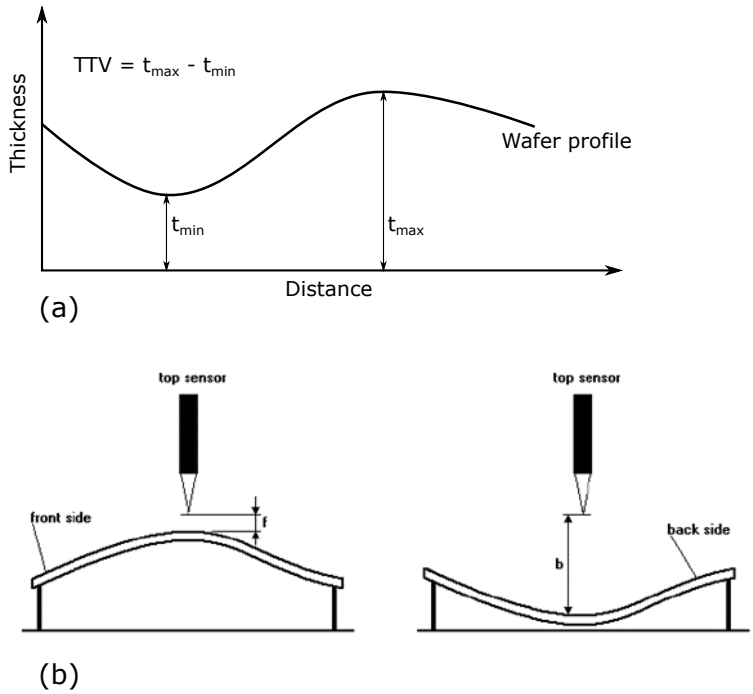


Figure 2.23: (a) Method of measurement of the Total Thickness Variation (TTV) using a wafer thickness profile (b) Procedure for measurement of a wafer's bow, the bow is then obtained using equation 2.12

#### 2.1.7.4 Thin film characterization

In order to asses the final sc-Si film thickness after transfer on a polymer layer, several methods can be evaluated :

- High Resolution X-Ray Diffraction (HRXRD). The thickness fringes width and frequencies around a Bragg peak are a function of the number of atomic planes of a crystalline film. $\omega-2\theta$ coupled scans are performed with a Bruker D8 diffractometer (copper anode $\lambda_{k\alpha} = 1.540\,56$ Å). The scans are performed around the (004) silicon peak position.

- X-Ray Reflectivity (XRR). This technique is sensitive to electron density and surface roughness. Contrary to HRXRD it allows characterizing the thickness of amorphous layers. Kiessig fringes are measured and fitted to obtain a thickness value.

- Ellipsometry is another widespread method for thin film characterization in microelectronics. A polarized light is reflected on a sample surface. Polarization changes between the incident and reflected beam are modeled to extract thin film thickness value. A Nanometrics Atlas XP+ is used for in-line characterization and a M-2000 Ellipsometer from J.A. Woollam Co. is used for model developments.

#### 2.1.7.5 Raman Spectroscopy

The general theory behind Raman Spectroscopy and its application to stress measurement in semiconductors materials is detailed in annex A.1. The data presented in this thesis are obtained using a Horiba LabRam HR with paired with a He-Ne laser (632.81 nm, 17 mW). Hole and slit size are respectively 100 and 200 µm to achieve a confocal beam, the vertical resolution is 2 µm while the lateral resolution is 1 µm. A 100X objective is used. The laser power was limited to 10% of its nominal value to avoid thermal stress [Wolf, 1999].

The Raman is paired to a motorized stage ($50 \times 70 \times 4$ mm). A bulk silicon sample was used as a reference before and after each measurement. In this chapter, all the stress measurement were performed assuming the stress in the (100) silicon plane is purely biaxial. The biaxial strain $\varepsilon_{bi}$ can be obtained using equation 2.14 with the experimental Raman peak shift $\Delta\omega$ and the strain shift coefficient $b_{bi} = -723$ [Nakashima

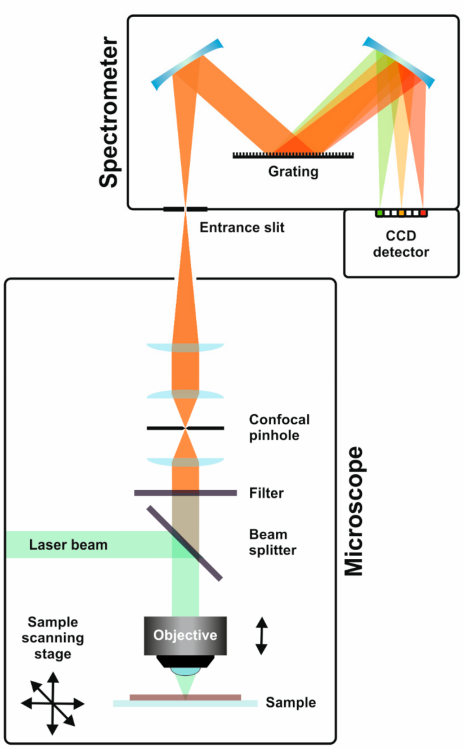


Figure 2.24: Schematic of a confocal Raman spectrometer microscope [Schmid and Dariz, 2019]

et al., 2006; Peng et al., 2009] The biaxial stress $\sigma_{bi}$ is then expressed in equation 2.15 using Hooke's law and silicon biaxial Young modulus $B_{100} = 180\,\text{GPa}$ [Hopcroft et al., 2010].

$$\Delta\omega = b_{bi}\varepsilon_{bi} \tag{2.14}$$

$$\sigma_{bi} = \frac{\Delta\omega}{b_{bi}} B_{100} \tag{2.15}$$

All the Raman spectra were fitted with a Python routine. This routine also performed calibration from the reference spectrum and stress calculation as described above. The code is available on a GitHub repository [Michaud et al., 2019].

#### 2.1.7.6 Topography

Surface roughness is a key parameter in wafer bonding as detailed in chapter 1. Depending on the roughness and surface monitored, different techniques are used. The parameter used to describe the surface roughness is $R_q$ the root mean squared of the surface height to the mean surface as detailed in equation 2.16 and figure 2.25. The peak to valley maximum distance was also used in addition to $R_q$ in case of surfaces with inhomogeneous topography.

$$R_q = \sqrt{\frac{h_1^2 + h_2^2 + h_3^2 + \ldots + h_n^2}{n}} \tag{2.16}$$

For larger scale (*i.e.,* above 100 µm × 100 µm) characterization of a surface nanotopography, an interferometer microscope was used. A beam is separated in two parts, one is reflected on a mirror (reference) and one on the sample. Sample topography induces interference in the combination of the two beams. Displacement of the reference surface allows for a reconstruction of the sample topography with an order of magnitude of $\lambda/4$ where $\lambda$ is the wavelength of the light source (632 nm). The tool used here is a Wyko NT 3300 from the manufacturer Veeco.

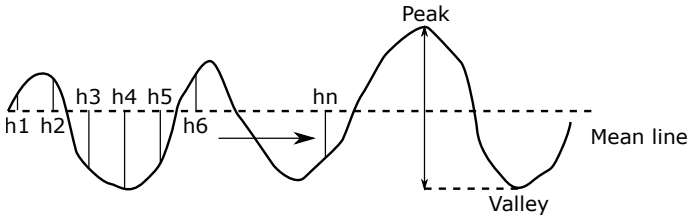


Figure 2.25: Schematic to illustrate the metrics used to describe surface roughness and nanotopographgy

For smaller surface (*i.e.*,below100 µm × 100 µm) analyses and smoother topography (*i.e.*,roughness lower than 10 nm) an Atomic Force Microscopy (AFM) is used. A Bruker FastScan tool was used in "ScanAsyst" mode which is a particular mode of peakforce tapping developed by Bruker.

## 2.2 Wafer preparation for silicon single-crystal layer transfer

### 2.2.1 Decreasing top Silicon thickness

As detailed in table 2.1, the SOI used as starting wafer has a 200 nm thick silicon and a 400 nm thick BOX. Actual thicknesses obtained by ellipsometry are 206 ±11 nm and 403 ±2 nm. These data are obtained on 25 wafers with 49 data points per wafer. The table 2.4 presents the different layers thicknesses after oxidation and etching for the preparation of stack **A1**. The target oxide thicknesses were calculated using equation 2.1. Snapshots of the resulting SOI are presented in figure 2.26. SOI substrates with top silicon thickness varying from 20 to 205 nm were thus available.

| | Oxidation | | | Etching | |
|---|---|---|---|---|---|
| Final silicon thickness target (nm) | BOX (nm) | Top silicon layer (nm) | Oxide (nm) | BOX (nm) | Top silicon layer (nm) |
| 20 | 404.2 ± 0.1 | 19.5 ± 1.0 | 408.2 ± 0.4 | 404.4 ± 0.1 | 19.3 ± 1.3 |
| 50 | 403.2 ± 0.1 | 61.5 ± 0.9 | 333.1 ± 0.6 | 404.1 ± 0.1 | 62.1 ± 0.2 |
| 100 | 403.5 ± 0.3 | 106.5 ± 4.4 | 220.9 ± 0.2 | 403.9 ± 0.2 | 106.9 ± 4.7 |
| 150 | 403.2 ± 0.1 | 151.6 ± 1.0 | 115.3 ± 0.1 | 403.7 ± 0.1 | 151.5 ± 0.9 |

Table 2.4: Oxide and silicon thickness during the oxidation and etching of SOI wafers

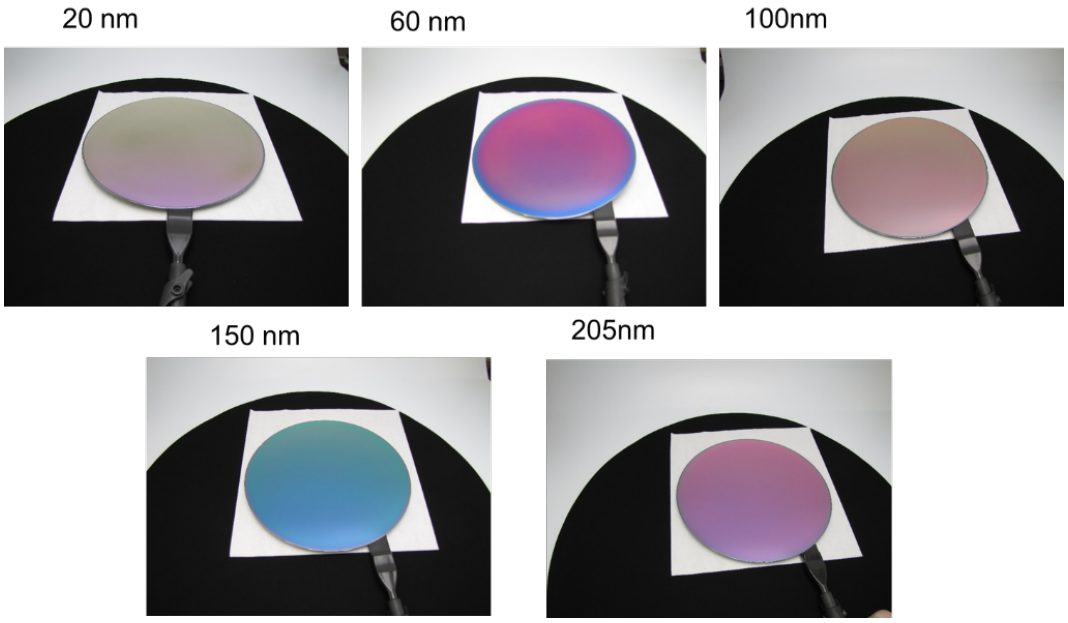


Figure 2.26: Snapshots of 200 mm SOI with different top silicon thicknesses. The thickness smaller than 205 nm are obtained by oxidation and etching of the 205 nm thick initial top silicon layer.

### 2.2.2 Patterning

Figure 2.27 presents snapshots of SOI after photolithography, etching and photoresist removal. The patterns are designed to be used as tensile test sample. Wafer pictured in figure 2.27(a) and (b) were produced using soft masks. Only one pattern orientation is present as the masks could be rotated to obtain any desired orientation. For the 1X chromium mask (figure 2.27(c) the mask is aligned with the wafer notch. So two orientations ([110] and [100]) of $2 \times 24\,mm^2$ ribbons were patterned as well as disks.

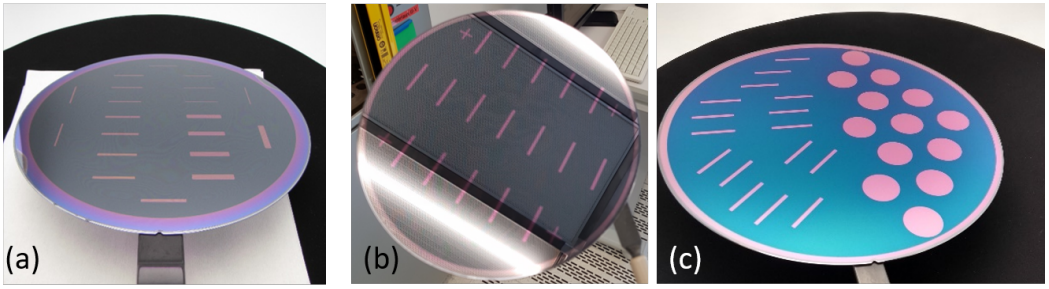


Figure 2.27: SOI wafers with a patterned 205 nm top silicon layer. (a-b) Two different soft masks (c) Final 1X chromium mask

One of the motivation behind the use of a 1X chromium mask was to achieve a smoother edge definition. As seen in figure 2.28 (b,c), patterns edges can deviate as far as 1 µm from a straight line. This is due to inhomogeneity in the ink used in the mask as seen in snapshot in figure 2.28 (a). The 1X chromium mask offered a much better resolution for the macroscopic patterns used to design tensile test sample. With an optical microscope, no roughness is observed on the pattern edge (see figure 2.28 (d,e)).

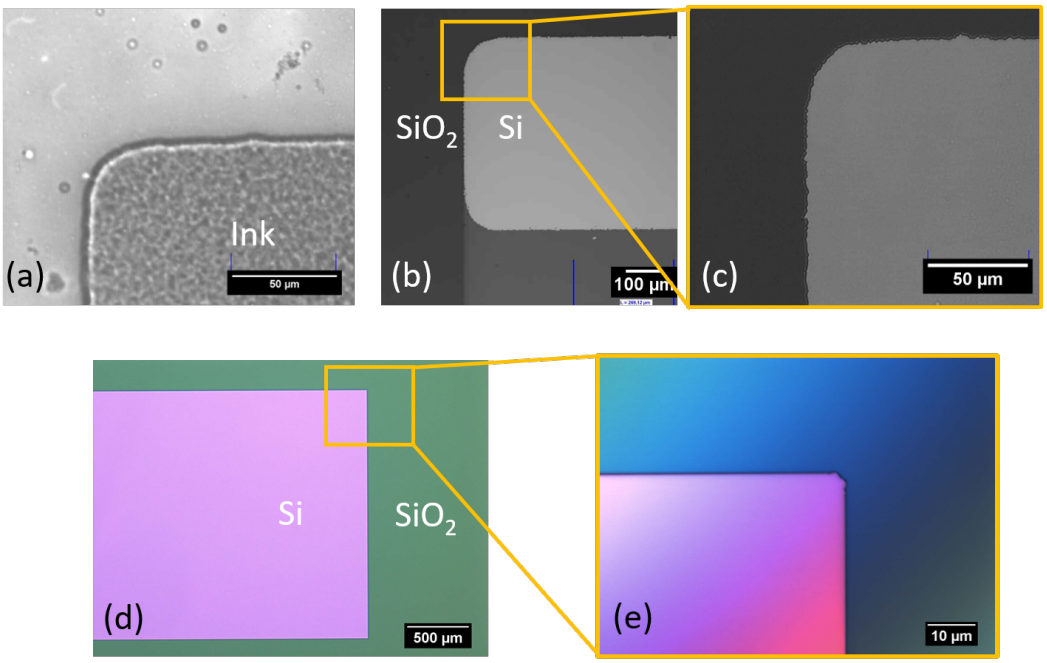


Figure 2.28: (a) Micrograph of soft mask (b,c) Micrographs of pattern defined on a SOI top silicon layer using a soft mask (d,e) Micrographs of pattern defined on a SOI top silicon layer using a 1X chromium mask

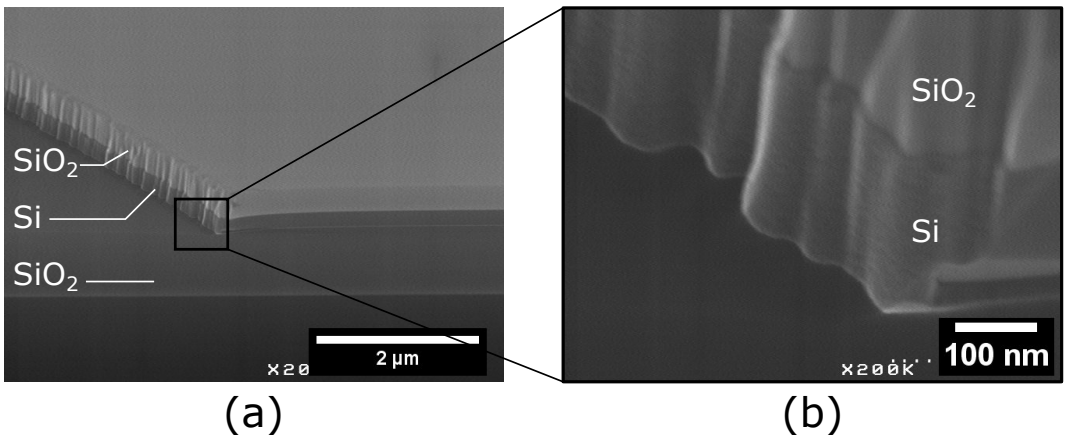


Figure 2.29: Tilted SEM cross-sectional observation of an oxidized SOI after photolithography and etching. The pattern is oriented along the [100] direction of the silicon film (a) Full stack (b) Detail of the silicon/oxide pattern edge

Nevertheless SEM observations (figure 2.29) revealed some sub-micronic variations in pattern edges after a standard lithography process as used previously. As described in paragraph 2.1.3.2, to smooth the pattern edge, an anisotropic etching step was performed on silicon patterns (**A4**, detailed in figure 2.4(b)).

Micrographs of the patterns after anisotropic etching presented in figure 2.30 show characteristic undercut for TMAH etching on the ribbon corners [Pal et al., 2014]. A silicon underetch can also be observed for the two different ribbons orientations. The [110] oriented ribbons presented a 1.6 ± 0.5 µm underetch whereas it was significantly higher for [100] oriented ribbons (22 ± 0.5 µm).

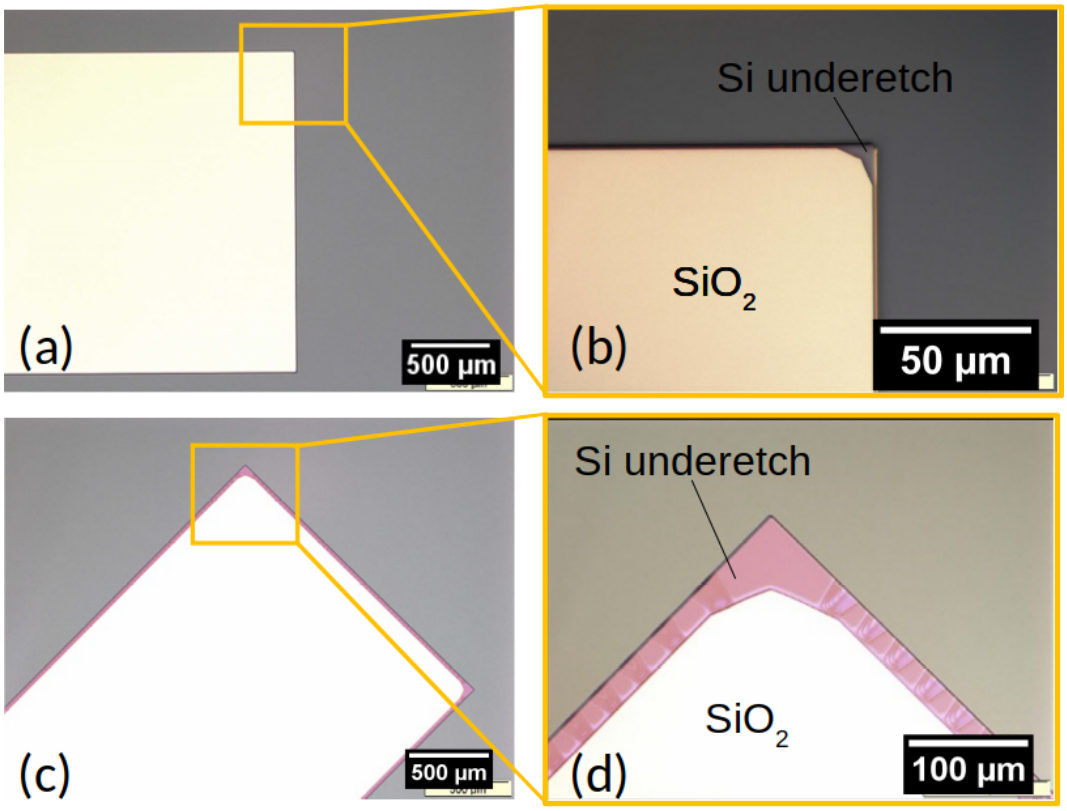


Figure 2.30: Micrography of silicon ribbons after anisotropic TMAH etching of their sidewalls.
(a,b) [110] oriented ribbon (c,d) [100] oriented ribbon

Other SEM observations were performed during the pattern edge smoothing process. Cross-sectional observations of a [100] oriented ribbon are presented in figure 2.31 The silicon underetch is visible in figure 2.31(a). As seen in Figure 2.31 (b) the sidewalls presented a low surface roughness and were formed by (100) planes. A similar cross-sectional view of a [110] oriented ribbon is visible in figure 2.32(a). A bevel was formed on the silicon edges with an angle of 54 ± 1° between the edges and (001) plane. Silicon etch rate in a 25 wt% aqueous TMAH solution at 80 °C is 0.5 µm/min for (100) planes and 0.9 µm/min for (110) planes. And the etch rate ratio for (111)/(100) silicon crystalline planes is estimated to 0.05 [Tabata et al., 1992]. It explains that higher order planes were revealed on the edges of [110] oriented ribbons. Those planes present higher activation energies and thus lower etch rate. Pattern edges parallel to (100) planes were etched at a linear rate without revealing higher order planes, resulting in a more significant underetch and smooth (100) sidewalls.

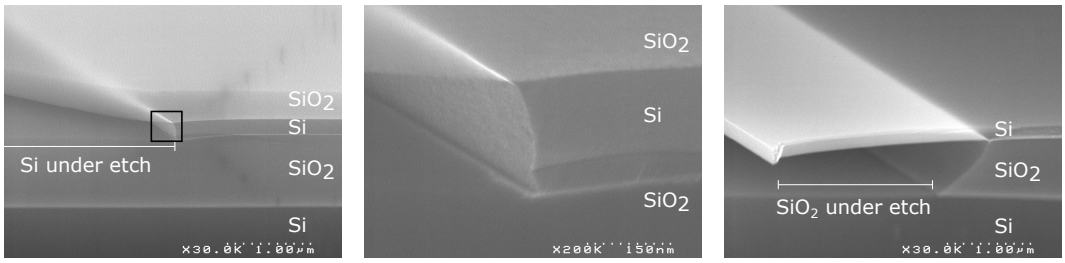


Figure 2.31: SEM observation of [100] pattern edge smoothing with TMAH anisotropic chemical etching. (a) After TMAH etching (b) Detail of the black square (c) After wet etching of $SiO_2$

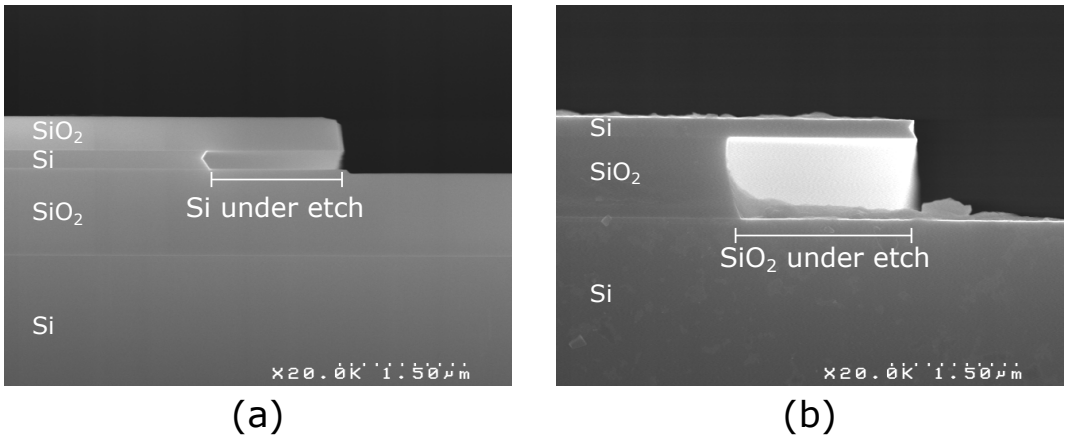


Figure 2.32: SEM observation of [110] pattern edge smoothing with TMAH anisotropic chemical etching. (a) After TMAH etching (c) After wet etching of $SiO_2$

As seen in figure 2.31(c) and 2.32(b), the 1 µm thick BOX was entirely removed during the wet etching of the 400 nm thick thermal oxide layer protecting the patterns surface during anispotropic etching. A significant oxide underetch is observed (1.5 µm), leaving the edge of the silicon pattern suspended. The difference between the expected and actual structure are illustrated in figure 2.33. Implication of this overetch on the transfer of silicon pattern on a polymer substrate will be discussed later in this chapter.

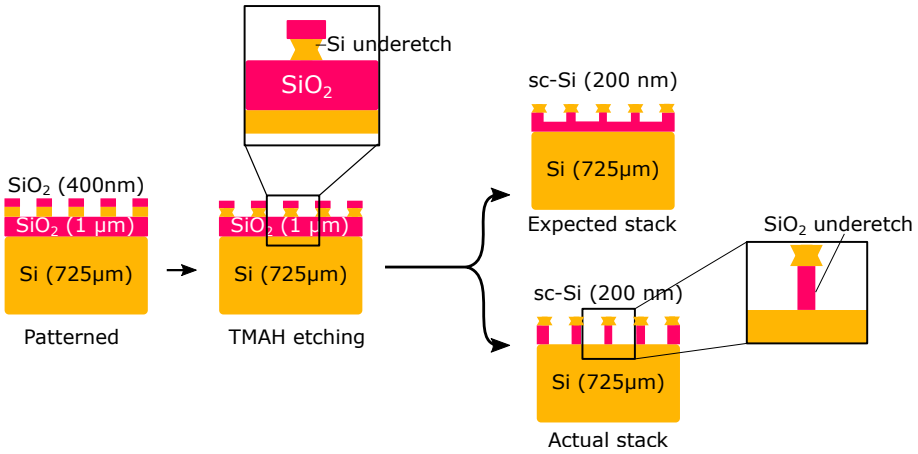


Figure 2.33: Schematic of the TMAH anistropic etching atfter patterning of an oxidised SOI with the expected structure and the one actually observed

### 2.2.3 Wafer edge trimming and defectivity

Microscopic observations of the bonded stack with and without trimming are presented in figure 2.34. As expected, the thin and fragile edges were not present after grinding in the case of an edge trimmed wafer. However the glue was in contact with the trimmed edge. Moreover edge trimming of the SOI wafer resulted in a significant particles contamination of the surface: 1300 defects are observed for a threshold detection of 500 nm. As shown in figure 2.35, a megasonic cleaning of the surface reduced the particles contamination to about 300 remaining particles measured with a threshold of 500 nm.

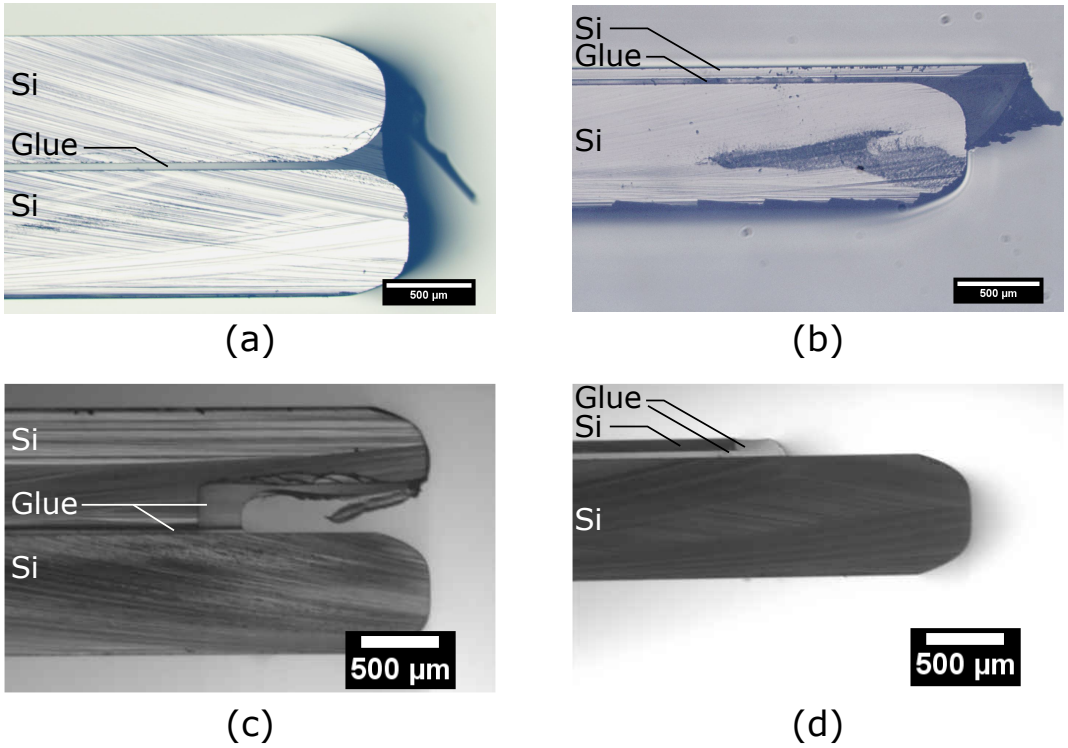


Figure 2.34: Cross-section optical microscope observations of a bonded pair before and after a mechanical grinding step (a-b) Without edge trimming (c-d) With an edge trimming step described in subsection 2.1.3.3

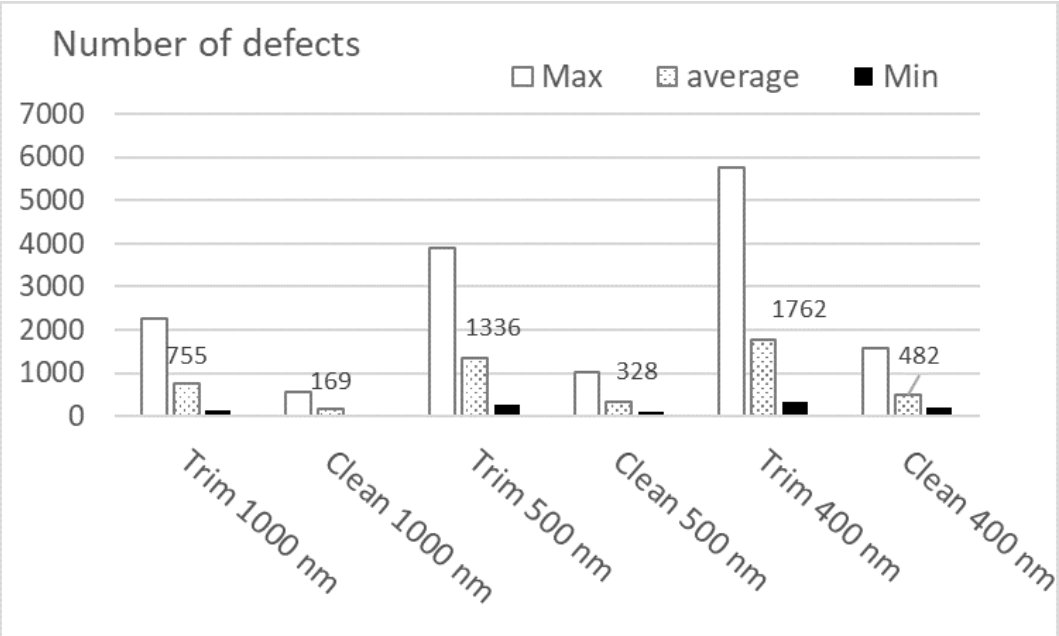


Figure 2.35: Defectivity of edge trimmed wafers before and after megasonic isopropyl alcohol (IPA) cleaning for different defect size threshold

### 2.2.4 Adherence energy

The adherence energy of different bonded stacks was evaluated using the DCB method (section 2.1.7.2). The results are presented in table 2.5.

For BSI, the adherence energy of BSI/Si is around $2\,J/m^2$ and the opening interface is the bonding interface. If a fluorinated polymer (3M 2702) is used, the adherence BSI/2702 is less than $0.4\,J/m^2$ and thus lower than the BSI/Si adherence. BSI/2702 is the opening interface. It clearly indicates that 3M 2702 coating acts as an AS layer for the BSI glue.

For SPIS 21, the adherence is $1\,J/m^2$. The weakest interface is the bonding interface.

We know that a mechanical dismounting is easy and safe when the adherence is lower than $1.2\,J/m^2$ [Abadie et al., 2019]. SPIS 21 is suitable for the dismounting while an AS coating is needed for stacks using BSI as a glue. With the bonding and lamination parameters used in this study, the SPIS remains on the laminated wafer after blade insertion.

| $1^{st}$ interface | $2^{nd}$ interface | Temperature (°C) | Adherence energy ($J/m^2$) | Reference |
|---|---|---|---|---|
| BSI 305 | Silicon wafer | 210 | 4<br>2.5 ± 0.5 | [Montméat et al., 2018]<br>this work |
| BSI 305 | 3M 2702 | 210 | 0.4 ± 0.1<br>0.1 ± 0.01 | [Montméat et al., 2018]<br>this work |
| BSI 305 | Glass | 210 | 1.56 ± 0.31 | This work |
| SPIS 21 | Silicon | 100 | 0.93 ± 0.2 | This work |

Table 2.5: Adherence energy for different bonded stacks

The choice of glue and AS coating in the bonding step (stacks **B1** to **B5**) will defined the separation interface during the dismounting of the transferred film. The results presented below will detailed the effect of the bonding stack and bonding energy on the transfer of a sc-Si film on a flexible polymer substrate.

## 2.3 Glue as flexible substrate for silicon thin films

After polymer bonding and removal of the SOI backside, the sc-Si film is effectively transferred on a polymer layer (SPIS or BSI). As illustrated in step **K2** of figure 2.2, the glue can be peeled off the carrier to obtain a stand-alone silicon on glue flexible structure. To do so, the weakest interface needs to be the one between the glue and the rigid carrier.

### 2.3.1 BSI (BrewerBond™305-30)

Here an evaluation of the transfer process using bonded pair **B1** with BSI is detailed.

#### 2.3.1.1 Bonding and backside removal

The bonding step was performed at 210 °C without edge trimming. Corresponding SAM images can be observed in figure 2.36. The bonding interface did not present any defect. It remained intact during the two successive grinding steps (**D** and **E**).

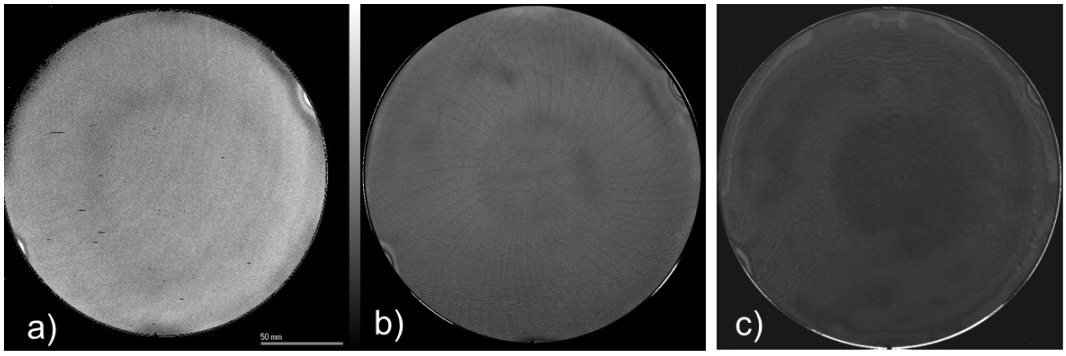


Figure 2.36: (a) SAM image of the structure after bonding (b) After grinding the SOI backside down to 200 µm (c) After grinding the SOI backside down to 50 µm.

Cross section of the stack are visible in figure 2.37 (a,b). Apart from the bonding stack edges, the glue layer remained homogeneous and void free on the full stack diameter. After grinding the top silicon layer down to 200 µm and 50 µm the bows were 200 µm and 300 µm (convex shape with the SOI on top), respectively. The grinding operations led to sub-surface damages and caused compressive strain on the upper, ground, surface of the silicon substrate[Haapalinna et al., 2004].

Thickness profiles are presented in figure 2.38. After grinding the SOI wafer backside down to 200 µm, the full stack presented a pyramidal profile (a) as well as the top silicon layer. The fine grinding step greatly decreased this trend for both full stack and top silicon layer (c,d). For the top silicon layer, the higher TTV values are due to thickness variations in the glue thickness on the wafer edge. The IR Silicon thickness measurement presented in figure 2.38 yielded a TTV of 7.5 and 5.3 µm. Both topographies (200 and 50 µm) were very similar and the TTV values were close to 5 µm for both wafers. It has already been demonstrated that the TTV value of a thinned wafer bonded to a carrier depended only of the bonding process[Montméat et al., 2015]. We can now also conclude that the TTV values were not affected by the grinding process and do not depend on the thickness of the thinned wafer. Our bonded structure is thus compatible with a back grinding process and led to a very homogeneous silicon wafer in term of thickness.

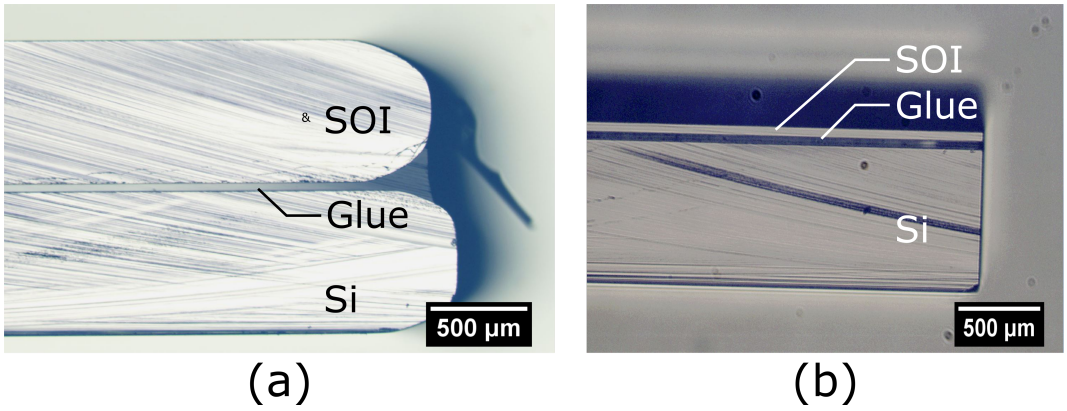


Figure 2.37: (a) Cross-section of a SOI bonded to Silicon handling wafer using a 40 µm BSI layer (b) Previous stack after mechanical grinding of the SOI backside down to 50 µm

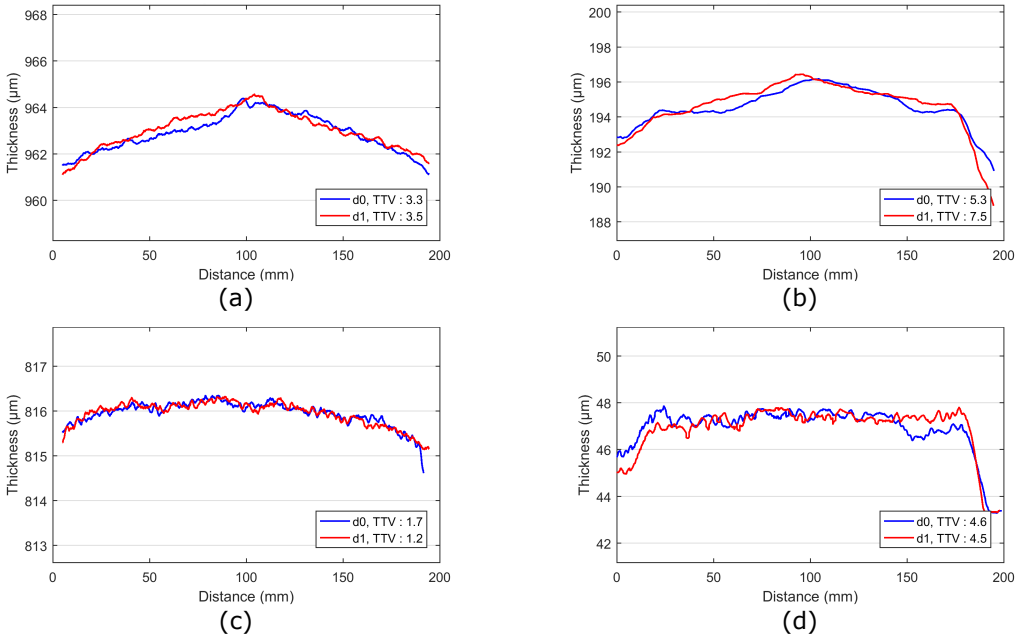


Figure 2.38: Thickness profile in two diameter of a 200 mm bonded stack (a) DC measurement of the full stack thickness after coarse grinding of the SOI backside down to 200 µm (b) Corresponding IR measurement of the Bulk silicon layer (c) DC measurement of the full stack thickness after fine grinding of the SOI backside down to 50 µm (d) Corresponding IR measurement of the Bulk silicon layer

After chemical etching of the remaining bulk silicon and BOX (step **F** and **G**), the 205 nm did not present any crack or undulation. The silicon thin film color is a function of its thickness, a visual inspection confirmed the pink color expected for a 205 nm Si film presented in figure 2.39 (a) [Mirshafieyan and Guo, 2014]. A 500 µm over-etch was also observed at the notch (figure 2.39). Figure 2.40 presents SEM observations the stack **H** that confirmed the thickness (205 nm) of the transferred silicon film and that no voids or inhomogeneities were present at this scale. Ellipsometry measurements yielded a silicon thickness of 203.5 ± 1.6 nm.

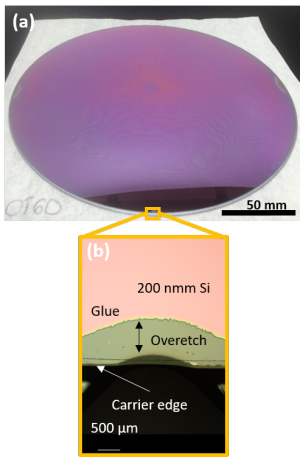


Figure 2.39: (a) Snapshot of stack **H** with a 205 nm thick sc-Si film. (b) Micrograph of the notch after chemical etching of the BOX

2

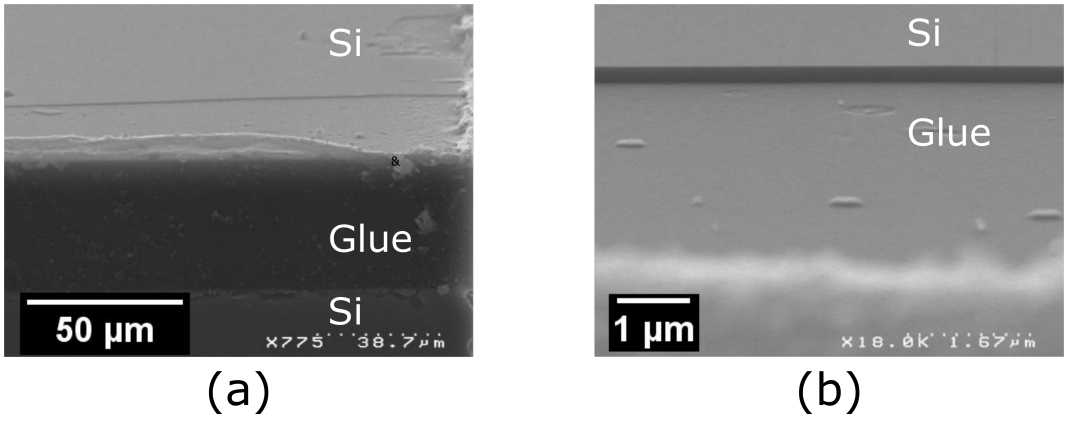


Figure 2.40: Cross-sectional SEM observations of a 200 mm thick sc-Si film transferred on a 40 µm thick glue layer (a) Full stack (b) Detail of the step formed by the sc-Si film on the polymer layer

AFM topography images of the sc-Si thin film HF-last surface are presented in figure 2.41. The two surfaces, in the wafer center and on an external diameter, presented a roughness lower than 0.2 nm. This indicates that no morphological modification and particularly roughness modification were induced by the transfer process as the previous value are consistent with the roughness of a donor wafer during Smart-Cut™ (figure 1.18), *i.e.*, lower than 0.5 nm. As exposed in chapter 1, this roughness is below the specification required for direct wafer bonding. The roughness for a BSI 40 µm layer after spin coating on a bulk silicon wafer is 0.43 nm. This demonstrates that a 205 nm silicon layer retains its initial roughness after transfer on a BSI layer.

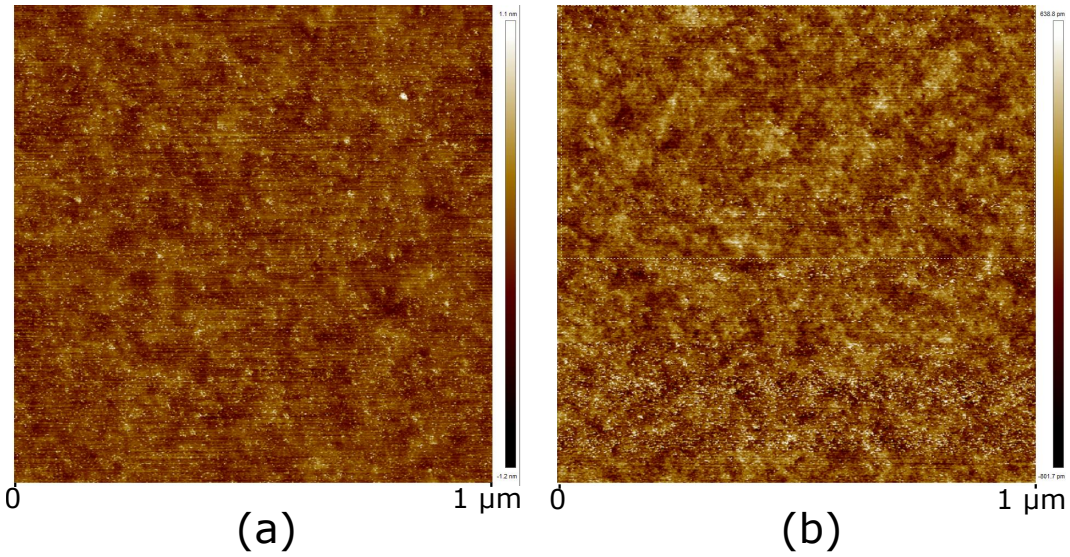


Figure 2.41: AFM topographic image of a sc-Si film after transfer on a 40 µm layer of BSI held by a rigid carrier (a) Wafer center, Roughness $R_q$ = 1.5 Å (b) Wafer outer diameter, $R_q$ = 1.7 Å.

#### 2.3.1.2 Dismounting and stress analysis

As presented in subsection 2.2.4, the expected separating interface in the present bonded stack is the BSI/AS one. As a result, the glue layers could be easily peeled of the carrier (step **J2** of figure 2.2). Figure 2.42 shows a snapshot of the manual peeling of the structure. The result is a SOP with a 40 µm thick BSI layer acting as a flexible substrate. No cracks or undulations were observed. The structure is convex with the sc-Si film face up as shown in figure 2.43(b). This curvature indicated that the two layers are under different stress level. The origin of this difference is the mismatch in Coefficient of Thermal Expansion (CTE) between the BSI ($8 \times 10^{-5}$ °C$^{-1}$) and the Silicon layer ($2.6 \times 10^{-6}$ °C$^{-1}$). After bonding, when the structure is cooled from Tg (≈ 70 °C) down to Room temperature (RT), the mechanical coupling between the layers will prevent full relaxation. To quantify the stress in the silicon layer, the biaxial stress is evaluated in the silicon layer with a Raman spectrometer. For a 205 nm transferred after bonding at 210 °C (in fact only the $T_g$ value is important), the mean biaxial tensile silicon stress is 40 MPa before peeling as illustrated in figure 2.43(a). After dismounting of the rigid carrier, the silicon is under a compressive stress of 60 MPa as a new equilibrium is reached between the two remaining layers. The compressive stress is consistent with the curvature observed in figure 2.43(b). The silicon prevents full relaxation of the polymer layer.

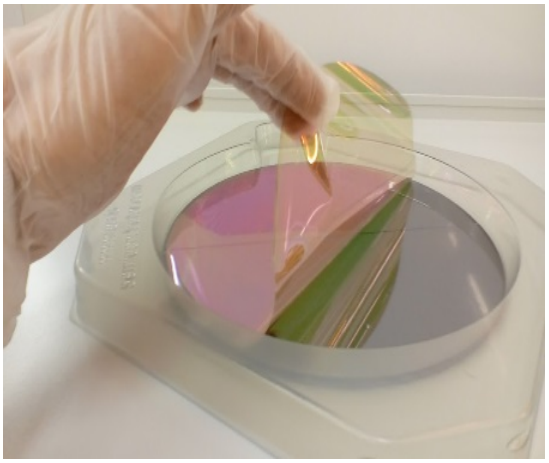

Figure 2.42: Snapshot of the manual peeling of a BSI/Si structure from a 200 mm silicon carrier wafer

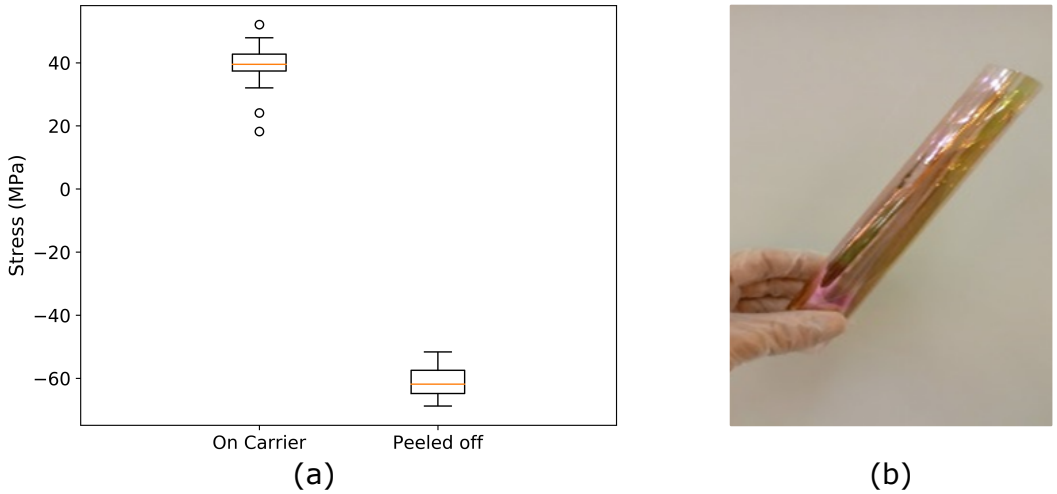


Figure 2.43: (a)Biaxial stress in a 200 nm sc-Si layer on glue before and after being peeled off its rigid carrier. Stress is calculated from raman spectrum collected on a $500 \times 500\,\mu m^2$ (b) Snapshot of a silicon on glue after being peeled off, the silicon is on the outside of the cylinder.

In the literature, compressive stress of similar magnitude in silicon film transferred on polymer substrate are reported [Byun et al., 2010; Argoud, 2012]. It is accepted that, given a significant difference in CTE between a silicon wafer and a polymer, the main driving force is the difference between the "mechanical" assembly temperature (related to the $T_g$) and the final temperature. Argoud used a simple law of scale, which yields a stress of similar magnitude. The law is described in equations 2.17 and 2.18 where $\Delta T$ is the difference between the assembly temperature and RT, $\Delta\alpha$ the difference between the polymer and silicon CTE, $E_1$ and $E_2$ the Young modulus, $h_1$ and $h_2$ the thickness for respectively the silicon film and the polymer substrate.

$$\varepsilon = \frac{\Delta\alpha\Delta T}{1+\xi} \tag{2.17}$$

With $\xi$ the ratio defined as :

$$\xi = \frac{E_1 h_1}{E_2 h_2} \tag{2.18}$$

In the case of a 200 nm thick silicon film on a 40 µm thick BSI layer, it yields an order of magnitude of 0.5 % strain or 700 MPa stress, which is an order of magnitude higher of the experimental results presented here.

A suitable model was used, stress in bonded heterostructures can be calculated using Timoshenko theory on bi-metal thermostat [Timoshenko, 1925].

For two layers, the radius of curvature can be calculated with the equation 2.19 where $E_i$ is the Young modulus, $v_i$ the Poisson ratio,$d_i$ the thickness and $\alpha_i$ the CTE of material $i$. $T_i$ and $T_f$ are the initial and final temperature. For $m = d_1/d_2$ and $n = E1 * (1-\nu_2)/(E_2 * (1-\nu_1) = E_1'/[E_2'$

$$1/\rho = \frac{6\left(1+m^2\right)(\alpha_1-\alpha_2)\left(T_f-T_i\right)}{(d_1+d_2)\left(3(m+1)^2+\left(m^2+\frac{1}{mn}\right)(mn+1)\right)} \tag{2.19}$$

$$\frac{1}{\rho}-\frac{1}{\rho_0} = \frac{6\left(1+m^2\right)(\alpha_1-\alpha_2)\left(T_f-T_i\right)}{(d_1+d_2)\left(3(m+1)^2+\left(m^2+\frac{1}{mn}\right)(mn+1)\right)} \tag{2.20}$$

The stress in the different layers is then computed using equations 2.21 and 2.22.

$$\sigma_1 = \frac{1}{\rho}\left[E_1'\left(z-\frac{d_1}{2}\right)+\frac{1}{d_1}\left(\frac{E_1' d_1^3 + E_2' d_2^3}{6(d_1+d_2)}\right)\right] \tag{2.21}$$

$$\sigma_2 = \frac{1}{\rho}\left[E'_2\left(z - d_1 - \frac{d_2}{2}\right) - \frac{1}{d_2}\left(\frac{E'_1 d_1^3 + E'_2 d_2^3}{6(d_1+d_2)}\right)\right] \tag{2.22}$$

This model can be adapted to heterostructures with more than 2 layers [Feng and Liu, 1983]. Figure 2.44(a) presents the results for a Silicon (725 µm) / BSI (40 µm) / silicon (205 nm) structure formed at $T_{eff}$ and cooled down to RT. Stress in the glue and the polymer layer is plotted against $T_{eff}$ as Tg can vary with the cooling down kinetic and it is unclear below which temperature the elastic energy can be stored in the polymer. The polymer stress increases with $T_{eff}$ and is always positive (*i.e.*, tensile). It is consistent with the observation made in figure 2.43. Without the rigid carrier, the polymer will retract and the silicon film will prevent full relaxation of the polymer at the interface with the sc-Si film, resulting in a cylindrical structure with the silicon on the outer part. However, no matter the $T_{eff}$ value proposed here, the model gives a negative stress in the silicon layer which is inconsistent with experimental values (40 MPa).

An hypothesis to explain the origin of this tensile stress of the silicon layer when the structure is held by a rigid carrier is a temperature difference between the two heating elements of the bonder (figure 2.8). Here the SOI coated with BSI is placed on the bonding chuck and the carrier is placed on top. In figure 2.44 (b,c) the structure stressed is represented as a function of $\Delta T = T_{top} - T_{bot}$.

For the graph (b), $T_{top}$ is set to 70 °C. For negative value of $\Delta T$ (*i.e.*, the cooling down of the bonding chuck is faster), the model gives positive values of stress in the silicon layer. For the graph (c), $T_{bot}$ is set to 70 °C. The stress in the silicon layer also reaches positive values for negatives values of $\Delta T$ but it would still be below the detection limit of a Raman stress measurement.

With the use of this model, we showed that tensile stress in the top silicon layer of stack **H** could be explained by a difference in cooling speed of the bonding chuck and piston in the bonder. However the experimental values are still higher that the calculation. It could be explained by initial stress in the different SOI layers.

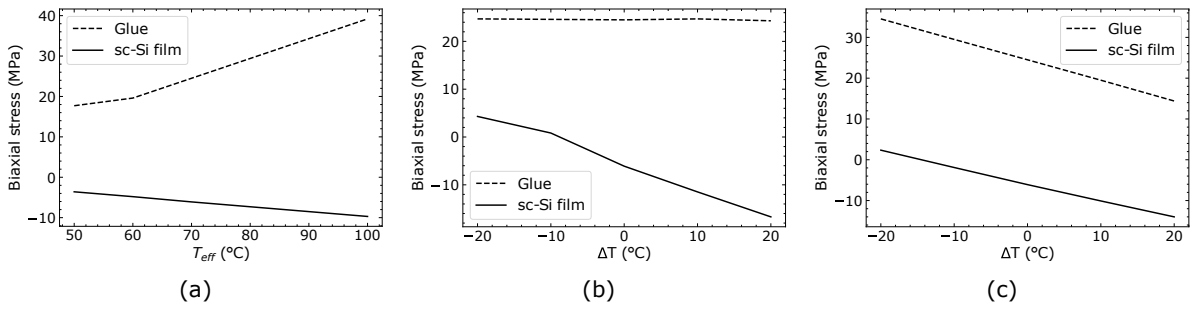


Figure 2.44: Stress in a transferred 200 nm sc-Si on BSI as a function off different bonding parameters. (a) Effective bonding temp (b) Initial temperature gradient between the top and bottom wafer, the glue and sc-Si thin film are placed on the bottom. $\Delta T = T_{top} - T_{bot}$ Here $T_{top}$ is set to 70 °C (c) Stress as function of $\Delta T$ with $T_{bot}$= 70 °C.

#### 2.3.1.3 Transfer of sc-Si film thinner than 200 nm

Previous results presented the transfer of 205 nm thick silicon layer. As the objective is to obtain high strain in the transferred thin film, one could assume that a lower thickness allows achieving higher maximum strain by decreasing the elastic energy necessary to reach a certain strain value. The SOI previously used were oxidized and etched to obtain the desired thickness with targeted thicknesses of 20, 60, 100 and 150 nm as shown in table 2.4. The resulting film was transferred without edge trimming, using bonded stack **B1** on a BSI layer on rigid carrier (stack **H**). Ellipsometry measurements presented in table 2.6 shows that the desired

| Goal (nm) | Thickness after oxidation and etching of a SOI (nm) | Silicon thickness after transfer on glue (nm) |
|---|---|---|
| 20 | 19.3 ±1.4 | 19.6 ± 1.7 |
| 50 | 61.9 ±1.7 | 61.9 ± 2.9 |
| 100 | 106.9 ± 1.8 | 107.7 ± 3.3 |
| 150 | 151.6 ±1.2 | 151.9 ± 2.6 |
| 205 | 206 ± 1.1 | 203.5 ± 1.6 |

Table 2.6: Silicon thickness measurement by ellipsometry. The first measurement are made on a SOI after oxidation and etching of the resulting oxide layer (step A1). The second measurement is performed after the removal of the SOI backside (step F)

silicon thickness was effectively transferred from the SOI to the glue

Snapshots of the transferred wafers are presented in figure 2.45 (a-c). Initial visual observation of the thin film color already indicated the transfer of varying sc-Si thicknesses [Mirshafieyan and Guo, 2014], and they are consistent with the color observed on the starting SOI seen in figure 2.26. Subfigures (d-f) illustrate the effect of a point defect at the bonding interface on the sc-Si film topography at for different thicknesses. A particle of a given size at the bonding interface will result in a larger affected area at lower film thickness.

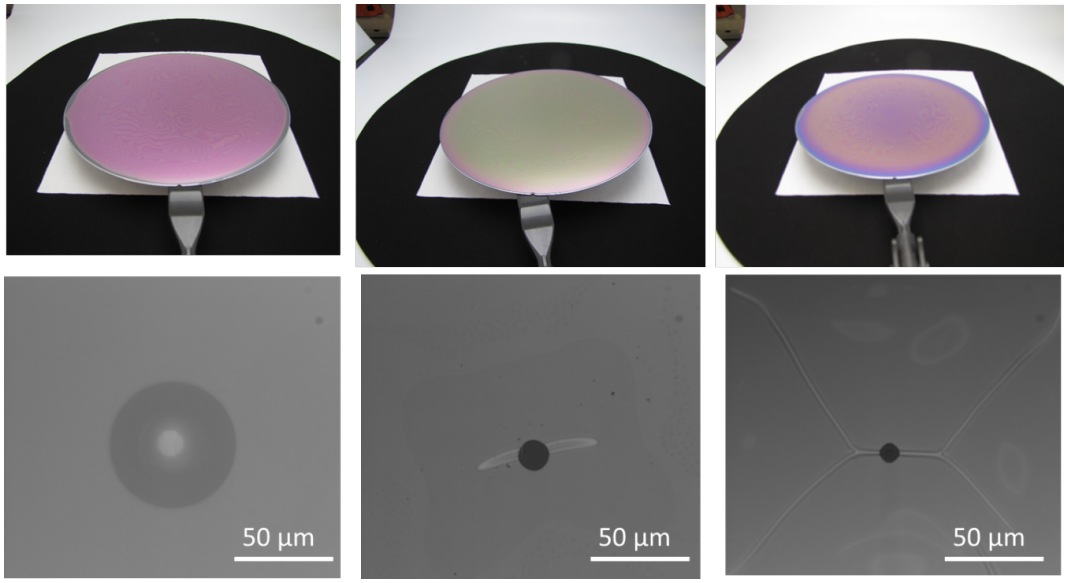


Figure 2.45: (a-c) Snapshots sc-Si film on different thickness transferred on a 40 µm BSI layer (a) 200 nm (b) 150 nm (c) 60 nm (d-f) Corresponding SEM observations of defects on the sc-Si film surface

Defect analyses revealed an inverse relation between the silicon thickness and the number of defects as presented in table 2.7. Corresponding defect mappings are presented in figure 2.46. The increase in defect number for 150 nm can be explained by the overetch on the stack edge which led to an unusual number of defects in this area. Figure 2.47 (a) shows an overetch after the WET etching of the BOX. This is caused by glue thickness inhomogeneity on the wafer edges, they are visible on SAM c-scan in between the mechanical grinding step (figure 2.47). If a 5 mm edge exclusion is applied, the decreased in defectivity with increase of silicon thickness remains observable for these wafers.

| sc-Si film thickness (nm) | Defect number (1 µm threshold) |
|---|---|
| 20 | 4238 |
| 60 | 2888 |
| 100 | 1495 |
| 150 | 5231 |
| 205 | 624 |

Table 2.7: Defectivity of sc-Si films transferred on a 40 µm thick BSI layer for different silicon thicknesses

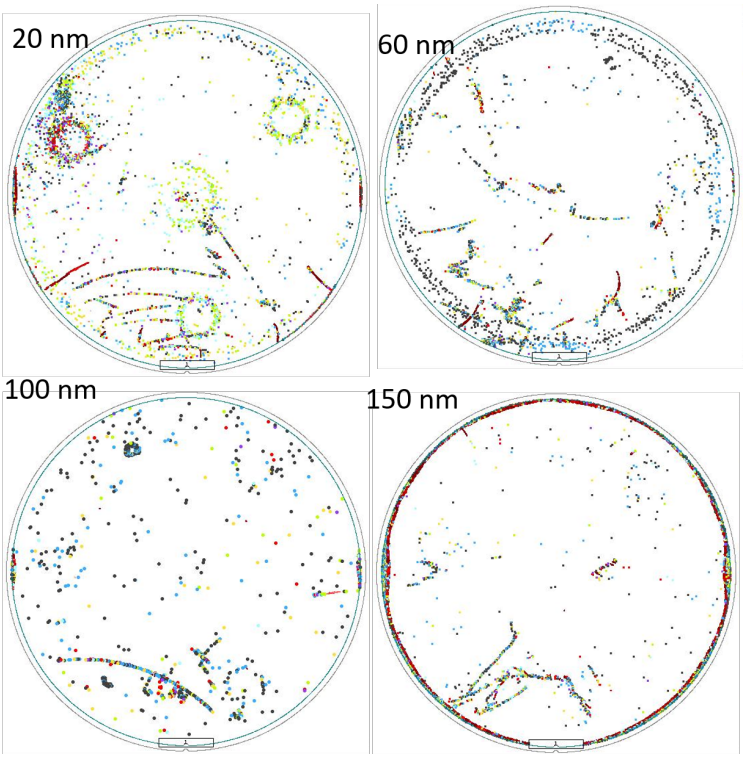


Figure 2.46: Defectivity map of sc-Si films transferred on a 40 µm thick BSI layer for different silicon thicknesses

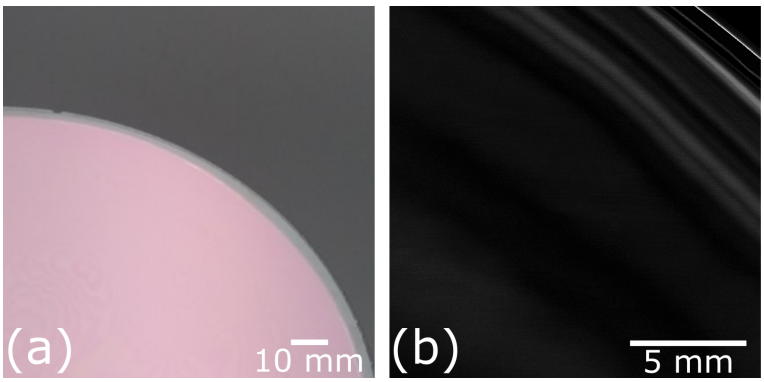


Figure 2.47: (a) Snapshot of a wafer overetch (b) SAM c-scan of the stack after grinding of the SOI backside down to 200 µm

### 2.3.2 Dry film : SPIS 21

A 205 nm thick sc-Si film was also transferred on a 60 µm thick SPIS layer. The polymer was laminated on the SOI and the bonding was performed at 100 °C. Figure 2.48 present SAM images after bonding, coarse grinding and fine grinding.

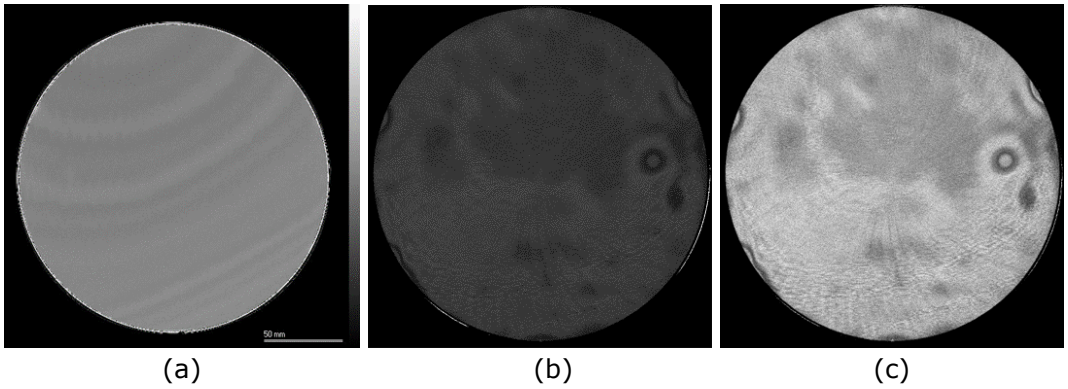


Figure 2.48: SAM c-scan of the bonding interface of a bonded stacks (**A4**) with SPIS 21 as an adhesive. (a) After bonding (b) After mechanical grinding of the SOI backside down to 200 µm (c) After mechanical grinding of the SOI backside down to 50 µm

As with BSI, the thickness and TTV values are monitored during the two grinding steps (**D** and **E**). The thickness profiles displayed in figure 2.49 attest that the stack present an homogeneous thickness and a TTV low enough to be processed by industrial equipment. The TTV values were 4.3 and 3.3 µm for 200 and 50 µm silicon layer respectively. These values are lower than the one obtained with BSI glue.

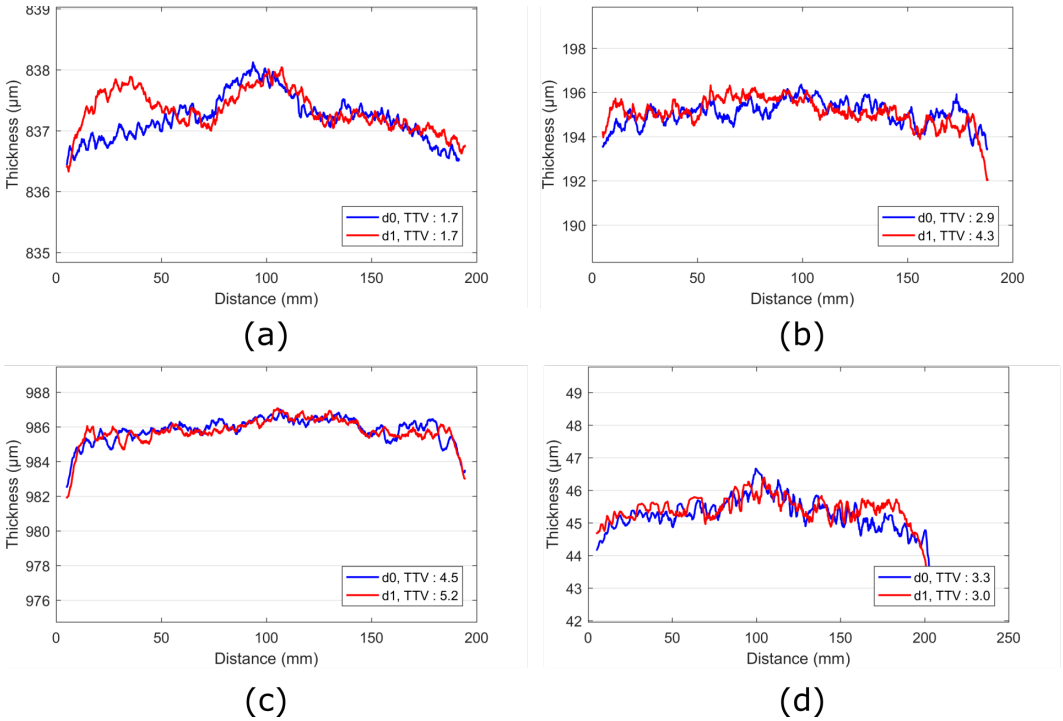


Figure 2.49: Thickness profiles in two diameter of a 200 mm bonded stack with SPIS as an adhesive. (a) DC measurement of the full stack thickness after coarse grinding of the SOI backside down to 200 µm (b) Corresponding IR measurement of the Bulk silicon layer (c) DC measurement of the full stack thickness after coarse grinding of the SOI backside down to 50 µm (d) Corresponding IR measurement of the Bulk silicon layer

Higher TTV can be linked to glue inhomogeneties on the wafer edges. Indeed figure 2.50 presents thicknesses measurement performed on BSI and SPIS after spin coating and lamination respectively. Spin coat-

ing resulted in excess material behind present on the wafer edges whereas laminating yields a more homogeneous glue layer.

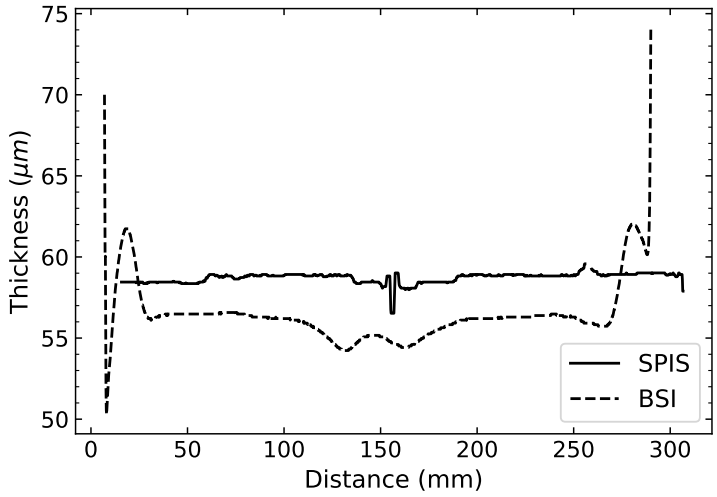


Figure 2.50: Thickness profiles for SPIS after lamination and BSI glue after spin coating

WET etching of the SOI silicon backside and BOX yielded a 205 nm sc-Si film on SPIS on a rigid silicon carrier. No cracks, undulation of delamination were observed in the sc-Si film. Moreover, there was no overetch in the sc-Si film edge. As shown earlier in figure 2.50, laminating the SPIS allows to avoid excess in glue thickness on the carrier edges.

Figure 2.51 presents a defect map obtained with a SP2 tool showing 327 defects with a 1 µm size threshold. This value is significantly lower than previous results obtained with BSI for similar thickness (624). And the absence of overetch on the stack edge prevent abnormally high defectivity values. The absence of AS is the case of SPIS adhesive also removed a particle contamination source.

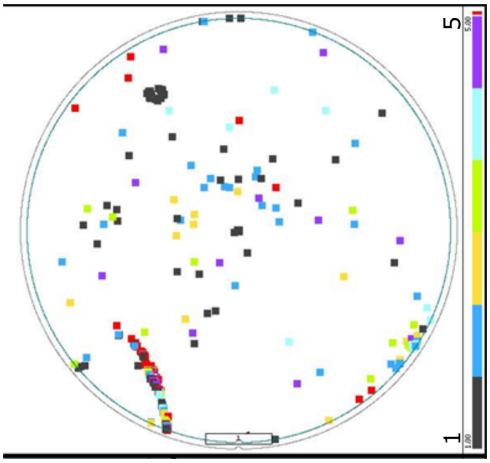


Figure 2.51: Defectivity map of a 205 nm thick sc-Si film transferred on a SPIS layer. Detection threshold is 1 µm.

The dry film can be peeled from the rigid carrier, indicating that the bonding interface is weaker than the laminated interface (figure 2.52). However, the shear strength of the dry film is low and did not allow for a clean peel-off of the whole 200 mm film. The SPIS offers ideal bonding properties at low temperature for a layer transfer, but is not a suitable candidate for a standalone flexible substrate.

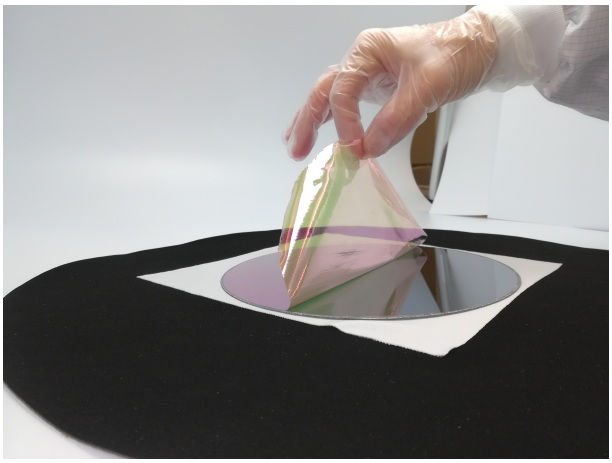

Figure 2.52: Peeling of a sc-Si thin film on a 60 µm thick SPIS layer. Under mechanical stress, cracks appear both in the polymer substrate and in the sc-Si film.

## 2.4 Using a second polymer as a flexible substrate for silicon thin films

The two types of bonding material presented could be engineered to provide suitable properties for the transfer of a sc-Si films of thickness ranging from 20 to 205 nm. But they are not designed to sustain high tensile stress needed to strain significantly the sc-Si film as it will exposed in chapter 3. Rather than trying to find a polymer that meets all those requirements (*i.e.*, proper adherence, thermal budget and mechanical properties), one can transfer the sc-Si film to a second polymer such as a dicing tape after the first transfer on glue. Moreover the use of a flexible substrate with a diameter larger than 200 mm allows the use of a DISCO metallic frame. This improve greatly the sample handling and standard metallic DISCO frame are compatible with some EVG tools. It is a key point for a scalable process in an industrial environment.

### 2.4.1 Transfer onto a second polymer with chemical cleaning of the glue

For the bonded pairs **B1** and **B4** (*i.e.*, where the glue is structured on the sc-Si thin and the release interface is the one between the glue and the carrier, allowing the fabrication of a silicon on glue structure) a tape can be laminated on the sc-Si thin film to dismount only the rigid carrier (step **J1** and **K1**). This yielded a sc-Si thin film encapsulated in between a glue layer and the Furukawa tape without any cracks (figure 2.53(a)). A chemical removal of the BSI layer was performed, the result is presented in figure 2.53. Undulation and cracks can be observed in the sc-Si layer. Argoud observed similar structure in silicon film transferred on caoutchoutic polymer [Argoud, 2012]. The buckling of a silicon thin film on a soft substrate is well documented (see review [Wang et al., 2016]). Buckling induces wrinkles through mechanical strain mismatch [Lin et al., 2008; Ohzono and Shimomura, 2004], thermal strain mismatch [Bowden et al., 1998; Lin and Yang, 2007] or other methods such as surface treatments [Moon et al., 2007; Kim and Crosby, 2011]. In our structure, the lamination of the tape onto the Si thin film could only increase the compressive stress of the sc-Si film. The release of the strain in the tape results in a wrinkling of the Si thin film (figure 2.53 (a,b)). The surface can be straightened by applying external tensile stress on the SOP (figure 2.53 (c,d)).

In order to increase the young modulus of the tape and avoid the apparition of cracks and undulation during the chemical removal, Furukawa tape was exposed to a 3 J/cm$^2$ dose of UV light (365 nm). An increase in the young modulus from 34 MPa to 67 MPa was measured after exposure to UV light. And a good quality transfer after the BSI removal was possible as illustrated in figure 2.54. The surface roughness of the Furukawa tape, measured by a 5 µm × 5 µm AFM scan, is 25 ±3 nm, UV exposure has no influence on this value. It is two orders of magnitude higher than the sc-Si film initial roughness.

The same process could be applied to the stack **B4** with a 60 µm SPIS layer. A clean surface was difficult to obtain as SPIS dewetted the surface under the action of the solvent of formed small polymer droplet on

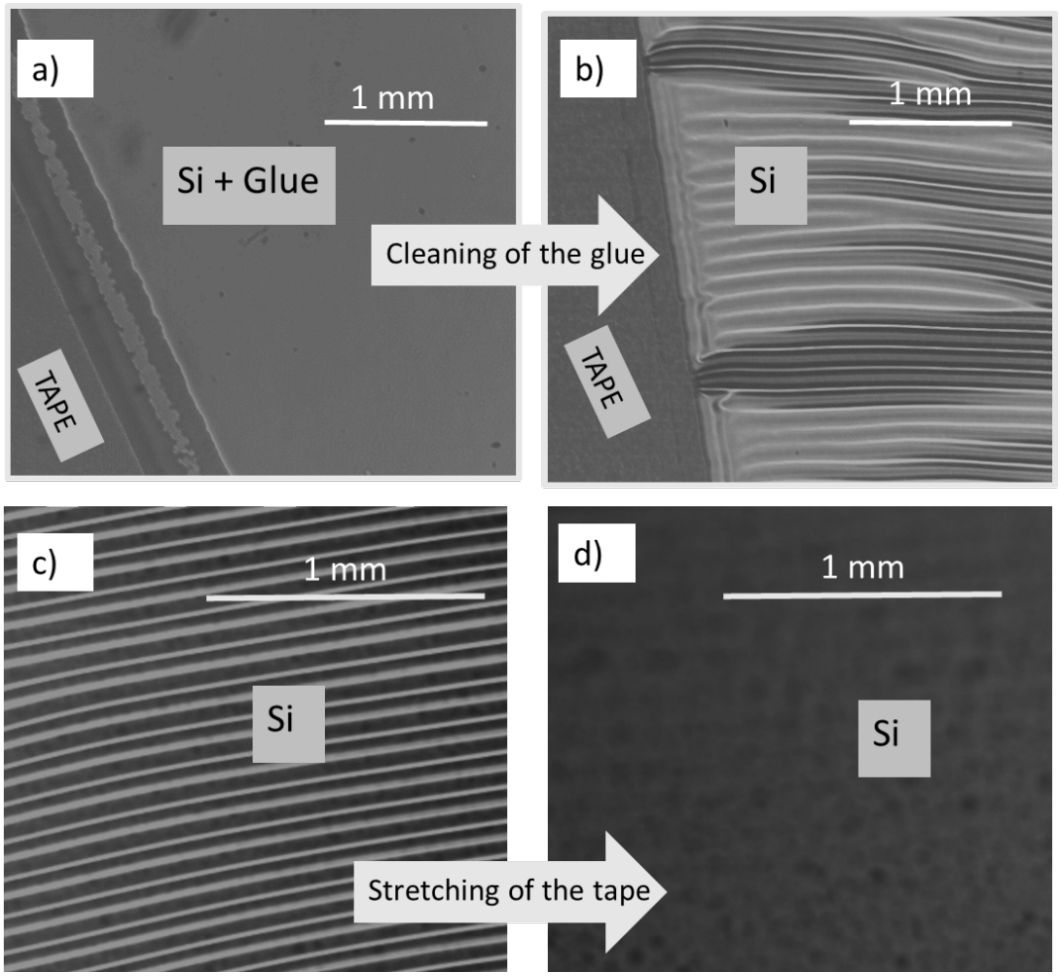


Figure 2.53: Micrograph of the 205 nm thick sc-Si film transferred onto a 230 µm thick Furukawa tape. (a) With BSI glue (40 µm) on top (b,c) After stripping of the glue (d) After the stretching of the tape

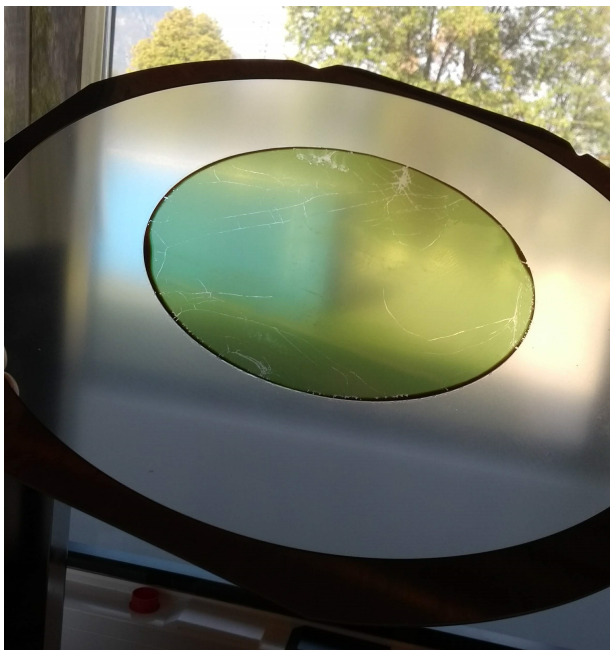

Figure 2.54: A 205 nm sc-Si thin film on a Furukawa tape after exposure to a 3 J/cm$^2$ UV dose and D-limonene cleaning of BSI layer

the surface (around 20 µm diameter) as seen in figure 2.55. The cracks visible are due to external mechanical stress applied to strain the sc-Si film and are not caused by the transfer process.

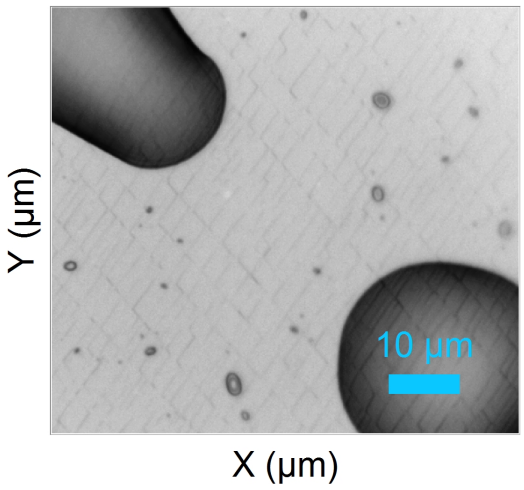


Figure 2.55: Micrograph of a sc-Si surface after chemical removal of a 60 µm thick SPIS layer.

### 2.4.2 Transfer onto a second polymer without chemical cleaning of the glue

The chemical removal presented earlier allowed to keep a bonded stack designed for a transfer on glue and to obtain a final structure with a second polymer as a flexible substrate. However the chemical removal of the first adhesive material is time consuming and led to contamination of the sc-Si surface by organic compounds. This is not an issue for mechanical characterization but it can prevent achieving surface specifications for direct bonding of a sc-Si thin film. Here the cases where the AS was coated on the SOI substrate (**B3** and **B4**) and where SPIS was laminated on the carrier (**B5**) will be presented. The aim was to obtain a silicon on tape structure without relying on solvent to remove the glue from the sc-Si thin film.

#### 2.4.2.1 BrewerBond™305-30

To obtain a release layer between the glue and the sc-Si thin film, the stack **B2** was used with an AS coated on the sc-Si thin film. For a 205 nm thick sc-Si film, a 210 °C bonding temperature and edge trimming (step **A1**), no difference were observed with the results presented in section 2.3.1 until the manufacturing of the stack **H** after final chemical etching of the BOX. After lamination of a Furukawa tape on the structure, the sc-Si film could be easily dismounted from the rigid carrier and the BSI layer. A water contact angle measurement of 105 ± 2° confirmed the presence of the AS coating on the surface of the transferred silicon film. A snapshot of a transferred film can be observed in figure 2.56 (a), the full 200 mm film is transferred but a visual inspection indicates the presence of cracks on the whole surface. As for chemical removal of the glue, increasing the rigidity of the tape allowed avoiding cracks formation during the transfer on Furukawa tape. The evolution of the tape young modulus and the peeling force which is linked to the tape adherence energy are represented in figure 2.56(e) as a function of UV dose. The Young modulus increased with UV dose whereas the peeling force or adherence was first decreased and then slightly increased for higher UV doses (> 3 J / cm$^2$, three times the manufacturer recommendation for dismounting). The decrease in adherence energy is linked to the polymer chains reticulation under UV light exposure. The increase at higher doses can be caused by a raise in temperature due to UV exposure [Imachi, 1986; Mizuno et al., 2005]. Nevertheless, this increase in peeling force or adherence for the tape, allowed a transfer of the full sc-Si film onto the dicing tape without any cracks visible with an optical microscope (see snapshot in figure 2.56 (d)).

Observations at different UV doses are detailed in table 2.8 and corresponding snapshot are visible in figures 2.56 (b,c).

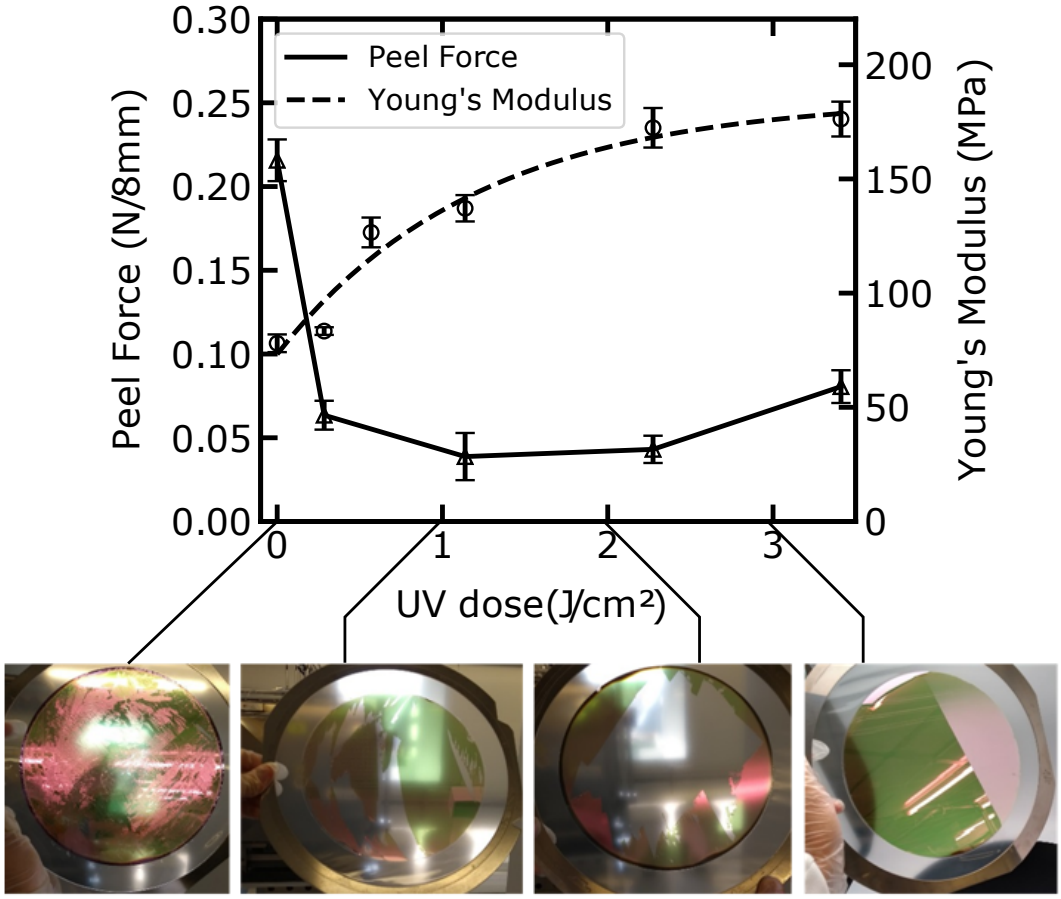


Figure 2.56: UV dose Young modulus and peel force for a Furukawa SP-537T-230 tape obtained with a Proxima tensile stage from micromecha. Peeling speed : 30 µm /s,Peeling angle : 180°. Corresponding snapshots of sc-Si film transferred on Furukawa tape at different UV doses are presented.

| UV dose (J /cm$^2$) | Transferred silicon surface (%) | Cracks presence |
|---|---|---|
| 0 | 100 | Yes |
| 1 | 50 | No |
| 2 | 30 | No |
| 3 | 100 | No |

Table 2.8: Observation on a sc-Si transferred from a glue layer to a Furukawa dicing tape after exposure to different UV doses

Further SEM observations (figure 2.57) showed that small defects can be present on the transferred films : micrometric delaminated surfaces or cracks. But large macroscopic surfaces are transferred without any defects as illustrated by figure 2.57.

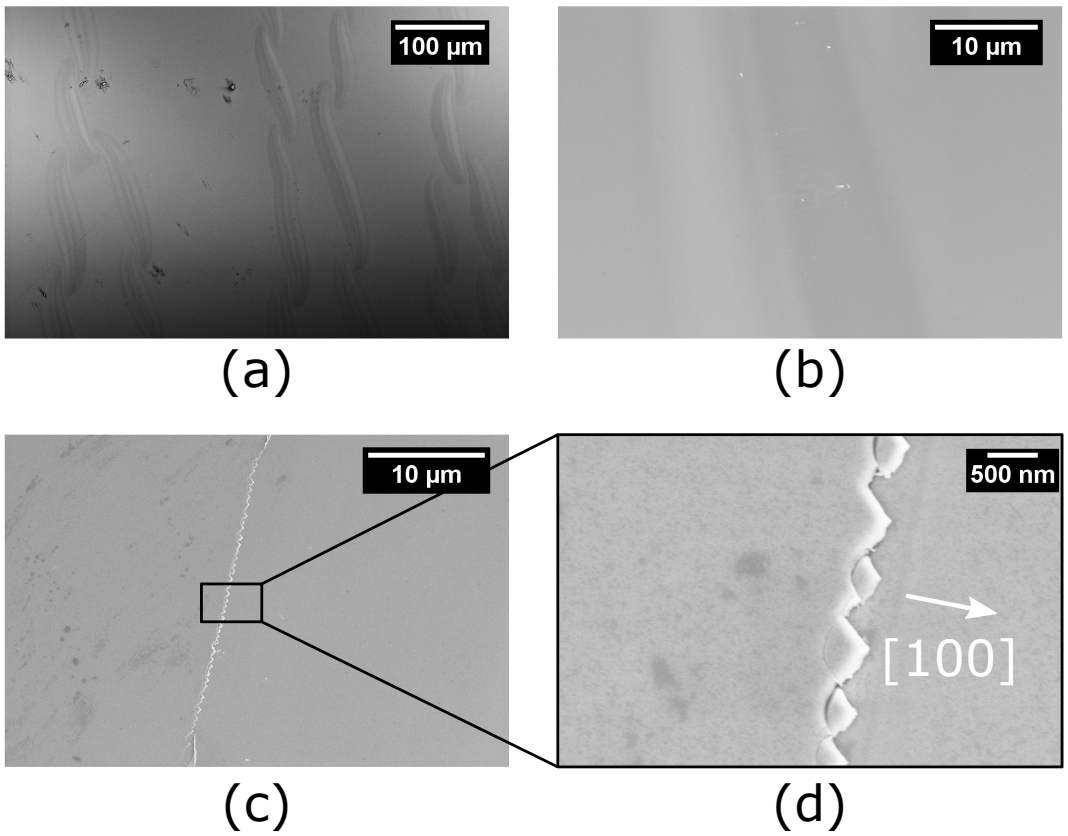


Figure 2.57: SEM images of a 205 nm sc-Si film on a 230 µm thick Furukawa dicing tape after UV exposure (3 J/cm$^2$). (a) Defect caused by delamination of the sc-Si film (b) Pristine surface (c) Crack (d) Crack detail

#### 2.4.2.2 SPIS

As shown earlier, no AS coating is needed for a safe and easy dismounting with the use of SPIS adhesive. To allow the mechanical transfer of the sc-Si film on a dicing tape (step **K2**), the stack **B5** was used with SPIS 21 as an adhesive laminated on the carrier. Until the mechanical grinding of SOI backside (step **F**), no differences were observed with the results presented with the SPIS laminated on the SOI(see subsection 2.3.2). But after WET etching of the remaining 50 µm of the SOI backside, numerous cracks were observed all over the surface of the 200 mm sc-Si silicon film as seen in figure 2.58. No similar observation were made with SPIS laminated on the SOI prior to the bonding step. Crack presence in the sc-Si film after transfer on SPIS is dependent on which wafer the glue was laminated, even tough the resulting bonding stack is similar. Cracks only appeared if SPIS was laminated on carrier and not on the SOI

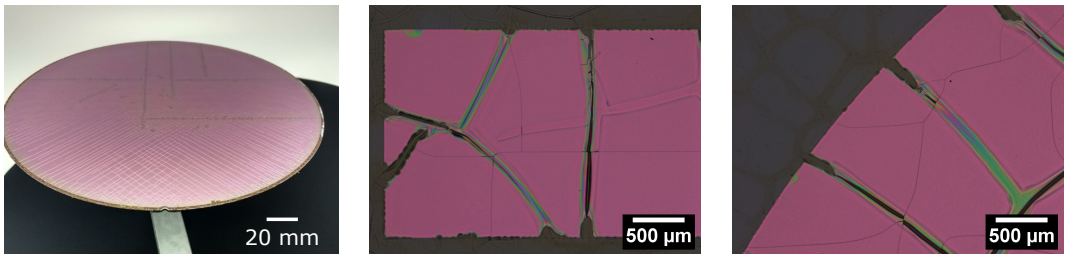


Figure 2.58: 200 nm thick sc-Si film transfer on a 60 µm thick adhesive SPIS layer using the bonding stack **B5** (a) Snapshot of a full sheet film (b,c) Micrographs of sc-Si patterns transfer with using the same process.

Several hypothesis are proposed to explain this asymmetry in the transfer process. The first one is that the elastic energy stored in the BOX is released after silicon chemical etching (step **F**). The compressive stress induced by the SmartCut™ process for SOI in the BOX is estimated to 290 MPa [Tiberj et al., 2002]. Given that the bonding interface is weaker than the lamination interface, slipping might occur between the sc-Si film and the adhesive layer for stack **B5**, preventing a mechanical coupling between the adhesive/carrier and the thin film/BOX. Relaxation of the oxide stress might cause the sc-Si stress to reach the tensile strength locally, leading to crack formation.

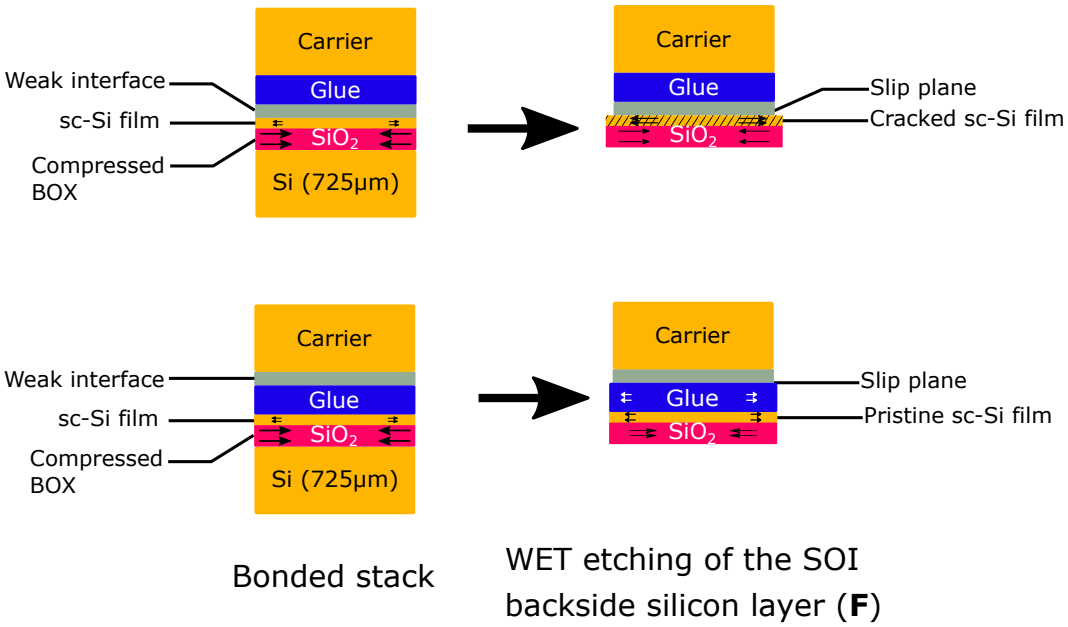


Figure 2.59: Weak interface position effect on the cracks presence after wet etching of the silicon backside layer

Another hypothesis is that the surface roughness of SPIS free surface is too high for the transfer of a sc-Si thin film. Local radius of curvature might induce stress level lower than the tensile strength of the film. Whereas the laminated surface presents a roughness more suitable for layer transfer.

To asses these hypothesis, stress measurement were performed on films after transfer. As well as transfer on a SPIS layer who underwent a bonding to a silicon carrier to decrease the surface roughness of the glue. The adhesive topography before and after compression of a bulk silicon wafer are presented in figure 2.60. A significant decrease in roughness ($R_q$) is observed: 27 to 10 nm. Though after transfer of the 205 nm film on the "flattened" SPIS layer, cracks were still observed.

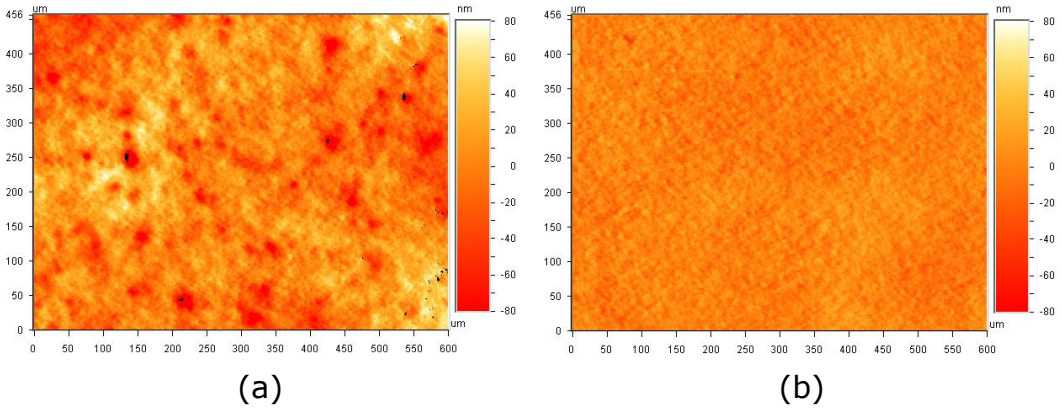


Figure 2.60: SPIS topography measured by a Veeco interferometer. (a) After lamination, $R_q = 27$ nm (b) After compression of a prime silicon wafer with a pressure of 6 kN at 80 °C, $R_q = 10$ nm

Results of biaxial stress measurement in 205 nm thick sc-Si films transferred on SPIS layer are presented in figure 2.61. It appears that there was indeed a noticeable difference of stress level between the different stacks. When the glue is laminated on the SOI, a compressive stress is observed whereas almost no stress is present in the layer transferred after lamination on the carrier. Flattening of the SPIS layer prior to the bonding step, induced a compressive stress similar to the one present when SPIS is laminated on SOI. But it did not have an influence on the presence of cracks. Surface roughness does not appear to be the main driving force for the fracture of the sc-Si film during the transfer process.

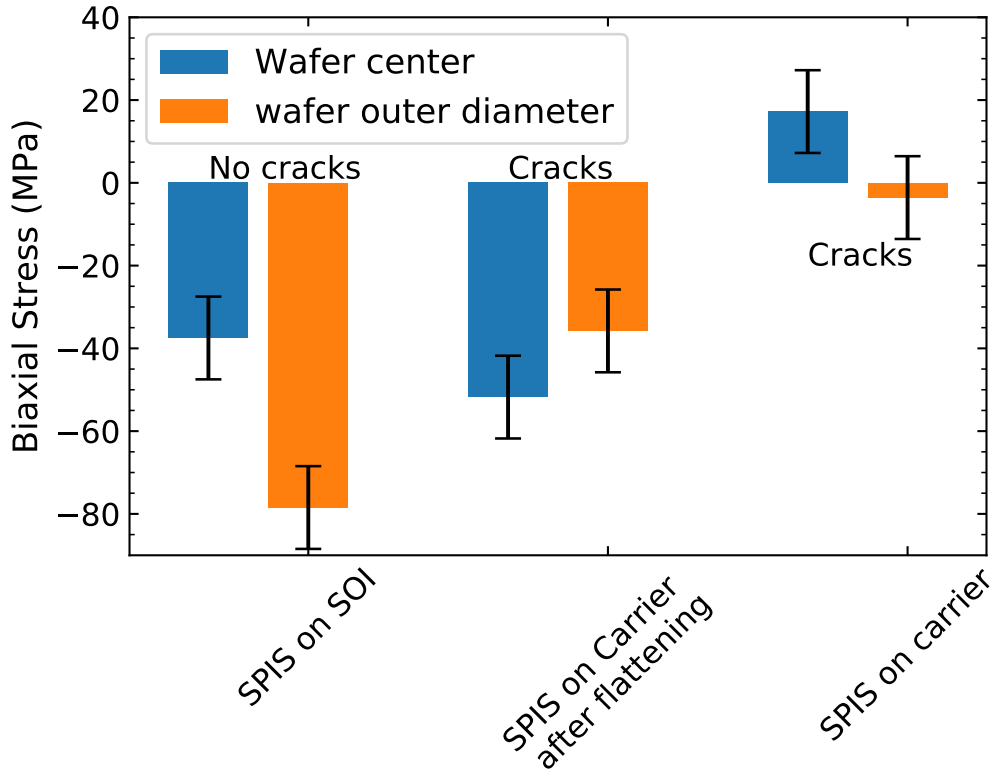


Figure 2.61: Raman stress measurements in 205 nm thick Si layer after transfer on a 60 µm SPIS layer held by a rigid carrier.

Despite cracks formation when the bonding stack **B4** is used with SPIS as an adhesive, the transfer process **K2** can still be carried on to transfer a 205 nm layer on a Furukawa dicing tape. The absence of any AS

coating allow to obtain a silicon surface free of any coating, making any future surface preparation steps easier. Though the presence of cracks deters the use of this transfer process for further mechanical loading.

#### 2.4.2.3 Thermal release tape

Figure 2.62 shows that the same process (step **K2**) could be performed with a thermal release tape (RevAlpha). BSI was used as an adhesive with the AS coated on the SOI surface (stack **B2**). This tape presents a higher young modulus (400 ± 50 MPa). This allows for a good quality transfer without any systematic cracks formation. Nevertheless some cracks can still be observed on the film edges as shown in 2.62 (b).

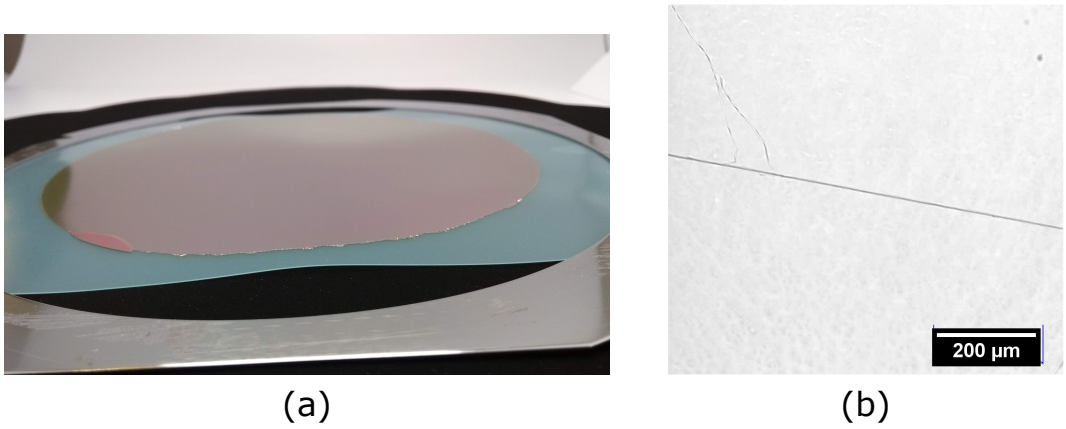


Figure 2.62: A 205 nm sc-Si layer transferred on a Thermal release double sided dicing tape (Revalpha). The sc-Si is on the thermal release adhesive. (a) Snapshot of the transferred structure (b) Micrograph

#### 2.4.2.4 PDMS

On the other hand, a PDMS layer was directly structured on the sc-Si layer as detailed in steps **J3** and **K3**. BSI was used as an adhesive with the AS coated on the SOI surface (stack **B2**). As expected, with the low Young Modulus of PDMS (1-2 MPa), the transferred film is cracked, nevertheless the entire surface is transferred. A snapshot of the transferred film is presented in figure 2.63.

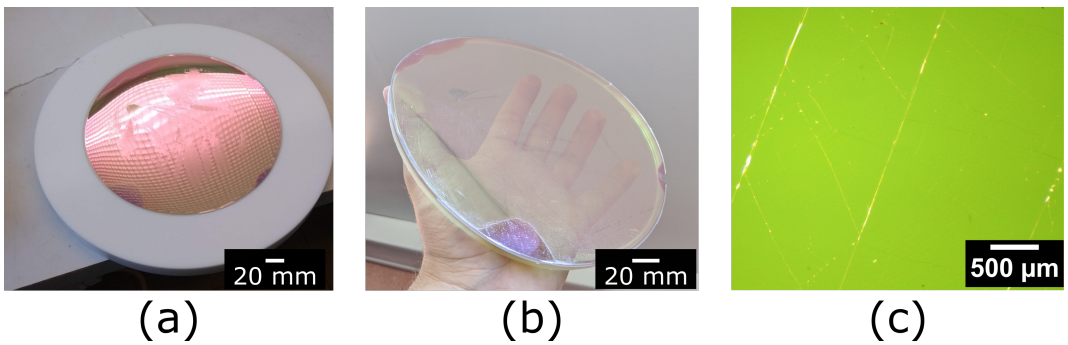


Figure 2.63: (a,b)Snapshots of a 205 nm thick Si film transferred on a 3 cm thick PDMS layer (c) Micrograph of the silicon on PDMS surface

### 2.4.3 Decreasing the silicon thickness with BSI as a glue

In order to transfer sc-Si film thinner than 200 nm on a second polymer, the same approach as in section 2.3 was used. SOI were oxidized, etched and then went through the transfer process, this time with the AS on SOI and BSI on carrier. This way the weak interface is place in between the sc-Si thin film and the glue, making the transfer from the glue to a second polymer possible without a chemical cleaning step.

Observation of the sc-Si thin film reveals that thinner samples displayed some cracks (figure 2.64). The micrographs are made of sc-Si pattern after transfer on BSI (stack **H**). No cracks were observed on film with a 150 nm, they started appearing for a 100 nm thickness even though some patterns were pristine, and below this thickness, all patterns were defective. The cracks are oriented along the < 100 > directions and have a periodicity of 140 ± 20 µm.

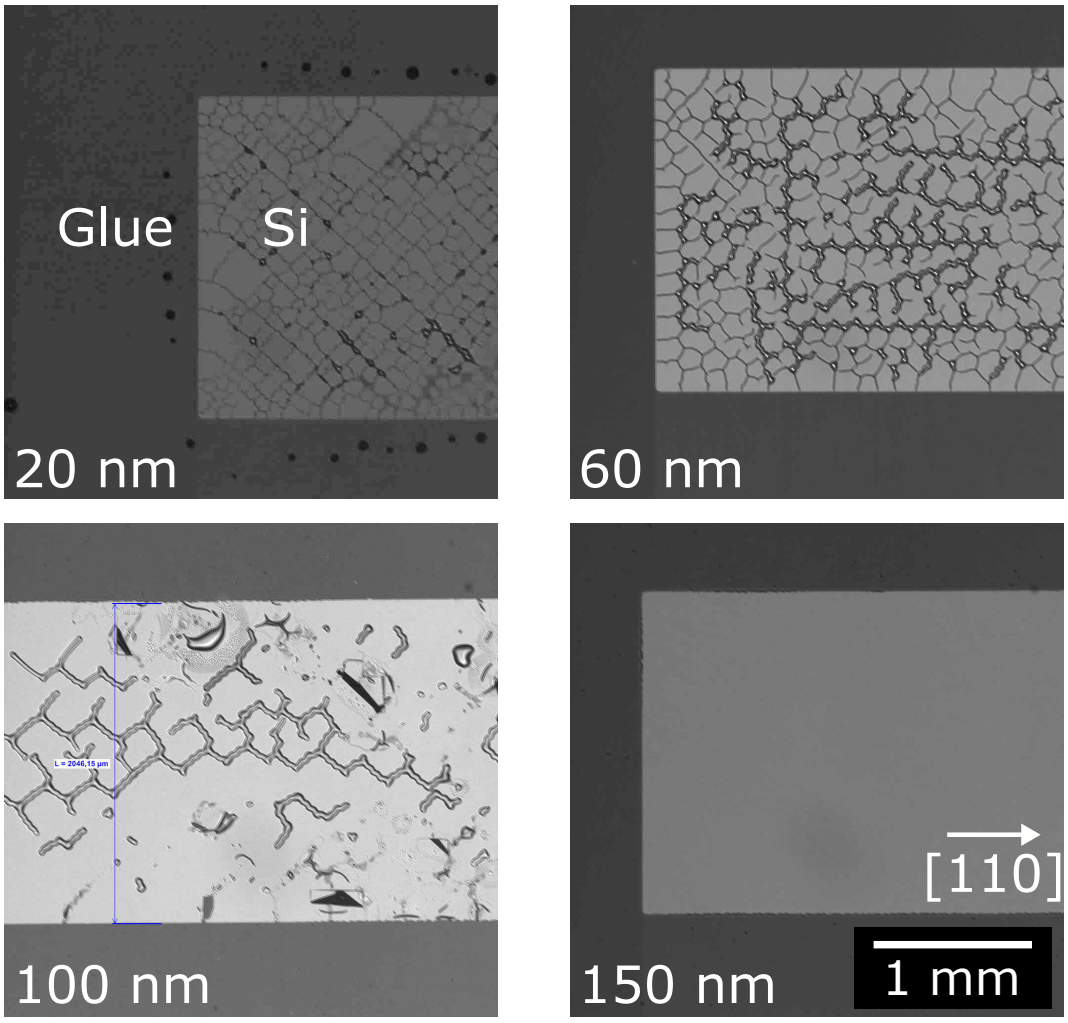


Figure 2.64: Micrographs of sc-Si film of different thickness after the final etching step of the process transfer on BSI Patterns are oriented along the [110] direction

The use of an AS coating underneath the sc-Si in this case is a source of particle contamination that could lead to cracks apparition for lower thicknesses. But the periodicity and orientation of the cracks did not indicate that a random distribution of particles was the main driving force for cracks presence. As with SPIS, the weak interface has a lower mechanical coupling and caused slipping between the glue and sc-Si film after WET etching of the remaining SOI silicon backside. The elastic energy transferred in the sc-Si from the BOX is thus more important. Indeed, this thermal oxide has a compressive biaxial stress of around 290 MPa for a 400 nm thick BOX and a thick 205 nm top silicon layer [Tiberj et al., 2002]. As the top silicon layer is sacrificially etched, the stress level of the BOX decreases whereas it increases in the top silicon layer. Tiberj et al. measured an increase from 2.3 MPa to 38.5 MPa associated with a decreases from 205 nm to 17 nm in the top silicon thickness.

If the silicon film is too thin, it cannot withstand the relaxation. One solution could be to use SOI wafer with thinner buried oxide layer. But it will affect its efficiency as an etch stop layer.

But a parallel can be made with the transfer on SPIS. For 205 nm thick sc-Si films, cracks only appeared if the SPIS was laminated on the carrier, no AS coating was used in the stacks **B4** and **B5**. This indicates an

asymmetry between the bonding interface and the lamination or coating adhesive for the transfer of a thin sc-Si film.

To validate the existence of this asymmetry in the case of the use of BSI and AS material, an additional process was evaluated. First the AS was coated on the SOI and then the BSI was coated on top of the AS (bonded stack **B3**). This caused some dewetting during the spin-coating as seen in figure 2.65. The bonding interface needs to be monitored closely as defect can arise from the dewetted parts. Annealing the defective stack at 150 °C for 90 min allowed to eliminate the bonding defects. Patterns of different thicknesses transferred on BSI with this stack and the stack **B2** are compared in figure 2.66. Pattern of slightly better quality are obtained with the stack **B3** but cracks also start appearing for a film thickness of 100 nm. Entire flake of silicon can be removed during the WET etching of the BOX.

This confirmed that in the case of a transfer using BSI and an AS coating, the position of the AS is determining for the quality of the sc-Si film. The position of the bonding interface does not have a strong influence and it is not worth risking bonding defects by coating BSI on AS due to dewetting of the glue

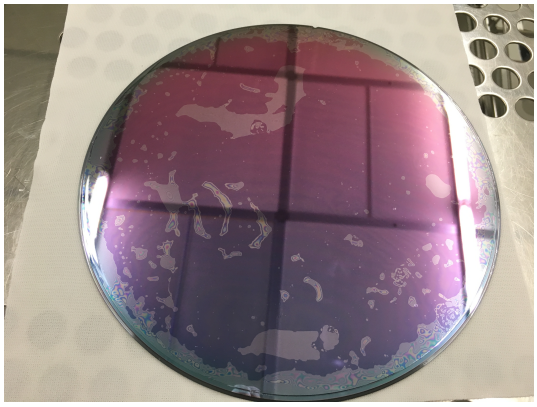

Figure 2.65: Dewetting of a 40 µm BSI layer on a SOI coated with 3M novtec 2702

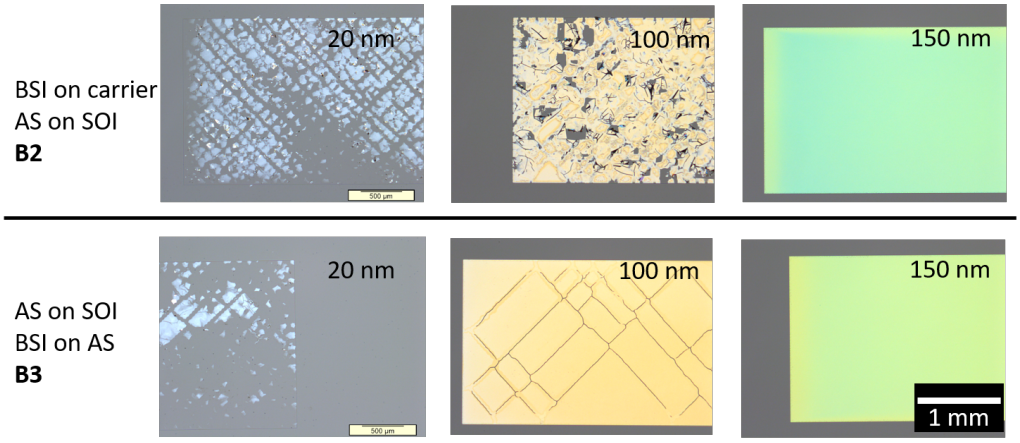


Figure 2.66: Micrograph of sc-Si patterns transferred on BSI (stack **H**) for different thicknesses and for two different bonding stack. In both cases an AS layer is coated on the SOI. For stack **B2**, the BSI is coated on the carrier and on the AS for stack **B3**.

No methods described above offered to transfer reliably a sc-Si film thinner than 150 nm on a glue layer than could be then reported to a second polymer substrate without the use of a solvent. For this reason, the optional plasma etching step was evaluated (step **I**). Rather than decreasing the thickness before the transfer on glue, the top sc-Si layer was etched after the transfer on BSI using bonding stack **B2**(optional step **I** described in section 2.1.5). To monitor the thickness of the sc-Si film on a glue layer after dry etching, High Resolution X-Ray Diffraction (HRXRD), X-Ray Reflectivity (XRR) and ellipsometry measurement were

performed. Examples of experimental and computed curves are presented in figure 2.67 along with ellipsometry theoretical and experimental curve for different silicon thicknesses. Both techniques are needed as they both lack precision at one end of the sc-Si thickness range obtain here. Around 20 nm, fitting HRXRD diffraction curve proved to be challenging while the thickness fringes in reflectivity curves displayed low amplitude for 100 nm films. HRXRD gives optimum results for thickness down to 50 nm whereas thickness fringes are more difficult to fit above 100 nm for XRR. Results of the three techniques are compared in table 2.9.

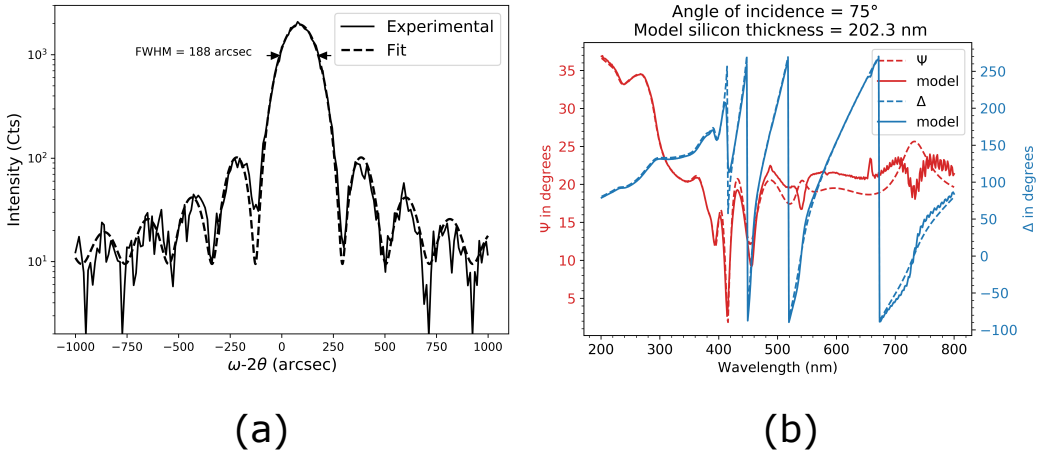


Figure 2.67: (a) HRXRD $\omega - 2\theta$ scan of a 100 nm thick SOP (b) Ellipsometry measurement and fit of a $(205 \pm 5)$ nm thick SOP

| Targeted thickness (nm) | XRR values (nm) | HRXRD values (nm) | Ellipsometry values (nm) |
|---|---|---|---|
| 20 | $22.6 \pm 6.5$ | $25.3 \pm 8.4$ | $20.8 \pm 7.2$ |
| 100 | $98.2 \pm 2.1$ | $92.7 \pm 1.8$ | $93.6 \pm 2.0$ |

Table 2.9: Silicon thickness measured after Plasma etching of a 205 nm thick sc-Si layer on a 40 µm thick BSI layer.

The modeling of the $\omega - 2\theta$ scan yields a silicon thickness of 92.8 ± 2.5 nm. Ellipsometry and X-Ray Reflectivity (XRR) performed in the same points, gave respectively a silicon thickness of 93.6 ± 2.8 nm and 98.2 ± 2.8 nm. HRXRD is not sensible to any non-crystalline or tilted silicon layer contrary to XRR and ellipsometry [Bowen, 2001; Garcia-Caurel et al., 2013]. The small difference in thickness between the three measurements indicates that only a few nm of silicon may have been damaged by the plasma etching and that the sc-Si remained intact during the transfer process. An additional defectivity measurement was performed on a full sheet wafer, a dry etching step reducing the top silicon thickness from 205 to 50 ± 2 µm induced an increase from 543 to 1916 defect number with a size threshold of 1 µm. This effect is similar for previous observation on oxidized and etched SOI (**A1**) transferred with bonded stack **B1**. In the case of plasma etching it is unclear if the defect number increase is only due to the decrease in thickness or to the etching process itself. Plasma etching can cause some surface modification in silicon, as an increase in roughness[Pétri et al., 1994].

X-Ray characterization techniques allowed us to build and validate a model for ellipsometry. This allowed for fast and automatic in line mapping of the silicon thickness. Figure 2.68 presents a snapshot of a sc-Si pattern before and after plasma etching. The phase change information was really sensible to the change of sc-Si film thickness as seen in figure 2.68. The mean square error remained significant in (82.69 160.2 and 116.3) Some inhomogeneity are confirmed by the ellipsometry measurement presented in figure 2.68 (d).

Compared to the initial sacrificial silicon etching, plasma etching after transfer on glue allowed to obtain a crack free sc-Si film as thin as 20 nm on BSI with a AS coating between the glue and the film, allowing the

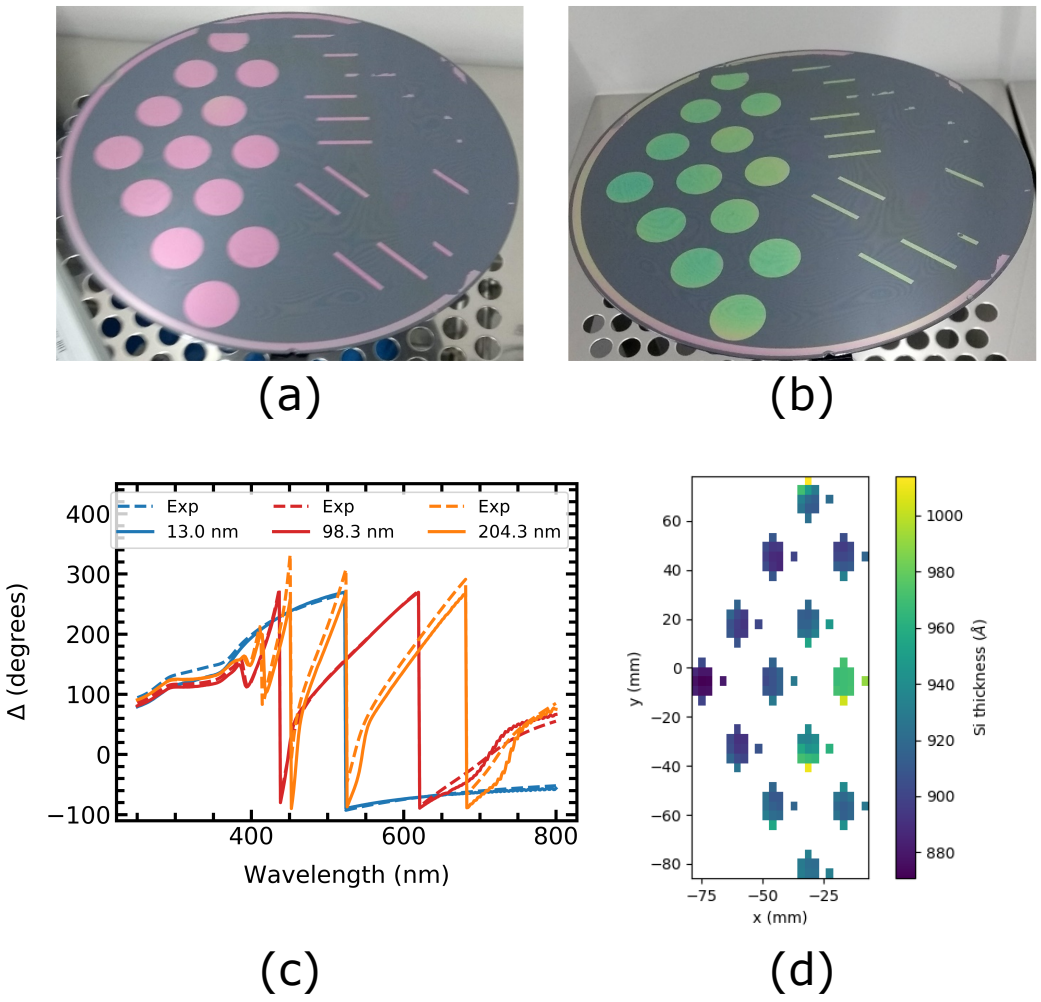


Figure 2.68: (a) Snapshot of 205 nm thick sc-Si patterns transferred on BSI before dry etching (b) After dry etching of the sc-Si layer down to $(92 \pm 3)$ nm (c) Phase difference obtained with reflective ellipsometry on SOP with varying thickness of sc-Si films. Dashed lines represent experimental data points and full lines the best fitting model with the corresponding silicon thickness (d) Silicon thickness mapping obtained by ellipsometry measurement after dry etching

transfer of the silicon film on a second flexible polymer such as a Furukawa dicing tape (figure 2.69. This process option offered more flexibility as the sc-Si film thickness is controlled by a single step, independent from the other transfer parameters. It comes at the cost of a loss in precision in the thickness control as characterizing a thin film on a commercial polymer is more challenging than on a silicon oxide layer.

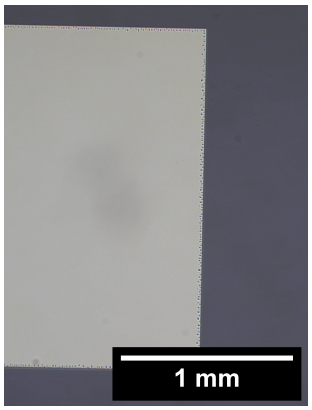


Figure 2.69: Micrograph of a 20 nm sc-Si film on BSI after plasma etching.

## 2.5 Pattern transfer

### 2.5.1 Effect of the transfer on pattern morphology

In order to produce SOP tensile test samples, the different transfer processes have been applied to patterned SOI (step **A2** or **A4** as described in subsections 2.1.3.2 and 2.1.3.4). No difference were observed in the different process options when using a pattern SOI compared to a 200 mm full sheet. Micrographs of 205 nm thick sc-Si patterns transferred on BSI and SPIS are presented in figure 2.70(a,b). Dimension and edge definition was conserved when using either a soft or the 1X chromium mask for both adhesive and standard lithography process (**A2**). Films of different thicknesses (20-205 nm) could be transferred with the limitations presented above.

For patterns who underwent a pattern sidewall smoothing step (**A4**), the characteristic undercut of anisotropic TMAH etching are still visible after transfer on BSI as seen in figure 2.70 (c,d). The complete etching and underetch of the 1 µm BOX was a concern for the transfer of the smoothed patterns. During the etching step of the remaining silicon of the SOI backside (**G**), the BOX acts as etch stop. Because of the underetch observed in figures 2.31 and 2.32, the etching solution of aqueous $HF/HNO_3$ might be in contact of the 205 nm silicon thin. However the observations made in figure 2.70 (c,d) indicate that it was not the case as the dimension and geometry of the silicon patterns were conserved during the transfer process. The high aspect ratio of silicon pattern also prevents changes of the macroscopic dimensions. Basically the AS and BSI acted as an etch stop layer for the pattern sidewalls as presented in figure 2.71.

As full sheet films, patterns were transferred on furukawa dicing tape. A total transfer of the silicon pattern as seen in figure 2.72. The initial edge roughness was conserved through the transfer on tape.

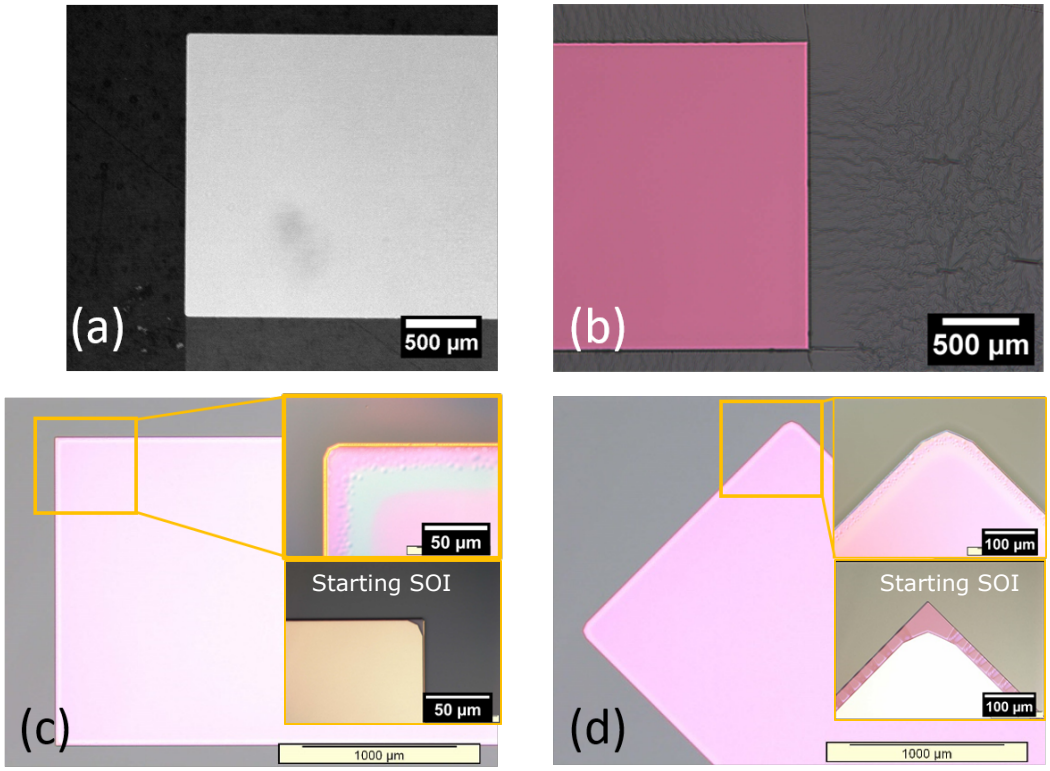


Figure 2.70: Micrographs of 205 nm thick sc-Si patterns after transfer on a polymer adhesive layer (stack **H**). (a) Pattern obtained with a soft mask on a BSI layer (b) Pattern obtained with a chromium mask on a SPIS layer (c) [110] oriented ribbon after anisotropic sidewall smoothing (**A4**) (d) [100] oriented ribbon after anisotropic sidewall smoothing (**A4**)

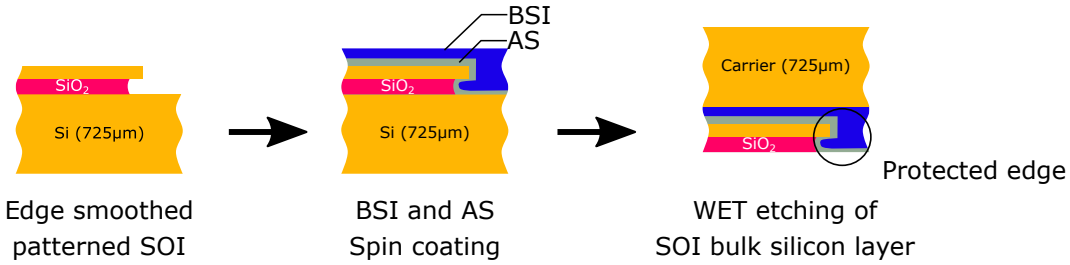


Figure 2.71: Schematic of a pattern during the transfer on glue after chemical isotropic sidewall smoothing

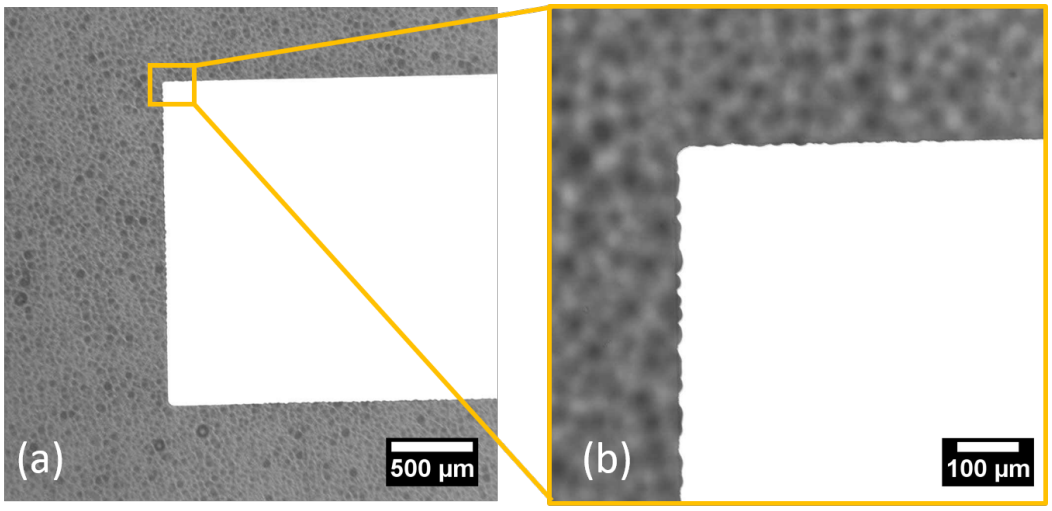


Figure 2.72: Micrograph of a 205 nm thick sc-Si pattern transferred on a 230 µm thick furukawa tape. A soft mask was used to pattern an SOI wafer prior to the transfer process.

### 2.5.2 Single pattern transfer from a full size patterned wafer

Single sc-Si patterns were successfully transferred on Furukawa tape using the process described in figure 2.17. Particle contamination was an issue after several transfer. If a particle was present on the surface on a sc-Si pattern, the Furukawa tape could not be correctly laminated, leading to a partial transfer as seen in figure 2.73.

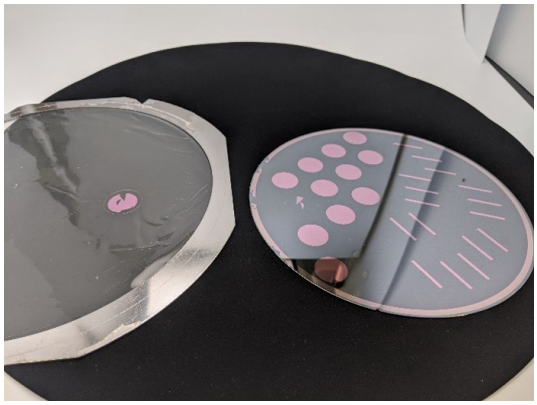

Figure 2.73: Transfer of a single pattern of Furukawa dicing tape from a patterned SOP, using a bonding stacks **B2**. After Transfer on glue, a Kapton mask is placed on the SOP before the tape lamination.

This method allowed to fully dissociate the dimension of the polymer substrate from the mask design. A SOP could be used with a 200 mm diameter substrate without sacrificing all patterns present on a glue layer. This proved to be useful for the fabrication of various tensile test sample without a new mask design. Moreover, several transfer conditions could be tested on a single wafer.

## Conclusion

This chapter detailed how a sc-Si film could be transferred to various flexible polymer substrates. Different process options were studied, in order to control dimensions of transferred films (thickness, patterns). Finally, various tensile test samples could be produced. Interface control was achieved (*i.e.* location of the release weakest interface), enabling the transfer sc-Si film either on the adhesive polymer layer used during the bonding process, or on a second polymer (tape or PDMS). Oxidation and etching of the starting sc-Si thin film was used to transfer films down to 20 nm on BSI glue. In the case where the weakest interface of the bonding stack is placed under the sc-Si film, cracks can appear for thicknesses lower than 100 nm with BSI as an adhesive. In this case an additional plasma etching step yields crack free samples that can be transferred on the desired flexible polymer substrate. In the case of pattern designed to be mechanistically characterized, different sidewall roughness were achieved with the use of different lithography mask and etching. The next chapter focus on the mechanical behavior of the resulting SOP.

Table 2.10 present a summary of the different process options that were exploited and the properties of the sc-Si film during and a the end of the process.

| Glue | Weak interface | Starting sc-Si thickness (nm) | Minimum thickness after dry etching (nm) | Transfer on glue | Transfer onto a second polymer |
|---|---|---|---|---|---|
| BSI/AS | Glue/Carrier | 205 | ok (20) | ok | ok (chemical cleaning) |
| | Glue/Carrier | 150, 100, 60, 20 | - | ok | ok (chemical cleaning) |
| | AS/SOI | 205 | ok | ok | ok (no chemical cleaning) |
| | AS/SOI | 150 | - | ok | ok (no chemical cleaning) |
| | AS/SOI | 100, 50, 20 | - | Cracked | Cracked |
| SPIS | Glue/Carrier | 205 | - | ok | ok (chemical cleaning) |
| | Glue/SOI | - | - | Cracked | Cracked |

Table 2.10: Results of the transfer of a sc-Si film on polymer from a SOI substrate with the different process split presented in section 2.1

## References

Abadie, K., Montméat, P., Enot, T., Fournel, F. and Wimplinger, M. [2019]. Application of temporary adherence to improve the manufacturing of 3D thin silicon wafers, *International Journal of Adhesion and Adhesives* **91**: 123–130.
**URL:** *http://www.sciencedirect.com/science/article/pii/S0143749619300739* 63

Argoud, M. [2012]. *Mécanismes de collage et de transfert de films monocristallins dans des structures à couches de polymères*, phdthesis, Université de Grenoble.
**URL:** *https://tel.archives-ouvertes.fr/tel-00848111/document* 53, 68, 74

ASTM and SEMI [2015]. MF053400 - SEMI MF534 - Test Method for Bow of Silicon Wafers.
**URL:** *https://store-us.semi.org/products/mf053400-semi-mf534-test-method-for-bow-of-silicon-wafers* 54

Bowden, N., Brittain, S., Evans, A. G., Hutchinson, J. W. and Whitesides, G. M. [1998]. Spontaneous formation of ordered structures in thin films of metals supported on an elastomeric polymer, *Nature* **393**(6681): 146–149. Number: 6681 Publisher: Nature Publishing Group.
**URL:** *https://www.nature.com/articles/30193* 74

Bowen, D. K. [2001]. X-ray metrology by diffraction and reflectivity, *AIP Conference Proceedings*, Vol. 550, AIP, Gaithersburg, Maryland (USA), pp. 570–579. ISSN: 0094243X.
**URL:** *http://aip.scitation.org/doi/abs/10.1063/1.1354458* 84

Byun, K. Y., Ferain, I., Song, S., Holl, S. and Colinge, C. [2010]. Single-Crystalline Silicon Layer Transfer to a Flexible Substrate Using Wafer Bonding, *Journal of Elec Materi* **39**(10): 2233–2236. Number: 10.
**URL:** *https://doi.org/10.1007/s11664-010-1264-7* 68

El-Zein, M. S. and Reifsnider, K. L. [1988]. Evaluation of$G_{IC}$ of a DCB Specimen Using an Anisotropic Solution, *CTR* **10**(4): 151–155. Number: 4 Publisher: ASTM International.
**URL:** *http://www.astm.org/DIGITAL_LIBRARY/JOURNALS/COMPTECH/PAGES/CTR10278J.htm* 52

Feng, Z. and Liu, H. [1983]. Generalized formula for curvature radius and layer stresses caused by thermal strain in semiconductor multilayer structures, *Journal of Applied Physics* **54**(1): 83–85. Publisher: American Institute of Physics.
**URL:** *https://aip.scitation.org/doi/10.1063/1.331690* 69

Fournel, F., Continni, L., Morales, C., Da Fonseca, J., Moriceau, H., Rieutord, F., Barthelemy, A. and Radu, I. [2012]. Measurement of bonding energy in an anhydrous nitrogen atmosphere and its application to silicon direct bonding technology, *Journal of Applied Physics* **111**(10): 104907. Number: 10.
**URL:** *http://aip.scitation.org/doi/10.1063/1.4716030* 52

Fournel, F., Continni, L., Morales, C., Fonseca, J. D., Moriceau, H., Cocher, C. M., Rieutord, F., Barthelemy, A. and Radu, I. [2013]. (Invited) Direct Bonding Energy in Anhydrous Atmosphere, *ECS Trans.* **50**(7): 3. Number: 7 Publisher: IOP Publishing.
**URL:** *https://iopscience.iop.org/article/10.1149/05007.0003ecst/meta* 52

Garcia-Caurel, E., De Martino, A., Gaston, J.-P. and Yan, L. [2013]. Application of Spectroscopic Ellipsometry and Mueller Ellipsometry to Optical Characterization, *Appl Spectrosc* **67**(1): 1–21. Number: 1.
**URL:** *http://journals.sagepub.com/doi/10.1366/12-06883* 84

Guillemenet, J. and Bistac, S. [2001]. Crack propagation in adhesively bonded steel assemblies, *International Journal of Adhesion and Adhesives* **21**(1): 77–83. Number: 1.
**URL:** *http://www.sciencedirect.com/science/article/pii/S0143749600000336* 53

Haapalinna, A., Nevas, S. and Pähler, D. [2004]. Rotational grinding of silicon wafers—sub-surface damage inspection, *Materials Science and Engineering: B* **107**(3): 321–331. Number: 3.
**URL:** *http://www.sciencedirect.com/science/article/pii/S0921510703006858* 45, 64

Hadamovsky, H.-F. [1990]. *Werkstoffe der Halbleitertechnik: mit 64 Tabellen*, 2., überarb. aufl edn, Grundstoffindustrie Leipzig, Leipzig. OCLC: 74889624. viii, 45

Hopcroft, M. A., Nix, W. D. and Kenny, T. W. [2010]. What is the Young's Modulus of Silicon?, *Journal of Microelectromechanical Systems* **19**(2): 229–238. Number: 2. 50, 56

Imachi, M. [1986]. Effect of bonding temperature on the interfacial bonding strength of polyethylene/polypropylene and other polymers, *Journal of Polymer Science Part C: Polymer Letters* **24**(10): 537–540. Number: 10 _eprint: https://onlinelibrary.wiley.com/doi/pdf/10.1002/pol.1986.140241008.
**URL:** *https://onlinelibrary.wiley.com/doi/abs/10.1002/pol.1986.140241008* 76

Kim, H. S. and Crosby, A. J. [2011]. Solvent-Responsive Surface via Wrinkling Instability, *Advanced Materials* **23**(36): 4188–4192. Number: 36 _eprint: https://onlinelibrary.wiley.com/doi/pdf/10.1002/adma.201101477.
**URL:** *https://onlinelibrary.wiley.com/doi/abs/10.1002/adma.201101477* 74

Lin, P.-C., Vajpayee, S., Jagota, A., Hui, C.-Y. and Yang, S. [2008]. Mechanically tunable dry adhesive from wrinkled elastomers, *Soft Matter* **4**(9): 1830–1835. Number: 9 Publisher: Royal Society of Chemistry.
**URL:** *https://pubs.rsc.org/en/content/articlelanding/2008/sm/b802848f* 74

Lin, P.-C. and Yang, S. [2007]. Spontaneous formation of one-dimensional ripples in transit to highly ordered two-dimensional herringbone structures through sequential and unequal biaxial mechanical stretching, *Appl. Phys. Lett.* **90**(24): 241903. Number: 24.
**URL:** *http://aip.scitation.org/doi/10.1063/1.2743939* 74

Maszara, W. P., Goetz, G., Caviglia, A. and McKitterick, J. B. [1988]. Bonding of silicon wafers for silicon-on-insulator, *Journal of Applied Physics* **64**(10): 4943–4950. Number: 10.
**URL:** *https://aip.scitation.org/doi/abs/10.1063/1.342443* 52

Michaud, L. G., Nikitskiy, N. and Tardif, S. [2019]. Raman_solflex. Programmers: _:n3211.
**URL:** *https://github.com/mcdlrt/Raman_solflex.git* 56

Mirshafieyan, S. S. and Guo, J. [2014]. Silicon colors: spectral selective perfect light absorption in single layer silicon films on aluminum surface and its thermal tunability, *Opt. Express* **22**(25): 31545. Number: 25.
**URL:** *https://www.osapublishing.org/oe/abstract.cfm?uri=oe-22-25-31545* 66, 70

Mizuno, J., Ishida, H., Farrens, S., Dragoi, V., Shinohara, H., Suzuki, T., Ishizuka, M., Glinsner, T., Lindner, F. and Shoji, S. [2005]. Cyclo-olefin polymer direct bonding using low temperature plasma activation bonding, *The 13th International Conference on Solid-State Sensors, Actuators and Microsystems, 2005. Digest of Technical Papers. TRANSDUCERS '05.*, Vol. 2, pp. 1346–1349 Vol. 2. ISSN: 2164-1641. 76

Montméat, P., Enot, T., Enyedi, G., Pellat, M., Thooris, J. and Fournel, F. [2018]. Development and adhesion characterization of a silicon wafer for temporary bonding, *International Journal of Adhesion and Adhesives* **82**: 100–107.
**URL:** *http://www.sciencedirect.com/science/article/pii/S0143749618300095* 43, 63

Montméat, P., Enot, T., Pellat, M., Fournel, F., Bally, L., Baud, L., Dechamp, J., Eleouet, R., Vignoud, L. and Zussy, M. [2015]. Origin of the TTV of thin films obtained by temporary bonding ZoneBond® technology, *Microsyst Technol* **21**(5): 987–993. Number: 5.
**URL:** *https://doi.org/10.1007/s00542-015-2431-9* 64

Moon, M.-W., Lee, S. H., Sun, J.-Y., Oh, K. H., Vaziri, A. and Hutchinson, J. W. [2007]. Wrinkled hard skins on polymers created by focused ion beam, *PNAS* **104**(4): 1130–1133. Number: 4 Publisher: National Academy of Sciences Section: Physical Sciences.
**URL:** *https://www.pnas.org/content/104/4/1130* 74

Nakashima, S., Mitani, T., Ninomiya, M. and Matsumoto, K. [2006]. Raman investigation of strain in Si/SiGe heterostructures: Precise determination of the strain-shift coefficient of Si bands, *Journal of Applied Physics* **99**(5): 053512. Number: 5.
**URL:** *http://aip.scitation.org/doi/10.1063/1.2178396* 55

Ohzono, T. and Shimomura, M. [2004]. Ordering of microwrinkle patterns by compressive strain, *Phys. Rev. B* **69**(13): 132202. Number: 13 Publisher: American Physical Society.
**URL:** *https://link.aps.org/doi/10.1103/PhysRevB.69.132202* 74

Pal, P., Haldar, S., Ashok, A., Yan, X. and Sato, K. [2014]. A detailed investigation and explanation of the appearance of different undercut profiles in KOH and TMAH, *J. Micromech. Microeng* **24**(9): 095026. Number: 9. 60

Pei, Z. J., Fisher, G. R. and Liu, J. [2008]. Grinding of silicon wafers: A review from historical perspectives, *International Journal of Machine Tools and Manufacture* **48**(12): 1297–1307. Number: 12.
**URL:** *http://www.sciencedirect.com/science/article/pii/S0890695508001089* 45

Penado, F. [1993]. A Closed Form Solution for the Energy Release Rate of the Double Cantilever Beam Specimen with an Adhesive Layer, *Journal of Composite Materials* **27**(4): 383–407. Number: 4.
**URL:** *http://journals.sagepub.com/doi/10.1177/002199839302700403* 53

Peng, C.-Y., Huang, C.-F., Fu, Y.-C., Yang, Y.-H., Lai, C.-Y., Chang, S.-T. and Liu, C. W. [2009]. Comprehensive study of the Raman shifts of strained silicon and germanium, *Journal of Applied Physics* **105**(8): 083537. Number: 8.
**URL:** *http://aip.scitation.org/doi/abs/10.1063/1.3110184* 56

Pétri, R., Brault, P., Vatel, O., Henry, D., André, E., Dumas, P. and Salvan, F. [1994]. Silicon roughness induced by plasma etching, *Journal of Applied Physics* **75**(11): 7498–7506. Number: 11.
**URL:** *http://aip.scitation.org/doi/10.1063/1.356622* 84

Schmid, T. and Dariz, P. [2019]. Raman Microspectroscopic Imaging of Binder Remnants in Historical Mortars Reveals Processing Conditions, *Heritage* **2**(2): 1662–1683. Number: 2 Publisher: Multidisciplinary Digital Publishing Institute.
**URL:** *https://doi.org/10.3390/heritage2020102* viii, 56

Schwartz, B. and Robbins, H. [1976]. Chemical Etching of Silicon: IV . Etching Technology, *J. Electrochem. Soc.* **123**(12): 1903. Number: 12 Publisher: IOP Publishing.
**URL:** *https://iopscience.iop.org/article/10.1149/1.2132721/meta* 45

Soejima, K., HIRAYAMA, T., Shimokawa, D., Sato, M. and Arimitsu, Y. [2013]. Heat-peelable pressure-sensitive adhesive sheet for cutting laminated ceramic sheet and method for cut-processing laminated ceramic sheet. Inventors: _:n3188 Issue: US8524361B2 Library Catalog: Google Patents.
**URL:** *https://patents.google.com/patent/US8524361/en* 38

Tabata, O., Asahi, R., Funabashi, H., Shimaoka, K. and Sugiyama, S. [1992]. Anisotropic etching of silicon in TMAH solutions, *Sensors and Actuators A: Physical* **34**(1): 51–57. Number: 1.
**URL:** *http://www.sciencedirect.com/science/article/pii/092442479280139T* 41, 42, 60

Tiberj, A., Fraisse, B., Blanc, C., Contreras, S. and Camassel, J. [2002]. Process-induced strain in silicon-on-insulator materials, *J. Phys.: Condens. Matter* **14**(48): 13411–13416. Number: 48.
**URL:** *https://iopscience.iop.org/article/10.1088/0953-8984/14/48/396* 79, 82

Timoshenko, S. [1925]. Analysis of Bi-Metal Thermostats, *J. Opt. Soc. Am.* **11**(3): 233. Number: 3.
**URL:** *https://www.osapublishing.org/abstract.cfm?URI=josa-11-3-233* 68

Wang, Y., Li, Z. and Xiao, J. [2016]. Stretchable Thin Film Materials: Fabrication, Application, and Mechanics, *J. Electron. Packag* **138**(2). Number: 2 Publisher: American Society of Mechanical Engineers Digital Collection.
**URL:** *https://asmedigitalcollection.asme.org/electronicpackaging/article/138/2/020801/372726/Stretchable-Thin-Film-Materials-Fabrication* 74

Wolf, I. D. [1999]. Stress measurements in Si microelectronics devices using Raman spectroscopy, *J. Raman Spectrosc.* **30**(10): 877–883. Number: 10.
**URL:** *http://onlinelibrary.wiley.com/doi/10.1002/(SICI)1097-4555(199910)30:10<877::AID-JRS464>3.0.CO;2-5/abstract* 55

# Chapter 3

# Silicon On Polymer mechanics

## Contents

# Introduction

This chapter will expose the main challenges for the mechanical characterization of Silicon On Polymer (SOP) materials and the solutions developed within the framework of this thesis. First a presentation of the peculiarities of SOP behavior will be given along with methods used to observe them. Then a detailed study of the samples obtained with the process described in the previous chapter will be exposed. The objective of the experimental work presented here is to have a better understanding of the mechanical behavior of SOP material under tensile stress. Through process tuning and reproducible tensile tests, the ultimate strength of sc-Si thin film was improved. To do so, a framework was developed for mechanical characterization of crystalline materials on flexible substrates. Results of the mechanical characterizations were used to tune the strain in a sc-Si thin film, both in amplitude and orientation. An extended study of the SOP materials also gave an overview of the different options for the next milestone of this thesis: bonding a strained sc-Si thin film on a rigid substrate in order to impose a permanent strain.

## 3.1 Tensile test and strain measurements

### 3.1.1 Generality on tensile testing and the studied structures

Part of this work was dedicated to the study of the mechanical behavior of SOP structures. To do so, the flexible polymer acting as the substrate is subjected to the applied external mechanical stress. Shear stress at the polymer/silicon interface will in turn impose the deformation in the silicon film. Figure 3.1 presents the hetero-structure that will be studied here. The product of the Young modulus (E) by the thickness is of the same order of magnitude for both the silicon film and the polymer substrate, which means that even though the silicon film is significantly thinner, it can be expected to have a measurable influence over the macroscopic behavior of the structure. In terms of mechanical testing, only tensile stress could be easily applied, given the nature of the structure. Additionally, some adjustments had to be made compared with standard tensile test procedures, as described hereafter.

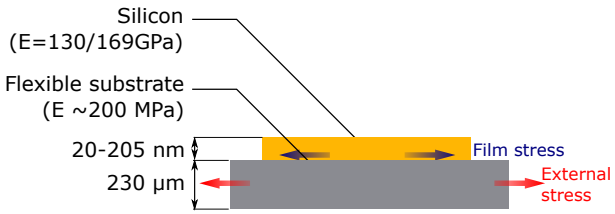


Figure 3.1: Schematic of the SOP stack studied in this chapter. An external tensile stress is applied to the flexible substrate

#### 3.1.1.1 Mechanical behavior under tensile test

Tensile tests are a common way to characterize mechanical properties of materials. They are usually conducted in accordance with well defined standards depending on the nature of the material like metals [ASTM International, 2013], polymers [ISO, 2017] or ceramics and brittle materials [ASTM International, 2018].

During a tensile test, a standardized test sample is subjected to mechanical loading and its response is recorded, usually in terms of strain, but other physical properties can be measured simultaneously. Typically, the test can be driven either by controlling the applied force (stress control) or the applied elongation (strain control). The sample strain ($\varepsilon$) is usually plotted against the applied stress ($\sigma$). These parameters are calculated from the experimental observables (force and length) using equations 3.1 and 3.2, where $L_0$ is

the initial sample length, $L = \Delta L + L_0$ the sample length under an applied force F, and S is the initial sample section in the direction perpendicular to the applied force.

$$\varepsilon = \frac{\Delta L}{L_0} = \frac{L - L_0}{L_0} \tag{3.1}$$

$$\sigma = \frac{F}{S} \text{Pa} \tag{3.2}$$

$L_0$ and L can either be defined as the distance between the tensile test apparatus clamps or in between two given points on the sample. For example, for dog bone shaped sample, the two points are chosen on the samples length where the section is the smallest.

Examples of typical tensile curves are given in figure 3.2. Three tensile curves are represented, each one corresponding to a different mechanical behavior. The curve I is typical of a brittle material such as silicon, the strain is fully elastic and no plastic deformation is observed up to the sample failure. Curves II and III are representatives of ductile materials such as metals and polymers. Indeed, past an elastic limit, additional stress will result in a permanent (*i.e.,* plastic) strain of the structure. A residual strain is observed for plastic deformation even after the external stress is removed.

Different parameters can be extracted from these curves:

- $\sigma_m$: maximum tensile stress recorded in extending the test piece to a breaking point.
- $\varepsilon_m$: strain corresponding to $\sigma_m$
- $\sigma_b$: tensile stress at the moment of the rupture, it can be different from $\sigma_m$
- $\varepsilon_b$: strain corresponding to $\sigma_b$
- $\sigma_y$: Tensile stress at yield, it is the stress at the point at which an increase in strain occurs without an increase in stress for rubber material or when a plastic deformation can be observed in metallic material.
- $\varepsilon_y$: strain corresponding to $\sigma_y$
- E: Elastic modulus, the slope of the line between the origin and the point defined by $\varepsilon = \varepsilon_y$ and $\sigma = \sigma_y$.

Additional parameters can be extracted from tensile curves of metallic materials such as true strain or absorbed energy.

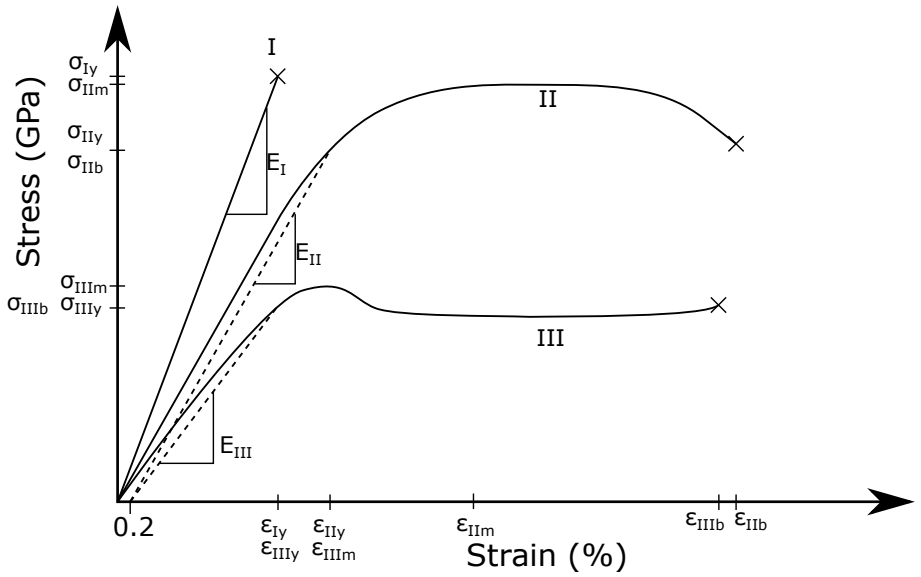


Figure 3.2: Example of tensile curves for different types of mechanical response. Curve I, II, III are representative of brittle materials, metals and polymers, respectively

The present work is focused on a heterostructure composed of a polymer bonded to a brittle semiconductor single crystal, thus with very different mechanical behaviors. The polymers used in this study typically show a plastic behavior, whose origin lies in the polymer chains reorganization along the direction of the tensile stress [Lin and Argon, 1994]. For brittle material such as silicon, no plastic deformation is observed in macroscopic test pieces. In crystalline or polycrystalline materials, plasticity is usually linked to a high density of dislocations with a high mobility, as typically observed in metals. In a crystal, a dislocation can be seen as a stacking fault in the otherwise perfect atomic arrangement. Two types of perfect dislocations (a pure screw dislocation and a 60° dislocation) were thus described in the diamond lattice of silicon, where the slip plane is {111} and the slip direction is invariably < 110 > [Anderson et al., 2017; Hornstra, 1958] It is also worth noting that the single crystal silicon wafers used in this study have an extremely low initial density of dislocations (*i.e.,* comparable to bulk value).

#### 3.1.1.2 The Silicon on polymer case

As presented earlier, a silicon film and a polymer substrate have widely different mechanical behavior. One is a brittle semiconductor whereas the other is a visco-elastic polymer. On the one hand, a sc-Si film shows a dominant elastic behavior. It can thus be modeled by an ideal spring with a $K_{Si,hkl}$ spring constant that depends on the $hkl$ crystal orientation. On the other hand, the polymer mechanical response is time dependent. Under constant applied strain, the stress will relax (and typically decrease), whereas at constant applied stress, creeping will occur (*i.e.* strain will slowly increase).

For a uniaxial tensile test, the set-up is represented in figure 3.3. The sample can be divided in three parts :

- Two silicon-free parts near the clamps. The clamps could not be placed directly on the sc-Si film to avoid any damage from the clamp contact. Only the polymer substrate is put under tension in these areas.

- A cracked silicon area. Preexisting cracks could be present in the sc-Si film due to the fabrication process or sample handling. They could also appear during the tensile test. At these cracks locations, tensile stress is only imposed on the polymer substrate. These cracked areas can be assimilated to the silicon-free substrate present near the clamps.

- The rest of the sample is the polymer substrate covered by a sc-Si layer. Assuming a perfect mechanical coupling between the Si and the polymer, the strain of both materials will be equal in both layers.

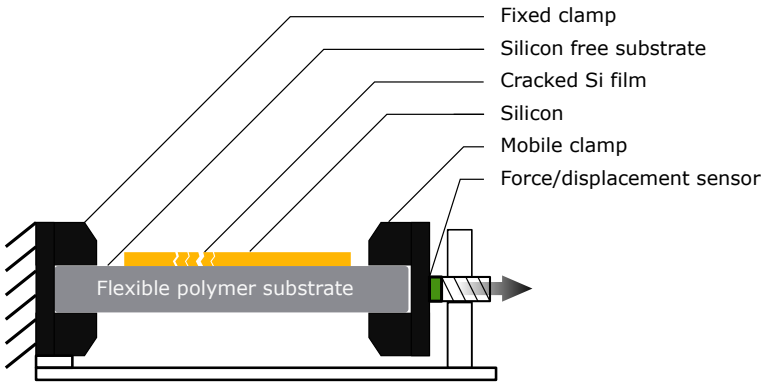


Figure 3.3: Schematic of a uniaxial tensile test set-up for a SOP sample with the illustration of parts with different mechanical behavior

The whole sample can be modeled using the Standard Linear Solid Model (SLSM). A schematic Maxwell representation of the model is presented in figure 3.4. It is composed of a spring connected in series to a damper with another spring in parallel.

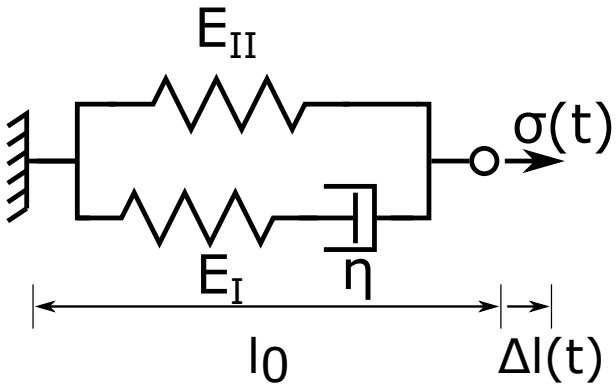


Figure 3.4: Maxwell schematic representation of the SLSM

Springs display a pure elastic response with $\sigma = E\varepsilon$ where $\sigma$ is the stress, $\varepsilon$ the strain and E the Young modulus or elastic constant. The damper mechanical response is time dependent as described by equation 3.3.

$$\sigma_d = \eta \frac{d\varepsilon_d}{dt} \tag{3.3}$$

With $\sigma_d$ and $\varepsilon_d$ being the stress and strain of the damper and $\eta$ its viscosity. From this, the constitutive equations of the SLSM can be derived:

$$\sigma_{II} = E_{II}\varepsilon \text{ and } \sigma_I + \frac{\eta}{E_I}\dot{\sigma}_I = \eta\dot{\varepsilon} \tag{3.4}$$

With $\sigma(t) = \sigma_I + \sigma_{II}$ and in the case of stress relaxation at constant strain $\varepsilon_0$ the stress evolution can be defined by equation 3.5 [Roylance, 2001].

$$\sigma(t) = \left(E_{II} + E_I e^{-\frac{t}{\tau_1}}\right)\varepsilon_0 \tag{3.5}$$

With $\tau_1 = c_1/E_1$ the relaxation time.

In the case of creeping at constant stress $\sigma_0$, the strain is expressed by equation 3.6:

$$\varepsilon(t) = \frac{\sigma_0}{E_e}\left(1 - \frac{E_1}{E_1 + E_e} \cdot e^{-\frac{t}{\tau_2}}\right) \tag{3.6}$$

With $\tau_2 = \eta\frac{(E_1+E_e)}{E_1 E_e}$ and $\varepsilon(t) = \frac{\Delta l(t)}{l_0}$

In the SOP case, the resulting tensile curve will be similar to the one obtained for a visco-elastic material. However a stress/strain curve issued from a tensile stage sensors would not give specific information from the silicon layer, which is the point of interest in the SOP structure. In order to have access to information about the local stress and strain in the sc-Si film, additional characterizations had to be performed during tensile tests (XRD and Raman spectroscopy, see subsections 3.1.4 and 3.1.5 as well as annex A). A stress/strain curve plotted with the local information obtained with these methods would be linear by definition as the strain measured is purely elastic and the stress is obtained through Hooke's law (as the local stress cannot be accessed directly). This is why the local silicon strain is represented as a function of macroscopic strain (or total sample strain). As illustrated in figure 3.5, such a tensile curve can be divided in several zones depending on the evolution of the curve second derivative:

- Tensioning zone: the SOP sample is not initially taut after installation in the tensile stage clamps. Some undulation or misalignment of the substrate might also increase the range of this zone. This cause an offset between the increase of macroscopic strain and local silicon strain values. Absolute macroscopic strain value is not essential for the work presented here but one could propose a pre tensioning apparatus to reduce any incertitude arising from this phenomena.

- Linear zone: the relaxation rate of the polymer substrate is negligible for low strain values. The ratio between local and macroscopic strain is constant as the deformation is fully elastic. From this zone, a strain ratio can be extracted to describe the coupling between the substrate and the sc-Si film. The Young modulus of the whole sample can also be computed from this zone.

- Substrate relaxation and silicon fracture: the separation is not clear between this two areas. At higher strain, relaxation in silicon free substrate was significant, causing the local silicon strain to increase at a lower rate than macroscopic strain. Cracks apparition in the sc-Si film has a similar influence on the tensile curve slope. Discrimination between the two phenomena is made possible with a full field observation (*e.g.,* an optical microscope coupled or not with a Digital Image Correlation (DIC) set-up)

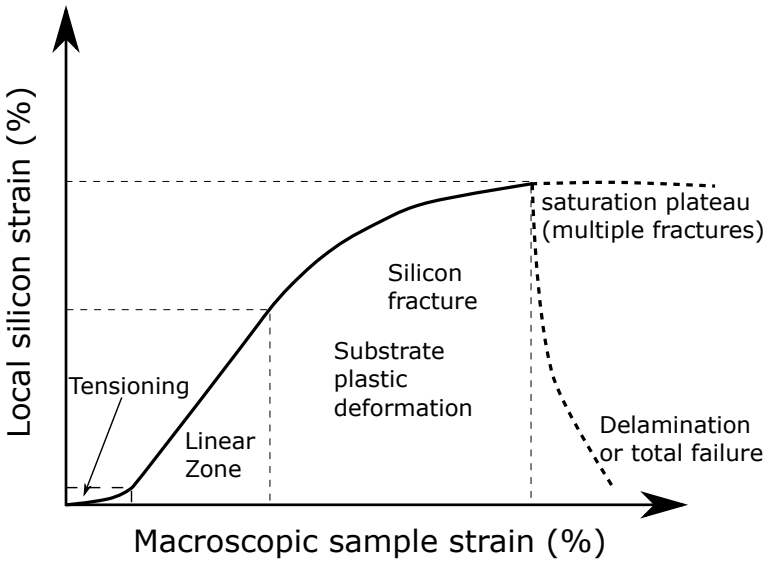


Figure 3.5: Typical mechanical behaviors for a SOP sample under uniaxial tensile stress. Different parts of the curve can be identified based on the second derivative.

### 3.1.2 Tensile stages used for Silicon On Polymer characterization

#### 3.1.2.1 Uniaxial tensile stage

To apply a unxial stress along a sample long axis, a unixial tensile stage adapted to the sample dimension was used (Proxima, MicroMecha company) and its specifications are presented in table 3.1. Samples can be placed horizontally or at a 40° for Micro Laue X-ray Diffraction. Standard sample dimensions are 10 mm × 40 mm for the polymer and 2 mm × 24 mm for the sc-Si Thin film. A snapshot of the MicroMecha tensile stage mounted on manual xy stage under a confocal Raman spectrometer is presented in figure 3.6. Standard dog bone shaped sample were not used for the polymer substrate. Indeed the area of interest is the Silicon covered rectangle, so extra stress concentration wasn't needed in the polymer. Furthermore it made the cutting process easier and avoided any local stress concentration in sharp corners which can be problematic for high aspect ratio substrate.

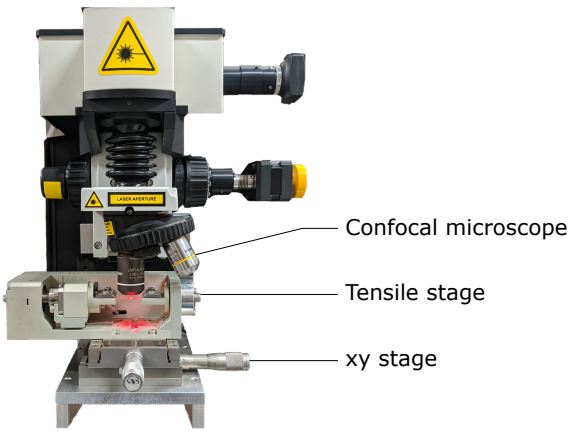


Figure 3.6: Micromecha tensile staged mounted under a Horiba LabRam HR Raman spectrometer

The tensile stage is connected to a control panel. Force and displacement values are recorded at a frequency of 1 Hz with a 50 N load cell and an optical encoder respectively. The displacement speed was set to 2 µm/s for step by step tensile tests and 0.2 µm/s for continuous measurements. A calibration procedure

is carried out at the beginning of each recording to reset the reference point of the force and displacement sensors.

| Property | Value |
|---|---|
| Displacement range | 15 mm |
| Displacement resolution | 20 nm |
| Clamped sample length | 2 × 8 mm |
| Sample width | 10 mm |
| Force Sensor range | 50 N |
| Force Sensor resolution | 0.25 N |
| Minimum/maximum speed | 0.1-30 µm/s |

Table 3.1: Specification of the Proxima uniaxial tensile stage from Micromecha

#### 3.1.2.2 Bulge test

The proxima tensile stage offered a precise tool for tensile test but does not have sufficient capacity for wide range biaxial tensile test.

Here, we also used a simple, cost effective and scalable technique to induce biaxial strain in our samples, namely the bulge test.
The bulge test stage is composed of a circular pressurized chamber closed by the tightly clamped SOP structure. A general schematic of the set-up is presented in figure 3.7, two sizes of stage were used with an internal diameter of 20 or 30 mm.

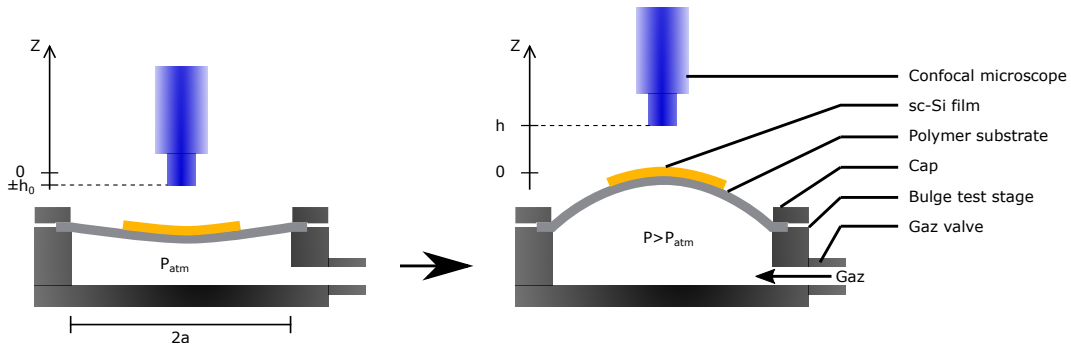


Figure 3.7: Schematic of a bulge test apparatus before and after the application of gas pressure into the chamber. The distance between the microscope objective and the silicon surface is fixed. The microscope is mounted on a vertically motorized stage

The height of the bulge is obtained with a confocal microscope, from this value, the biaxial strain in the central area can be derived from the equation 3.7 [Small and Nix, 1992; Tsakalakos, 1981]. With $a$ the bulge radius, $h$ the bulge height, $h_0$ the initial bulge height relative to the theoretic taut surface. The pressured chamber was connected to a dry air network with a manometer that allowed control of pressure with a precision of 0.1 bar

$$\varepsilon = \frac{2}{3a^2}(h^2 - h_0^2) \tag{3.7}$$

An experimental challenge relies in the precise determination of the origin of $h$ and $h_0$. Wrinkles in the flexible substrate can prevent its measurement. An uncertainty arises from this parameter as a perfectly taut sample is almost impossible to obtain, though one could envision adding complex surface flatness measurement techniques, e.g. using light reflection on the silicon. $h_0$ is estimated to be lower than 0.5 mm

Alternatively, the pressure can be deduced from the bulge height as presented in equation 3.8.

$$P = \frac{8Yt}{3a^4}h^3 \tag{3.8}$$

Where $t$ is the film thickness, P the pressure, Y the biaxial modulus define as $E/(1-\nu)$ and $\nu$ the Poisson's ratio.

From theses equations, calibration curves were established to estimate the expected strain and bulge height from the applied pressure. These curves are presented in figure 3.8 for our experimental parameters ($a$ = 5 mm, $t$ = 230 µm, $\nu$ = 0.3 and E=70 MPa )

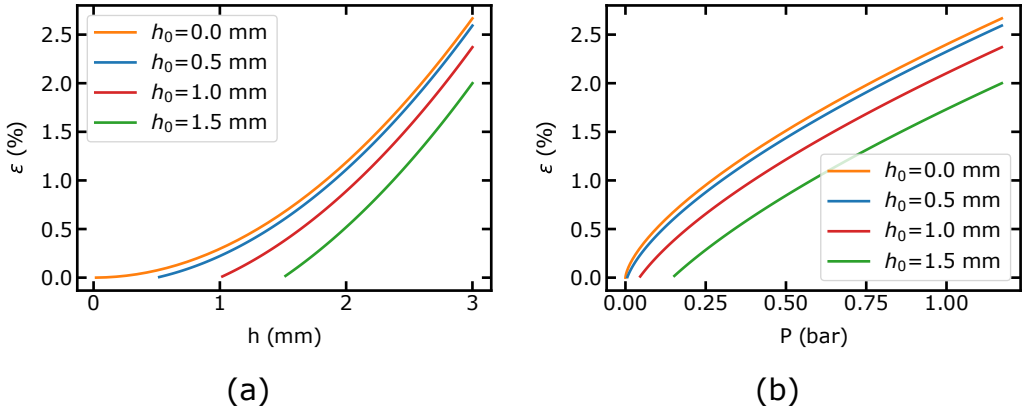


Figure 3.8: Theoretical bulge parameters (a) Strain as a function of bulge height for different height offsets (b) Strain as a function of pressure for different height offsets ($a$ = 15 mm, $t$ = 230 µm, $\nu$ = 0.3, E = 70 MPa)

The strain polar components are given in equation 3.9.

$$\varepsilon_\xi = \varepsilon \quad \varepsilon_\phi = \varepsilon\left[1 - \frac{r}{a}^{(1-\nu)/\nu}\right] \tag{3.9}$$

With ε as the bulge biaxial strain given by equation 3.7, $\varepsilon_\xi$ the radial strain component and $\varepsilon_\phi$ the tangential strain component. The radial strain component remains constant on the full bulge radius but the tangential component only reaches its maximum value ($\varepsilon_\xi$ or ε) for $r = 0$. It implies that only the bulge center is under pure biaxial stress [Tsakalakos, 1981]. So mapping of a small surface were performed around samples center (*i.e.*, ± 0.5 mm).

#### 3.1.2.3 Biaxial tensile stage

Measurements were performed on the biaxial tensile stage developed by Geandier et al. for the DiffAbs beamline at SOLEIL synchrotron. These measurement were done in collaboration with P.O. Renault and T. Chommaux from Poitier university and D. Thiaudière from SOLEIL synchrotron. This stage allows one to obtain a flat and homogeneous macroscopic surface under biaxial stress. A snapshot of the experimental set-up is presented in figure 3.9. The machine is 19 cm × 19 cm × 8.5 cm in size with an empty center and is designed to allow x-ray diffraction at glancing angles with no shadowing edges. Two couples of motors and force sensors are fixed to the device frame. The four motors can be actuated separately in order to keep the studied area at a fixed position in the goniometer. The load cells have a 200 N range. The optical microscope is composed of a telecentric lens and a CCD detector. It prevents any measurement artifact due to change in focal height. The size of the region of interest at the sample surface is 18 mm × 12.6 mm [Geandier et al., 2010]. Digital Image Correlation (DIC) is used to measure in-plane displacement fields of the substrate and to evaluate the average in-plane strains. It consists in registering pictures at different loading steps.

Speckles of white paint are used as visual markers on the sample surfaces to compute the displacement field from the optical microscope images. A global approach to DIC is used. A discretized displacement field is measured with a finite element mesh made of four-noded elements with a bilinear displacement interpolation [Besnard et al., 2006]. More detailed explanations about this technique are given in annex A.3.

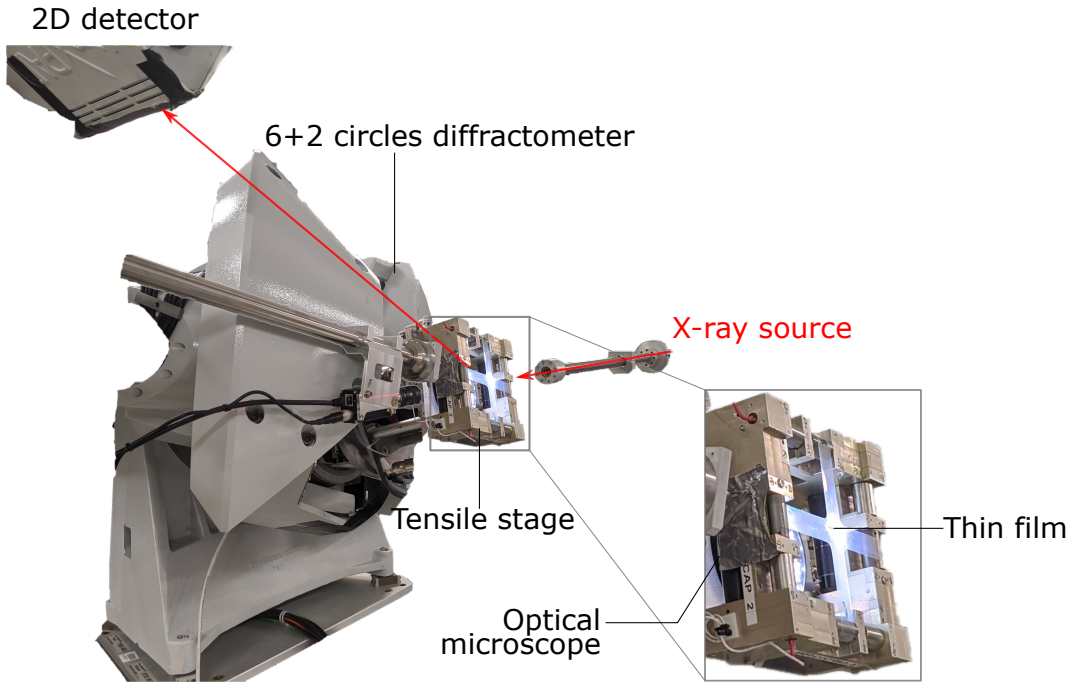


Figure 3.9: Snapshop of the Biaxial tensile stage installed on the DiffAbs beamline at SOLEIL synchrotron

### 3.1.3 Samples for tensile test

#### 3.1.3.1 Geometry

The different geometries for tensile test samples are represented in figure 3.10. Three types of substrate shapes were used, ribbons for uniaxial tensile test, disks for bulge tests and cross for biaxial tensile tests.

The fabrication process is described in the chapter 2 section 2.5. For practical reasons, ribbons shaped silicon patterns were also used for bulge test or biaxial tensile tests, the substrate was simply cut to the desired shape (disk or cross) around the centered pattern. The cutting of the sample was always performed on silicon free substrate to avoid fracture initiation.

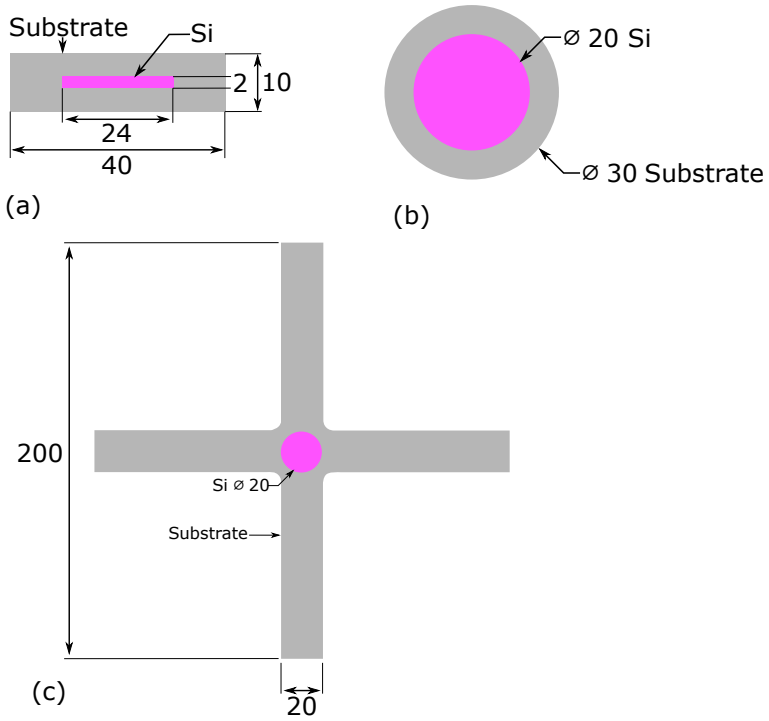


Figure 3.10: Top view schematics of the tensile test sample used for the mechanical characterization of SOP materials. All dimensions are given in mm. (a) uniaxial tensile test, the silicon present a (001) orientation normal to the surface and the long axis of the sample can either be < 100 > or < 110 > direction. (b) Disks used for bulge tests, ribbons shaped silicon can also be used with the substrate cut this way (c) Biaxial tensile test sample designed for the stage installed on DiffAbs beamline at SOLEIL synchrotron. Silicon ribbons were also transferred on cross shaped substrate.

#### 3.1.3.2 Synchrotron beam damage

During synchrotron experiment, beam damage could also be observed on the surface on the free surface of the sc-Si film using a white beam on beamline BM32. Figure 3.11 presents a post mortem micrograph of a sample after X-ray irradiation and tensile test. Surface damages can clearly be observed where acquisition were made. They caused a loss of the diffracted signal in the probed area. The nature of the damages is still unknown as further SEM observation were challenging on this kind of stack. A nitrogen flow on the sample surface did not solve this issue. The solution was to encapsulate the silicon layer with a second layer of Furukawa adhesive tape (230 µm thick). This prevented further beam damages and signal loss during long acquisition in a single point (*i.e.*, longer than 10 s)

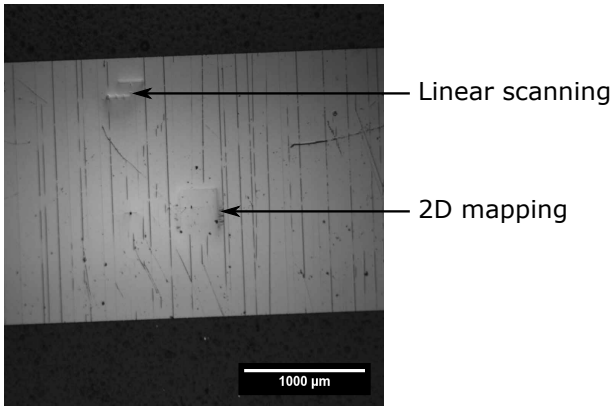


Figure 3.11: Beam damages caused by the exposition of the free surface of a SOP sample to a poly-chromatic X-ray beam (5 keV to 25 keV)

### 3.1.4 Raman spectroscopy

The theory of strain characterization in silicon when using Raman spectroscopy is detailed in chapter 1. Experimentally, the displacement of the silicon LO phonon scattering is measured. The nature of the stress has to be known to use the right coefficient in equation 3.10.

$$\Delta\omega = b\varepsilon \tag{3.10}$$

Where $\Delta\omega$ is the silicon raman peak displacement, $b$ the strain/shift coefficient and $\varepsilon$ the silicon local strain. The values of $b$ used in this work were $b_{[100]} = -260\,\mathrm{cm}^{-1}$ [Wolf, 1996], $b_{[110]} = -336\,\mathrm{cm}^{-1}$ [Peng et al., 2009]and $b_{biax} = -733\,\mathrm{cm}^{-1}$ [Peng et al., 2009] for respectively uniaxial strain along [100] crystal axis, uniaxial strain along [110] crystal axis and biaxial strain in the (001) plane.

The Raman spectrometer used here is a Horiba LabRam HR paired to a HeNe Laser (632.8 nm, 17 mW). Hole and slit size are respectively 100 and 200 µm to achieve a confocal beam, the vertical resolution is 2 µm while the lateral resolution is 1 µm. A 100x objective is used. The Raman is equipped with a motorized stage ($50 \times 70 \times 4$ mm), but it can not be used with the tensile stage due to weight limitation. The staged was placed on a manual xy stage while the motorized stage was only used for static measurements (e.g., mapping of rigid sample). Schematic and snapshot of the set-up are visible in figures 3.12 and 3.6.

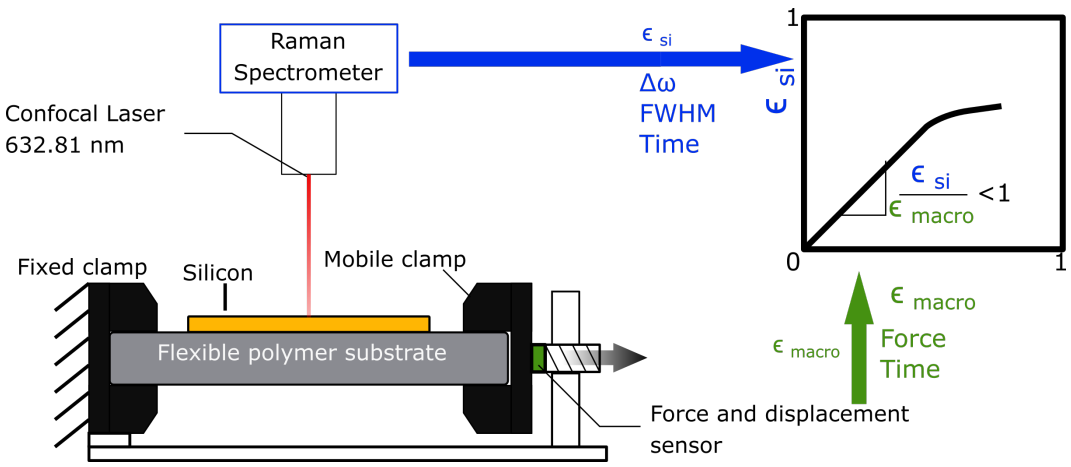


Figure 3.12: Schematic of the coupling of a Raman spectrometer and a uniaxial tensile stage for SOP mechanical testing

After and before each sample, a bulk silicon reference sample was measured to determine the position of the main silicon Raman peak at around $520.7\,\mathrm{cm}^{-1}$. High laser power can induce thermal strain in thin films during Raman measurement [Wolf, 1996]. Induced Raman shift caused by this thermal strain is dependent of the thin film thickness and nature of the substrate. Figure 3.13 presents the calibration curves used to choose the optimal filter to limit the thermal strain while keeping a maximum Signal to Noise Ratio (SNR). For silicon films between 205 and 100 nm thick, a 1.7 mW laser power was chosen (10% of the laser nominal power). The induced thermal shift was less than $0.1\,\mathrm{cm}^{-1}$. For lower thicknesses or fast acquisition a 4.25 mW power was used. It implied a noticeable thermal shift that was corrected thanks to the calibration curves. Several accumulation of the Raman signal have to be made in order to remove spikes from the signal and obtain a smoother mean response.

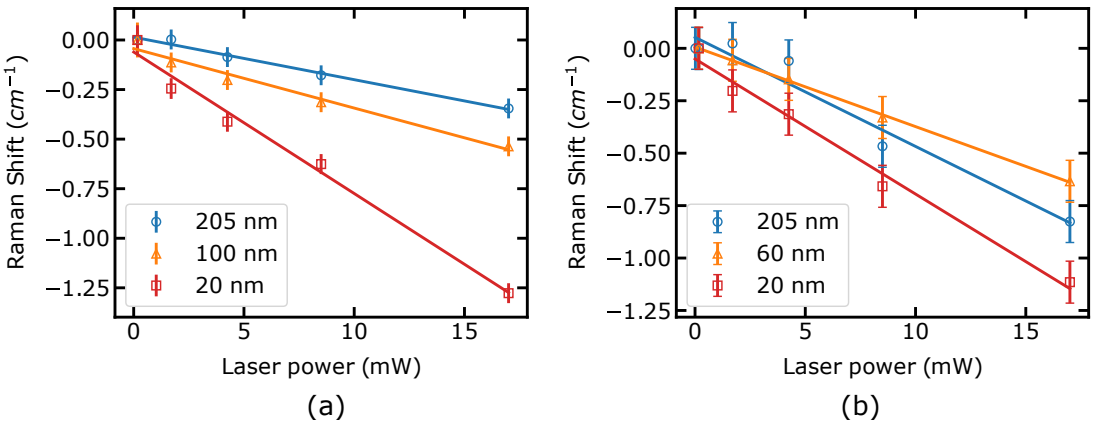


Figure 3.13: Raman shift as a function of laser power for different sc-Si film thickness, (a) with Furukawa dicing tape as a substrate, (b) with BSI glue as a substrate.

From an experimental point of view, the analysis of Raman spectrum can be decomposed in several steps:

- Fitting the Raman spectrum of the sample as well as the initial and final reference spectra. Peaks are fitted with a Lorentzian function using a least square method. Peak position, FWHM and intensity are extracted.

- Peak position is adjusted thanks to the initial an final reference, assuming a linear drift, as detailed in equation 3.11:

$$\omega' = \omega + (t - t_i) x \frac{(\omega_f - \omega_i)}{(t_f - t_i)} \tag{3.11}$$

  Where $\omega'$ is the calibrated peak position, $\omega_i$ the initial reference silicon peak position, $\omega_f$ the final reference silicon peak position, $t$ the absolute time at which the sample was measured, $t_i$ and $t_f$ the time at which the initial and final reference were measured. This step is essential to limit the uncertainty arising from temperature variations in the laboratory and thermalisation of the spectrometer. During the hottest months and even with a temperature control system, up to 0.1 $cm^{-1}$ shift could be measured for the reference sample on a couple hours range.

- Peak position is also adjusted according to the corresponding thermal stress. $\omega'' = \omega' + f(t_{Si}, \omega_{laser})$ where $\omega$ is the final silicon Raman shift $t_{si}$ is the silicon film thickness and $\omega_{laser}$ the laser power usually expressed in a percentage of the nominal power. For this task, the data are obtained from calibration curves shown in figure 3.13.

- Knowing the silicon crystal orientation, type of stress (uniaxial or biaxial) and stress orientation, the stress and strain value are calculated from the Raman peak shift ($\omega''$). Corresponding coefficient are presented in chapter 1.

Given the simplicity of the signal and the large number of spectrum to analyze, a python script was developed to automate the task. The source code is available on GitHub [Michaud et al., 2019]. A flow chart of the program is displayed in figure 3.14. The use of a python program allowed for a smooth access to the meta-data written in the files containing the Raman spectrum. It enables a fast analysis of dimensional scan (*i.e.*, time scan, z-axis scan or x-y mapping) in environment adapted to the handling of such multidimensional data set.

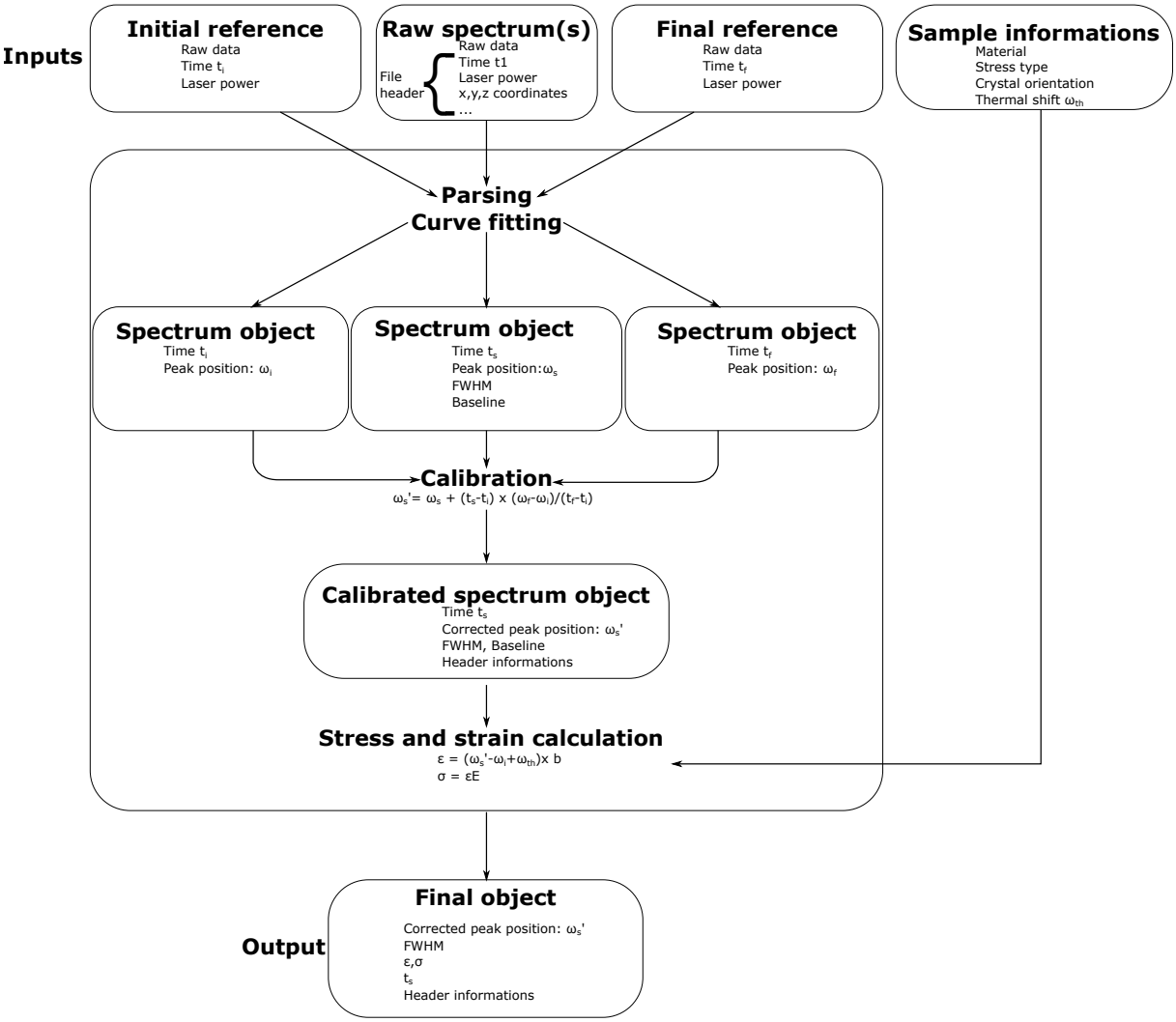


Figure 3.14: Flow chart of the python script developed to parse, fit and analyze silicon Raman spectra. An initial reference, a final reference and sample spectrum(s) are input as well as stress configuration, crystal orientation and laser power. The final object contains silicon strain, stress and Raman peak FWHM in addition to the raw data and files header

### 3.1.5 X-ray diffraction

Local strain was probed using two different X-ray diffraction methods, either monochromatic XRD (DiffAbs, SOLEIL synchrotron), or Micro Laue X-ray Diffraction (BM32, European Synchrotron Radiation Facility). The theoretical framework of each method is developed in annex A.2. In this chapter only the experimental set-up and data processing are detailed.

#### 3.1.5.1 monochromatic synchrotron XRD

A 6-circle goniometer allows one to access many Bragg peaks, especially since the tensile stage used there is designed to avoid shadowing at grazing angles. A 2D imXPAD s140 detector is used to performed rocking curve around Bragg's positions. The beam energy is set to 18 keV using monochromators. Rocking curves are performed to determine the 2θ angular position of the 0 0 4, 0 0 8 and 0 0 12 reflections of the silicon film. The lattice parameter $c$ of (001) plane can be calculated with Bragg's law and the experimental 2θ peak position as detailed in equations 3.12 and 3.13.

$$d_{00l} = \frac{\lambda}{2sin(\theta)} \tag{3.12}$$

$$c = d_{00l}\, l \tag{3.13}$$

The corresponding strain is computed $\varepsilon_{33} = \frac{c}{c_0}$ with $c_0$ =5.431 020 Å the relaxed silicon lattice parameter. With the hypothesis of a pure biaxial stress ($\sigma_{11} = \sigma_{22} = \sigma_{||}$ and $\sigma_{33} = 0$) and using generalized Hooke's law, the in plane strain component $\varepsilon_{||}$ can be expressed by equation 3.14:

$$\varepsilon_{||} = \varepsilon_{11} = \varepsilon_{22} = -\frac{c_{11}\varepsilon_{33}}{2c_{12}} \tag{3.14}$$

Where $\varepsilon_{11}$, $\varepsilon_{22}$ and $\varepsilon_{33}$ are the diagonal strain tensor component in the crystal reference frame. $c_{11}$ = 165.5 GPa and $c_{12}$ = 63.9 GPa are silicon elastic constants [Hopcroft et al., 2010].

#### 3.1.5.2 Micro Laue X-ray Diffraction

The Micro Laue X-ray Diffraction experiments were performed on BM32 beamline at European Synchrotron Radiation Facility Ulrich et al. [2011]. The schematic in figure 3.15 presents the beamline with two different tensile stages. The source of the beamline is a bending magnet that generates a white X-ray beam over the 5-25 keV energy range. The beam is focused down to 500 x 500 $nm^2$ at the sample position (the silicon surface) using elliptical mirrors. The sample stages are tilted at 40° and the Laue patterns were collected on a sCMOS camera located 77 mm above the sample (2016 × 2018 pixels, 73.4 µm square pixel size). The position of the test sample at the X-ray focal spot was controlled using a secondary optical microscope with a narrow focus aligned on that of the X-ray mirrors. A snapshot of the installation is presented in figure 3.16 The geometry of the setup was calibrated using a standard Ge sample and the collected Laue patterns were processed using the software suite LaueTools Micha and Robach [2020].

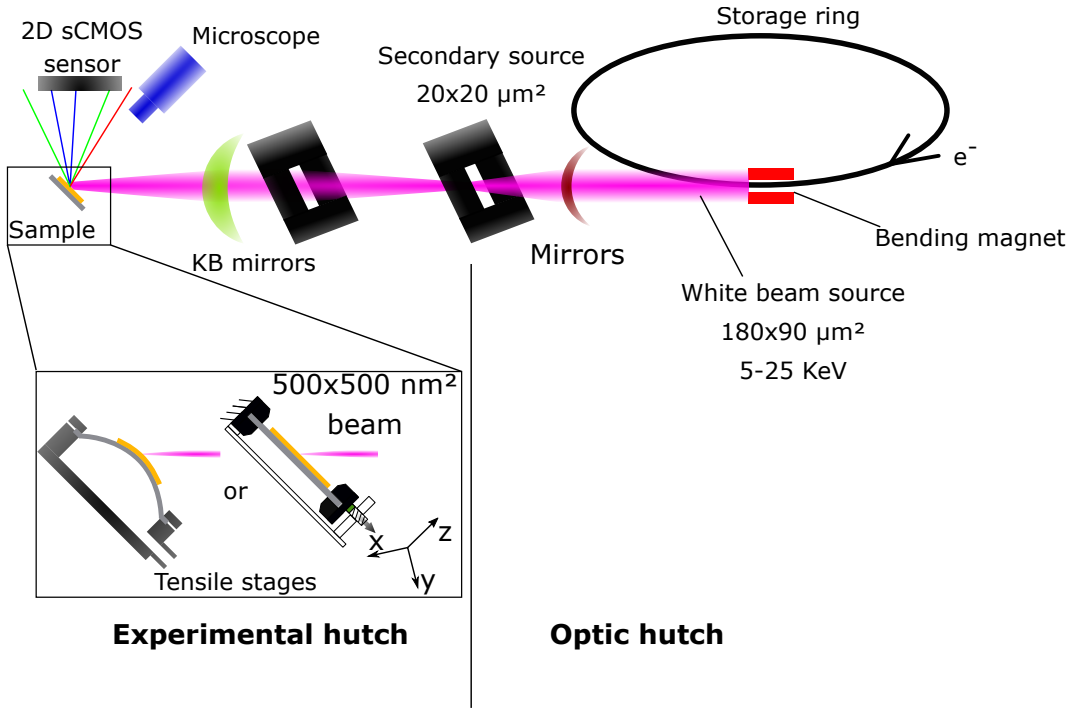


Figure 3.15: Schematic of BM32 beamline at ESRF for µLaue experiment coupled with tensile stages

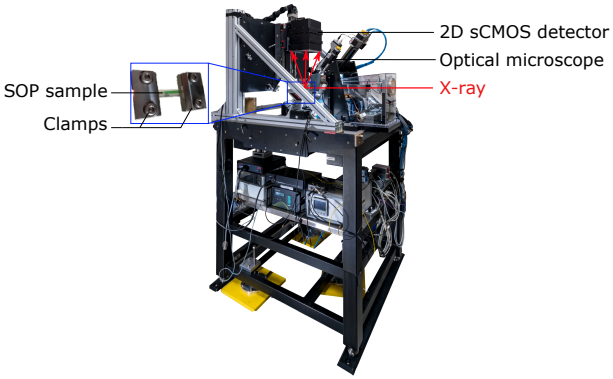


Figure 3.16: Snapshot of BM32 beamline (ESRF) set up used to perform tensile tests on SOP materials while probing the local silicon strain with µLaue an optical microscope

Given the visco-elastic mechanical behavior of the SOP structure, long acquisition time can results in loss of focus, stress relaxation or creeping in the polymer substrate. To avoid those issues and perform precise strain mapping, single point acquisition time had to be minimal, forbidding long signal integration to observe weak intensity diffraction peaks. Silicon being a relatively light element, with thicknesses of 205 nm and lower, the SNR can be low and caused difficulty for fast and automated data processing. To address these problems, an image processing work flow was used as detailed in figure 3.17. Region Of Interest (ROI) are defined around expected peak position in the Laue diffraction pattern. The single crystal nature of the films implies that peaks will only shift around their initial position under strain or small rotation due to local curvature. There was no need to search for an entirely different Laue pattern between two frames which greatly reduce processing time and errors.

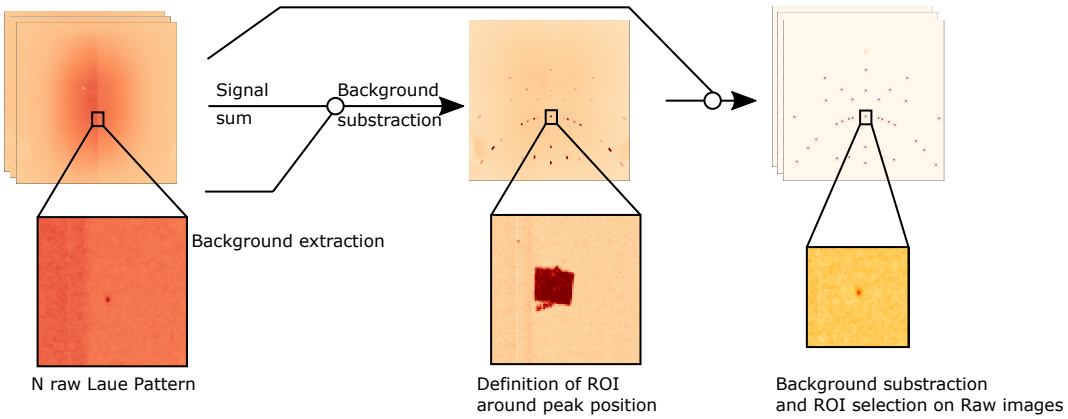


Figure 3.17: Image processing flow chart for silicon Laue diagram obtained from a (001) oriented thin film. First the signal background is extracted from the full images set and subtracted to the image sum. This allows one to determine the Region Of Interest (ROI) where peaks are positioned on the Laue pattern. Finally, the signal background is removed from individual images as well as any experimental artifact outside of the previously defined ROI.

As detailed in chapter 1, µLaue provides a measurement of the deviatoric strain tensor as well as the three Euler angles describing the crystal orientation without any *a priori* knowledge. Experimentally, peaks are first fitted and their position converted to angular coordinates. There are next indexed to extract the different lattice properties. Figure 3.18 details the workflow to extract a deviatoric strain tensor from an experimental Laue diffraction pattern.

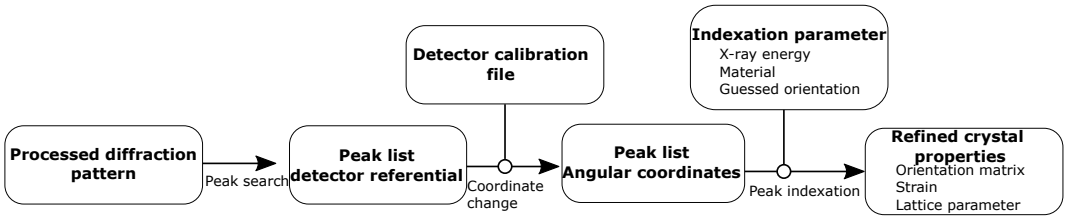


Figure 3.18: Flow chart of the process to extract crystal properties from a 2D Laue diffraction pattern using the software suite LaueTools Micha and Robach [2020, 2015]. After image processing of raw diffraction image, peaks are fitted with two dimensional Gaussian functions and there positions on the detector extracted. The calibration of the detector allows to convert these positions in angular coordinates. From this theoretical peak positions are fitted to the experimental values order to determine the crystal lattice parameter, angles and orientation.

### 3.1.6 Data analysis and acquisition strategy

As reported earlier, the mechanical behavior of a SOP structure can be modeled using the SLSM used for visco-elastic behavior. This calls for an adequate data acquisition strategy. Two parameters have to be taken into accounts :

- The sample surface height. Both µLaue and Raman spectroscopy relies on the surface being on focus. Working with a flexible substrate implies surface height variation if the sample is not taut. For bulge test, creeping occurred at a given pressure, increasing the surface height with time (1.0 µm/min and 2.2 µm/min for a 20 mm diameter bulge sample at respectively 0.2 bar and 0.5 bar).
- Stress relaxation at a given strain. For Furukawa tape the characteristic time was estimated to (103 ± 10) s. Many parameter can influence this metric. Three times the given value was used to obtain a stable stress in the sample during tensile tests.

From these observations, two strategies can be adopted, either in "stop and go" or "continuous" mode.

#### 3.1.6.1 "stop and go" acquistions

In "stop and go", the macroscopic strain is increased step by step, while allowing the sample to relax before performing long acquisitions. The displacement steps were 50 µm, *i.e.* around 0.2 % macroscopic strain and separate by at least 2 minutes. Figure 3.19 (a) shows the stress as a function of time during mapping of a uniaxial tensile test sample. The graphs of figure 3.19 is the detailed of the relaxation of the second step of the left curve. After fitting a function corresponding to the SLSM (see equation 3.5), the corresponding relaxation time $\tau_\sigma$ can be extracted. This strategy was used for long acquisition like µLaue strain mapping or with thinner sample where integration is crucial (with Raman spectroscopy or µLaue).

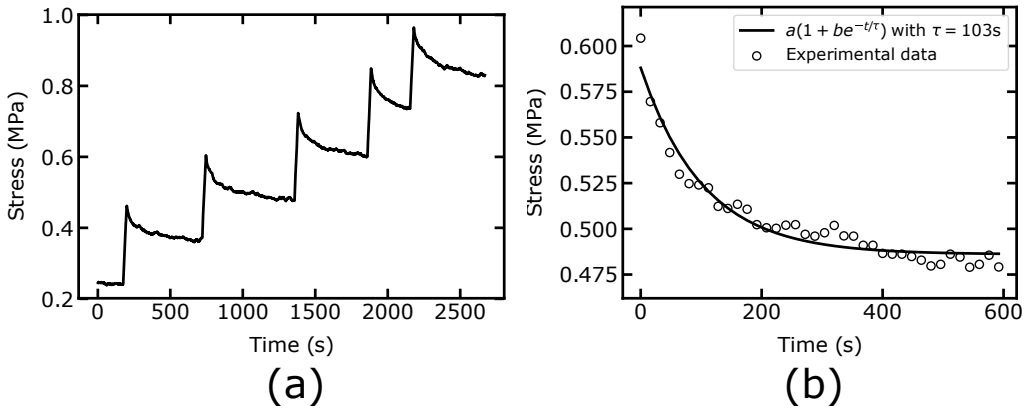


Figure 3.19: Uniaxial sample stress as a function of time, obtained during a step by step strain mapping of a SOP tensile sample. (a) Several steps (b) Detail of the second step, time offset is removed from the x-axis

#### 3.1.6.2 "continuous" acquisitions

Another strategy was to do shorter acquisition in order to perform a continuous tensile test. The displacement speed was set to 0.2 µm/s. This technique was particularly suited for the Raman set-up where the absence of motorized stage only allowed for single point measurement. Moreover, an auto-focus routine was used to prevent any artifact due to loss of surface focus. Displacement speed was set to 0.2 µm/s while a Raman spectrum was recorded every 20 s, *i.e.* during the integration time the sample was elongated by 4 µm and strained by about 0.02%. An additional python parser, coupled to the one described in figure 3.14 allowed to match data from the tensile stage sensor with the information extracted from the Raman spectra Michaud et al. [2019].

## 3.2 Mechanical behavior

Sample, stages and the methods described above allowed for a detailed study of the mechanical behavior of the various samples produced using the process presented in chapter 2. First a general overview of SOP

experimental tensile curves will be given as well as an evaluation of the possibilities achievable by the different tensile stage used in this work. Then the influence of different parameters (silicon thickness, crystal orientation, pattern edge definition) on the mechanical response of such materials will be detailed.

### 3.2.1 SOP : a composite material

#### 3.2.1.1 Uniaxial testing

A uniaxial tensile test performed on a 205 nm thick sc-Si film on a 40 µm thick BSI layer is used as an introduction to the analysis of experimental tensile curves obtained for SOP material. Figure 3.20 presents the resulting tensile curve. The stress is applied along the long axis of the sample corresponding to a < 110 > direction in th sc-Si film. Strain along a < 110 > direction was extracted from Raman measurements, as well as the Raman peak FWHM. They are plotted against the macroscopic strain in figure 3.20. We note that an initial compressive strain is observed in the sc-Si film. This is explained by the difference between the coefficient of thermal expansion of silicon and of the glue. These two materials are bonded at 210 °C, thus cooling the assembly results in compression and tension in the silicon and the polymer, respectively as detailed in chapter 2. As the macroscopic strain increases, the strain in the sc-Si film also increases with a sub-linear relationship ($\varepsilon_{Si} = -0.20\varepsilon_{macro}^2 + 0.64\varepsilon_{macro} - 0.14$, $R^2 = 0.9985$ ) up to a maximum macroscopic strain of 1.5 % and the brittle fracture of the glue. The 0.64 coefficient indicates that silicon strain is always smaller than the macroscopic strain due to the presence of small, silicon-free surfaces between the silicon pattern and the tensile stage clamps. It is unknown if sliding of the silicon film is occurring at the polymer interface. A local measurement of the substrate strain at a microscopic scale is needed to rule out this possibility. In the case of a Cu/W nanocomposite film on a Kapton substrate, Djaziri et al. used Digital Image Correlation and XRD to show that locally the strain of a substrate and film strain were matching to within $1 \times 10^{-4}$ in the domain of small elastic deformation (*i.e.,* less than 0.3 %). So although it is highly possible that no gliding is taking place in between the glue and the silicon, further characterization are needed in the case of the SOP structure studied here.

The good linearity up to about 0.5 % macroscopic strain indicates a quasi-elastic behavior. Above 0.5 % the silicon strain increases slower and slower compared to the macroscopic strain. Silicon free areas display a more ductile behavior and a higher strain than the silicon covered part. The Raman FWHM does not change with strain over the whole testing range, indicating that the local silicon crystal quality is unchanged. The maximum macroscopic strain of 1.5% limited by the glue mechanical failure shows that despite its good adhesion to silicon, the glue is not suitable to achieve large strain amplitude due to its brittle behavior and the maximum local silicon strain is limited to about 0.36 %. It justifies the need to be able to transfer a sc-Si film on a second polymer, more suitable for tensile loading than BSI glue. Tensile test were not performed on silicon on SPIS samples as the dry film was prone to shear fracture even during manual peeling from a rigid silicon carrier.

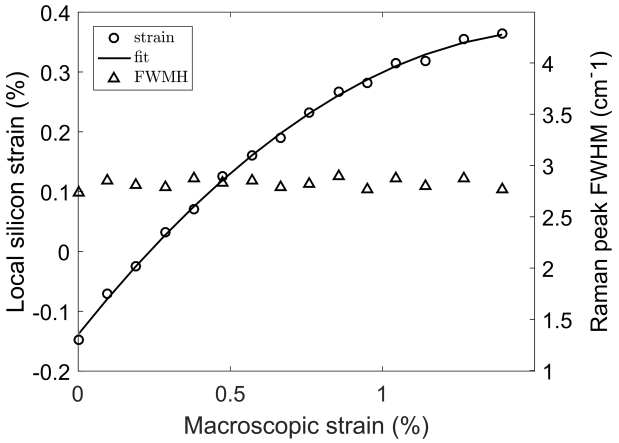


Figure 3.20: Tensile test curve of a 205 nm thick sc-Si on a 40 µm thick BSI layer. The pattern is 2 mm wide, oriented along a < 110 > direction and was obtained after patterning a SOI with the use of a soft lithography mask. Silicon strain is obtained with Raman spectroscopy and the macroscopic strain with a displacement sensor embedded in the tensile stage. The test was ended when cracks made signal acquisition too difficult and prevented any increase in local silicon strain.

Figure 3.21 presents the results of uniaxial tensile tests performed on Furukawa and BSI blank sample (*i.e.* without Si). Here the BSI sample fracture occurred at 3.6 % strain, in the sample center. It displayed an elastic modulus one order of magnitude higher than the one of Furukawa (1.6 GPa for BSI and 0.2 GPa for Furukawa). On the other hand, Furukawa tape presents a maximum strain larger than 10%. For a SOP structure with a ratio of local strain to macroscopic strain around 0.5, the expected maximum local silicon strain can be achieved before the breaking of the substrate. So despite its lower rigidity, Furukawa was choosen as a substrate for high strain application. The contribution of the silicon layer to the macroscopic mechanical properties is more important as the ratio $\frac{E_{Si} * t_{Si}}{E_{Substrate} * t_{substrate}}$ is increased. $E_{Si}$ and $E_{substrate}$ are the elastic modulus for respectively the silicon film and substrate, and $t_{Si}$ and $t_{subtrate}$ the corresponding thicknesses.

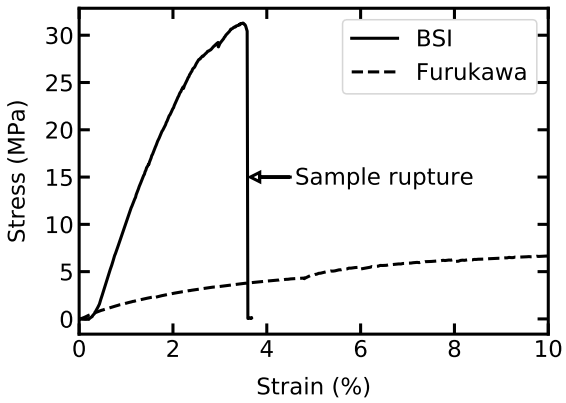


Figure 3.21: Uniaxial tensile curve for BSI and Furukawa blank sample (2 mm initial width in the sample center and 24 mm length

Uniaxial tensile tests were performed on a 205 nm thick sc-Si thin film transferred on tape. Strain tensor components were measured using µLaue in silicon-on-tape samples as well as uniaxial strain along along a < 110 > direction using Raman spectroscopy. The Furukawa tape did not reach rupture over the whole testing range. The strain along the stress direction measured using µLaue is reported against the macroscopic strain in figure 3.22 (a), alongside similar measurements obtained using Raman spectroscopy. For both curves, an initial linear zone is present. The ratio 1:2 between the slopes in the elastic regime for both samples stems from the sample dimension (Si film width = 1 mm and 2 mm for Raman and µLaue respec-

tively). A decrease in the curve derivative is observed above 2% macroscopic strain, indicating the onset of plasticity in the substrate and apparition of cracks in the Si thin film. A strain offset is observed, similar to the silicon on glue sample. This is due to the tape being laminated on the silicon while it is still in a compressive state on the glue (figure 2.14, step **J1**). Additionally, the tape is laminated which also introduces a (uniaxial) tensile strain. A 1.5% maximum uniaxial strain is reached in the silicon film. Above this point, no further increase in macroscopic strain can compensate the strain relaxation in the silicon layer due to crack apparition. Furthermore signal acquisition is more and more difficult. This increase in the maximum strain reached in the silicon, compared to the results presented before (figure 3.21), validate the use of Furukawa tape over BSI for tensile tests.

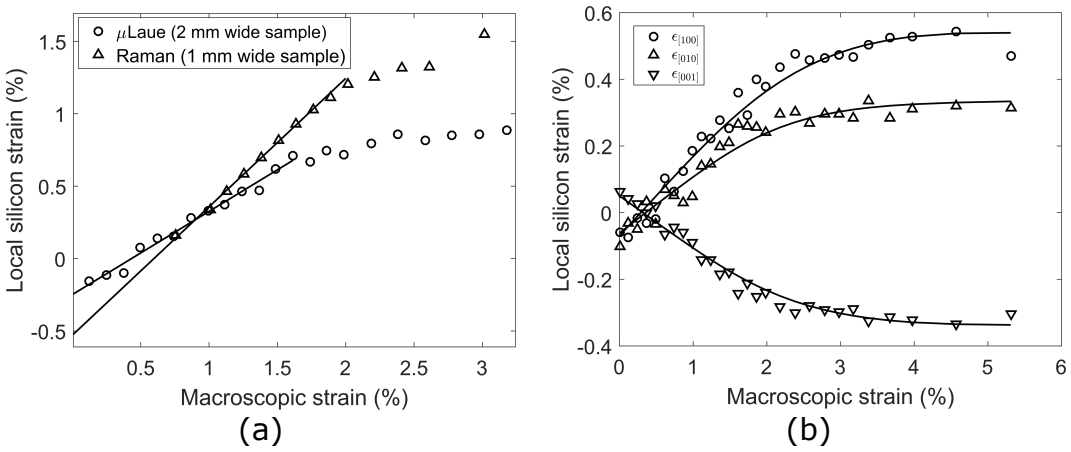


Figure 3.22: (a) Uniaxial strain along < 110 > for two samples. The local silicon strain is obtained by Raman spectroscopy and μLaue. The μLaue sample is 2 mm wide and the Raman sample is 1 mm wide.(b) Diagonal components of the strain tensor along the canonical crystal axis of a 205 nm silicon on tape sample, lines are guides for the eye.

The canonical strain components are also extracted from μLaue measurements Their evolution against macroscopic strain is presented in figure 3.22(b). Their evolution during the tensile test shows that the principal stress is applied almost along the <110> direction, with a small average angle difference $\theta_{eff}$ of 4.6° in the (001) plane as illustrated in figure 3.23. This value is obtained by diagonalizing the stress tensor expressed in the crystal reference frame, *i.e.* $\theta_{eff}$ represents the angle between the eigenvector of the stress tensor in the crystal reference frame and the [110] direction. The $\theta_{eff}$ angle is due to misalignment during the photolithography process, cutting of the samples, miscut during the SOI fabrication process and alignment on the tensile stage. In figure 3.22, all component cancel out at about 0.5 % macroscopic strain and vary linearly between 0 % and 2 % macroscopic strain. They reach a plateau at larger macroscopic strain values.

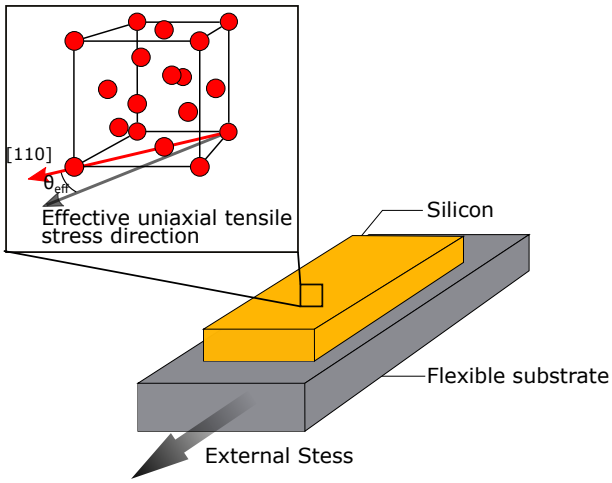


Figure 3.23: Schematic of a uniaxial tensile test on a < 110 > oriented silicon ribbon on a flexible substrate. $\theta_{eff}$ is the misalignment between the [110] silicon direction and the principal direction of stress in the silicon crystal in the (001) silicon plane. It can be obtained from µLaue measurements

Previous µLaue results showed that a uniaxial strain can be applied in a SOP structure with a tensile stage, confirming the use of adequate strain/shift Raman coefficient. However those measurements were performed on a single point. Strain mapping were obtained using µLaue during a tensile test to evaluate the homogeneity of the strain over the macroscopic sample surface. Initial state of the Si thin film strain tensor over a 2200 µm × 2200 µm surface is shown is figure 3.24. The external stress is applied along the y-axis of the sample ($[\bar{1}, 1\,0]$ crystal direction). Both $\varepsilon_{xx}$ and $\varepsilon_{yy}$ component are negative as the transferred film was initially compressed in the (001) plane. However, $\varepsilon_{yy} > \varepsilon_{xx}$ since the film needs to be under a minimal tensile stress to be taut. This way, a macroscopic area is at the focal point of the microscope for two dimensional mapping. The compression in the (001) plane induce a positive strain value in the direction normal to the surface (*i.e.*, $\varepsilon_{zz} > 0$). Shear components are close to zero.

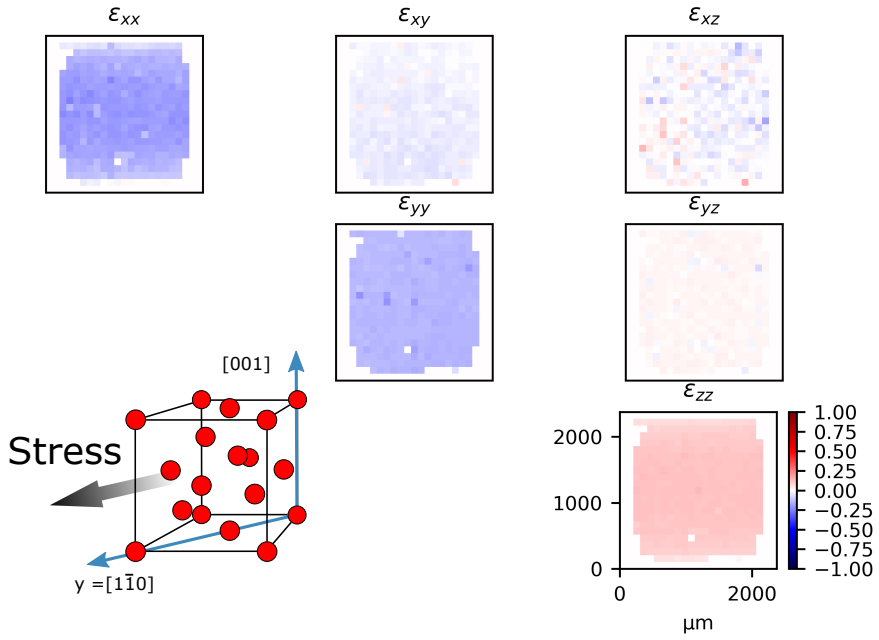


Figure 3.24: Initial strain tensor of a 100 nm thick sc-Si on a Furukawa tape under uniaxial loading along < 110 >. The tensor components are given in the [1 1 0], [$\bar{1}$, 1 0], [0 0 1] reference frame. The full strain tensor mapping is performed with µLaue on a 2200 × 2200 µm$^2$ surface

A strain mapping of the same surface is performed after the application of 0.95 % macroscopic strain in the SOP sample (figure 3.25). The strain curve of the whole test is also represented, each point corresponds to the mean strain value over the whole probed surface. Inhomogeneities and defect appeared on the silicon surface due the application of external stress on the tensile sample. Two blank parallels blank lines are visible on the mapping, as no signal could be extracted from the corresponding Laue patterns. This is due to delamination and local curvature of the sc-Si film, Bragg peaks either had a low intensity or were not indexed as their position was significantly different from the expected one. This induces a shear strain in the central part of the sample. Overall, where a diffraction pattern can be collected, the resulting diagonal present a good homogeneity on the whole sample width. The maximum mean $\varepsilon_{yy}$ value reached for this sample (0.5%) is significantly lower than the previous results presented for single point acquisition. Stress relaxation and signal loss in the two parallel zone prevented further exploitable strain mapping.

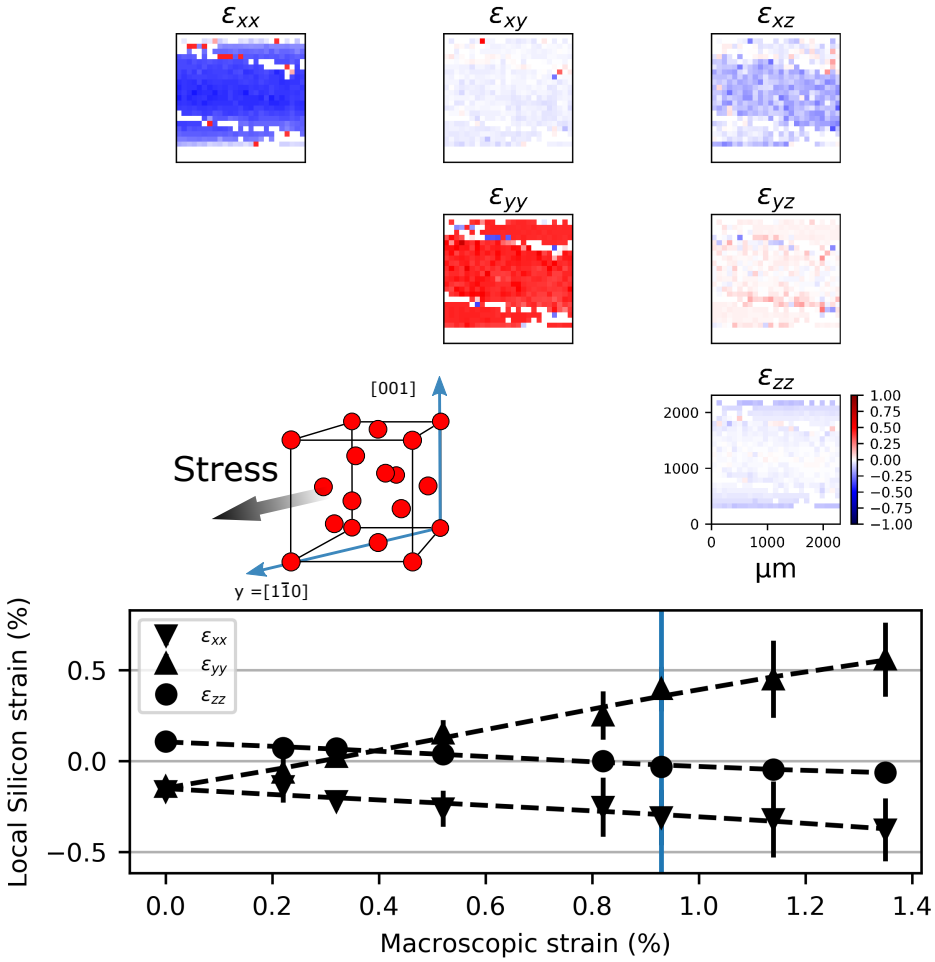


Figure 3.25: Strain tensor of a 100 nm thick sc-Si on a Furukawa tape under uniaxial loading along < 110 >. The strain tensor components are given in the [1 1 0], [$\bar{1}$, 1 0], [0 0 1] reference frame. The full strain tensor mapping is performed with µLaue on a $2200 \times 2200\,\mu m^2$ surface. The bottom graph gives the mean strain value for the whole tensile test. The blue line indicates the position of the full strain map presented above.

Mapping at a smaller scale ($20 \times 20\,\mu m^2$) were also performed during the same tensile test. Figure 3.26 presents the initial state and figure 3.27 a mapping at 0.94% macroscopic strain along with the full tensile curve. Despite some missing data points, the strain is as homogeneous as the larger scale mapping. Mean uniaxial strain along the <110> direction is slightly lower at smaller scale but still within the standard deviation of the larger scan. No variation in the shear component are observed here. This illustrates the homogeneity of the deformation at various scale for a macroscopic tensile test sample.

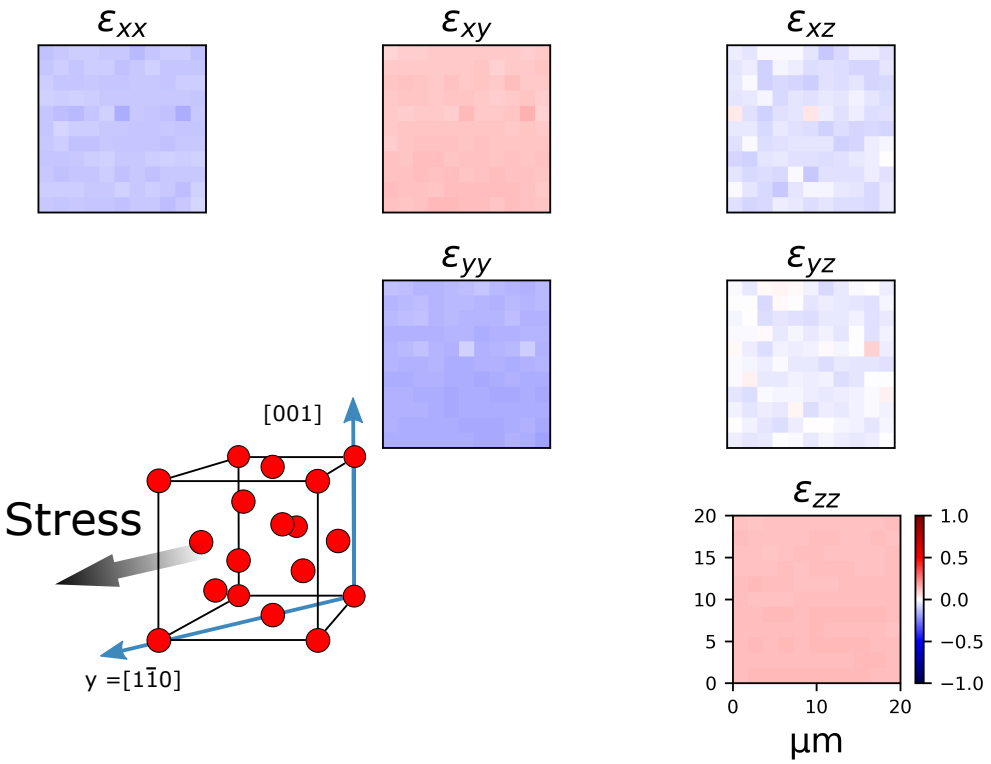


Figure 3.26: Initial strain tensor of a 100 nm thick sc-Si on a Furukawa tape under uniaxial loading along < 110 >. The strain tensor components are given in the [1 1 0], [$\bar{1}$, 1 0], [0 0 1] reference frame. The full strain tensor mapping is performed with µLaue on a $20 \times 20\,\mu m^2$ surface.

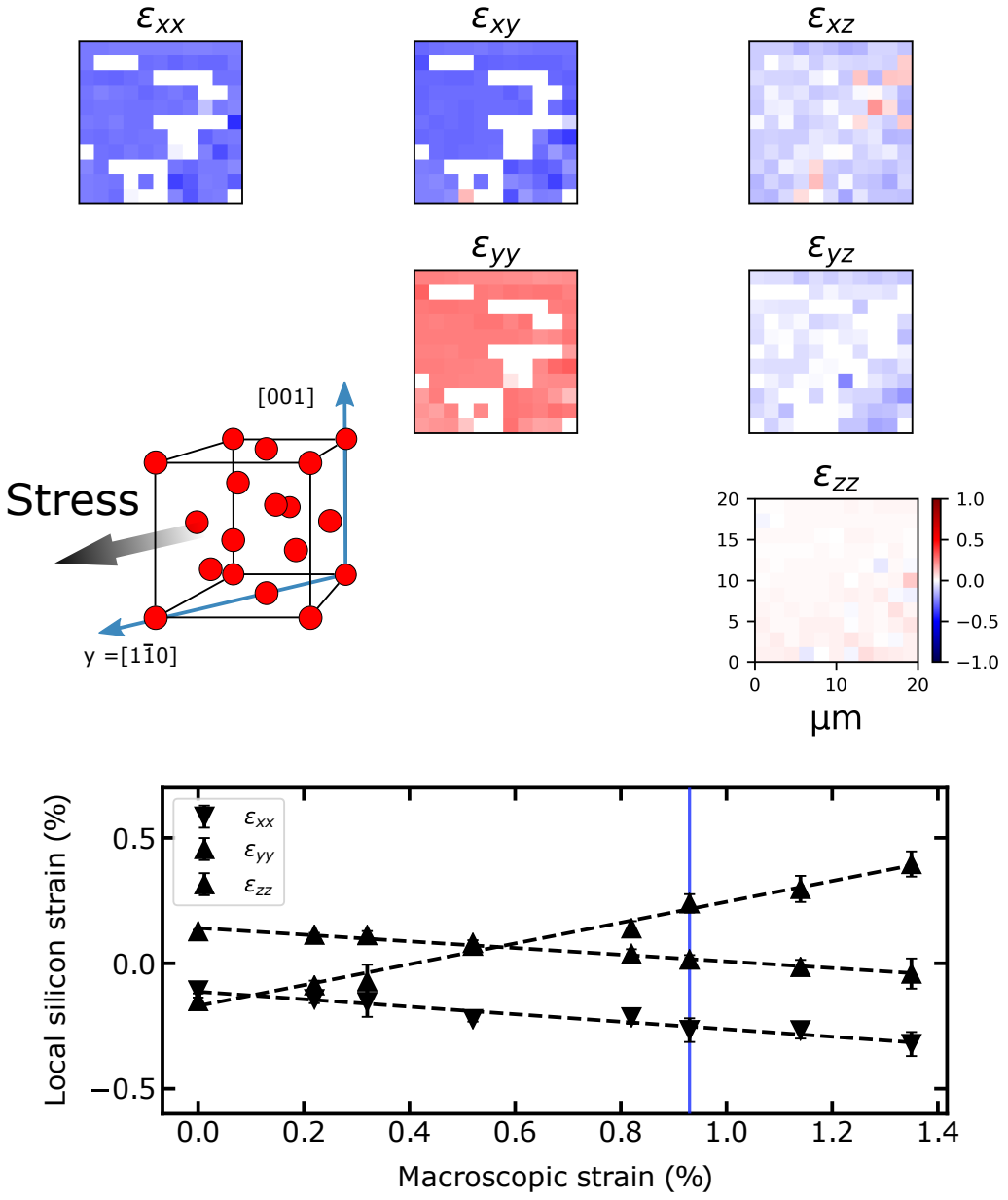


Figure 3.27: Strain tensor of a 100 nm thick sc-Si on a Furukawa tape under uniaxial loading along < 110 >. The strain tensor components are given in the [1 1 0], [$\bar{1}$, 1 0], [0 0 1] reference frame. The full strain tensor mapping is performed with µLaue on a $20 \times 20\,\mu m^2$ surface.

Crystal rotation can also be extracted from the indexation of Laue patterns. A straightforward and qualitative approach can be taken by superposing all the Laue pattern collected on the sample at a given strain. Figure 3.28(a) shows the evolution of selected, sample-averaged Bragg peaks with strain. All Laue diagram collected on the sample surface at a given loading step are superposed to observe the peak position distribution. For both 0 0 4 and 0 2 6 Bragg's peak, the initial distribution is isotropic (*i.e.* the peak distribution is similar in both x-axis and y-axis of the detector). Under strain application the distribution is getting narrower along the x-axis. This indicates a rotation of the sample around the stress direction as illustrated by simulation in figure 3.28(b). The experimental distribution width is 23 pixel and 66 pixels for the 0 0 4 and 0 2 6 reflection respectively, which corresponds to a rotation of $(0.6 \pm 0.1)°$ or a 190 mm curvature radius.

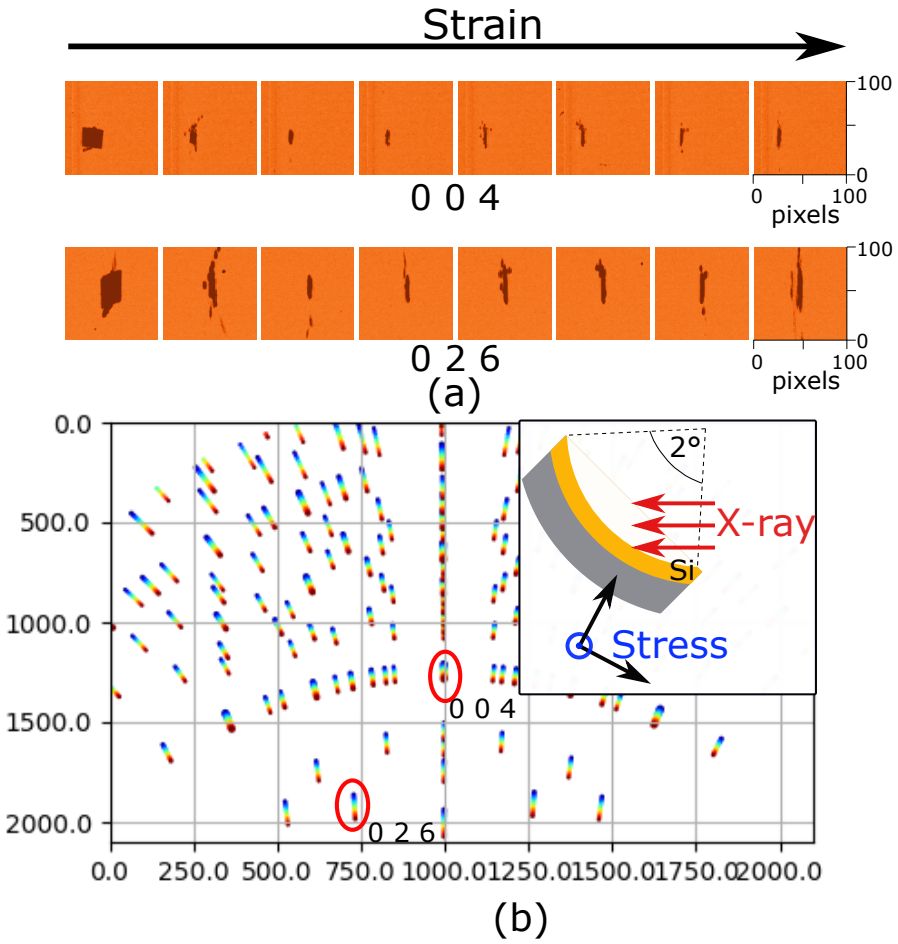


Figure 3.28: Effect of sample curvature on Laue diagram (a) Sum of Laue patterns probed on the whole sample surface for two different Bragg peak and strain level. (b) Simulation of Laue patterns of a silicon crystal being rotated of 2° around the [010] crystal axis

The previous results showed how a uniform uniaxial strain was applied on a thin sc-Si film using a tensile test apparatus. The combined use of µLaue and Raman spectroscopy allowed to validate the use of an adequate model for the later technique. An in depth discussion of the fabrication parameters effect on the mechanical behavior will be given later in this chapter.

#### 3.2.1.2 Bulge and biaxial tensile test

As for uniaxial tensile testing, the strain tensor and strain homogeneity for bulge and biaxial testing is first directly characterized using x-ray microdiffraction. This allows to validate the use of Raman spectroscopy with the corresponding assumption on the stress applied to the silicon crystal.

Figure 3.29 presents the diagonal of a 100 nm thick sc-Si as a function of the macroscopic strain applied in the center of the bulge test sample. The silicon film is encapsulated in between two Furukawa tape layers.

As presented earlier, the extra layer of Furukawa tape prevented beam damage to the sc-Si film during signal acquisition. The first point was obtained for 1 % biaxial macroscopic strain as the SOP sample needed to be taut and the height increase due to the polymer creeping needed to be low enough to perform a mapping without losing the focus on the sample surface. Diagonal components in the (001) plane were positive and increased with the macroscopic strain, while the component normal to the surface sample decreased down to -0.91% compressive strain for 6.5 % macroscopic strain. As the maximum in-plane diagonal components are 1.14 and 1.40 %, using Hooke's law with a 0.26 Poisson ratio for silicon [Hopcroft et al., 2010], the expected compressive strain normal to the sample surface would be -0.58 %. The origin of this difference can be the initial stress present in the sc-Si layer due to the fabrication process and lamination of the different Furukawa tape layers. Overall a biaxial strain larger than 1.1% was applied in the sc-Si film (001) plane thanks to the use of a bulge test stage. Above this point, the diffracted signal was too low, creeping of the polymer and cracks in the silicon layer prevented the test to be carried on.

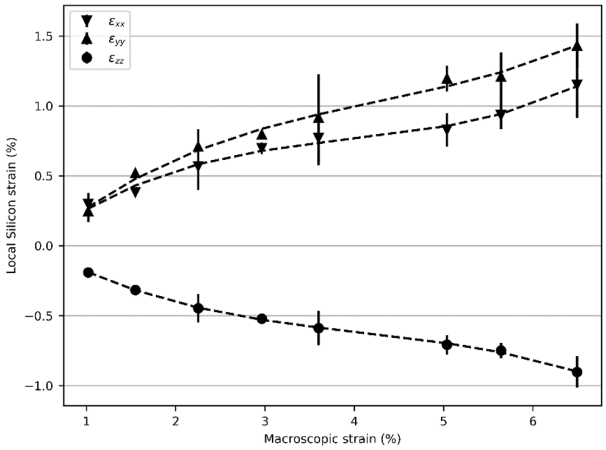


Figure 3.29: Diagonal strain component in the crystal reference frame of a 100 nm thick sc-Si film on Furukawa during a bulge test. Diameter of the disk is 30 mm. Each point is obtained from a $20 \times 20\,\mu m^2$ mapping of the surface with µLaue.

To assess the homogeneity of the strain and its biaxial character, maps of the ratio of the in plane diagonal components ($\varepsilon_{[100]}/\varepsilon_{[010]}$) are represented in figure 3.30, for different values of the mean biaxial strain (indicated in each panel). Accessing the full strain tensor with µLaue allows to quantify the biaxial character of the stress rather than making an assumption as it can be done for Raman spectroscopy or single lattice parameter measurement from a XRD rocking curve. A ratio close to one indicates a good match with a pure biaxial deformation. On the contrary, lower or higher ratio indicates a mechanical anisotropy, *i.e.* a non-equi-biaxial deformation, which can arise from sample geometry or polymer microstructure. At low macroscopic strain, there is a strong dispersion in the strain ratio. Then, with the increase in macroscopic strain, the ratio progressively got close to 1 and the strain homogeneity on the probed surface increased. The $\varepsilon_{[010]}$ component remained larger than $\varepsilon_{[100]}$, even at higher strain value, which is attributed to the uniaxial strain induced by the tape lamination. Mapping at higher strain value are not represented as the missing data point were to important due to loss of signal in certain area of the probed sample surface.

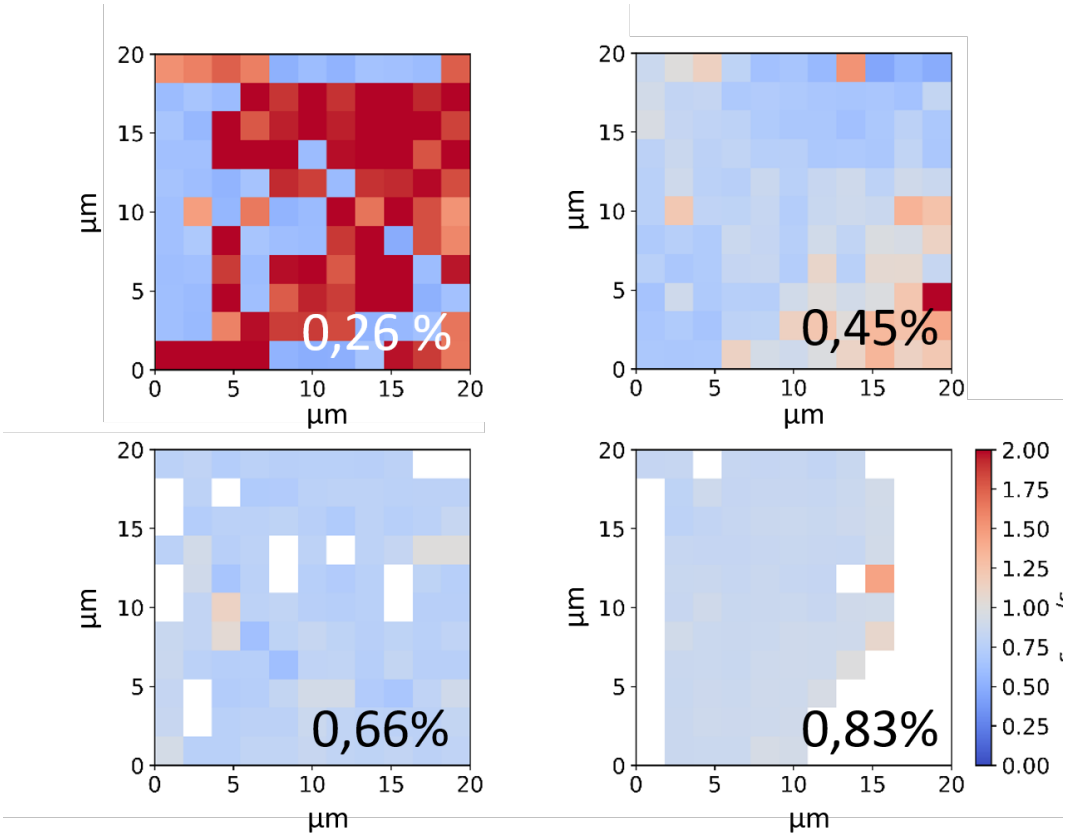


Figure 3.30: Mapping of $\varepsilon_{[100]}/\varepsilon_{[010]}$ in a 100 nm thick sc-Si under biaxial stress. Strain tensor components were obtained using µLaue during a bulge test. Each map corresponds to a macroscopic strain value of the bulge center calculated from the bulge height, indicated in the lower left of each panel.

Bulge test were also carried under a Raman spectrometer. A strain curve obtained for a 200 nm thick sc-Si on Furukawa is presented in figure 3.31. This test was performed on a silicon disk with a bulge stage of 20 mm internal diameter. Disk shaped patterns were more prone to cracking at lower macroscopic strain than ribbons shapes one, this prevented any significant increase in local silicon strain, even at higher pressure. As stated in chapter 2, the lithography technique used for pattern definition yields rough pattern edges. It might be even more problematic from curved patterns as opposed to ribbons oriented along specific crystal directions.

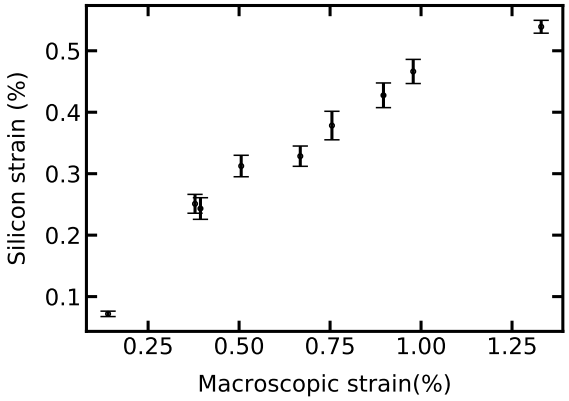


Figure 3.31: Biaxial strain in a 200 nm thick sc-Si film on Furukawa tape, measured by Raman spectroscopy during a bulge test. Bulge diameter is 20 mm. Each point is the mean value of 9 data points from a 40 µm × 40 µm surface

As mentioned earlier, biaxial loading was also tested using the biaxial tensile rig at DiffAbs beamline at SOLEIL, using simultaneous *in situ* DIC and XRD. Data processing of the combined measurement is still undergoing while this thesis is being written and an in-depth analysis of the whole data-set is not available. However preliminary results can be presented and still offer an interesting preview of the information that can be accessed thanks to the unique set-up and the results obtained in a stripe sample loaded biaxially are discussed hereafter. Figure 3.32 (a) shows an example of a zone analyzed with DIC. Strain component are extracted from both the whole observation area (substrate only and SOP) and the silicon covered zone on the right of the micrograph. Speckles of white paint used as optical marker are clearly visible on both areas. The curves presented in figure 3.32 are the in-plane strain components from different samples obtained with DIC. The strain curves presented in graph (b) were obtained for a step by step experiment while the curve (c) and (d) are issued from a continuous tensile tests. For the step by step measurement, a clear relaxation is observed during the measurement, similar to uniaxial tensile test performed on the micromecha stage. The biaxial strain of the silicon covered area is systematically lower than the whole sample strain. This highlights the importance of a local strain analysis of the substrate and the influence of the silicon thin film on the mechanical behavior of the whole SOP structure. Figure 3.32(d) shows a significant different between the in-plane strain components $\varepsilon_{11}$ and $\varepsilon_{22}$ for the silicon covered substrate, indicating a strong sample anistropy. Analysis of XRD data will allow one to determine the relation with local silicon strain and deviation from pure biaxial strain.

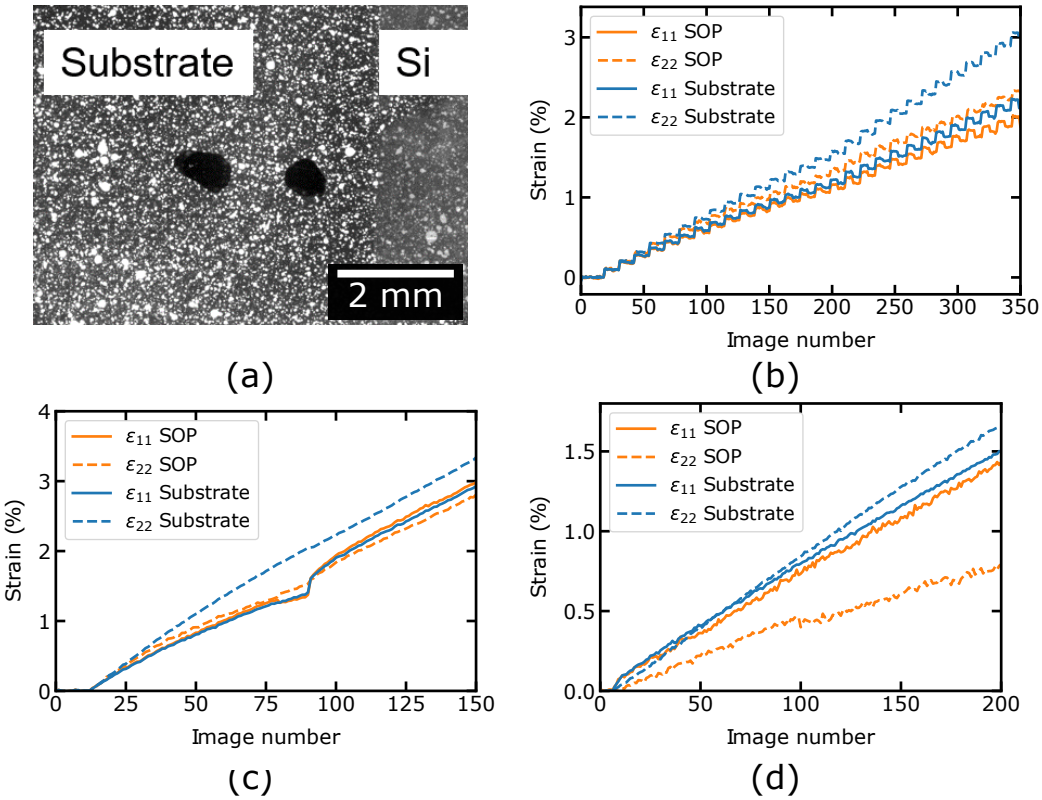


Figure 3.32: In plane strain components for SOP samples under biaxial stress obtained with DIC on different area of the samples: silicon free and silicon covered parts as illustrated in micrograph (a).For curve (b), the motor were stopped during x-ray acquisition while the tests presented in (c) and (d) are continuous.

XRD rocking curves were performed around the 0 0 4, 0 0 8 and 0 0 12 Bragg peaks of the sample subjected to a step by step biaxial loading. The angular space maps of the Bragg peaks are presented in figure 3.33 for selected loadings. With increasing strain, the peak position shifts to higher 2θ values, indicating a contraction of the silicon lattice in the direction normal to the sc-Si film surface. At higher strain, the Φ position and width of the peaks also changes. The lattice parameter $c$ of (001) plane can be calculated with Bragg's Law from the 2θ peak position. The corresponding strain is computed $\varepsilon_{33} = \frac{c}{c_0}$ with $c_0$ =5.431 020 Å the unstrained silicon lattice parameter. With the hypothesis of a pure biaxial strain and using generalized Hooke's law, the in-plane strain component $\varepsilon_{||}$ can be expressed by equation 3.15:

$$\varepsilon_{||} = \varepsilon_{11} = \varepsilon_{22} = -\frac{c_{11}\varepsilon_{33}}{2c_{12}} \tag{3.15}$$

Where $\varepsilon_{11}$, $\varepsilon_{22}$ and $\varepsilon_{33}$ are the diagonal strain tensor component in the crystal reference frame. $c_{11}$ = 165.5 GPa and $c_{12}$ = 63.9 GPa are silicon elastic constants [Hopcroft et al., 2010].

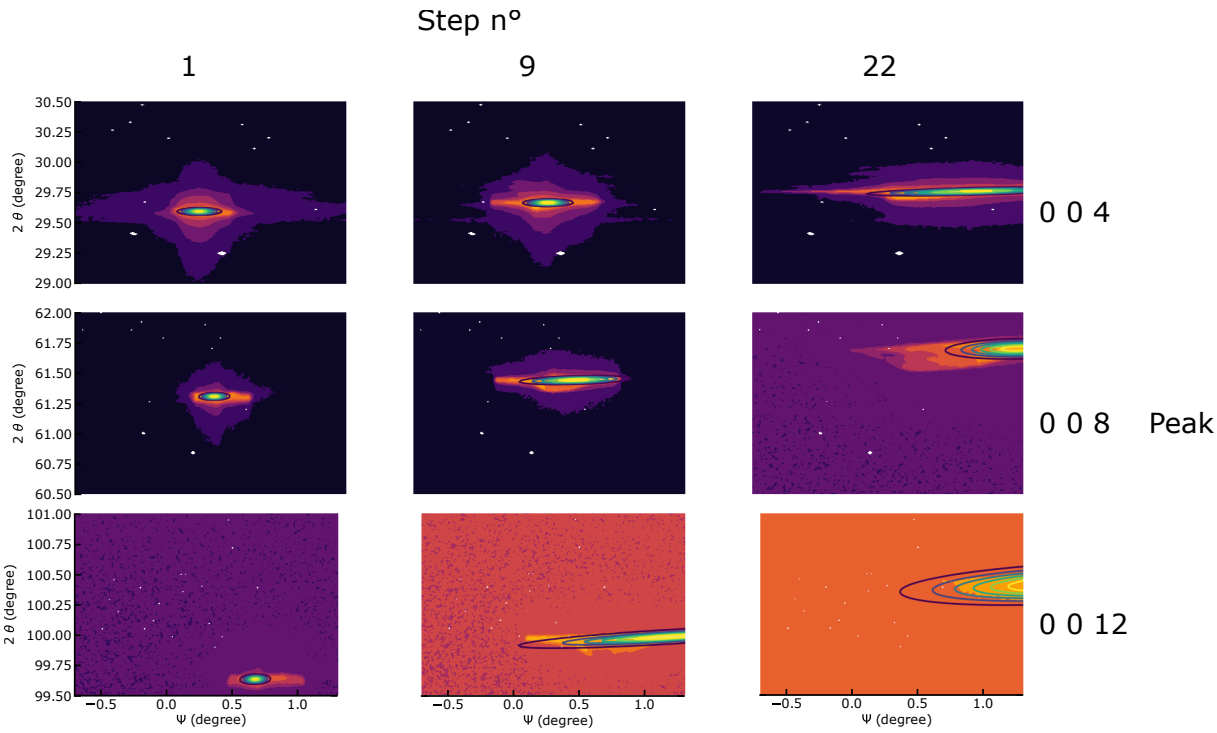


Figure 3.33: 0 0 4, 0 0 8 and 0 0 12 Bragg's peak for a 205 nm thick sc-Si film under biaxial stress. The external biaxial stress applied on the sample is increased between each step. Contour of the 2D gaussian functions used to fit the peak position of morphology are also represented.

Figure 3.34 presents the combined DIC and XRD results obtained for the different loading steps of the sample. DIC value are averaged over the XRD measurement time range. Even for the local information obtained on the silicon covered area, the local silicon strain is significantly lower than the substrate strain. Below the 23rd loading step, the strain extracted from the three different Bragg peaks is similar. Above this point some outlier values are present in the strain extracted from 0 0 8 and 0 0 12 reflection. This stems in the peak broadening observed in figure 3.33. Also the slope of the microscopic substrate strain is increasing above this point whereas the one of the silicon crystal strain is decreasing. These observations indicates possible fracture of the silicon film and the presence of several crystallites.

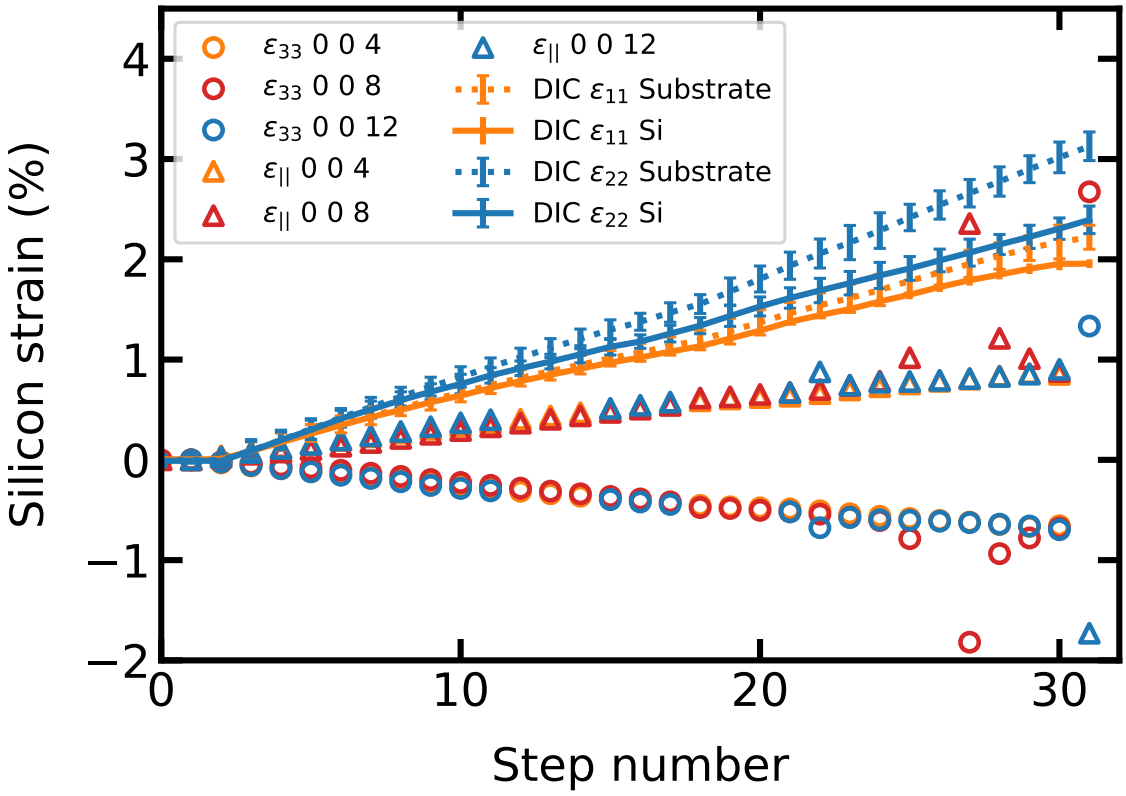


Figure 3.34: Strain as a function of loading step number in a biaxial test performed on a 205 nm tick sc-Si on Furukawa. For silicon films $\varepsilon_{33}$ was obtained by measurement of 0 0 4, 0 0 8 and 0 0 12 Bragg peak position. $\varepsilon_{11}$ was computed using Hooke's law. Strain derived from DIC measurement are also represented, both for whole sample and silicon covered surface.

Proper calibration of the detector angular position has not been implemented yet in the data analysis routine and silicon strain value presented in figure 3.34 are relative to the initial state. To illustrate the difference of mechanical behavior between the different parts of the sample, in-plane biaxial silicon strain was plotted against the mean biaxial strain measurement in the substrate with DIC. Figure 3.35 shows the clear difference in strain ratio for the whole sample surface and the silicon covered surface. Still, the ratio for the silicon covered substrate is lower than $\frac{1}{2}$ which is even lower to the value obtained with total macroscopic sample strain during uniaxial testing. Cracks were presents in this sample surface although it still does not exclude the existence of slipping at the polymer/silicon interface or delimitation in the early stage of tensile testing. Further analysis of other samples results will tell if this is a recurring observation. Measurements of in-plane (*e.g* 2 2 0) and asymmetric (*e.g.* 1 1 3) Bragg peaks were also performed and might give a better understanding of the local mechanical coupling between the polymer substrate and the sc-Si film during biaxial tensile testing. This example shows how the biaxial tensile test set-up at DiffAbs beamline allows strain probing at different scales for crystalline materials on polymer substrates.

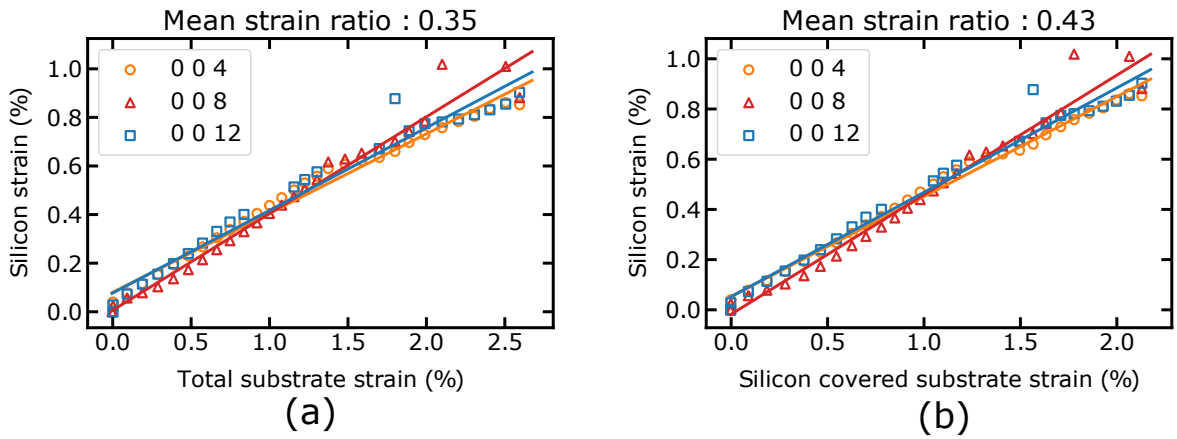


Figure 3.35: Local silicon strain as a function of macroscopic strain measurement with DIC. (a) For the silicon covered area (b) For the whole probed surface

### 3.2.2 Influence of crystal orientation on uniaxial tensile tests

In the case of uniaxial tests, two different ribbon sample orientations were studied. Figure 3.36 presents the overlay of strain curves for two similar SOP samples with different ribbons crystalline orientations: [100] and [110]. They were both transferred from the same wafer. The [100] oriented sample presents a linear strain ratio until the sc-Si fracture and delamination (above 3% macroscopic strain) whereas the strain ratio of the [110] oriented sample decreased progressively with the increase of the macroscopic strain applied to the sample. This is a consequence of the cracks orientation in the sc-Si. There are always oriented along a [110] direction. This implies that for [110] oriented sample, the cracks are perpendicular to the applied stress and cracks free zone continue to be strained. A post-mortem micrograph of a [110] oriented sample can be observed in figure 3.37(a). For [100] oriented samples the cracks appear later but the 45° angle with respect to the ribbon sidewall implies a dramatic fracture mode where all the cracks appear simultaneously. As seen in figure 3.36, after the apparition of cracks (figure 3.37(b)), the local silicon strain drops instantly to its initial value and can not be increased by further external mechanical loading.

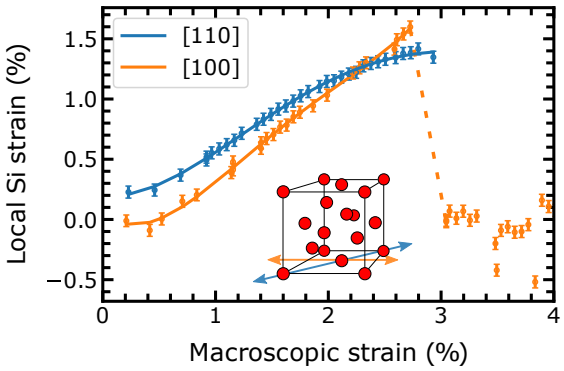


Figure 3.36: Tensile curves for 100 nm thick silicon on Furukawa tape sample for two different ribbon orientations. Strain is derived from Raman spectroscopy acquisition during a continuous tensile test.

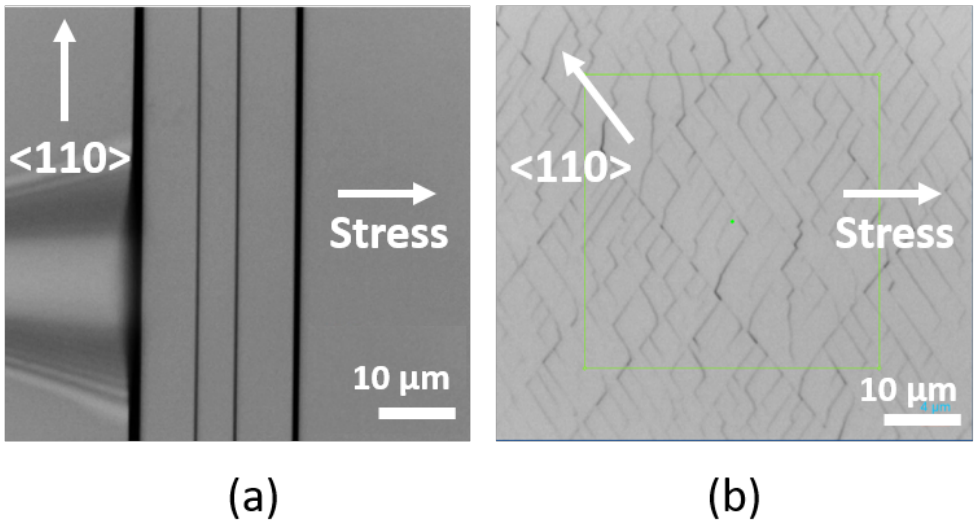


Figure 3.37: Micrographs of SOP samples surface after fracture during a uniaxial tensile test. (a) [110] oriented ribbon (b) [100] oriented ribbon

To assess the coupling between sc-Si films and polymers substrate, a strain ratio can be extracted from continuous Raman acquisition during uniaxial tensile tests. The strain ratio is defined as $\varepsilon_{Si}/\varepsilon_{macro}$ where $\varepsilon_{Si}$ is the local silicon strain obtained with Raman spectroscopy and $\varepsilon_{macro}$ is the sample macroscopic strain. A ratio of 1 would indicates a sample fully covered by crack free sc-Si film while a lower ratio indicates presence of crack or silicon free zone of the extremities. Figure 3.38 present the results obtained for 20, 100 and 200 nm sc-Si thick uniaxial tensile test sample in two orientations ([100] and [110]). There is a strong dispersion in measurements values (*i.e.*, between 0.5 and 0.95). This is caused by the brittle behavior of silicon, especially for [110] oriented samples were fractures can appear for low strain values during a tensile stress. The dispersion is smaller for [100] oriented samples as the sc-Si is crack-free during the initial linear part of the tensile curve. No significant trends can be linked to the silicon thickness. However the ratio is significantly higher for [100] oriented ribbon at 100 and 200 nm thicknesses. Silicon Young modulus is lower in this direction, lowering the elastic energy needed for a given strain ($E_{[100]}$ = 130 GPa, $E_{[110]}$= 169 GPa.)

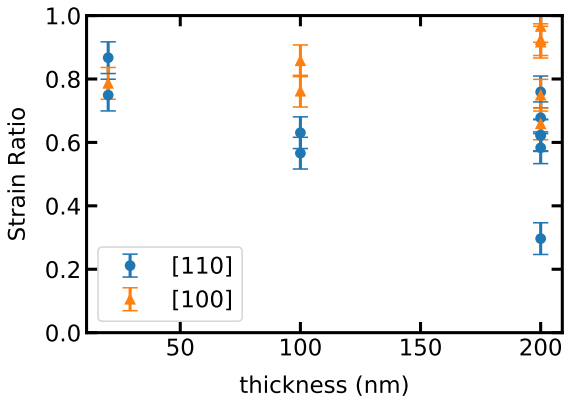


Figure 3.38: Initial ratio between the local silicon strain and the macroscopic strain.

Another metric extracted from the tensile test curve was the elasticity modulus of the SOP structure. It is based solely on the data from the Proxima tensile stage and is extracted from the initial linear part of the tensile curve. The results presented in figure 3.39 showed that the influence of a sc-Si thin film is not negligible in the structure mechanical response. The [110] oriented samples have a linear relation between the silicon thickness and the elastic modulus of the structure. For [100] samples there is a strong dispersion for 205 nm thick sample but the effect is still visible at lower thicknesses. It illustrates that even the low thickness sc-Si film influence on the hetero-structure mechanical response is not negligible. By extrapolating the Young modulus for a silicon free substrate, one can obtain a value of 40 MPa which is significantly lower than the value previously stated for the substrate (70 MPa). This is due to the viscous mechanical response of the substrate, a slower displacement speed will result in a lower rigidity.

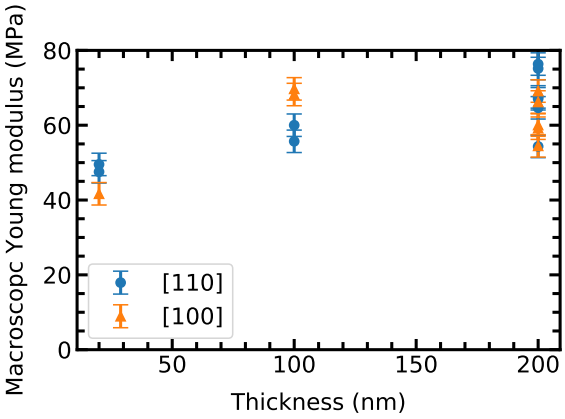


Figure 3.39: SOP Young's modulus for different sc-Si thickness and ribbon orientation. The substrate is a 230 µm thick Furukawa tape and data were obtained from continuous tensile test at 2 µm /s displacement speed.

### 3.2.3 Elastic behavior

All the results in this chapter are obtained using the assumption that the strain is purely elastic. This stems from the fact that the strain measurement methods used here are only sensitive to the elastic strain of crystalline silicon. The model used for Raman is a first order development of a solution to the secular equation presented in annex A.1. For example, in Germanium, a non-linearity was observed for the stress/Raman peak shift at higher strain value (*i.e.* over 1%) [Gassenq et al., 2017]. The strain measured by µLaue is purely elastic. It is derived from the Bragg's peak fit and indexation in the Laue pattern, furthermore only the deviatoric part of the strain tensor is experimentally measured here. Observation of plasticity in silicon is often associated with the apparition of amorphous phase [Zhang and Zarudi, 2001] or in high temperature conditions [Gallagher, 1952]. In a single crystal nanostructure, even at high strain (> 10%), pure elastic deformation were observed until the brittle fracture of the silicon [Zhang et al., 2016]. A first clue of induced plasticity in the case of the tensile test performed here is the strain after unloading. A [110] oriented SOP sample with a 20 nm thick silicon layer was strained up to 1.3 % and then dismounted and left to relax for 12 h. As visible in figure 3.40, the strain fully relaxed is even smaller than the initial measurement performed after tensioning on the tensile stage. All three FWHM are similar given the margin of error for the fit at low signal extracted from a sc-Si thinner than 20 nm. It indicates that no major modification of the crystal structure was induced by the applied stress.

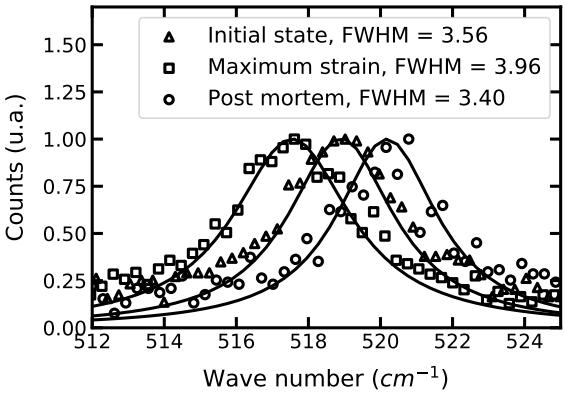


Figure 3.40: Raman spectrum for different loading step of a [110] oriented 20 nm silicon film on polymer. Initial measurement was made after the mounting and minimal tensioning if the sample on a tensile stage. Maximum strain corresponds to the highest red-shift observed during a uniaxial tensile test. Post mortem spectrum was collected 12 h after dismounting the sample from the tensile stage.

On the other hand, the evolution of Raman response was also evaluated for a [100] oriented sample brought to total failure at high strain value. Raman spectrums of a 205 nm thick [100] oriented sample are represented in figure 3.41. A first spectrum is collected during the initial tensioning phase of the tensile test, the external force applied on the sc-Si film is negligible here. The initial shift from a bulk reference sample is only due to process-induced strain. A second spectrum is collected at the maximum local strain in the sc-Si film, the significant peak shift can be observed ($7\,cm^{-1}$, corresponding to a strain of 3.1 % in the case of a pure uniaxial tensile deformation along the sample long axis. The peak FWHM remained unchanged and comparable to the bulk reference value ($3.5\,cm^{-1}$) [Richter et al., 1981]. A last spectrum is collected after the fracture of the sc-Si thin film. As presented earlier in figure 3.37, for a uniaxial sample oriented along a < 100 > direction the cracks are present on the whole sample surface with a characteristic length of 2 µm. After the rupture of the sc-Si thin film, the position of the silicon Raman peak is back to its initial position, indicating a relaxation of a pure elastic strain possibly due to a delamination from the substrate. The peak FWHM increased after fracture. Such increase have been linked to size effect in thin film [Poborchii et al., 2015] and cristallite size [Fauchet and Campbell, 1988]. Here the peak broadening may stem from the laser beam size being similar to the post fracture silicon flakes dimension. The signal is coming from different crystallites presenting inhomogeneous strain levels. Furthermore, such a peak broadening was not observed in [100] oriented samples where the characteristic length of crack-free silicon surface is much higher than the laser beam size.

Thus, these results confirm the hypothesis that the strain induced in the sc-Si film was purely elastic and that crystalline quality remained intact during tensile tests.

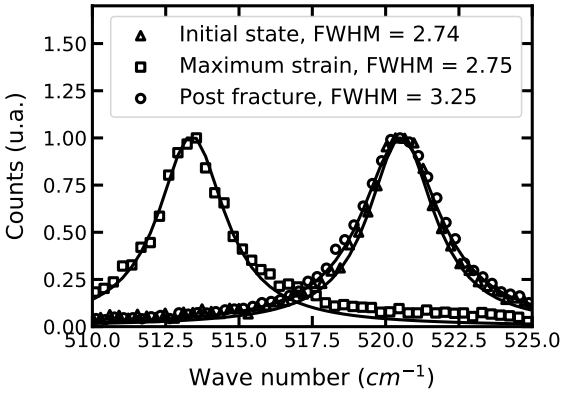


Figure 3.41: Raman peak during a tensile test performed on a 205 nm thick, [100] oriented sample. The initial spectrum is represented along with the one corresponding to the highest strain value and a one after the complete fracture of the sample surface. Black lines represent the lorentzian curve used to fit the experimental data points and extract the data of interest (peak position and FWHM)

### 3.2.4 Defects

While µLaue is a diffraction technique, based on the crystalline nature of silicon and thus sensible to pure elastic strain, it can be used to look for markers of plastic deformation. A good indicator is the morphology of Laue diffraction spots. For a perfect crystal on an ideal diffraction setup, a diffraction peak would be represented by a Dirac function. For a real finite sample on a real setup, the diffraction peak has a certain width depending on the crystal dimension, orientation, crystallinity, defects and experimental parameters (*e.g.*, beam-size, optics. [Ungár, 2004]).

In particular, peak width broadening can be caused by the presence of dislocations. In this case, only peaks on certain zone axis are affected. To quantify the evolution of the diffraction peak morphology, a

continuous µLaue measurement was performed on a sample under tensile test. The sc-Si film was 100 nm thick. The elongation speed was 0.1 µm/s and the full width of the sample was scanned in 22 points separated by 100 µm with a 1 s acquisition time per point. Total acquisition time for a line was 49 s corresponding to a total displacement of 4.9 µm. Given the x-ray beam-size (500 nm × 500 nm), this meant that even in the sample center, the scanned surface is not the same in-between transverse scans. The evolution of the strain tensor diagonal components is presented is figure 3.42 with a schematic of the experiment. The decrease in uniaxial tensile strain observed above 2 % of macroscopic strain is due to the presence of a crack perpendicular to the displacement direction (y). As stated above, the scanned area is moving compared to the X-ray beam position along the x axis. Indeed around 3 % macroscopic strain, no signal can be retrieved as the crack is under the beam.

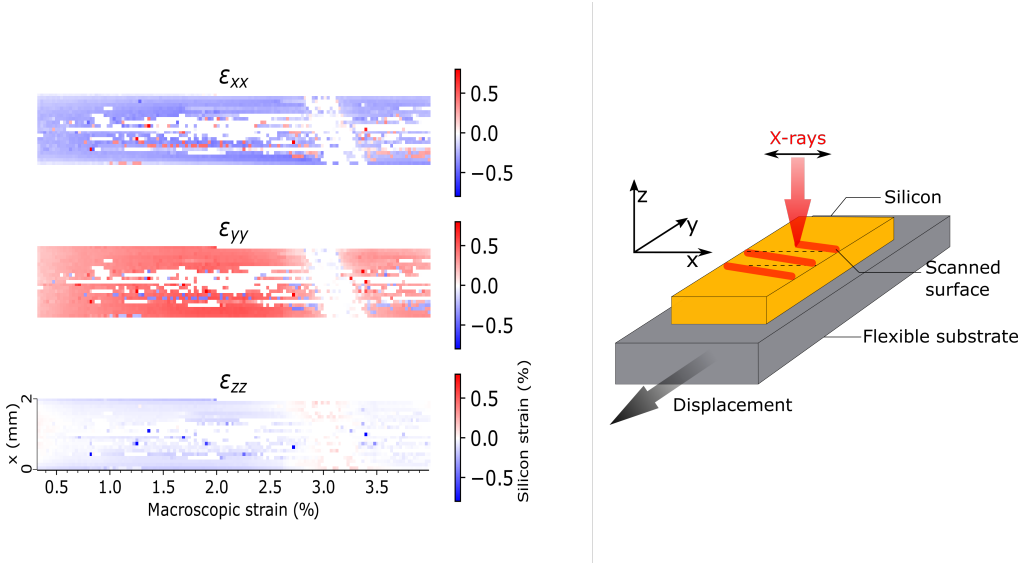


Figure 3.42: Mapping of the diagonal strain component of a 100 nm thick sc-Si film on a Furukawa substrate. The reference frame is [-110] [110][001] and the stress is applied along [110]

To understand the signal loss, a direct observation of the Bragg peak evolution is necessary. Figure 3.43 presents three different peaks obtained from distinctive area of the sample width. As seen in figure 3.42, signal coming from the central part of the sample is lost due to extreme broadening of the peaks or a displacement of the peak outside of the analyzed region of interest. Peak broadening is the more plausible scenario as the peaks gradually disappear. This is caused by important local curvature, the diffracted signal becomes too low to be distinguished from the background noise as the initial signal is already low due to short acquisition time and low silicon thickness. For both upper and lower areas, the signal is almost always exploitable but peak broadening can still be observed. A complete absence of diffracted signal is confirmed at 3% macroscopic strain. Peak elongation and displacement is similar for the three different Bragg's reflections here.

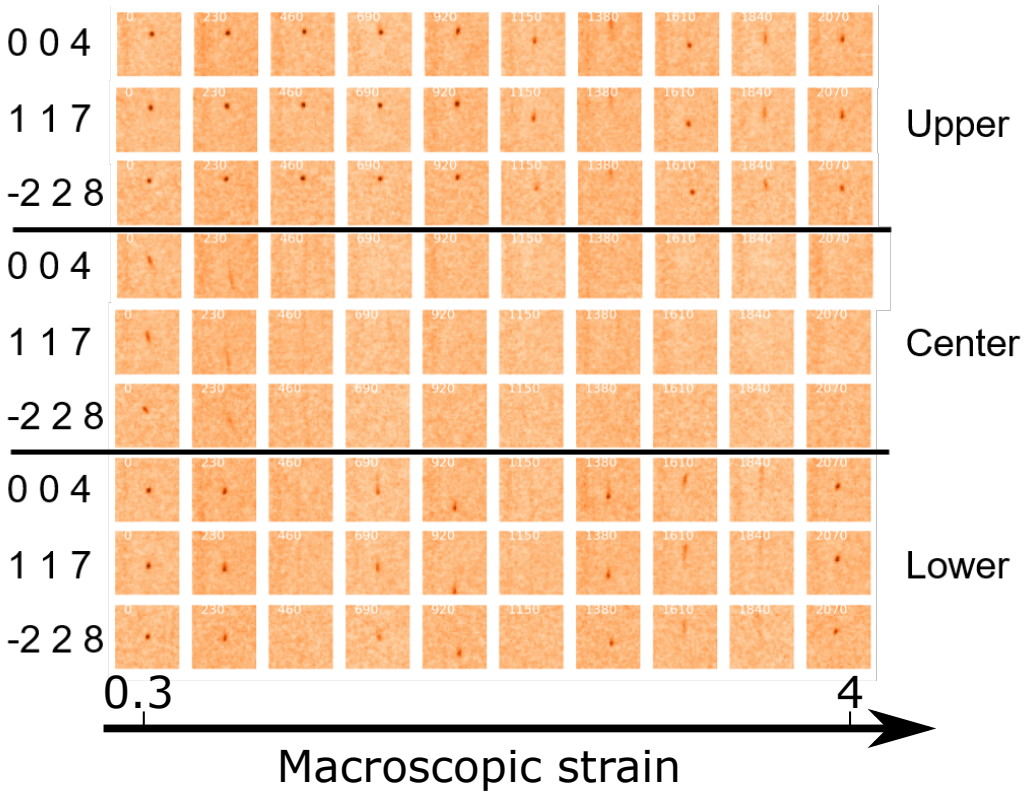


Figure 3.43: Bragg peak morphology evolution for different orientation during a uniaxial tensile test performed on a 100 nm thick sc-Si film on a Furukawa substrate.

Diffraction peaks morphology evolution can be quantified using the width of the 2D Gaussian function used to fit their position. The peaks' FWHM is plotted along with the mean uniaxial silicon strain as a function of macroscopic strain in figure 3.44. During the increase to maximum strain, no general tendencies can be observed as the FWHM oscillate around a constant value. Close to the silicon fracture, a similar increase is observed for the three analyzed peaks, indicating an increase in local curvature.

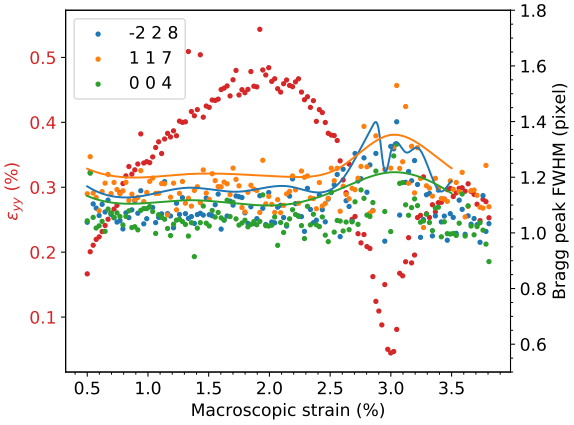


Figure 3.44: Silicon strain along a < 110 > direction and different Bragg's peak FWHM as a function of whole sample macroscopic during a continuous uniaxial tensile testing.

Finally the three Euler angles can be extracted from the indexed Laue pattern. Figure 3.45 present the evolution of the three angle as a function of macroscopic strain for the whole sample surface. As represented in the schematic, the angles are given with reference to the laboratory reference frame. Absolute values are not essential but it can be noted that angle θ defining the tilt between the two normal is dispersed around 40°. This value is expected as it corresponds to the inclination of the tensile stage. The data is rather

noisy due to low SNR but the curvature of the sample along the stress direction can be observed in the Φ mapping. The distribution around 45° is consistent with the [110] crystal direction being aligned with the tensile stress orientation. Another rotation is visible in the Ψ values near the crack, indicating an important local curvature caused by delamination.

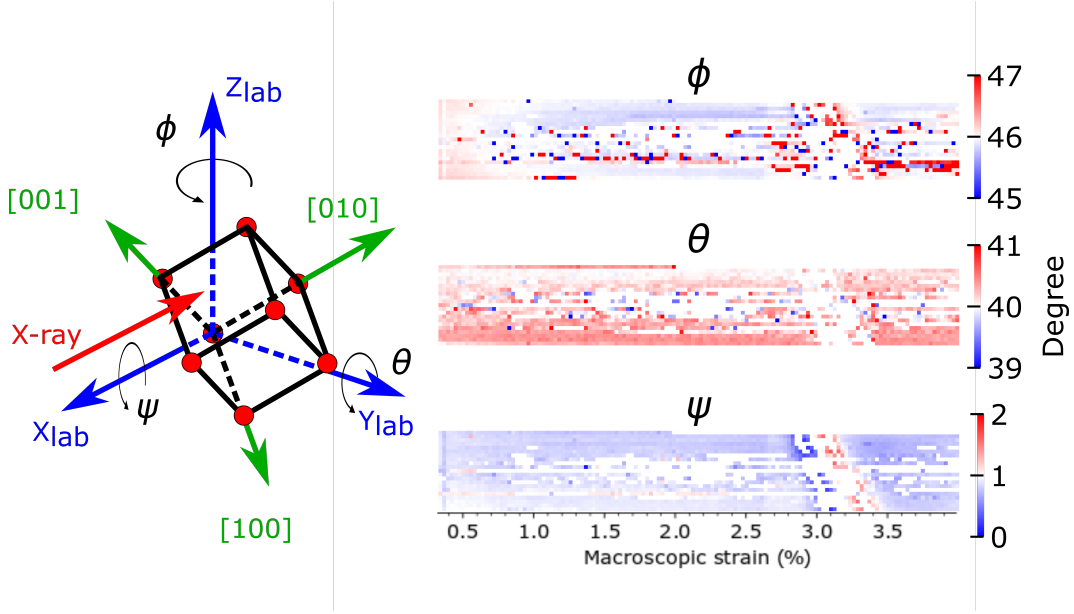


Figure 3.45: Linear scanning of Euler angles during a continuous tensile test as a function of macroscopic strain sample. The angles are given relatively to the laboratory reference frame as shown in the schematic. The stress is applied along the [110] direction.

## 3.3 Approaching the strain limit

### 3.3.1 Film thickness

As presented in chapter 2, several methods to transfer films thinner that 200 nm were studied (wet etching before the sc-Si film transfer or dry etching after). The goal was to decrease the elastic energy needed in the system to reach a given strain value. In a pure elastic deformation, the energy density needed to reach a certain strain is given by equation 3.16.

$$w_{el} = \frac{1}{2} E \varepsilon^2 \tag{3.16}$$

Where $w_{el}$ is the elastic energy density, E the Young modulus and ε the strain. The total energy is also proportional to the volume, and thus varies linearly with the silicon thickness for given sample dimensions. Furthermore size effects can be observed in micro and nano object (*e.g.*, increase in Young modulus or maximum strength). These effects are observed in metallic materials [Jang et al., 2011] as well as in silicon [Soler et al., 2014; Namazu et al., 2000]. To test this approach, tensile tests were performed on samples which were dry etched after transfer on BSI to lower the silicon thickness and then transferred on Furukawa tape using a mechanical separation between the glue and the sc-Si. The maximum strain obtained as a function of silicon film thickness and crystal orientation is reported in figure 3.46. As opposed to what could be expected, the maximum strain achieved in sc-Si thinner than 200 nm was lower than the maximum strain in the initial 205 nm thick films. 20 and 100 nm thick samples gave similar results. Thus, the additional plasma etching step that was used to achieve silicon thickness below 200 nm might have contributed to decrease the maximum strain achievable. Pétri et al. showed that such a process was linked to an increase in silicon surface roughness.

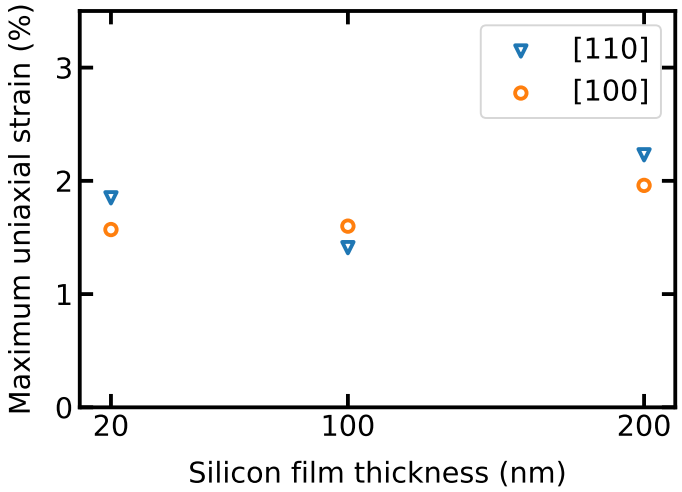


Figure 3.46: Maximum uniaxial tensile strain reported for different silicon thickness and crystal orientations. All patterns were defined using the same chromium mask and strain collected using Raman spectroscopy during a continuous tensile test.

### 3.3.2 Edge definition

As presented in the chapter 2, efforts were made to transfer silicon patterns with the smoothest sidewalls possible. Indeed, mechanical tests performed on pattern defined with a soft mask showed that edge roughness could be a point of fracture initiation. Even before cracks formation, some delaminated film can be observed near the pattern edges (figure 3.47(a,b). Figure 3.47(c) shows the same sample after external stress application and crack apparition. The crack is oriented along a [110] direction, perpendicularly to the stress direction, and appeared on a local maximum of the pattern edge curvature. Using a standard 1X chromium/glass lithography mask, edge roughness could not be observed with an optical microscope. Crack morphology remained similar compared to patterns produced using soft mask.

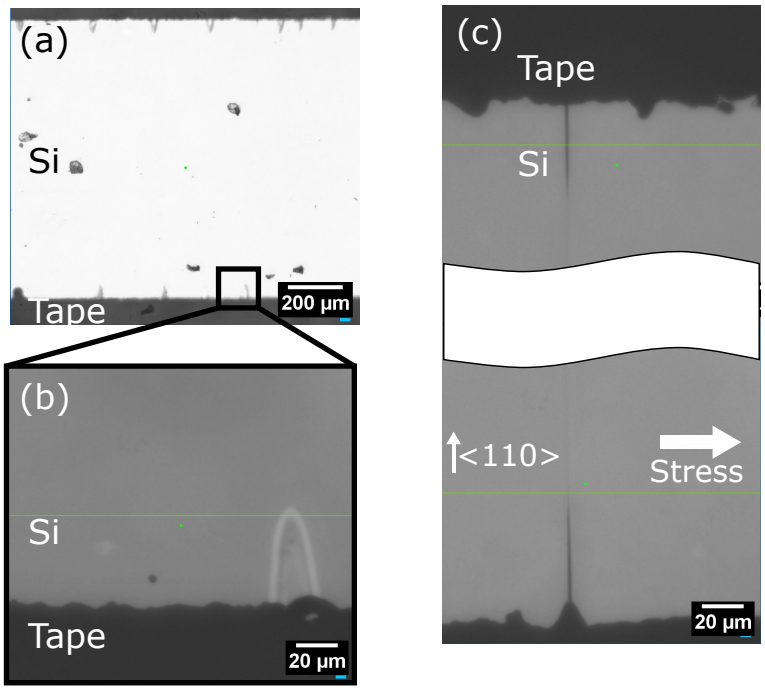


Figure 3.47: (a) Micrograph of the full width sample prior to crack apparition (b) Detail of a delamination present of the pattern edge. (c) Cracks formed on a 200 nm thick sc-Si thin during a uniaxial tensile test. The pattern was transferred using a soft lithography mask.

Figure 3.48 present strain curves displaying the maximum strain obtained for different sample fabrication methods. A first observation is that, as expected, the use of a 1X chromium mask increased the achievable maximum strain for both samples orientation. The apparition of cracks was delayed as the pattern edges were considerably smoother. Cracks morphology remained unchanged for the different lithography process (*i.e.*, [110] oriented). The anisotropic TMAH etching allowed improving significantly the maximum strain achievable in [100] oriented samples: from 1.96 % to 3.07 %. As shown in chapter 2, (100) planes were revealed on the pattern sidewalls and allowed to delay the apparition of cracks (figure 2.31). For [110] oriented ribbons, SEM observations showed that a bevel composed of two (111) plane was formed on the patterns edges (2.32). A decrease in maximum strain was observed for [110] oriented TMAH etched ribbons, indicating that a stress concentration at the edges bevel favored the crack formations at lower macroscopic strain level. On graph 3.48 (b), discontinuity are present in the strain curve of the TMAH etched sample at higher strain value. They are due to loss of surface focus. With such important displacement, the initial auto-focus range was not large enough to compensate for surface height changes. Clamp movement was temporary halted to re-focus on the surface, causing the substrate to relax. Macroscopic strain offset are also present in between the tensile curves. They arise from the difficulties to determine the relaxed state of the flexible polymer substrate. The displacement needed to achieve a taut sample is dependent on sample curvature and manual clamping. Curve slope and local silicon strain remain comparable in between experiments. Offsets in initial silicon strain are due to process parameters as exposed in chapter 2. A significant offset difference is observed between the sample produced with chromium mask only and with a chromium mask and TMAH chemical smoothing.

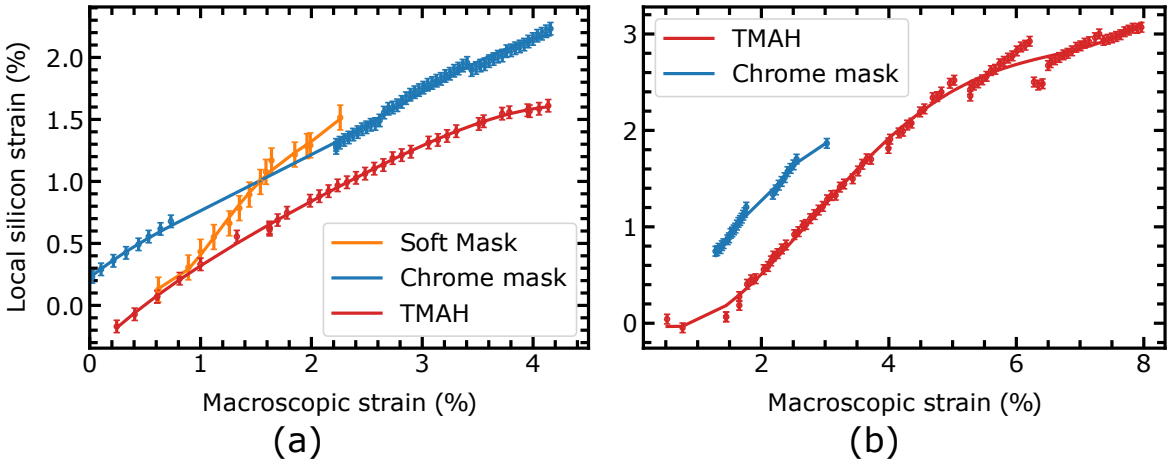


Figure 3.48: Comparison of tensile curves for 200 nm thick samples produced with different mask. Soft mask, chromium mask and anisotropic chemical smoothing(see section 2.1.3.4). (a) [110] oriented ribbons (b) [100] oriented ribbons. Lose of focus caused the absence of data point in certain parts of the curves. Local discontinuity are due to a pause in the tensile test to refocus the microscope on the sample surface.

## 3.4 Conclusion

This chapter was dedicated to the study of the mechanical behavior of SOP material. Suitable means of characterization were used and developed to probe the local silicon strain: µLaue, Raman spectroscopy and XRD. A detailed description of the data acquisition strategy and processing was given in order to deal with the nature of the composite material studied here. All these developments allowed for a study of a wide range of parameters of the mechanical behavior of SOP under tensile stress.

Coupling of macroscopic and microscopic strain measurement techniques of substrate and silicon strain highlighted the slower increase of silicon strain relatively to substrate strain. No slipping was directly observed, implying that only silicon free substrate area at the origin of this phenomenon. Combined DIC and XRD datas are still being processed to provide a microscopic information on this phenomenon. Once cracks appeared in the silicon film, part of the silicon strain were relaxed but further increase of the applied stress could lead to local increase of strain. The cracks are always oriented along <110> directions which implied that fractures modes varies depending the orientation of the sample and the applied stress.

In order to improve the maximum uniaxial strain in the silicon layer transferred on polymer, several parameters were studied. Decreasing the sc-Si film thickness from 205 nm to 100 or 20 nm did not improve maximum strain, possibly due to the surface roughening due to the sample thinning. Decreasing silicon surface can be a more efficient method to lower the elastic energy needed to strain the structure. The fabrication of a new lithography mask is required to evaluate this approach. Uniaxial sample orientation does not have a significant influence on the maximum strain despite the different behavior during the tensile test and the earlier apparition of fractures for [110] oriented patterns. The edge roughness of tensile test patterns has a strong impact on the ultimate silicon film strength. Stress concentration on the pattern edges led to the apparition of fracture, using a lithography mask with lower CD and a chemical smoothing process led to some unprecedented results (3.1 % of uniaxial strain along a <100> direction).

These improvements of the transfer process in order to reach higher strain were possible thanks to the validation of a reliable and reproducible Raman test bench for SOP material. X-rays based techniques allowed for a finer understanding of the mechanism at the microscopic scale and confirmed the validity of hypothesis made for Raman measurements. Local rotation of the crystal were observed near cracks as well as local curvature of the film due to the high aspect ratio substrate. No clear sign of plastic deformation were observed during the tensile test.

Table 3.2 gives the maximum strain and stress reached in a sc-Si film for different thickness, crystal

orientation, type of stress and lithography method. All these results were obtained on a flexible polymer substrate. The next step for the fabrication of a permanently strained silicon film is the transfer under tension from a flexible substrate to a rigid one.

| Type of stress | sc-Si thickness (nm) | Lithography process | Maximum strain (%) | Maximum stress (GPa) |
|---|---|---|---|---|
| Uniaxial [110] | 205 | Soft mask | 1.5 | 2.5 |
| | 205 | chromium/glass mask | 2.2 | 3.8 |
| | 205 | chromium/glass with chemical smoothing | 1.6 | 2.7 |
| | 100 | chromium/glass mask | 1.4 | 2.4 |
| | 20 | chromium/glass mask | 1.8 | 3.1 |
| Uniaxial [100] | 205 | chromium/glass mask | 2.0 | 2.5 |
| | 205 | chromium/glass with chemical smoothing | 3.1 | 4 |
| | 100 | chromium/glass mask | 1.8 | 2.3 |
| | 20 | chromium/glass mask | 1.7 | 2.2 |
| Biaxial | 200 | chromium/glass mask | 1.0 | 1.8 |
| | 100 | chromium/glass mask | 1.1 | 2.0 |

Table 3.2: Summary of the maximum stress and strain achieved in sc-Si film during tensile tests on SOP samples. Uniaxial tensile test results were obtained using Raman spectroscopy, biaxial results were extracted from μLaue measurement and XRD scans.

## References

Anderson, P. M., Hirth, J. P. and Lothe, J. [2017]. *Theory of Dislocations*, Cambridge University Press. Google-Books-ID: LK7DDQAAQBAJ. 96

ASTM International [2013]. ASTM E8 / E8M-13 Test Methods for Tension Testing of Metallic Materials, *Technical report*, ASTM International.
**URL:** *http://www.astm.org/cgi-bin/resolver.cgi?E8E8M-13* 94

ASTM International [2018]. ASTM C1273 - 18 Standard Test Method for Tensile Strength of Monolithic Advanced Ceramics at Ambient Temperatures, *Technical report*, ASTM International.
**URL:** *http://www.astm.org/cgi-bin/resolver.cgi?C1273-18* 94

Besnard, G., Hild, F. and Roux, S. [2006]. "Finite-Element" Displacement Fields Analysis from Digital Images: Application to Portevin–Le Châtelier Bands, *Exp Mech* **46**(6): 789–803.
**URL:** *https://doi.org/10.1007/s11340-006-9824-8* 102

Djaziri, S., Renault, P.-O., Hild, F., Le Bourhis, E., Goudeau, P., Thiaudière, D. and Faurie, D. [2011]. Combined synchrotron X-ray and image-correlation analyses of biaxially deformed W/Cu nanocomposite thin films on Kapton, *J Appl Crystallogr* **44**(5): 1071–1079.
**URL:** *http://scripts.iucr.org/cgi-bin/paper?S0021889811030226* 111

Fauchet, P. M. and Campbell, I. H. [1988]. Raman spectroscopy of low-dimensional semiconductors, *Critical Reviews in Solid State and Materials Sciences* **14**(sup1): s79–s101.
**URL:** *http://www.tandfonline.com/doi/abs/10.1080/10408438808244783* 130

Gallagher, C. J. [1952]. Plastic Deformation of Germanium and Silicon, *Phys. Rev.* **88**(4): 721–722.
**URL:** *https://link.aps.org/doi/10.1103/PhysRev.88.721* 129

Gassenq, A., Tardif, S., Guilloy, K., Duchemin, I., Pauc, N., Hartmann, J. M., Rouchon, D., Widiez, J., Niquet, Y. M., Milord, L., Zabel, T., Sigg, H., Faist, J., Chelnokov, A., Rieutord, F., Reboud, V. and Calvo, V. [2017]. Raman-strain relations in highly strained Ge: Uniaxial ?100?, ?110? and biaxial (001) stress, *Journal of Applied Physics* **121**(5): 055702.
**URL:** *http://aip.scitation.org/doi/10.1063/1.4974202* 129

Geandier, G., Thiaudière, D., Randriamazaoro, R. N., Chiron, R., Djaziri, S., Lamongie, B., Diot, Y., Le Bourhis, E., Renault, P. O., Goudeau, P., Bouaffad, A., Castelnau, O., Faurie, D. and Hild, F. [2010]. Development of a synchrotron biaxial tensile device for *in situ* characterization of thin films mechanical response, *Review of Scientific Instruments* **81**(10): 103903.
**URL:** *http://aip.scitation.org/doi/10.1063/1.3488628* 101

Hopcroft, M. A., Nix, W. D. and Kenny, T. W. [2010]. What is the Young's Modulus of Silicon?, *Journal of Microelectromechanical Systems* **19**(2): 229–238. 107, 120, 123

Hornstra, J. [1958]. Dislocations in the diamond lattice, *Journal of Physics and Chemistry of Solids* **5**(1): 129–141.
**URL:** *http://www.sciencedirect.com/science/article/pii/0022369758901380* 96

ISO [2017]. ISO 37:2017. Library Catalog: www.iso.org.
**URL:** *https://www.iso.org/cms/render/live/en/sites/isoorg/contents/data/standard/05/30/53023.html* 94

Jang, D., Gross, C. T. and Greer, J. R. [2011]. Effects of size on the strength and deformation mechanism in Zr-based metallic glasses, *International Journal of Plasticity* **27**(6): 858–867.
**URL:** *http://www.sciencedirect.com/science/article/pii/S0749641910001427* 133

Lin, L. and Argon, A. S. [1994]. Structure and plastic deformation of polyethylene, *J Mater Sci* **29**(2): 294–323.
**URL:** *https://doi.org/10.1007/BF01162485* 96

Micha, J.-S. and Robach, O. [2015]. La microdiffraction Laue, *Reflets de la physique* (44-45): 68–71.
**URL:** *http://www.refletsdelaphysique.fr/10.1051/refdp/20154445068* 109

Micha, J. S. and Robach, O. [2020]. LaueTools: Distribution of LaueTools Package from gitlab.esrf.fr repository for pip.
**URL:** *https://sourceforge.net/projects/lauetools/* 107, 109

Michaud, L. G., Nikitskiy, N. and Tardif, S. [2019]. Raman_solflex.
**URL:** *https://github.com/mcdlrt/Raman_solflex.git* 105, 110

Namazu, T., Isono, Y. and Tanaka, T. [2000]. Evaluation of size effect on mechanical properties of single crystal silicon by nanoscale bending test using AFM, *Journal of Microelectromechanical Systems* **9**(4): 450–459. Conference Name: Journal of Microelectromechanical Systems. 133

Peng, C.-Y., Huang, C.-F., Fu, Y.-C., Yang, Y.-H., Lai, C.-Y., Chang, S.-T. and Liu, C. W. [2009]. Comprehensive study of the Raman shifts of strained silicon and germanium, *Journal of Applied Physics* **105**(8): 083537.
**URL:** *http://aip.scitation.org/doi/abs/10.1063/1.3110184* 104

Pétri, R., Brault, P., Vatel, O., Henry, D., André, E., Dumas, P. and Salvan, F. [1994]. Silicon roughness induced by plasma etching, *Journal of Applied Physics* **75**(11): 7498–7506.
**URL:** *http://aip.scitation.org/doi/10.1063/1.356622* 133

Poborchii, V., Hara, M., Morita, Y. and Tada, T. [2015]. Raman spectroscopy of ultrathin strained-silicon-on-insulator: Size effects in strain, elastic, and phonon properties, *Appl. Phys. Lett.* **106**(9): 093107.
**URL:** *http://aip.scitation.org/doi/10.1063/1.4914031* 130

Richter, H., Wang, Z. P. and Ley, L. [1981]. The one phonon Raman spectrum in microcrystalline silicon, *Solid State Communications* **39**(5): 625–629.
**URL:** *http://www.sciencedirect.com/science/article/pii/0038109881903379* 130

Roylance, D. [2001]. ENGINEERING VISCOELASTICITY. 97

Small, M. K. and Nix, W. [1992]. Analysis of the accuracy of the bulge test in determining the mechanical properties of thin films, *Journal of Materials Research* **7**(06): 1553–1563.
**URL:** *http://www.journals.cambridge.org/abstract_S0884291400017027* 100

Soler, R., Wheeler, J. M., Chang, H.-J., Segurado, J., Michler, J., Llorca, J. and Molina-Aldareguia, J. M. [2014]. Understanding size effects on the strength of single crystals through high-temperature micropillar compression, *Acta Materialia* **81**: 50–57.
**URL:** *http://www.sciencedirect.com/science/article/pii/S1359645414005989* 133

Tsakalakos, T. [1981]. The bulge test: A comparison of the theory and experiment for isotropic and anisotropic films, *Thin Solid Films* **75**(3): 293–305.
**URL:** *http://www.sciencedirect.com/science/article/pii/0040609081904077* 100, 101

Ulrich, O., Biquard, X., Bleuet, P., Geaymond, O., Gergaud, P., Micha, J. S., Robach, O. and Rieutord, F. [2011]. A new white beam x-ray microdiffraction setup on the BM32 beamline at the European Synchrotron Radiation Facility, *Review of Scientific Instruments* **82**(3): 033908.
**URL:** *https://aip.scitation.org/doi/abs/10.1063/1.3555068* 107

Ungár, T. [2004]. Microstructural parameters from X-ray diffraction peak broadening, *Scripta Materialia* **51**(8): 777–781.
**URL:** *http://www.sciencedirect.com/science/article/pii/S1359646204002738* 130

Wolf, I. D. [1996]. Micro-Raman spectroscopy to study local mechanical stress in silicon integrated circuits, *Semicond. Sci. Technol.* **11**(2): 139.
**URL:** *http://stacks.iop.org/0268-1242/11/i=2/a=001* 104

Zhang, H., Tersoff, J., Xu, S., Chen, H., Zhang, Q., Zhang, K., Yang, Y., Lee, C.-S., Tu, K.-N., Li, J. and Lu, Y. [2016]. Approaching the ideal elastic strain limit in silicon nanowires, *Science Advances* **2**(8): e1501382.
**URL:** *http://advances.sciencemag.org/content/2/8/e1501382* 129

Zhang, L. and Zarudi, I. [2001]. Towards a deeper understanding of plastic deformation in mono-crystalline silicon, *International Journal of Mechanical Sciences* **43**(9): 1985–1996.
**URL:** *http://www.sciencedirect.com/science/article/pii/S0020740301000248* 129

# Chapter 4

# Transfer of a strained film onto a rigid substrate

## Contents

# Introduction

Previously we proposed different process flows to transfer a sc-Si thin film on various polymer substrates with a fine control on its dimensions and quality. An extended study of the mechanics of SOP material was provided in the previous chapter. The last step towards the fabrication of a permanently strained silicon layer is the transfer of a strained layer from a flexible substrate to a rigid substrate. Direct bonding was chosen as a way to transfer the strained silicon layer. Covalent bonds at the interface will prevent any strain relaxation. Furthermore direct bonding allows the formation of an interface with a low thermal budget compatible with organic components. Finally a bonding without any additional adhesive is necessary for further processing of strained silicon layer with standard CMOS methods. Several technical challenges arise to perform such a bonding compared to standard processes. Indeed, flexible polymer substrates have widely different mechanical properties and topology from standard wafers typically used for direct bonding. We adapted surface preparation steps to SOP structures to be able to perform an hydrophilic direct bonding of a sc-Si film from a polymer substrate to a rigid substrate. Two bonding stages were evaluated to obtain the highest sc-Si transfer rate. Raman and µLaue measurements were performed in order to characterize the strain of the transferred film and its crystalline state. This chapter is organized around two objectives: to demonstrate the feasibility of a report from a flexible substrate and to apply and characterize strain in the reported sc-Si thin film.

## 4.1 Adapting direct bonding procedures to a flexible silicon on polymer structure

### 4.1.1 Surface preparation

The first step in a direct bonding process is to obtain two surfaces meeting the roughness requirements presented in chapter 1. The first surface is the sc-Si film transferred on a flexible polymer substrate. As reported in chapter 2, the surface roughness of sc-Si films "as-transferred" on a flexible substrate is below 10 Å RMS. Direct bonding was performed with 205 nm thick silicon film to avoid any additional surface roughening from thinning process (*i.e.,* due to sacrificial etching or plasma etching[Pétri et al., 1994]). The second surface is that of the receiving rigid substrate, on which the strained thin film will be transferred. The receiving wafers were purchased directly from microelectronic materials suppliers and the surface roughness was suitable for direct bonding (*i.e.,* smaller than 0.5 nm RMS [Moriceau et al., 2010]), thus usually requiring no additional Chemical-mechanical Polishing (CMP) steps. Standard bulk (001) silicon wafer were used. An oxide layer was either thermally grown (145 nm thickness) or deposited and annealed at 1200 °C (5 µm thickness).

Once the roughness requirements are met, both sc-Si thin film and receiving substrate surfaces have to be prepared so that they are hydrophilic. This step is followed or combined with a removal of particle contamination and thus performed as close as possible to the actual bonding step. The detailed surfaces preparation process is represented in figure 4.1.

Full sheet 200 mm receiving substrates with a 145 nm thick thermal oxide layer were cleaned in a FSI Magellan tool with different standard surface preparations for direct bonding ($O_3$ exposition before RCA cleaning [Kern, 1990]). The resulting surface is hydrophilic. For thick oxide substrate, a short time CMP is performed (commonly known as a "touch"). Only a few nanometers of oxide are removed in order to achieve suitable roughness and remove surface defects for bonding of a deposited material [Moriceau et al., 2010]. For SOP samples, the surface preparation was divided in two steps:

- UV exposure under $O_3$ atmosphere to remove organic compounds at the surface of the silicon film. The duration of this step was determined by monitoring the water contact angle on a control sam-

ple. Indeed, this treatment decreases the surface affinity for organic compound and increases the hydrophilic character of the surface. It is a central parameter for the type of bonding here. Remaining Anti Stiction (AS) on the silicon surface is also removed as it is an organic compound.

- Wet cleaning in $NH_3$ aqueous solution with a megasound activation (1 MHz,10 W) using EVG 301 tool.

The latter wet cleaning step was performed on an industrial tool compatible with a Disco metallic frame. This metallic frame, presented in in chapter 2, is essential for the easy handling of SOP. It also allows the industrialization of a transfer process. Thus for the transfer of a sc-Si film from a flexible substrate to a rigid carrier, only silicon on tape samples were used (stack **L1** in figure 4.1). For the transfer of strained sc-Si individual patterns, full 200 mm receiving wafer were cut into 20 mm × 20 mm dies on a dicing tape held by a metallic frame. The surface preparation steps were similar to the one described for SOP samples. Different process parameters were used to accommodate the different natures of the substrate. The UV/$O_3$ cleaning can be performed in a single 10 min step and the megasound power could be increased to 90 W as thermal budget and film brittleness are not a concern in this case.

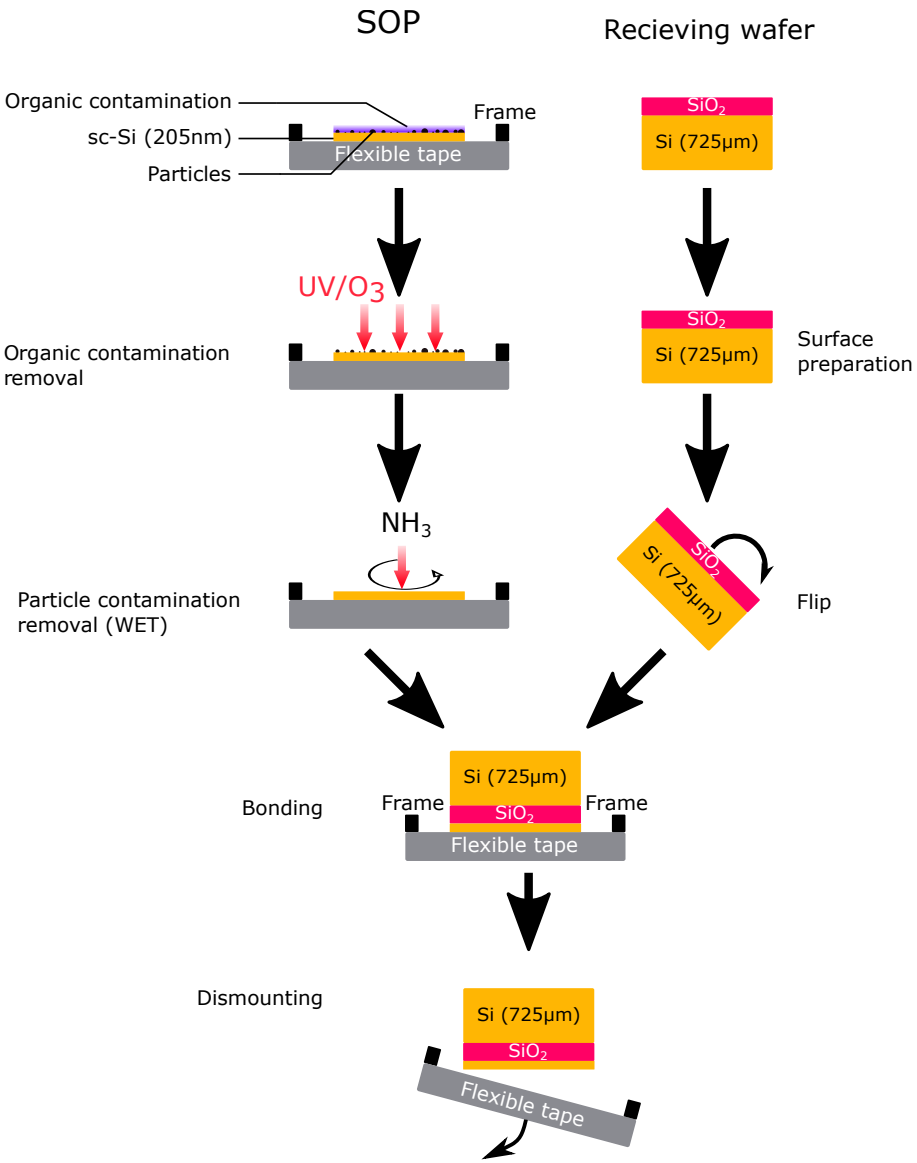


Figure 4.1: Schematic of the transfer of a sc-Si thin film from a polymer flexible substrate to a rigid substrate using direct bonding

### 4.1.2 Bonding stages

After both SOP samples and receiving wafer or dies were cleaned and presented an hydrophilic surfaces, the actual bonding step was performed. Dedicated bonding stages were used to that end. The first one detailed in figure 4.2 was designed for preliminary studies with 200 mm diameter silicon films and to experimentally validate that SOP can be transferred back on a rigid substrate, independently of the strain state. Thus, the force applied on the SOP is not intended to induce significant strain in the silicon film but to obtain a flat and taut surface. The stage is simply composed of a support to hold the metallic frame surrounding the tape and a 200 mm wide flat chuck to apply pressure on the SOP backside.

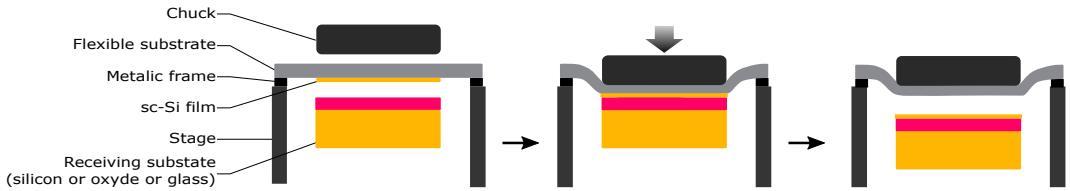


Figure 4.2: Schematic of a direct bonding process between a 200 mm full sheet SOP and a rigid carrier. The SOP is first put under tension by a chuck applying a force of the flexible substrate backside. Then the taut sc-Si thin film is put in contact with the receiving wafer.

Once the transfer feasibility was demonstrated, a second stage was designed to transfer strained Si patterns. It is actually a bulge test apparatus re-purposed to that end, with a bulge diameter of 30 mm. In this case, the SOP is mounted with the Si facing the inside of the chamber. The chamber is evacuated instead of being pressurized, which has the double advantage of presenting a convenient positioning of the receiving substrate and maintaining a clean atmosphere. The primary vacuum does not prevent water from being present at the bonding interface. The strain/bulge height relations presented in chapter 3 are valid for a free surface.

The height of the receiving die can be finely adjusted by using a spacer underneath it (such as another $(725 \pm 2)$ µm thick die).

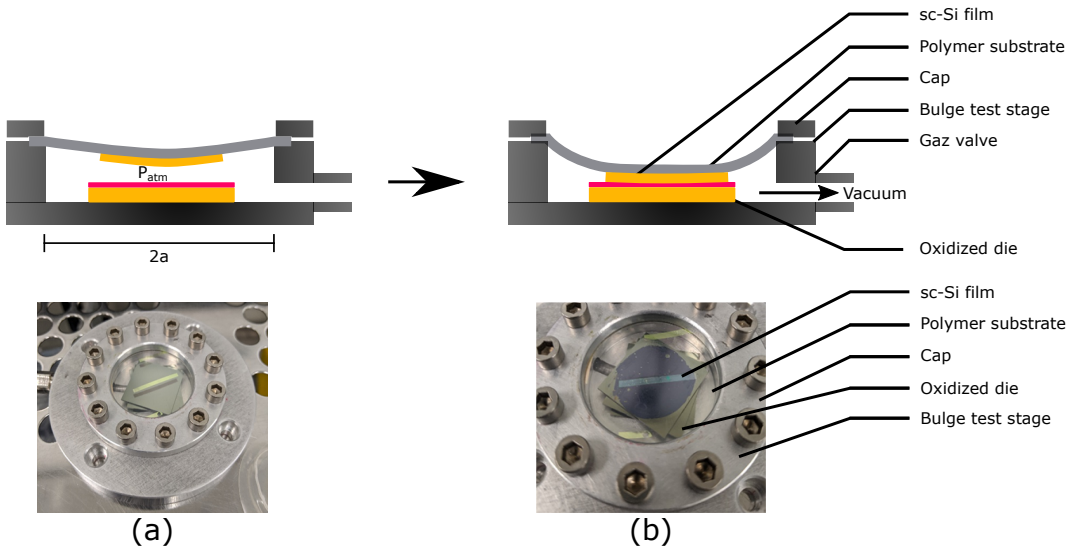


Figure 4.3: Bulge test stage modified to allow the direct bonding of the sc-Si film from a SOP to a die

### 4.1.3 Characterization

#### 4.1.3.1 Bonding interface of a re-transferred thin film

Usual techniques to monitor a bonding interface are IR imaging during the bonding and SAM for a more precise observation after the bonding. In the case of a bonding of SOP on a rigid substrate, IR imaging is not required as the polymer substrate is transparent and a standard visible camera can be used to monitor the closing of the interface. SAM does not have a sufficient resolution to observe the bonding interface of a 205 nm film. After the transfer, the distinctive color of the silicon thin film allows the transferred film to be observed with an optical microscope. [Mirshafieyan and Guo, 2014] As described in chapter 2, ellipsometry can be used to probe the thickness of different layer. Knowing the optical indices of silicon and silicon dioxide, the experimental phase and intensity of reflected polarized light can be compared to a model to confirm the transfer of a given silicon thickness.

#### 4.1.3.2 Evaluating the strain in a re-transferred thin film

Additional characterization steps are required to measure the strain of the transferred silicon layer. Raman spectroscopy and µLaue were used, as presented in chapter 1 and 3.

*Raman spectroscopy*

The Raman spectrometer is mounted on a confocal microscope, *i.e.* the depth resolution on the order of the wavelength, thus it could distinguish the surface bonded silicon film from the bulk silicon receiving substrate. As shown in figure 4.4, either in depth scan were performed (along z-axis) or scan along a transverse cut (x-axis scan).

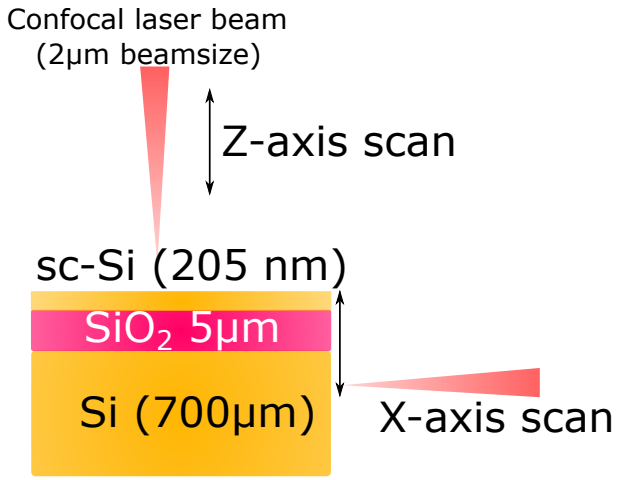


Figure 4.4: Raman analysis of of sc-Si film reported on a oxide layer by direct bonding. The Z-axis is possible thanks to the confocal microscope used with the Raman spectrometer

The Raman lateral and vertical resolution is 2 µm and the laser absorption coefficient α is $3.27 \times 10^3\,\mathrm{cm}^{-1}$ in Si [Green and Keevers, 1995]. Intensity at a given depth $z$ is given by Lambert law (equation 4.1), with I the intensity and $I_O$ the initial intensity.

$$I = I_0 e^{(-\alpha z)} \tag{4.1}$$

The characteristic absorption depth at which $I = I_0/e$ is equal to 3.058 µm. $SiO_2$ is fully transparent at this wavelength [Gao et al., 2013]. It confirms that confocal Raman spectroscopy is a perfectly valid method to analyze the type of structure presented here and that the laser beam absorption by the silicon or oxide is not a concern. It implies that the less intense signal from the silicon film cannot be discriminated from the bulk silicon signal in the case of a receiving wafer with a $SiO_2$ thickness below 1 µm. Thus, Raman stress analysis was only performed on film reported on a 5 µm thick $SiO_2$ layer, thick enough to separate the surface film from the bulk substrate. Figure 4.5 displays the intensity of the Raman silicon peak as a

function of microscope height for a 205 nm silicon film on a 5 µm thick $SiO_2$ layer on a bulk Si substrate. There are two local maxima, the most intense one corresponds to the bulk silicon substrate while the less intense one at the surface (Z = 0) corresponds to Si thin film. The distance between the two peaks is smaller than 5 µm as the refractive index of $SiO_2$ is larger than 1 (1.4761 at the He-Ne laser wavelength [Gao et al., 2013]).

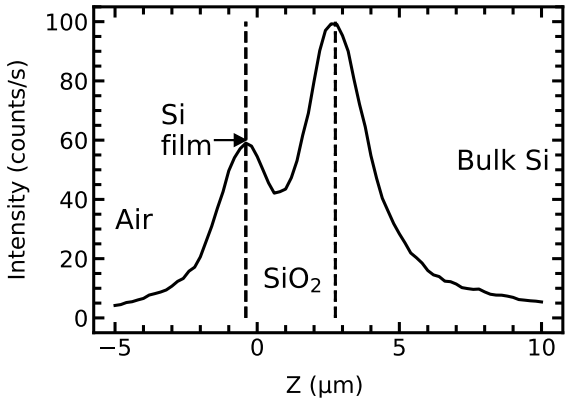


Figure 4.5: Silicon Raman peak intensity as a function of microscope height during an in-depth scan with a confocal microscope. The analyzed stack is composed of a 205 nm thick silicon film on a top of a 5 µm thick $SiO_2$ layer deposited on a bulk silicon wafer

*uLaue diffraction*

Micro Laue X-ray Diffraction, as presented in chapters 1 and 3, offers a direct and precise measurement of the silicon deviatoric strain tensor. In the stacks studied here, signal of a thin silicon film and a bulk substrate are easily distinguishable as long as both crystals are not perfectly aligned. Figure 4.6 presents a Laue pattern of a silicon thin film on an oxidized silicon substrate. The two silicon surfaces are (001) oriented and thin film present a 45° rotation in the (001) plan relatively to the silicon substrate. It allows a clear distinction between the two Bragg peaks position on the Laue patterns. Moreover, silicon thin film Bragg peaks are less intense as seen in figure 4.7. Both Laue patterns are processed using the LaueTools software suite to obtain crystal strain and orientation [Ulrich et al., 2011; Micha and Robach, 2010, 2020].

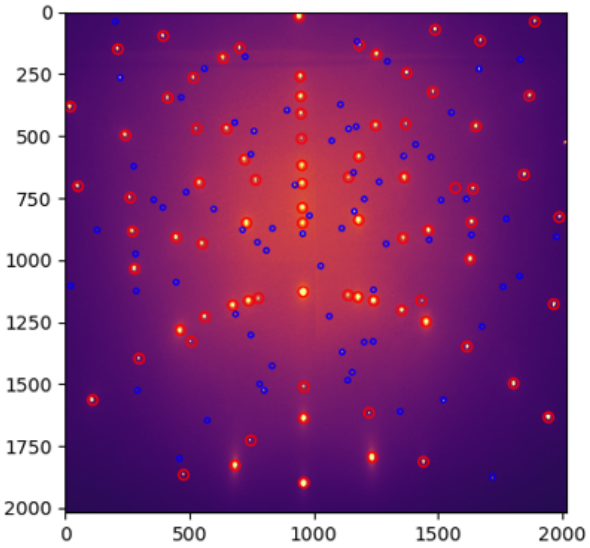


Figure 4.6: Laue pattern of a 205 nm thick sc-Si film on an oxidized bulk silicon carrier. Red circle indicates bulk silicon Bragg spots while blue circles are for thin film contribution.

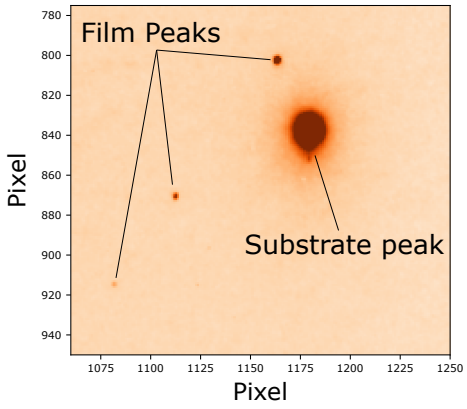


Figure 4.7: Bragg peak of a bulk silicon substrate (saturated intensity) next to less intense zone axis of a strained silicon thin film

## 4.2 Preliminary studies

### 4.2.1 Optimal surface state

To assess the feasibility of a silicon thin film transfer using direct bonding, an assembly composed of a SOP held by a rigid carrier and an oxidized silicon wafer was evaluated. The two wafers are bonded at RT and then annealed at 200 °C for 2 h. Figure 4.8 presents the two stacks evaluated along with SAM images of the bonded pair interfaces. Both stacks presents a defect free zone in the center while almost none of a 20 mm wide ring in the outer diameter is successfully bonded. On the outer diameter, the BSI glue thickness is lower than in the central zone. It prevents the contact of the two wafers and leads to a large un-bonded area. Usually the bonding wave can be initiated by applied pressure on a wafer edge. This was not possible for these stacks as only a pressure in a central point could initiate the bonding. The main takeaway information is that the silicon surface post-transfer on glue is compatible with direct bonding, confirming that the surface roughness is low enough after a first transfer on glue. Also even if an hydrophobic AS coating was previously present on the sc-Si surface, a UV/$O_3$ treatment was sufficient to remove it and allow an hydrophilic direct bonding.

Moving to a sc-Si film on flexible substrate, *i.e.* without carrier, and assuming that the silicon surface roughness was not affected, the main challenges are to obtain an hydrophilic surface and a low particle contamination. A 10 min UV/$O_3$ treatment changes the water contact angle from $(107 \pm 5)°$ to $(3 \pm 1)°$.

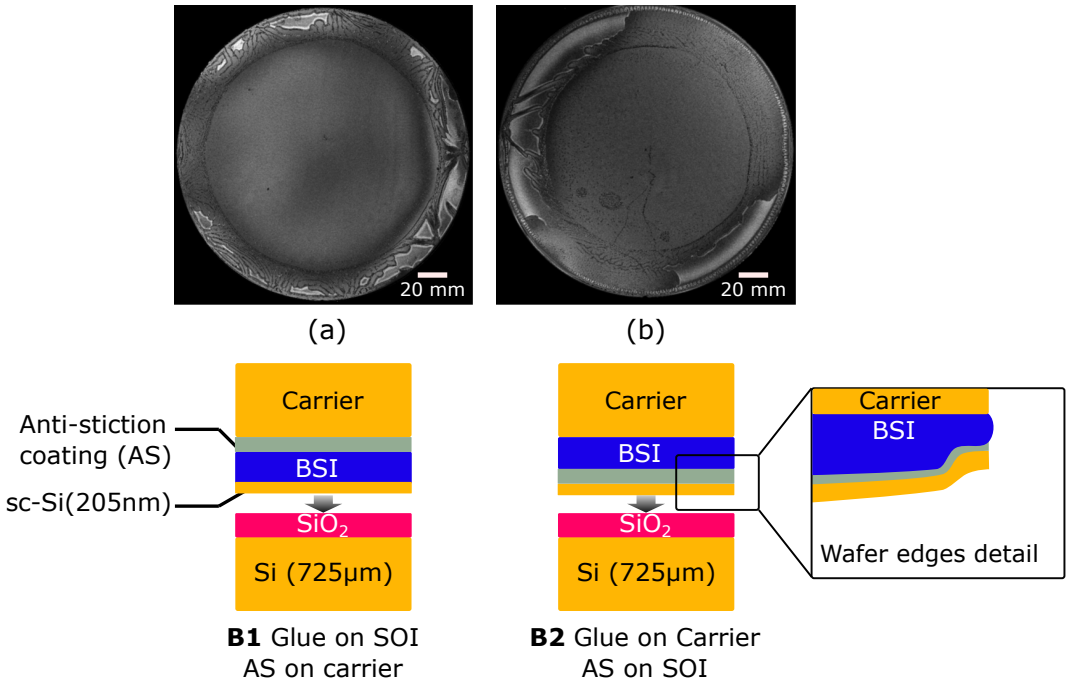


Figure 4.8: SAM images of a rigid SOP structure bonded to an oxidized silicon wafer (a)SOP manufactured from stack **B1** with an Anti Stiction (AS) layer in between a BSI layer and the rigid carrier (b) SOP manufactured from stack **B2** with an Anti Stiction (AS) layer in between a sc-Si thin film and a BSI glue layer

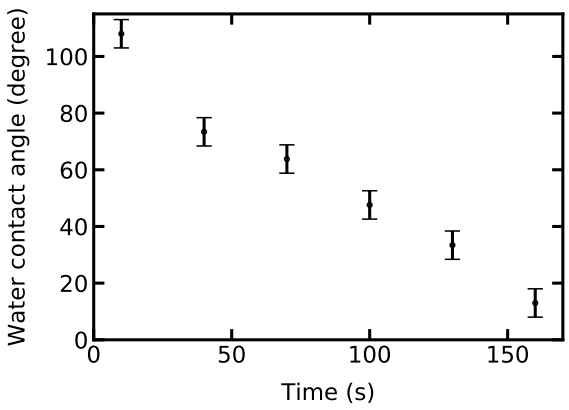


Figure 4.9: Water contact angle of a silicon wafer coated with an AS as a function of exposition time to UV/

In the case of flexible SOP with Furukawa tape as a substrate, the same observation is made. However the increase in temperature associated with UV/$O_3$ exposition (80 °C) induces an important dilatation of the substrate and degradation of the UV-sensible polymer. For 200 mm diameter films transferred on Furukawa tape this causes the apparition of cracks in the silicon film as presented in figure 4.10. To avoid overheating during the removal of organic contamination, the cleaning can be divided in several steps to let the tool and structure cool down (*e.g.*, 2 min of UV/$O_3$ exposition followed by 2 min rest time and repeated 5 time). The obvious downside is a major increase in processing time while requiring more manipulations. The kinetic is also slower and shorter steps cannot be performed without an increase in final water contact angle. For patterned sc-Si films, *i.e.* with small surfaces and chemically smoothed edges, a single 10 min step could be used. This underlines that rough edges and large surfaces plays a major role in cracks apparition during heating of the polymer substrate.

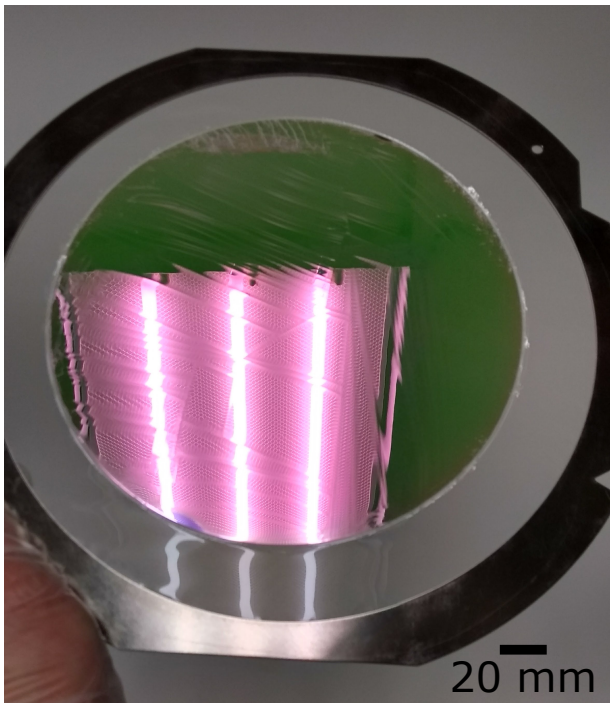


Figure 4.10: Snapshot of 205 nm thick silicon film on a Furukawa dicing tape held by a metallic frame. Cracks appeared after a 10 min UV/$O_3$ exposition.

No additional cracks appear after particle decontamination. The configuration of the structure (SOP on frame) forbids the use of standard metrology tools for particle contamination, however the use of this method has been validated in previous studies [Sanchez et al., 2018].

### 4.2.2 Surfaces contacts

Initial observations showed that small flakes of silicon could be transferred to an oxide layer by manually laminating a 205 nm thick SOP on the substrate. It proved that sc-Si surface was locally suitable for a transfer via direct bonding. Given the flexible nature of the polymer substrate, a good quality bonding cannot be performed by simply putting the SOP and rigid substrate in contact. Contrary to classic wafer bonding, the weak interactions at RT are not sufficient to overcome the local curvature. The full sheet bonding stage presented previously in figure 4.2 allowed obtaining a sufficiently flat surface for the SOP to bond macroscopic area of silicon film to the oxide. The bonding interface is strong enough to dismount the Furukawa polymer substrate from the sc-Si film using an acetone bath at RT as shown in figure 4.11 (a). Around 55% of the sc-Si film is transferred on the rigid carrier The resulting stack is annealed at 300 °C for 4 h and cleaned with an acetone bath. Micrograph of a macroscopic silicon flake before and after these steps are presented in figure

4.11 (b) and (c).

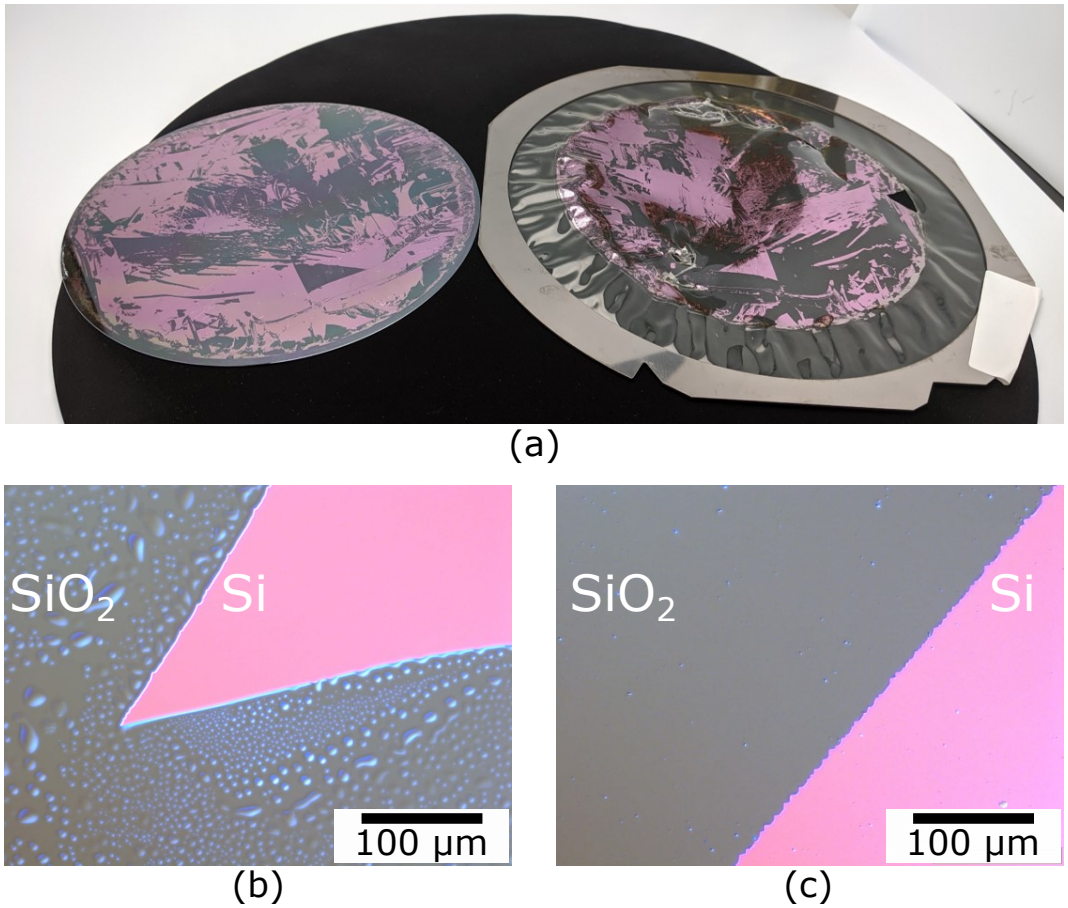


Figure 4.11: (a) Snapshot of a 205 nm thick sc-Si film (pink) partially transferred from a Furukawa dicing tape to 5 µm thick silicon dioxide layer (b) Micrograph of the reported sc-Si thin film after bonding and mechanical removal of the dicing tape (c) Bonded sc-Si thin film after thermal annealing and chemical cleaning

The stack was cleaved and analyzed using Raman spectroscopy on the exposed side. Figure 4.12 is a side-view micrograph of the stacks. A two dimensional Raman mapping (x-y axis) was performed on this sample, the mean Raman peak intensity and corresponding strain are presented in figure 4.13 (a). Both silicon substrate and silicon thin film contribution are distinguishable in the intensity curve. The two maximum are separated by 5 µm, which corresponds to the thickness of the oxide layer. Silicon Raman peaks of the substrate and silicon film are represented in figure 4.13 (b). A 0.71 $cm^{-1}$ red-shift is observed for the sc-Si peak relative to the substrate peak which acts as an internal reference. It corresponds to a 0.09% biaxial tensile strain. It is a low value but significant with our set-up. Especially since the sc-Si is initially in compression on the flexible polymer substrate. No increase in peak width is observed, hinting at a good crystalline quality.

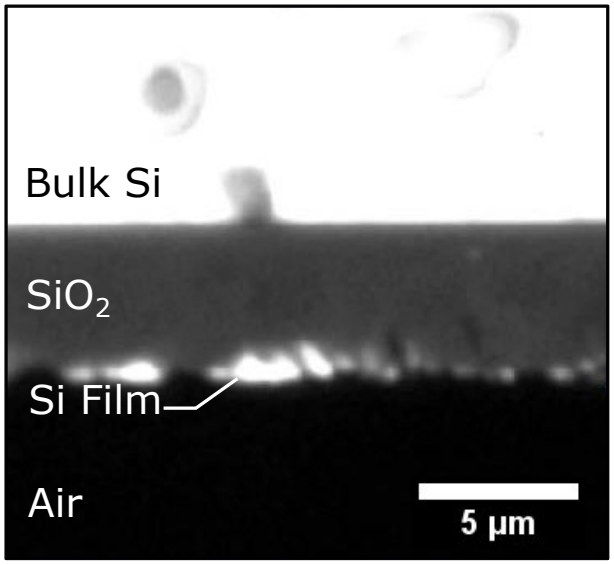


Figure 4.12: Micrograph of 205 nm thick sc-Si layer bonded on a 5 µm thick silicon dioxide layer.

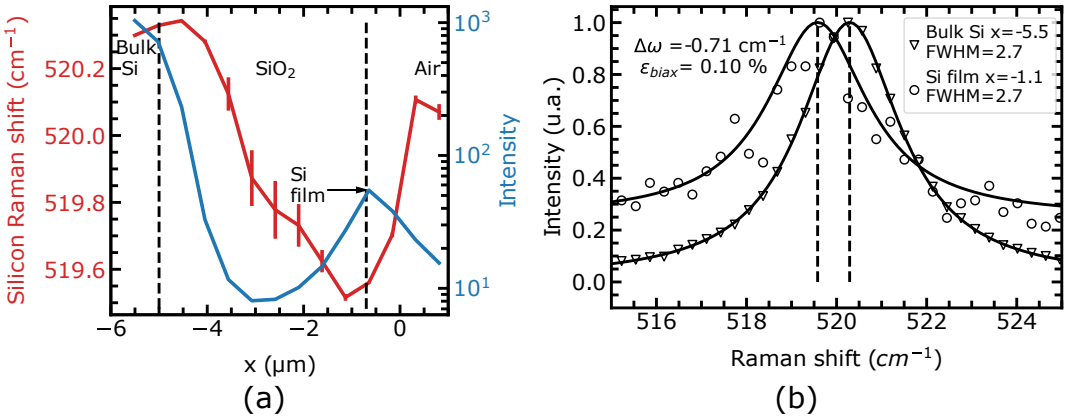


Figure 4.13: (a) Profile of silicon Raman peak intensity and biaxial strain for a 205 nm silicon filmed bonded on a 5 µm thick oxide layer. The thin film is situated at $x = -1$ µm(b) Raman peaks from the bulk silicon substrate and from the bonded sc-Si thin film.

A Raman depth-scan was also conducted on the same sample. Results are presented in figure 4.14. The sc-Si peak intensity is larger than in the side-cut scan, since the film covers entirely the micron-sized laser spot (as opposed to a thin slice in side-view). Comparison between the substrate and thin film yields a red-shift and strain level comparable to the one extracted from the side mapping (0.10 % and 0.09 %, respectively). The confocality of the microscope was sufficient to avoid any contribution of the thin film while probing the internal bulk silicon reference.

The full sheet bonding stage proved that macroscopic area of silicon could be transferred using direct bonding but the strain level are low. Furthermore, the preparation of a full sheet SOP proved to be difficult and time consuming to achieve a crack free surface suitable for direct bonding. Smoother edges would likely prevent some of the encountered issues.

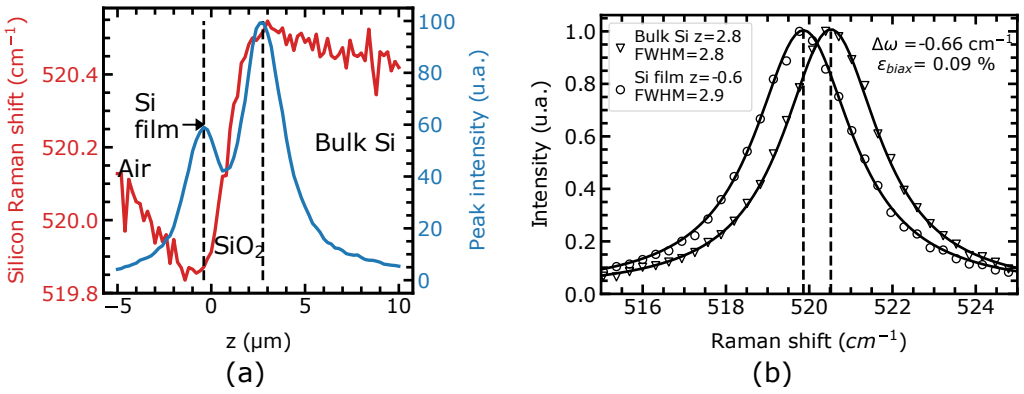


Figure 4.14: (a) In depth profile of silicon Raman peak intensity and biaxial strain for a 205 nm silicon filmed bonded on a 5 µm thick oxide layer (b) Raman peaks from the bulk silicon substrate and from the bonded sc-Si thin film.

## 4.3 Direct bonding of strained silicon film

Previous results exposed the feasibility and difficulties of direct bonding of SOP structures. Here we will present transferred film with significant strain level using the lithographed patterns introduced in chapter 2).

### 4.3.1 Crystalline state after transfer

Single 205 nm silicon patterns were transferred using the kapton cut-out method (presented in chapter 2) on a 200 mm tape. It allows to perform the cleaning and surface preparation process on single patterns. It removes any downtime prior to the actual bonding, ensuring optimal surface state. The adapted bulge state was used to induce strain and optimize surface contact between the flexible SOP and 20 mm × 20 mm oxidized die placed at the bottom of the bulge stage. The bonding was performed at RT. Placing the bulge stage on a hot plate proved to enhance surface contact but also increased the silicon/polymer adhesion. Around 60% of the patterns surface was transferred on oxidized die. A micrograph of transferred silicon pattern are presented in figure 4.15. Microscopic silicon flake are delimited by cracks separated, flake characteristic dimension are ranging from 20 µm to 550 µm with a distribution centered around 80 µm.

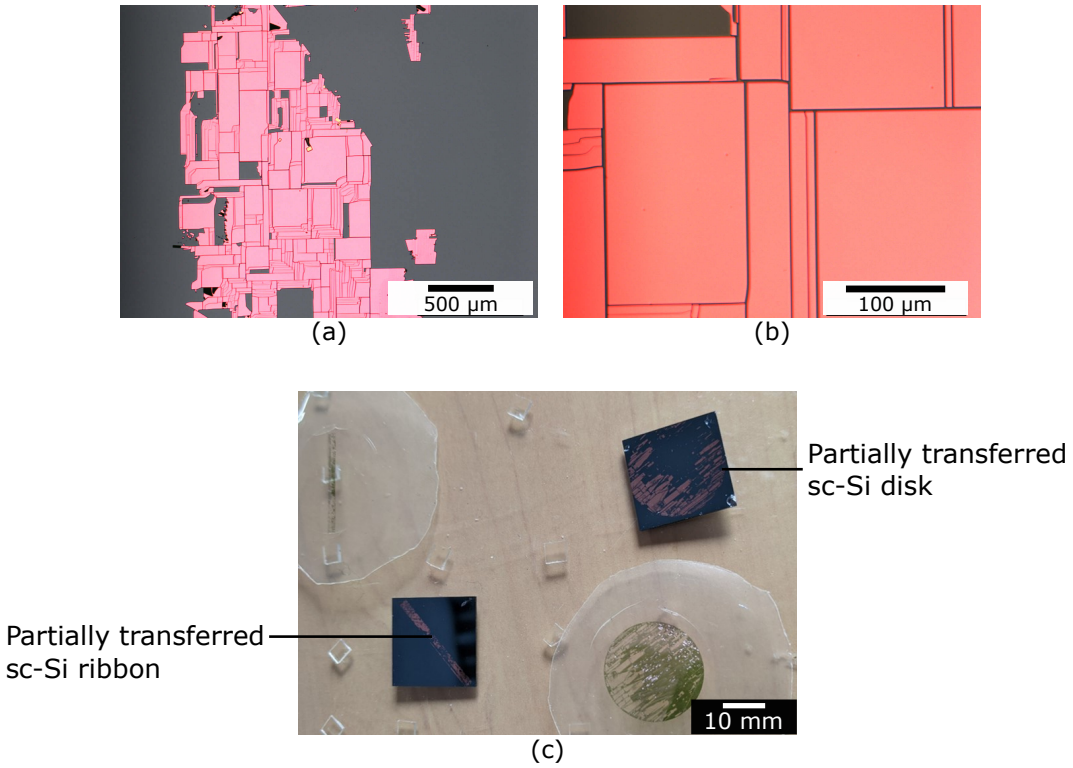


Figure 4.15: Micrographs (a,b) and picture (c) of a strained silicon film reported on a 145 nm thick $SiO_2$ layer.

Transferred films were directly analyzed with µLaue as the thin oxide (145 nm) excluded Raman analysis with our set-up. Figure 4.16 shows the mapping of the diagonal strain tensor component for both silicon bulk substrate and silicon thin film in the case if the transferred disk. Here no cracks were visible with an optical microscope. Strain gradients can be observed in the silicon film but overall the mean strain value is close to zero. A small tensile strain is observed in the (001) plane of the bulk silicon substrate. The probed depth is ranging from about 20 µm to about 2 mm depending on the X-ray energy [Chantler et al., 2005], the strain observed in the substrate is not due to the oxide or silicon layer on the surface.

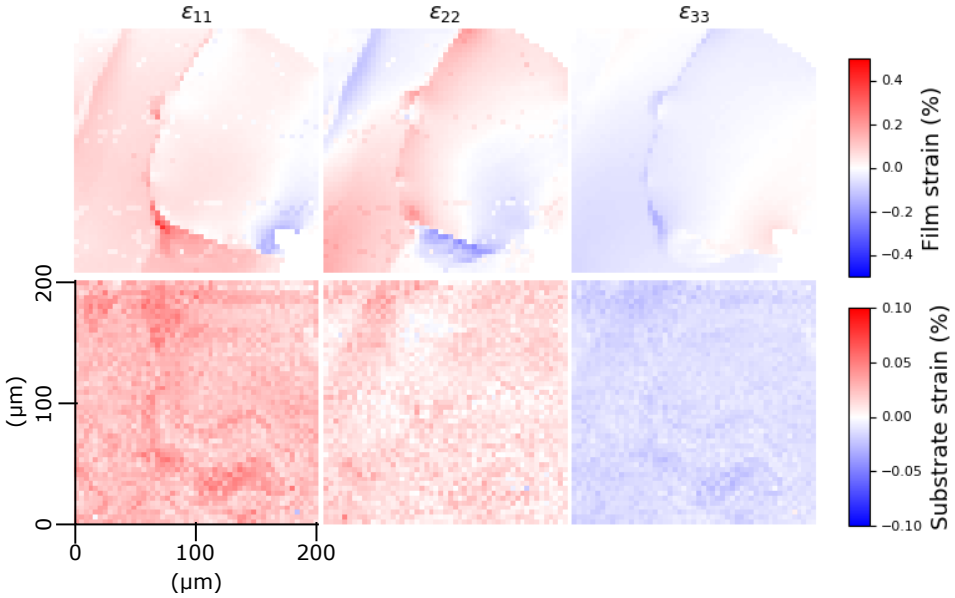


Figure 4.16: Disk sample: (Top) Diagonal component of the strain tensor of a 205 nm thick sc-Si thin on a oxidized wafer. (Bottom) Strain tensor diagonal component of the bulk silicon carrier (note the different colorscale). Data were obtained from Laue pattern indexation

A second sample was evaluated, similar to the previous one except for the shape of the silicon pattern, *i.e.,* ribbon instead of a disk. Figure 4.17 presents a micrograph of the probed area.

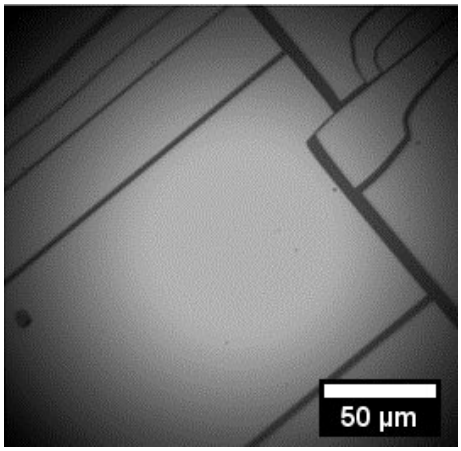


Figure 4.17: Micrograph of strained silicon film bonded on an oxidized bulk silicon wafer

The mapping of the diagonal strain component for both silicon thin film and substrate is presented in figure 4.18. The white bands are due to a loss of x-ray beam during acquisition. Here a significant biaxial tensile strain is present in the transferred thin film. The mean value is equal to 0.07 % but strain gradient are clearly visible on the edges of silicon flakes. Strain concentration is visible on a corner of the central flake, especially for $\varepsilon_{22}$ component. The maximum local biaxial strain is 0.48%. Given the diameter of the bulge and the depth of the stage (a=20 mm, h = 2.825 mm and $h_0$ <= 1 mm), the theoretic maximum strain in the bulge center can be calculated using equation 3.7 [Small and Nix, 1992]. The theoretical strain ranges from 1.1 to 1.3 %, which is significantly higher than the strain reported here. However, taking the experimental local silicon strain value during a bulge test of the same height, as presented in chapter 3, the local silicon strain is in the same range (between 0.46% and 0.52%). This tends to indicate that the strained film was successfully transferred, without any significant relaxation.

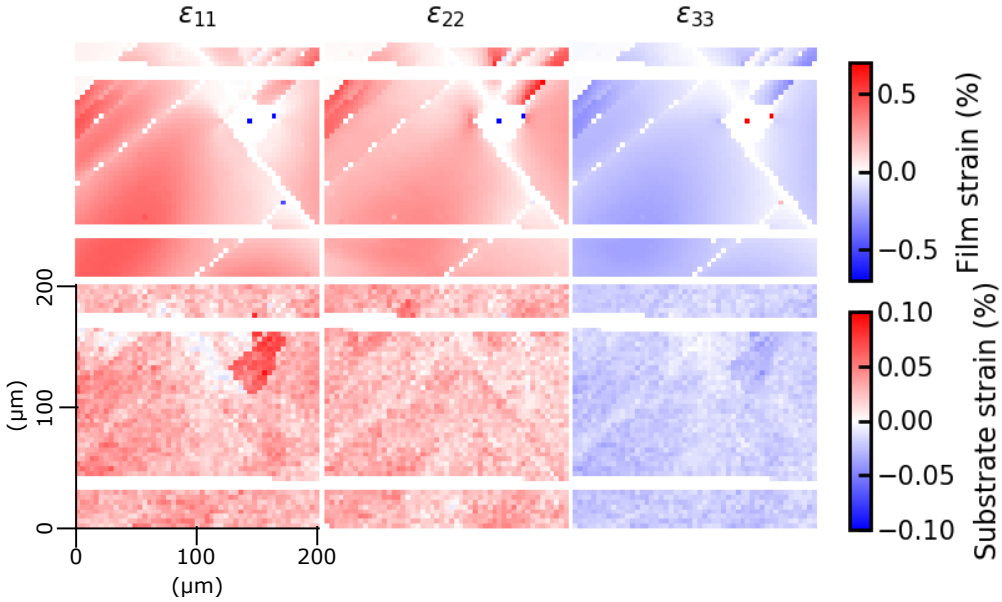


Figure 4.18: Ribbon sample: (Top)Diagonal component of the strain tensor of a 205 nm thick sc-Si thin on a oxidized wafer. (Bottom) Strain tensor diagonal component of the bulk silicon carrier. data were obtained from Laue pattern indexation

A profile of the in-plane diagonal strain components along a sample diagonal is displayed in figure 4.19. A clear decrease in strain is observed near flakes edges. In the large flake ($\approx$ 150 µm) the biaxial character of the strain is stronger but maximum strain along a given direction does not go above 0.45 %. Whereas in a smaller flake ($\approx$ 40 µm), there is an important difference between the $\epsilon_{11}$ and $\epsilon_{22}$ values,and $\epsilon_{22}$ reaches up to 0.7%. The inhomogenity is probably linked to the higher form factor of the smaller flakes. At smaller dimension, less energy is present in the film to drive strain relaxation.

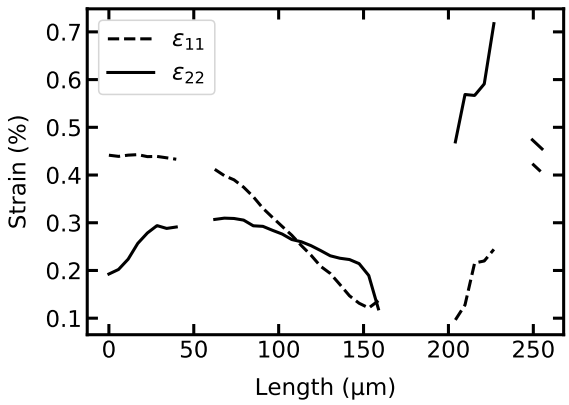


Figure 4.19: In plane biaxial strain profile of the ribbons sample after direct bonding on an oxidized silicon carrier wafer

Finally a mapping of crystal rotation is presented in figure 4.20. No undulation are observed for the $\theta$ and $\psi$ rotations. It indicates that the two surfaces were flat and well aligned at the moment of contact. A small $\phi$ rotation can be observed for the smaller flakes, although it is homogeneous on single flake surfaces. Without *in situ* measurement it is not possible to determine if it caused or was a result of the silicon film fracture.

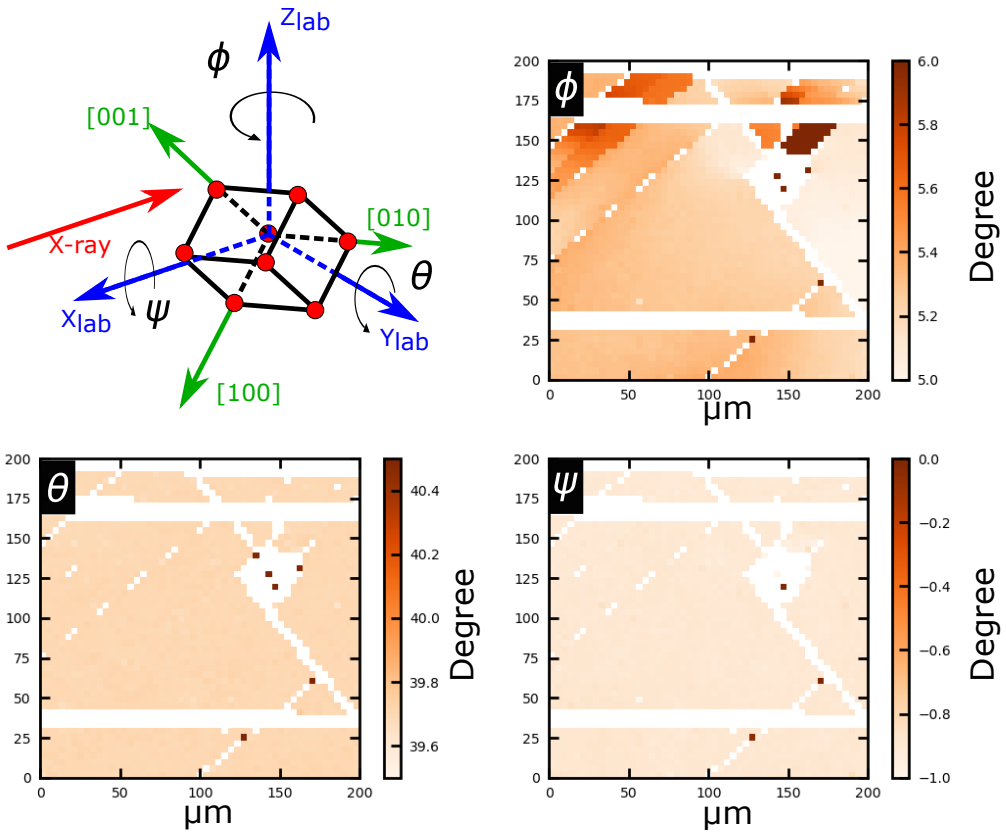


Figure 4.20: Euler angles of the strained sc-Si film reported on an oxidized bulk silicon wafer via direct bonding

## Conclusion

This chapter exposed how to adapt a direct bonding process to transfer a strained silicon film from a flexible polymer substrate to a rigid substrate in order to obtain a permanently strained silicon film. First, efforts were made to develop a surface preparation process to obtain a suitable bonding interface between a sc-Si film on a flexible substrate and a rigid standard oxidized silicon wafer. Surface roughness of the transferred films already met the requirement as they were obtained from commercial SOI. The transfer process did not alter the surface roughness in a significant way. Moreover the use of a compliant substrate suppresses any influence of larger scale surface height variation. The main achievement was to obtain an hydrophilic silicon surface on the flexible silicon film despite using an hydrophobic coating during the thin film elaboration process. The use of metallic frames allowed simple handling of the samples and access to standard industrial tools.

Then a modified bulge test apparatus proved that a sc-Si thin film can be transferred via direct bonding at RT while retaining a significant biaxial strain. As opposed to the bonding of two rigid wafers, low temperature bonding cannot occur in this case without the application of an external force to close the interface. Resulting maximum biaxial strain was significant (0.4%) but smaller than what has been achieved during stand-alone uniaxial (3.1 %) or biaxial tensile tests (1.5 %).

Further developments are needed to achieve higher permanent strain and to transfer larger homogeneously strained surface. Thus, these preliminary results set the path for a scalable method to produce strained silicon film with a tunable strain tensor. Additional characterizations are also needed to observe the sc-Si strain evolution during the bonding step. This can be done with X-ray Diffraction or a different Raman set-up than the one used here. By using polarized light, Raman spectroscopy can be used to characterize silicon layers separated by hundreds of nanometer of $SiO_2$ [Kurosawa et al., 2011; Loechelt et al., 1999]. Another possibility is to use a UV laser and to immerse in the glycerin a high numerical aperture objective lens [Moutanabbir et al., 2010]. The next chapter will detail the transfer of another material of

interest, showing the versatility of the transfer process presented here.

## References

Chantler, C., Olsen, K., Dragoset, R., Chang, J., Kishore, A., Kotochigova, S. and Zucker, D. [2005]. X-Ray Form Factor, Attenuation, and Scattering Tables. Last Modified: 2019-11-15T20:46-05:00.
**URL:** *https://www.nist.gov/pml/x-ray-form-factor-attenuation-and-scattering-tables* 153

Gao, L., Lemarchand, F. and Lequime, M. [2013]. Refractive index determination of SiO2 layer in the UV/Vis/NIR range: spectrophotometric reverse engineering on single and bi-layer designs, *Journal of the European Optical Society - Rapid publications* **8**(0). Number: 0.
**URL:** *https://www.jeos.org/index.php/jeos_rp/article/view/13010* 145, 146

Green, M. A. and Keevers, M. J. [1995]. Optical properties of intrinsic silicon at 300 K, *Progress in Photovoltaics: Research and Applications* **3**(3): 189–192. Number: 3 _eprint: https://onlinelibrary.wiley.com/doi/pdf/10.1002/pip.4670030303.
**URL:** *https://onlinelibrary.wiley.com/doi/abs/10.1002/pip.4670030303* 145

Kern, W. [1990]. The Evolution of Silicon Wafer Cleaning Technology, *Journal of the Electrochemical Society* **137**(6): 1887–1892. Number: 6. 142

Kurosawa, M., Sadoh, T. and Miyao, M. [2011]. Selective-mapping of uniaxial and biaxial strains in Si-on-insulator microstructures by polarized microprobe Raman spectroscopy, *Appl. Phys. Lett.* **98**(1): 012110. Number: 1.
**URL:** *https://aip.scitation.org/doi/10.1063/1.3535606* 156

Loechelt, G. H., Cave, N. G. and Menéndez, J. [1999]. Polarized off-axis Raman spectroscopy: A technique for measuring stress tensors in semiconductors, *Journal of Applied Physics* **86**(11): 6164–6180. Number: 11.
**URL:** *http://aip.scitation.org/doi/10.1063/1.371670* 156

Micha, J.-S. and Robach, O. [2010]. LaueTools: Laue X-ray MicrodiffractionAnalysis Software,. Programmers: _:n2089.
**URL:** *http://www.esrf.eu/home/UsersAndScience/ Experiments/CRG/BM32/lauetools–laue-x-ray-microdiffractionanalysis- software.html.* 146

Micha, J. S. and Robach, O. [2020]. LaueTools: Distribution of LaueTools Package from gitlab.esrf.fr repository for pip. Programmers: _:n3260.
**URL:** *https://sourceforge.net/projects/lauetools/* 146

Mirshafieyan, S. S. and Guo, J. [2014]. Silicon colors: spectral selective perfect light absorption in single layer silicon films on aluminum surface and its thermal tunability, *Opt. Express* **22**(25): 31545. Number: 25.
**URL:** *https://www.osapublishing.org/oe/abstract.cfm?uri=oe-22-25-31545* 145

Moriceau, H., Tiec, Y. C. L., Fournel, F., Ecarnot, L. F. L., Kerdilès, S. L. E., Delprat, D. and Maleville, C. [2010]. Direct Wafer Bonding Surface Conditioning, *Handbook of Cleaning in Semiconductor Manufacturing*, John Wiley & Sons, Ltd, pp. 501–541. Section: 14 _eprint: https://onlinelibrary.wiley.com/doi/pdf/10.1002/9781118071748.ch14.
**URL:** *https://onlinelibrary.wiley.com/doi/abs/10.1002/9781118071748.ch14* 142

Moutanabbir, O., Reiche, M., Hähnel, A., Erfurth, W., Motohashi, M., Tarun, A., Hayazawa, N. and Kawata, S. [2010]. UV-Raman imaging of the in-plane strain in single ultrathin strained silicon-on-insulator patterned structure, *Applied Physics Letters* **96**(23): 233105. Number: 23.
**URL:** *http://aip.scitation.org/doi/10.1063/1.3449135* 156

Pétri, R., Brault, P., Vatel, O., Henry, D., André, E., Dumas, P. and Salvan, F. [1994]. Silicon roughness induced by plasma etching, *Journal of Applied Physics* **75**(11): 7498–7506. Number: 11.
**URL:** *http://aip.scitation.org/doi/10.1063/1.356622* 142

Sanchez, L., Fournel, F., Montmayeul, B., Bally, L., Szelag, B. and Adelmini, L. [2018]. Collective Die Direct Bonding for Photonic on Silicon, *ECS Trans.* **86**(5): 223. Number: 5 Publisher: IOP Publishing.
**URL:** *https://iopscience.iop.org/article/10.1149/08605.0223ecst/meta* 149

Small, M. K. and Nix, W. [1992]. Analysis of the accuracy of the bulge test in determining the mechanical properties of thin films, *Journal of Materials Research* **7**(06): 1553–1563. Number: 06.
**URL:** *http://www.journals.cambridge.org/abstract_S0884291400017027* 154

Ulrich, O., Biquard, X., Bleuet, P., Geaymond, O., Gergaud, P., Micha, J. S., Robach, O. and Rieutord, F. [2011]. A new white beam x-ray microdiffraction setup on the BM32 beamline at the European Synchrotron Radiation Facility, *Review of Scientific Instruments* **82**(3): 033908. Number: 3.
**URL:** *http://aip.scitation.org/doi/10.1063/1.3555068* 146

# Chapter 5

# Application of the transfer process to other materials: the case of aluminium nitride

## Contents

# Introduction

The last three chapters were dedicated to the transfer, deformation and direct bonding of strained silicon thin film. Motivations to develop a process based on the transfer on a polymer flexible substrate using temporary polymer bonding were to lift the usual limitations associated with the manufacturing of strained semi-conductor films (*e.g.*, epitaxial growth or stressor layer use). A first proof of concept was presented for sc-Si films. To illustrate the versatility of the process, it was applied to different stacks containing aluminium nitride thin film. This work is the result of a collaboration with Edy Azrak, a post-doctoral researcher in our team. C-axis oriented AlN thin films were deposited on a Si substrate, and then double-transferred onto a flexible and stretchable substrate, resulting in AlN On Polymer (AOP). The transfer process was also applied to AlN based devices. In-situ Raman spectroscopy on a tensile stage was used to probe the nominal macroscopic strain externally applied to the AOP assembly. Raman strain and stress factor could be extracted for uniaxial and biaxial tensile stress.

## 5.1 Aluminium-Nitride transfer on flexible substrate

### 5.1.1 Material and applications)

Aluminium-Nitride (AlN) is a commonly used piezoelectric material for many MEMS as actuators [Giordano et al., 2009], radio-frequency filters [Piazza et al., 2007], and energy harvesters [Fei et al., 2018]. Indeed, AlN has a high resistivity, a large breakdown voltage [Aardahl et al., 1999], and a low dielectric loss compared [Kume et al., 2007] to other piezoelectric materials *e.g.*, ZnO [Look et al., 1998] or $Pb(Zr,Ti)O_3$ [Gubinyi et al., 2008; Chen, 1996]. For microelectronic applications, AlN is usually obtained with epitaxial growth techniques [Wang and Yoshikawa, 2004] or sputtering [Brien et al., 2007]. It presents an hexagonal wurtzite crystal structure. Theoretical studies show that straining piezoelectric crystals can induce a non-linear piezoelectric response, resulting in an increase of the piezoelectric constants [SHIMADA et al., 1998]. The strain effect on the piezoelectricity was observed experimentally for strained cadmium telluride (CdTe) crystals [Cibert et al., 1992].

### 5.1.2 AlN fabrication Method

A schematic of AlN-layer double-transfer to the flexible substrate is shown in figure 5.1. Polycrystalline (0002)-oriented AlN (Wurtzite) thin-films have been deposited on 200 mm Si (100) substrates using magnetron reactive pulsed DC sputtering at 350 °C (figure 5.1(a)). The AlN thickness is ranging from 200 to 1600 nm. The morphology of the AlN layers was studied with both SEM and AFM. Figure 5.2 displays SEM images for different AlN thickness after sputtering. Nanometric cristallites are visible and their lateral size increase with film thickness, the mean diameter is equal to 30 nm. Despite a preferential orientation along the c-axis, this methods yields highly poly-crystalline material. The surface roughness increases from 0.74 nm RMS to 4 nm between 200 nm and 1600 nm-thick layers (10 µm × 10 µm AFM topographic scan). This also indicates an inhomogeneous crystallite growth.

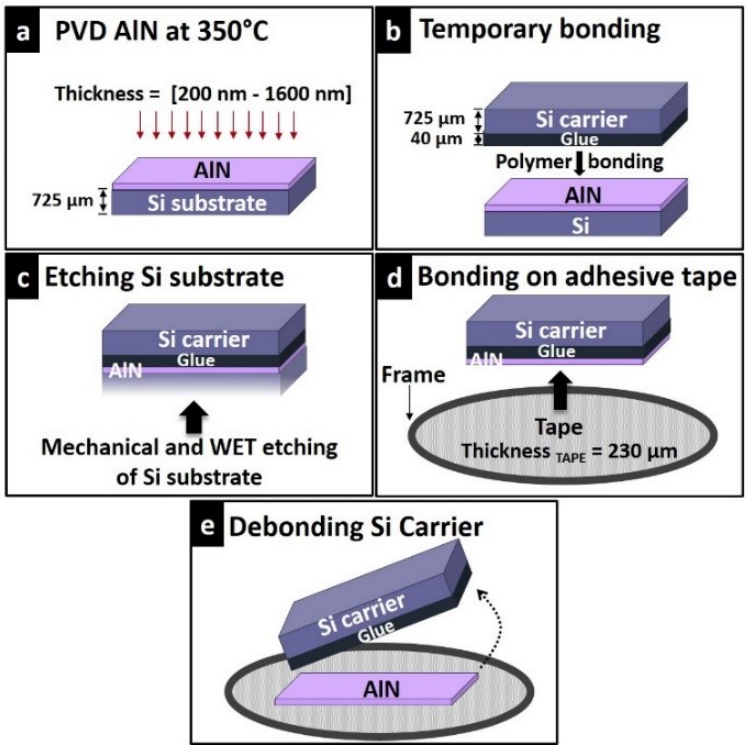


Figure 5.1: Schematic illustration of the fabrication steps. (a) AlN deposition at 350 °C, the deposited thicknesses are 200 nm and 1600 nm. (b) bonding a Si carrier coated with an adhesive glue onto the AlN surface at 210 °C. (c) grinding and etching the Si substrate. (d) bonding the Si carrier (carrying the AlN thin-film) on a flexible substrate (*i.e.,* dicing tape). (e) debonding the Si carrier.

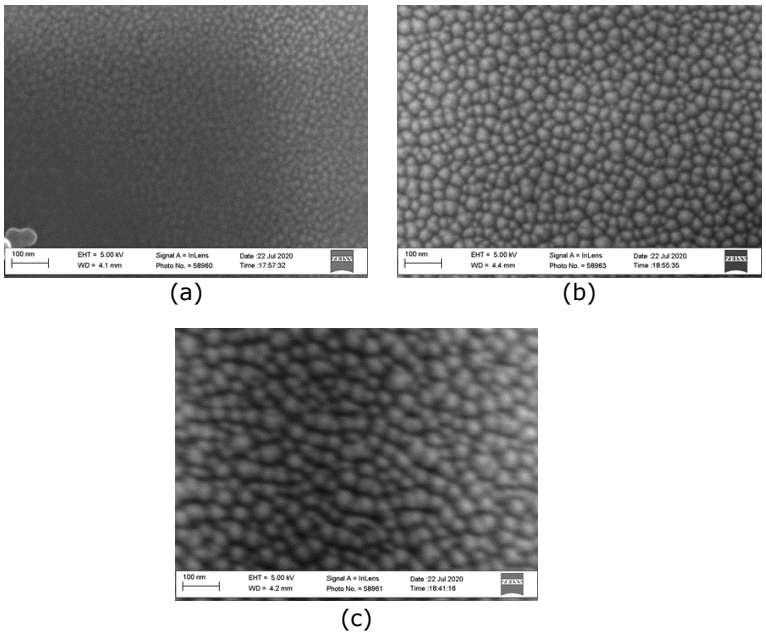


Figure 5.2: SEM images of C-axis oriented AlN films deposited on a silicon substrate for different layer thicknesses: (a) 200 nm (b) 800 nm(c)1600 nm. Images provided by Joël Eymery (CEA IRIG, Grenoble)

X-ray rocking curves of the AlN 0002 Bragg reflection are presented in figure 5.3. It illustrates the c-axis preferential orientation. The FWHM is inversely proportional to the film thickness. It decreased from 0.26 to 0.20° for an increase from 200 nm to 1600 nm in thickness. This indicates a strengthening of the C-axis preferential orientation at higher thicknesses. These FWHM values are one order of magnitude higher of what can be observed in molecular beam epitaxy grown crystals [Wang and Yoshikawa, 2004].

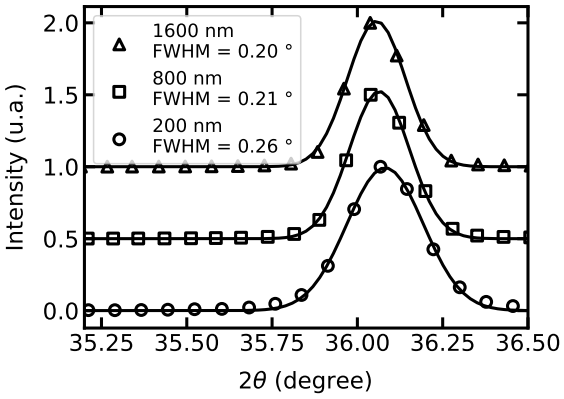


Figure 5.3: AlN 0002 Bragg peak for different film thickness obtained with PVD. Data courtesy of Nicolas R. Vaxelaire (CEA-Leti, Grenoble)

We then performed a temporary bonding on a 200 mm Si (100) carrier wafer. First, a 40 µm-thick organic glue BSI is spin-coated on the Si carrier, then it is temporarily bonded onto the AlN surface (figure 5.1(b)). The temperature and the force used to achieve a polymer bonding of sufficient strength are still 210 °C and 6 kN. The Si substrate used for the growth is then removed by a combination of mechanical grinding and chemical etching (figure 5.1(c) and 5.4). After grinding and etching the Si substrate, the AlN backside (the growth side) is exposed. AlN is used as an etch stop layer for the $HF/HNO_3$ solution. Compared to the transfer of sc-Si films presented in chapter 2, an oxide layer is not necessary. Then, the exposed AlN thin-film was bonded to a metal-framed, 230 µm thick adhesive tape (Furukawa SP-537T-230), as shown in figure 5.1(d). Finally, the carrier and the glue layer were manually dismounted, leaving the AlN thin-film on the surface of the adhesive tape *i.e.*, AOP (figure 5.1(e)). The adherence between the AlN thin-film and the glue is weaker than between the AlN and the tape. This is the result of a spin-coated AS nanolayer ($\approx$ 5 nm) located between the glue and the AlN thin-film.

The quality of the interface after the glue bonding and after the grinding processes was assessed by SAM. The marks (dark contrast area) on both sides (left and right indexed by two red arrows in figure 5.4(a)) of the wafer are caused by the bonding tool and do not affect the following steps of the process. As already described, the main Si substrate used for the growth is mechanically thinned after being bonded to the Si carrier. Figure 5.4(b) and 5.4(c) show the interface after a coarse (down to 200 µm thickness) and a fine grinding (down to 50 µm thickness) respectively. The outermost circular regions of the wafer change their contrast after the grinding procedures, this may be caused by non-uniform thicknesses of the glue and the Si main substrate. Nonetheless, these morphological defects do not harm the rest of the fabrication flow. A wet chemical etching removes completely the remaining Si layer using $HF/HNO_3$ mixture. Figure 5.4(d) shows a photograph of the carrier substrate after the chemical etching of the growth substrate. At this stage, the top layer is the AlN thin-film located directly on the glue layer of the Si carrier. In a first step, the flexible substrate (i.e. adhesive tape) is adhered on a metallic ring-frame. Second, the carrier wafer holding the AlN thin-film on its top is mounted on the flexible substrate (or polymer) as shown in figure 5.1(d). The AlN layer gets bonded on the surface of the flexible substrate. Third, the carrier is manually removed, thus, leaving the AlN thin-film on the tape (figure 5.1(e)). As shown in 5.5(a,b), 200 nm and 1600 nm thick AlN films have been successfully transferred onto flexible substrates. 800 nm thick AlN films were also transferred but are

not illustrated here.

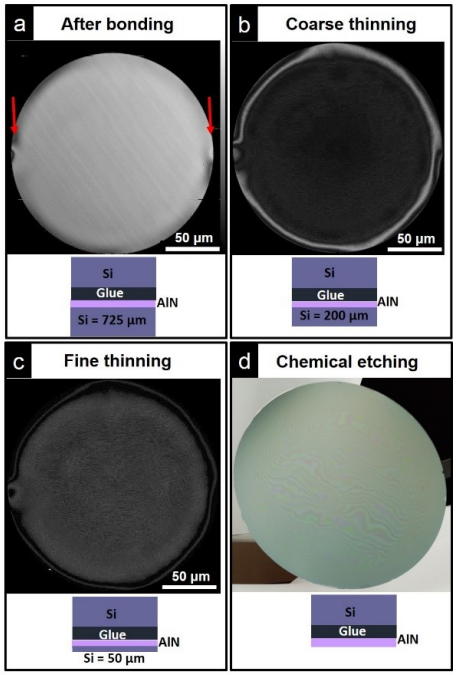


Figure 5.4: SAM images (a,b,c) and photograph (d) showing the results after polymer bonding, grinding and etching processes. (a) SAM image after the temporary carrier bonding The two red arrows show two defects produced by the bonding machine (b) SAM image after the coarse grinding process of Si to 200 µm. The acoustic frequency is 140 MHz. (c) SAM image after the fine grinding process of Si to 50 µm. (d) photograph after etching completely the Si substrate, leaving a 200 nm thick AlN thin-film on the organic glue layer.

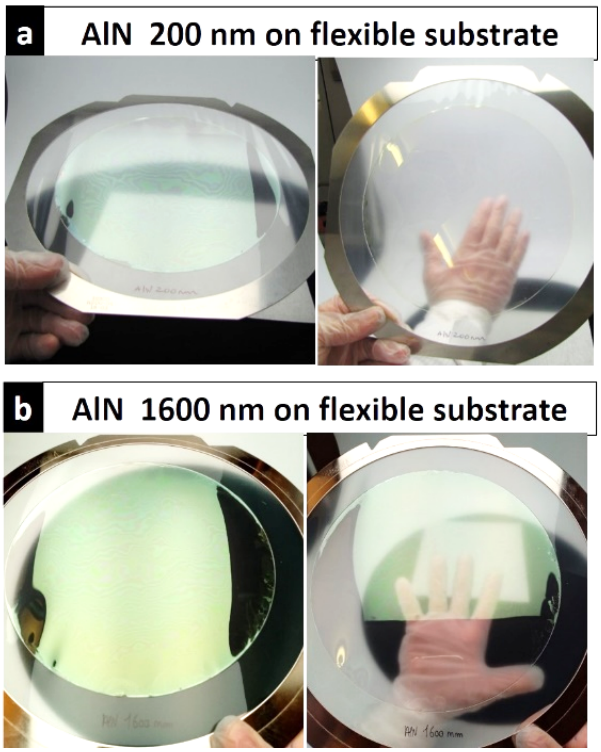


Figure 5.5: Snapshots of AOP, with AlN thickness of (a) 200 nm, (b) 1600 nm. The diameter of both transferred thin-films is 200 mm

Additionally, devices based on AlN were transferred on a Furukawa dicing tape. A snapshot of the transferred wafer is displayed in figure 5.6. Further electrical characterizations showed that the devices were functioning after the transfer on a flexible substrate. Detailed results are not available due to confidentiality concerns and go beyond the scope of this thesis. Nevertheless it shows the versatility of the transfer process as issues can often arise with stress built-in during the MEMS fabrication process [Argoud, 2012].

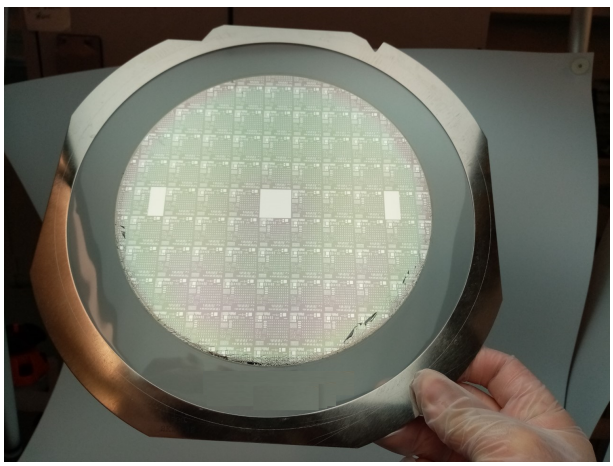

Figure 5.6: Snapshot of a 200 mm wide MEMS wafer transferred on Furukawa dicing tape and held by a metallic frame.

## 5.2 Controlling and measuring strain in AlN on Polymer structures

### 5.2.1 Tensile tests

Raman spectroscopy was used as a fast and simple technique to probe the vibration modes of the AlN thin-films, and thus indirectly their strain/stress state [McNeil et al., 1993; Gleize et al., 2003; Yang et al., 2011].

We focus on the shift of the $E_2$ (high) mode peak position, which has been demonstrated to be sensitive to the strain state of the AlN crystal [Sarua et al., 2004; Trodahl et al., 2006]. The experimental set-up is described earlier in this thesis, as it was used for SOP sample characterization (see subsection 3.1.4). For tensile tests, samples of AOP are cut as rectangles of 1 cm × 4 cm. A reference measurement is first done on a 200 nm-thick AOP as-cut sample (blue curve in figure 5.7(a). Then, the MicroMecha uniaxial tensile stage was used to apply a uniaxial stretch of the sample at a speed of 30 µm/s, with a step-size of 500 µm, and a maximum elongation length of 2500 µm. The stretching was stopped at each steps to measure the $E_2$ (high) peak, as shown in figure 5.7(a). Note that the Raman peaks are much broader compared to SOP samples due to the polycristalline nature of the AlN layer. A redshift of the peak is observed with the increase of the sample macroscopic strain. The $E_2$ (high) peak position is plotted in figure 5.7(b) as a function of the applied strain. The peak shift indicates a deformation of the AlN crystallographic structure, by a simple uniaxial elongation of the polymer substrate. Cracks were visible on the sample surface.

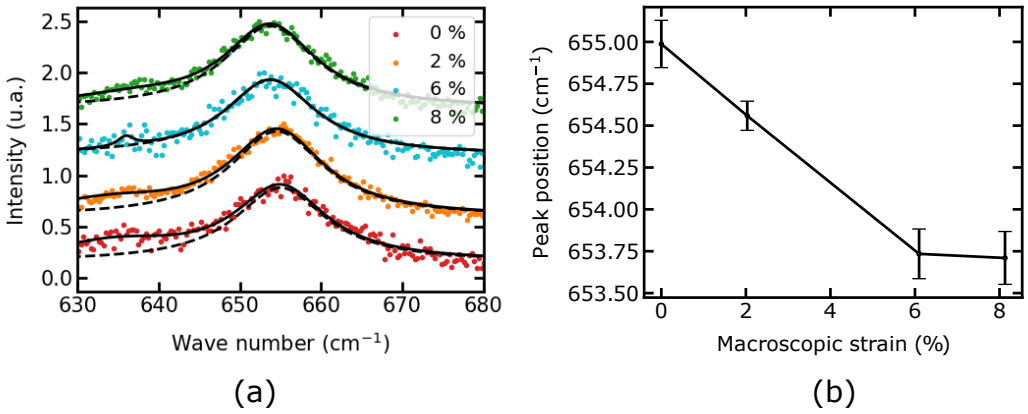


Figure 5.7: In-Situ Raman spectroscopy measurement for AlN controlled straining. (a) the characteristic peak $E_2$ at 655 cm$^{-1}$ of AlN variation function of different macro-strain values starting from 0% to 8%. (b) the $E_2$ pic position shift versus the macro-strain.

This initial observation showed that significant strain can be induced in the AlN layer by applying an external force on the AOP assembly. Different teams have studied the Raman stress factor to quantify the strain and stress in an AlN layer with the shift of the $E_2$ (high) phonon mode [Prokofyeva et al., 2001; Yang et al., 2011]. However these previous studies have been limited to biaxial stress study and no coefficient linking uniaxial stress to the shift of a phonon mode frequency is available in the literature. Nevertheless these results confirm that this method is a more straightforward method to tune *in fine* the properties of AlN thin-films (specifically the piezoelectric coefficients) than by using buffer layers.

### 5.2.2 Evaluation of Raman Raman-stress factor

#### 5.2.2.1 Sample fabrication

In order to determine precisely the local AlN stress without relying upon AlN Raman stress factor literature values, a 205 nm thick silicon layer was used as an internal reference underneath the AlN layer. A 800 nm-thick AlN layer was deposited on a patterned SOI wafer. This thickness provided exploitable Raman signal while keeping the force needed to stretch the whole assembly in an acceptable range. The transfer process presented in figure 5.1 was then applied to the AlN covered patterned SOI. The result was a 800 nm thick AlN layer on 205 nm thick sc-Si patterns with Furukawa dicing tape as a flexible substrate. Finally disks and ribbons tensile test samples are cut around the silicon patterns. The AlN layer is not patterned and thus is directly cut during tensile tests sample preparation. Its poly-crystalline structure prevents full fracture of the layer during the cutting process. Snapshots and schematics of the sample are presented in figure 5.8. Macroscopic silicon pattern are visible under the AlN layer.

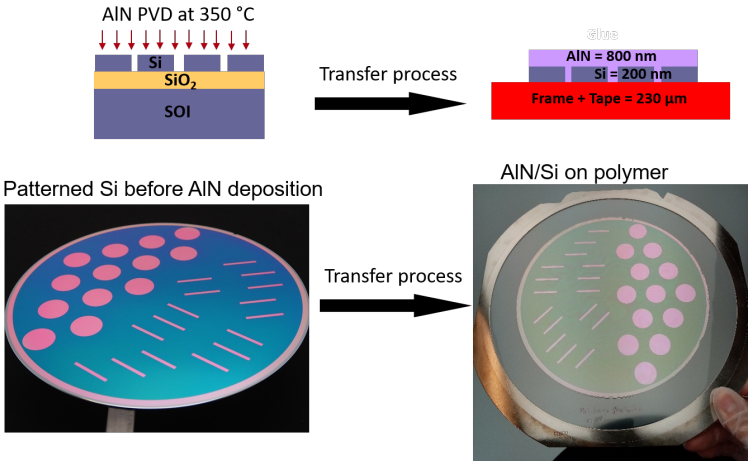


Figure 5.8: Snapshots and schematics of the fabrication of a AlN/Si/Furukawa tape flexible structure

#### 5.2.2.2 Results

Figure 5.9 presents a Raman spectrum of AlN on Silicon flexible sample. The crystallinity of the silicon implies a much sharper and intense Raman response but the two peaks are distinguishable with a single acquisition and no movements of the grating in the spectrometer.

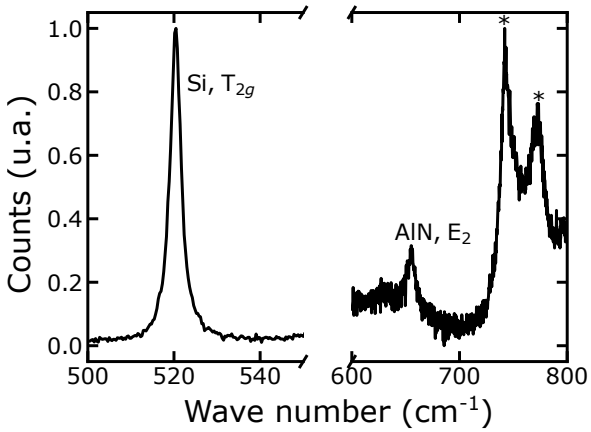


Figure 5.9: Raman spectrum of a 205 nm thick Si layer transferred along with a 800 nm thick AlN layer on a flexible Furukawa dicing tape. Peaks mark with a * symbol correspond to polymer substrate contribution.

A uniaxial tensile test is performed on this sample, the position of the two phonon mode response are presented in figure 5.10(a) as a function of macroscopic strain. A strong correlation between the Raman shifts is observed in figure 5.10(a). A linear regression is performed on the first four points of the curve to extract a Raman strain-factor of the initial loading part (figure 5.10(b)). A Raman strain factor of -5±0.4 $cm^{-1}/\%$ is obtained. Ideally the Raman stress-factor could be computed thanks to the generalized Hookes's law and compared to existing literature value for biaxial loading. However, in the case of uniaxial tensile strain, the texture of the layer is process dependent and any comparison with existing values is difficult. The elastic constant in a given sample direction does not necessarily match specific crystal value as the crystallites are rotated in the (0001) plane with respect to each other. Nonetheless the approach remains valid for a given material for comparison purposes. In order to obtain a universal value, the same process can be adapted to a layer with a well defined in-plane orientation and a higher crystalline character.

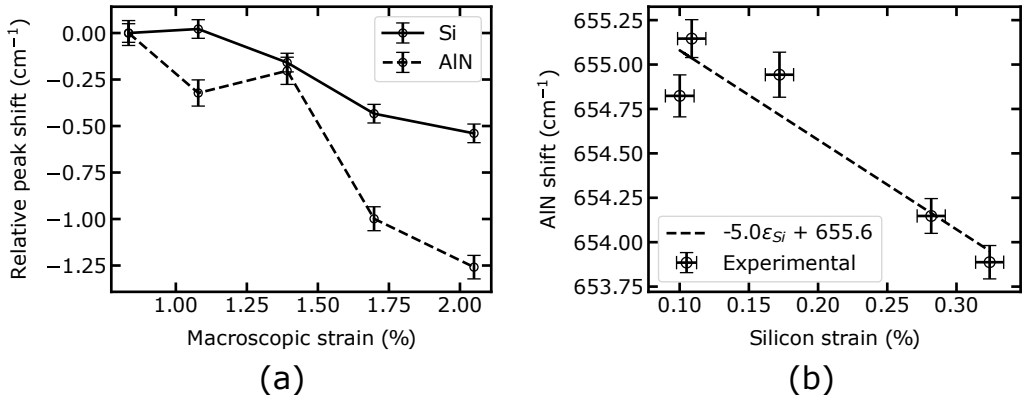


Figure 5.10: (a) Silicon and AlN Raman peak position as function of uniaxial macroscopic strain for a Si/AlN/Furukawa flexible structure (b) AlN $E_2$ (high) mode as a function of local silicon strain for the initial linear tensile curve. The data point are the first four of the linear part of curve (a)

To asses the validity of our approach through a comparison with literature values, bulge tests were performed on similar samples (800 nm AlN/205 nm Si/Furukawa). A post-mortem snapshot of a biaxial sample in the bulge stage is presented in figure 5.11(a). Under the application of differential pressure on the bulge, a red-shift was observed as seen in figure 5.11(b) for both AlN and Si contributions. The signal from the AlN layer is low as acquisition time were kept short to avoid the loss of focus associated with the creeping of the polymer substrate.

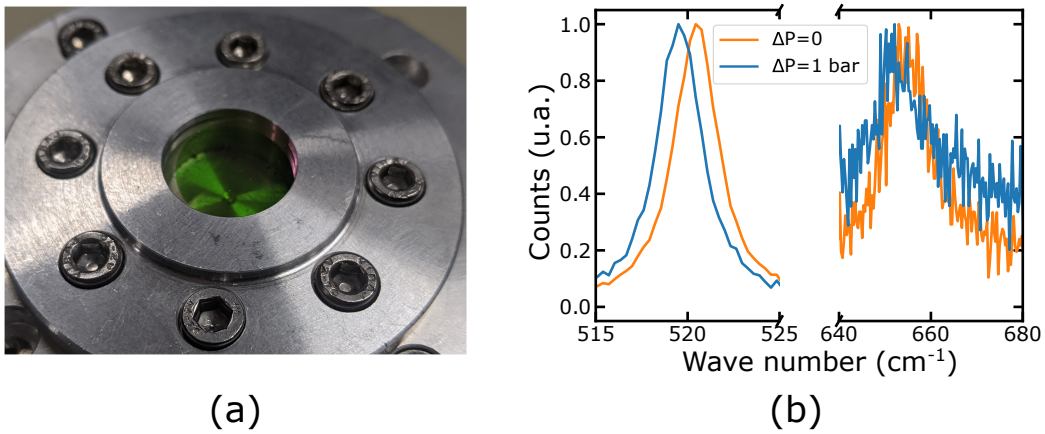


Figure 5.11: Bulge test results of a flexible AlN on silicon structure.(a) Bulge stage with a fractured AlN on silicon on polymer sample (b) Raman spectra for a Si/AlN/Furukawa structure subjected to a bulge test. Signal is acquired in the bulge center

The results from two similar samples are summarized in figure 5.12. The AlN $E_2$ (high) mode shift is plotted against the local silicon strain extracted from the silicon peak shift. A linear fit yields coefficient of 16.8 $\pm$0.4 cm$^{-1}$/% and 14.5 $\pm$ 0.3 cm$^{-1}$/%.

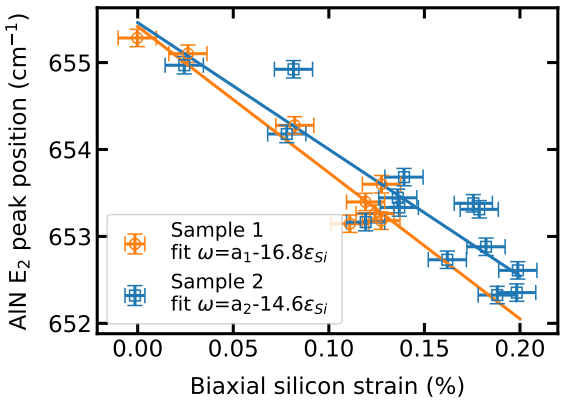


Figure 5.12: AlN $E_2$ mode as a function of local biaxial silicon strain induced with a bulge test.

Now assuming that the strain of the silicon and AlN layer are similar, one can deduce the AlN stress from the generalized Hooke's law :

$$\sigma_{||} = (c_{11} + c_{12} - \frac{2c_{13}^2}{c_{33}})\varepsilon_{||} \tag{5.1}$$

where $\sigma_{||}$ is the in-plane biaxial stress, $\varepsilon_{||}$ the in-plane biaxial strain and $c_{11}$, $c_{12}$, $c_{13}$ and $c_{33}$ the elastic stiffness constants. This hypothesis needs validation. A first unsuccessful attempt was made using Micro Laue X-ray Diffraction to probe both Si and AlN strain simultaneously. Signal acquisition of the AlN layer was challenging and further experiments will be made to overcome the initial issues.

Using the results presented in figure 5.12, the equation 5.1 and a set of elastic coefficients: 410, 140, 100 and 390 GPa [Deger et al., 1998], for $c_{11}$, $c_{12}$, $c_{13}$ and $c_{33}$, respectively, the Raman shift of the $E_2$(high) AlN phonon mode can be represented as a function of AlN biaxial stress.

The AlN Raman shift is then represented as a function of the calculated AlN biaxial stress in figure 5.13 for the two samples. Two Raman stress-factors can be obtained by fitting the respective datasets, *i.e.* $-3.9\,\mathrm{cm}^{-1}$/GPa and $-3.3\,\mathrm{cm}^{-1}$/GPa. These results are highly dependent on the set of elastic constant. For example using 410, 140, 100 and 190 GPa [Davydov et al., 1998], for $c_{11}$, $c_{12}$, $c_{13}$ and $c_{33}$, respectively, would yield $-4.9\,\mathrm{cm}^{-1}$/GPa and $-4.2\,\mathrm{cm}^{-1}$/GPa Raman stress factors.

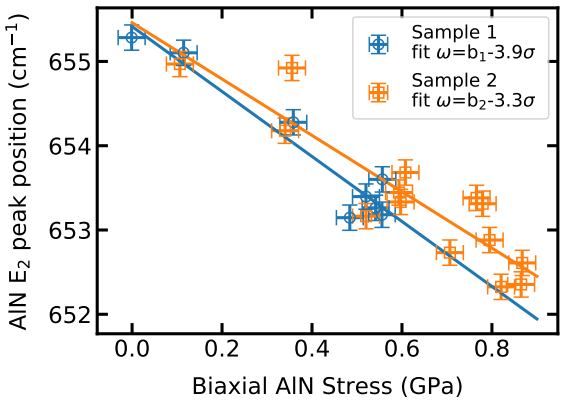


Figure 5.13: AlN $E_2$ phonon mode shift as a function of biaxial stress in the 800 nm thick AlN layer. AlN and silicon strained are assumed equal and the strain is computed from the Raman silicon shift. AlN stress is calculated using elastic stiffness constants from [Deger et al., 1998]

The mean value obtained with elastic constants from Deger et al. is presented with other values from the literature in table 5.1. The experimental value obtained here is well within the range of previous work. This

value dispersion comes from the different elastic coefficients used, which in turn are very dependent on the AlN growth technique [Österlund et al., 2019]. Indeed, the growth technique, and even the growth recipe for a given technique, has a strong influence on the crystal quality, texture and dislocation density [Yang et al., 2011]. Furthermore different methods were used to induce strain in AlN films: wafer bending [Sarua et al., 2004], lattice parameter mismatch with a buffer layer [Gleize et al., 2003], AlN layer thickness variation [Prokofyeva et al., 2001], changes in growth parameters [Trodahl et al., 2006] and layers with different CTE underneath AlN [Yang et al., 2011]. Most of these methods require the preparation of multiple samples, down time in-between data acquisition and additional strain characterization techniques such as XRD. All this requirements induce uncertainty in the measurement mainly because of thermalization issues that are time and material dependent. The Raman biaxial stress-factor found in this work is comparable to the values found in the literature and our method requires only one sample and a single continuous acquisition with an internal silicon reference sample. This eliminates a lot of uncertainty and simplify the process. To ensure an even more precise measurement, a stiffer substrate would be needed to decrease creeping and relaxation phenomena, enabling longer acquisition time. The methods we applied on a sputtered AlN layer can be adapted to other crystalline semiconductor or piezoelectric material as long as they can be grown or deposited on a silicon wafer, used as an etch stop layer and undergo our transfer process.

| Reference | Raman stress factor ($cm^{-1}$/GPa) | Fabrication method |
|---|---|---|
| [Wagner and Bechstedt, 2000] | $-2.56$ | *ab initio* calculation |
| [Trodahl et al., 2006] | $-2.9 \pm 0.3$ | Sputtering (PVD) |
| [Sarua et al., 2002] | $-3$ | Molecular beam epitaxy |
| [Gleize et al., 2003] | $-3.39 \pm 0.55$ | Molecular beam epitaxy |
| **This work** | $-3.6 \pm 0.3$ | Sputtering (PVD) |
| [Yang et al., 2011] | $-4.04$ | Metal organic vapor phase epitaxy and hydrid vapor phase epitaxy |
| [Prokofyeva et al., 2001] | $-4.5 \pm 1.0$ | Gas-source molecular beam epitaxy |

Table 5.1: Raman-stress factor for AlN thin films obtained in this study and in the literature

## Conclusion

As a conclusion, we have successfully transferred adapted our transfer method to (0002) oriented AlN thin-films and MEMS devices. The process was also adapted to actual devices based on AlN layer, proving its versatility. In situ Raman measurements of AlN On Polymer samples undergoing uniaxial and biaxial tensile strains were performed and an increasing shift of the E2 peak position was observed when increasing the applied uniaxial strain. Thus, the transmission of a controlled deformation from the flexible substrate to the AlN layer is possible. The use of buried silicon layer as an internal reference allowed to link AlN strain to the $E_2$ (high) phonon frequency shift. A Raman-stress factor comparable to literature value was determined

with this method. It can be adapted to determine experimental value of stress factor for a variety of material and stress configuration. Further X-ray *in-situ* measurement are needed to validate the hypothesis that silicon and AlN strains change is the same manner. These results illustrated the versatility of a transfer process initially developed with silicon thin film and gave an example of an application of our transfer process. This method can be used for other types of piezoelectric materials such as $LiNbO_3$, $LiTaO_3$ , PZT; or even semiconductor materials such as GaN, AlGaN, Ge, GeSn. Future work will involve the measurement of bulk acoustic wave devices fabricated using these thin film strain gauges for the purpose of characterizing the evolution of the electromechanical properties of the piezoelectric films as a function of strain.

## References

Aardahl, C. L., Rogers, J. W., Yun, H. K., Ono, Y., Tweet, D. J. and Hsu, S. T. [1999]. Electrical properties of AlN thin films deposited at low temperature on Si(100), *Thin Solid Films* **346**(1): 174–180.
**URL:** *http://www.sciencedirect.com/science/article/pii/S0040609098016186* 162

Argoud, M. [2012]. *Mécanismes de collage et de transfert de films monocristallins dans des structures à couches de polymères*, phdthesis, Université de Grenoble.
**URL:** *https://tel.archives-ouvertes.fr/tel-00848111/document* 166

Brien, V., Miska, P., Bolle, B. and Pigeat, P. [2007]. Columnar growth of ALN by r.f. magnetron sputtering: Role of the $\{101^{\bar{}}3\}$ planes, *Journal of Crystal Growth* **307**(1): 245–252.
**URL:** *http://www.sciencedirect.com/science/article/pii/S0022024807005817* 162

Chen, S.-Y. [1996]. Texture evolution and electrical properties of oriented PZT thin films, *Materials Chemistry and Physics* **45**(2): 159–162.
**URL:** *http://www.sciencedirect.com/science/article/pii/0254058496800952* 162

Cibert, J., André, R., Deshayes, C., Dang, L. S., Okumura, H., Tatarenko, S., Feuillet, G., Jouneau, P. H., Mallard, R. and Saminadayar, K. [1992]. Piezoelectric fields in CdTe-based heterostructures, *Journal of Crystal Growth* **117**(1): 424–431.
**URL:** *http://www.sciencedirect.com/science/article/pii/002202489290788K* 162

Davydov, V. Y., Kitaev, Y. E., Goncharuk, I. N., Smirnov, A. N., Graul, J., Semchinova, O., Uffmann, D., Smirnov, M. B., Mirgorodsky, A. P. and Evarestov, R. A. [1998]. Phonon dispersion and Raman scattering in hexagonal GaN and AlN, *Phys. Rev. B* **58**(19): 12899–12907. Publisher: American Physical Society.
**URL:** *https://link.aps.org/doi/10.1103/PhysRevB.58.12899* 170

Deger, C., Born, E., Angerer, H., Ambacher, O., Stutzmann, M., Hornsteiner, J., Riha, E. and Fischerauer, G. [1998]. Sound velocity of AlxGa1-xN thin films obtained by surface acoustic-wave measurements, *Appl. Phys. Lett.* **72**(19): 2400–2402. Publisher: American Institute of Physics.
**URL:** *https://aip.scitation.org/doi/10.1063/1.121368* 170

Fei, C., Liu, X., Zhu, B., Li, D., Yang, X., Yang, Y. and Zhou, Q. [2018]. AlN piezoelectric thin films for energy harvesting and acoustic devices, *Nano Energy* **51**: 146–161.
**URL:** *http://www.sciencedirect.com/science/article/pii/S2211285518304579* 162

Giordano, C., Ingrosso, I., Todaro, M. T., Maruccio, G., De Guido, S., Cingolani, R., Passaseo, A. and De Vittorio, M. [2009]. AlN on polysilicon piezoelectric cantilevers for sensors/actuators, *Microelectronic Engineering* **86**(4): 1204–1207.
**URL:** *http://www.sciencedirect.com/science/article/pii/S0167931708007004* 162

Gleize, J., Renucci, M. A., Frandon, J., Bellet-Amalric, E. and Daudin, B. [2003]. Phonon deformation potentials of wurtzite AlN, *Journal of Applied Physics* **93**(4): 2065–2068. Publisher: American Institute of Physics.
**URL:** *https://aip.scitation.org/doi/abs/10.1063/1.1539531* 166, 171

Gubinyi, Z., Batur, C., Sayir, A. and Dynys, F. [2008]. Electrical properties of PZT piezoelectric ceramic at high temperatures, *Journal of Electroceramics* **2**(20): 95–105.
**URL:** *https://www.infona.pl//resource/bwmeta1.element.springer-73eba2dd-b50d-3130-835f-472aa54cead0* 162

Kume, S., Yasuoka, M., Lee, S.-K., Kan, A., Ogawa, H. and Watari, K. [2007]. Dielectric and thermal properties of AlN ceramics, *Journal of the European Ceramic Society* **27**(8): 2967–2971.
**URL:** *http://www.sciencedirect.com/science/article/pii/S0955221906006479* 162

Look, D. C., Reynolds, D. C., Sizelove, J. R., Jones, R. L., Litton, C. W., Cantwell, G. and Harsch, W. C. [1998]. Electrical properties of bulk ZnO, *Solid State Communications* **105**(6): 399–401.
**URL:** *http://www.sciencedirect.com/science/article/pii/S0038109897101454* 162

McNeil, L. E., Grimsditch, M. and French, R. H. [1993]. Vibrational Spectroscopy of Aluminum Nitride, *Journal of the American Ceramic Society* **76**(5): 1132–1136. _eprint: https://ceramics.onlinelibrary.wiley.com/doi/pdf/10.1111/j.1151-2916.1993.tb03730.x.
**URL:** *https://ceramics.onlinelibrary.wiley.com/doi/abs/10.1111/j.1151-2916.1993.tb03730.x* 166

Österlund, E., Kinnunen, J., Rontu, V., Torkkeli, A. and Paulasto-Kröckel, M. [2019]. Mechanical properties and reliability of aluminum nitride thin films, *Journal of Alloys and Compounds* **772**: 306–313.
**URL:** *http://www.sciencedirect.com/science/article/pii/S0925838818333000* 171

Piazza, G., Stephanou, P. J. and Pisano, A. P. [2007]. Single-Chip Multiple-Frequency ALN MEMS Filters Based on Contour-Mode Piezoelectric Resonators, *Journal of Microelectromechanical Systems* **16**(2): 319–328. Conference Name: Journal of Microelectromechanical Systems. 162

Prokofyeva, T., Seon, M., Vanbuskirk, J., Holtz, M., Nikishin, S. A., Faleev, N. N., Temkin, H. and Zollner, S. [2001]. Vibrational properties of AlN grown on (111)-oriented silicon, *Phys. Rev. B* **63**(12): 125313.
**URL:** *https://link.aps.org/doi/10.1103/PhysRevB.63.125313* 167, 171

Sarua, A., Kuball, M. and Van Nostrand, J. E. [2002]. Deformation potentials of the E2(high) phonon mode of AlN, *Appl. Phys. Lett.* **81**(8): 1426–1428. Publisher: American Institute of Physics.
**URL:** *https://aip.scitation.org/doi/10.1063/1.1501762* 171

Sarua, A., Kuball, M. and Van Nostrand, J. E. [2004]. Phonon deformation potentials of the E2(high) phonon mode of AlxGa1-xN, *Appl. Phys. Lett.* **85**(12): 2217–2219. Publisher: American Institute of Physics.
**URL:** *https://aip.scitation.org/doi/10.1063/1.1793338* 167, 171

SHIMADA, K., SOTA, T., SUZUKI, K. and OKUMURA1, H. [1998]. First-Principles Study on Piezoelectric Constants in Strained BN, AlN, and GaN, *Jpn. J. Appl. Phys.* **37**(12A): L1421. Publisher: IOP Publishing.
**URL:** *https://iopscience.iop.org/article/10.1143/JJAP.37.L1421/meta* 162

Trodahl, H. J., Martin, F., Muralt, P. and Setter, N. [2006]. Raman spectroscopy of sputtered AlN films: E2(high) biaxial strain dependence, *Appl. Phys. Lett.* **89**(6): 061905. Publisher: American Institute of Physics.
**URL:** *https://aip.scitation.org/doi/full/10.1063/1.2335582* 167, 171

Wagner, J.-M. and Bechstedt, F. [2000]. Phonon deformation potentials of α-GaN and -AlN: An ab initio calculation, *Appl. Phys. Lett.* **77**(3): 346–348. Publisher: American Institute of Physics.
**URL:** *https://aip.scitation.org/doi/10.1063/1.127009* 171

Wang, X. and Yoshikawa, A. [2004]. Molecular beam epitaxy growth of GaN, AlN and InN, *Progress in Crystal Growth and Characterization of Materials* **48-49**: 42–103.
**URL:** *http://www.sciencedirect.com/science/article/pii/S0960897405000082* 162, 164

Yang, S., Miyagawa, R., Miyake, H., Hiramatsu, K. and Harima, H. [2011]. Raman Scattering Spectroscopy of Residual Stresses in Epitaxial AlN Films, *Appl. Phys. Express* **4**(3): 031001. Publisher: IOP Publishing.
**URL:** *https://iopscience.iop.org/article/10.1143/APEX.4.031001/meta* 166, 167, 171

# General conclusion

This thesis explored an alternative and original method to produce strained semi-conductor thin film and offered a new platform for the study of strain engineering in semi-conductors using flexible polymer substrates. The main issues were to evaluate the possibility of fabricating a permanently strained semi-conductor thin film using first a temporary bonding and transfer on a flexible polymer substrate and then a direct bonding step on a rigid substrate.

The first challenge was to transfer sc-Si films of controlled quality and dimension from commercial SOI onto various polymer substrates. The transfer was achieved by engineering the adherence of different interfaces during temporary bonding step. sc-Si films of thickness ranging from 18 nm to 205 nm were transferred on different types of adhesive flexible structures (glue, dicing tapes, PDMS). Full 200 mm diameter wafer can be transferred as well as millimetric silicon patterns. Selective chemical etching was used to obtain smooth edge at the nanometer level. Also a control of the release interface during thin film transfer is essential to transfer film of lower thickness (*i.e.*, 100 nm and below).

Then several experimental mechanical characterization setups for SOP material were used to determine the influence of fabrication processes on mechanical behavior. Uniaxial and biaxial tensile set-up were used along local strain characterization techniques, namely XRD, Raman spectroscopy, μLaue and DIC. The maximum strain achievable was greatly improved by having smoother pattern edges and reached up to 3.1% for uniaxial sample oriented along [100] direction. On the other hand, decreasing the thickness of the silicon thin film did not improve the maximum strain. Decreasing the surface area of silicon pattern can be another method to decrease the elastic energy needed to strain the structure in future study. This would eliminate any potential surface changes due to different transfer processes while providing a wider range of dimensions. The strain homogeneity and crystalline quality of SOP samples was also assessed during biaxial and uniaxial tensile tests. Overall, samples presented a homogeneous deformation on the whole silicon surface and no signs of plastic strain was observed. However fractures were often observed in silicon layers well before the maximum strain was reached. They did not prevent local strain increase but are the origin of a sublinear relationship between the macroscopic sample strain and local silicon strain. These results validate the use of a mechanical characterization platform for crystalline semiconductor material on flexible substrate. This platform was used to improve the mechanical properties of SOP material but one could use it for various applications in strain engineering or flexible electronics.

Development of this platform also allowed to combine mechanical stretching of SOP material with direct bonding method to obtain a proof of concept of a strained silicon film reported from a flexible polymer to a rigid oxidized silicon carrier. The use of μLaue allowed one to obtain a precise state of the reported silicon crystal. A significant strain (up to 0.45%) was achieved on a surface of several square micrometers. Further studies are needed to determine the origin of cracks in order to increase the surface of pristine strained film transferred. Different parameters and experimental setups can also be explored to tune the strain tensor of the reported thin film as it was done for *in situ* tensile test on flexible substrates.
Finally the application of the transfer process presented in this thesis to AlN layer showed the versatility of

the process for semiconductors and piezoelectric materials. The process was smoothly adapted to transfer sputtered AlN layers of thickness ranging from 200 nm to 1600 nm onto flexible polymer substrates. All the previous developments for transfer and strain characterization of silicon were used in the case of AlN to determine the Raman stress coefficients. In the case of biaxial stress, the results are in perfect agreement with the values found in the literature and are obtained in a repeatable way with a minimum number of samples. Moreover the versatility of our transfer process and mechanical test benches allow one to characterize AlN under uniaxial stress, something that has yet to be found in the literature.

To conclude, a really versatile process for semi-conductor was presented in this thesis. All the major steps were validated. Using an intermediate transfer on polymer flexible substrate, a strained silicon film on oxide was produced. Further studies are needed to increase the final strain level and determine the strain and bonding interface evolution during the transfer from flexible to a rigid substrate. The detailed transfer process and the mechanical characterization tools presented in this work should greatly facilitate any further development. The high strain values and different strain orientations obtained on flexible substrates are promising for future production of permanently strained materials. The application of the process to aluminium nitride offers interesting possibilities as it would be just as easy to adapt it to other piezoelectric materials or semiconductors (*e.g.*, Ge, GeSn, chLiTaO3(LTO), GaN or AlGaN).

# Appendix A

# Strain Characterization

The theoretical basis of the strain characterization method used in this work will be given below. Raman spectroscopy, X-ray Diffraction, Micro Laue X-ray Diffraction and Digital Image Correlation were used to probe material strain and stress at different scale and configuration. It is important to understand how strain is derived using theses different techniques to know the limitation and assumption associated with the results that will be presented later.

## A.1 Raman spectroscopy

Raman spectroscopy is chemical analysis technique which provide information on chemical structure, phase, stress or strain and impurity. It is based on light interaction with molecules. When an incident monochromatic light beam interacts with a molecule, photons can either be reflected,adsorbed or scattered. The scattering is in vast majority elastic but a small part of the incident photons go trough inelastic scattering. Raman spectroscopy relies on the later phenomena. The different interactions are presented in figure A.1(b). A schematic of a Raman spectrometer is presented in figure A.1(a). A laser beam is focused on a sample using a confocal lens. The scattered light is analyzed by a grating and collected on a detector to quantify the photon by wave-number shift with respect to the incident beam. A wave-number is defined as the inverse of a wavelength is usually expressed in inverse centimeter.

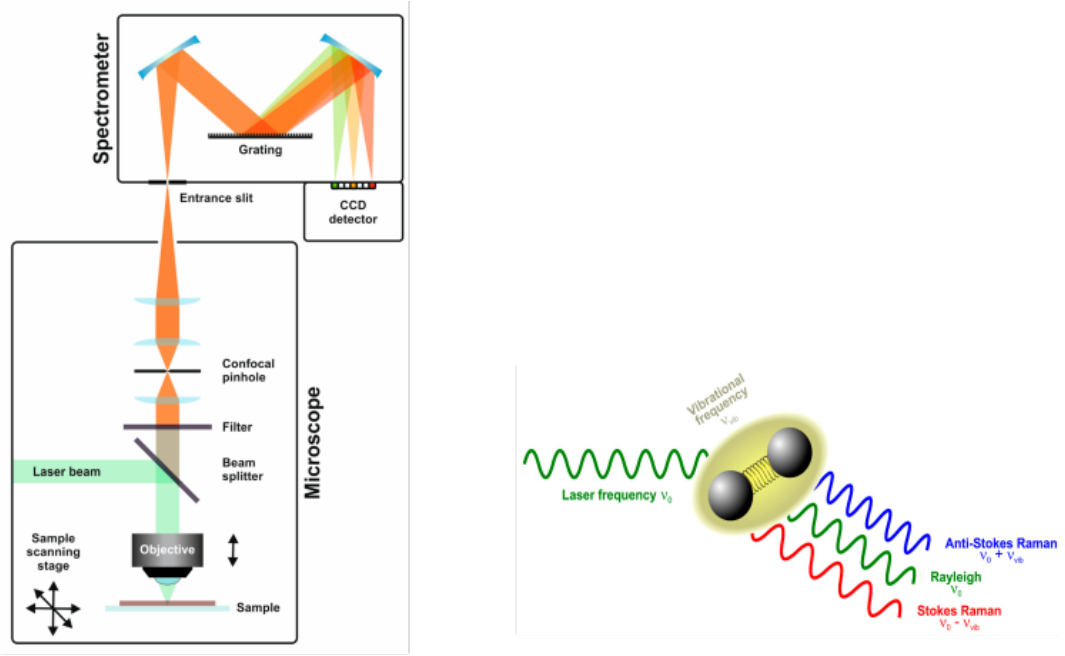


Figure A.1: (a) Raman spectrometer schematic [Schmid and Dariz, 2019] (b) Raman interactions

The Raman spectroscopy detects the phonon frequency of the semiconductors by the inelastic scattering of photons to emit phonons. At the presence of strain, the triply degenerate optical phonons split their vibrating frequencies, [Sui and Herman, 1993] and the shift of Raman frequency can be observed. Ganesan et al. detailed the effect of strain or stress Raman modes. The frequency of the three Raman modes can be obtained by solving the so-called secular equation presented in equation A.1

$$\begin{vmatrix} p\varepsilon 11 + q(\varepsilon 22 + \varepsilon 33) - \lambda & 2r\varepsilon_{12} & 2r\varepsilon 13 \\ 2r\varepsilon 21 & p\varepsilon 22 + q(\varepsilon 33 + \varepsilon 11) - \lambda & 2r\varepsilon 23 \\ 2r\varepsilon 31 & 2r\varepsilon 32 & p\varepsilon 33 + q(\varepsilon 11 + \varepsilon 22) - \lambda \end{vmatrix} = 0 \tag{A.1}$$

Where $\varepsilon_{ij}$ are the strain tensor component given in the crystal reference frame where X = [100], Y = [010] and Z = [001]. $p$, $q$ and $r$ are material constant, the phonon deformation potential. The difference in Raman frequency in each mode compared to the unstrained state can be calculated from the eigenvalue $\lambda_j$, as detailed in equation A.2:

$$\lambda_j = \omega_j^2 - \omega_{j0}^2 \text{ or } \delta\omega_j = \omega_j - \omega_{j0} \approx \frac{\lambda_j}{2\omega_{j0}} \tag{A.2}$$

The polarization direction of each mode, in the presence of stress, is described by the corresponding eigenvectors of the secular equation.

In the case of uniaxial stress σ along the [100] direction, the strain components are obtained by Hooke's law. $\varepsilon_{11} = S_{11}\sigma$, $\varepsilon_{22} = S_{12}\sigma$ and $\varepsilon_{33} = S_{12}\sigma$ where $S_{ij}$ are the elastic compliance tensor components. Solving equation A.1 and A.2 leads to :

$$\begin{aligned} \Delta\omega_1 &= \frac{\lambda_1}{2\omega_0} = \frac{1}{2\omega_0}\left(pS_{11} + 2qS_{12}\right)\sigma \\ \Delta\omega_2 &= \frac{\lambda_2}{2\omega_0} = \frac{1}{2\omega_0}\left[pS_{12} + q(S_{11} + S_{12})\right]\sigma \\ \Delta\omega_3 &= \frac{\lambda_3}{2\omega_0} = \frac{1}{2\omega_0}\left[pS_{12} + q(S_{11} + S_{12})\right]\sigma \end{aligned} \tag{A.3}$$

So, for back scattering from a (001) silicon surface, only the third Raman mode is observed and the

relation between the shift of this mode and the stress is given by the third relation in equation A.3 [Wolf, 1996]. Knowing the phonon deformation potential and silicon elastic compliance tensor [Hopcroft et al., 2010], one can write the relation between the change in frequency of the third raman mode and the stress or strain:

$$\Delta\omega_3 = b\varepsilon \tag{A.4}$$

Where $b$ is a strain/shift coefficient which value depends on the crystal and stress orientation. The different value found in the literature for (100) silicon under uniaxial or biaxial stress are presented in table A.1.

| Stress | Strain shift coefficient $b$ ($cm^{-1}$/%) | Temperature (K) | Wavelength (nm) | Reference |
|---|---|---|---|---|
| Uniaxial [110] | -337 | RT | 632.7 | [Anastassakis et al., 1970] |
| | -339 | RT | 647.1 | [Chandrasekhar et al., 1978] |
| | -389 | 110 | 1064 | [Anastassakis et al., 1990] |
| | -336 | RT | 488 | [Peng et al., 2009] |
| | -343 | RT | 458/364 | [Ureña et al., 2013] |
| Uniaxial [100] | -217 | RT | - | [Romain-Latu, 2006] |
| | -260 | RT | - | [De Wolf et al., 1996] |
| Biaxial | -733 | RT | 488 | [Peng et al., 2009] |
| | -723 | RT | 632.7 | [Anastassakis et al., 1970] |
| | -832 | 110 | 1064 | [Anastassakis et al., 1990] |
| | -715 | 295 | 457.9 | [Lockwood and Baribeau, 1992] |
| | -815 | RT | 488 | [Tsang et al., 1994] |
| | -455 | RT | 514 | [Meyer et al., 1991] |

Table A.1: Coefficient for stress and strain computation from silicon Raman shift as a function of crystal and stress orientation. These value are given for a (100) oriented silicon surface.

Strain characterization using Raman spectroscopy is based on a first order development and is valid for small elastic deformation ($\approx 1\%$). For example, with Germanium, a non-linearity in the strain/shift relation is absorbed that can lead to some over estimation of the strain [Gassenq et al., 2017]. Raman is precise and fast method to observe strain in semiconductor material although some strong hypothesis are needed to compute strains value from Raman shifts. This calls for direct methods of measurement to confirm those hypothesis as x-ray based techniques.

## A.2 X-ray diffraction

### A.2.1 Monochromatic X-ray Diffraction

X-ray Diffraction (XRD) allows a direct measurement of a crystal strain thanks to Bragg's Law :

$$n\lambda = 2d_{hkl}\ sin\ \theta \tag{A.5}$$

Where $\lambda$ is the wavelength of the incident beam, $d_{hkl}$ the interplannar distance for (hkl) planes and $\theta$ the angle of the incident beam with respect to the crystal surface. To compute the full strain tensor of a crystal, it is necessary to observe several Bragg's peaks. In a crystal, the intensity of the peaks is described by the structure factor :

$$F_{hkl} = \sum_{j=1}^{N} f_j e^{[-2\pi i(hx_j+ky_j+lz_j)]} \tag{A.6}$$

where f is the dispersion factor, $x_j$, $y_j$ et $z_j$ the coordinates of the j indice atom contained in the crystal lattice expressed in the crystalline system. In the case of silicon, the crystal lattice is a diamond lattice.It's a Face Centered Cubic FCC lattice with half of the tetrahedral interstitial sites occupied. In this case, equation A.6 gives the following extinction rules: (111), (220), (331), (400), (331) and (442).

### A.2.2 Micro Laue X-ray Diffraction

With standard monochromatic X-ray diffraction methods a wide range of 2θ angle is needed to obtain several Bragg peak and reconstruct a full strain tensor of the crystal. Some technical difficulty arise from this methods with a thin film on a flexible substrate. Alignment can be difficult to maintain during the time necessary to collect enough photons. That is why µLaue is a powerful method for SOP mechanical characterization. It's an historical diffraction method discovered by Max Von Laue. It has long been used only as an alignment method but regained some interest thanks to polychromatic synchrotron sources In the case of a perfect crystal.In the reciprocal space, an incident beam has a wave vector $\vec{k_i}$ and the diffracted beam has a wave vector of the same length (energy) but of different direction$\vec{k_f}$. The Ewald sphere is defined by the possible extremity of the diffusion vector $\vec{Q} = \vec{k_f} - \vec{k_i}$. $\vec{Q}$ and has the same origin as the reciprocal space of the crystal. The diffracting planes are the the one intercepting the Ewald sphere (see figure A.2)

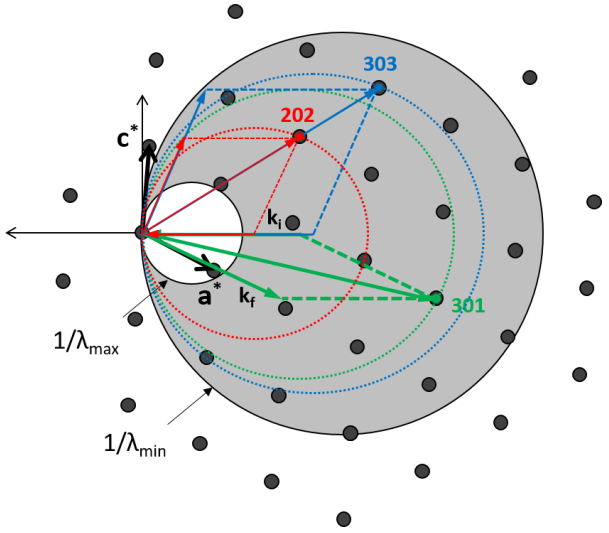


Figure A.2: Intersection of Ewald spheres of a polycrhomatic beam with atomic position in the crystal reciprocal space

With a white (i.e. poly-chromatic)incident X-ray beam at a fixed angle, the diameter of the Ewald sphere will vary between $1/\pi\lambda_{max}$ and $1/\pi\lambda_{min}$. This method, discovered by Laue, Friedrich and Knipping in 1912 with the use of a X-ray tube and a $CuSO_4$ crystal. The results is a Laue diagram presenting several diffraction peak corresponding to the intersection between the Sphere and the crystal plane in the reciprocal space. The figure A.3 presents a diffraction pattern obtain by Friedrich et al. in 1912 of a ZnS crystal, as well as the diffraction pattern of a (100) germanium crystal obtained on beamline BM32 at ESRF.

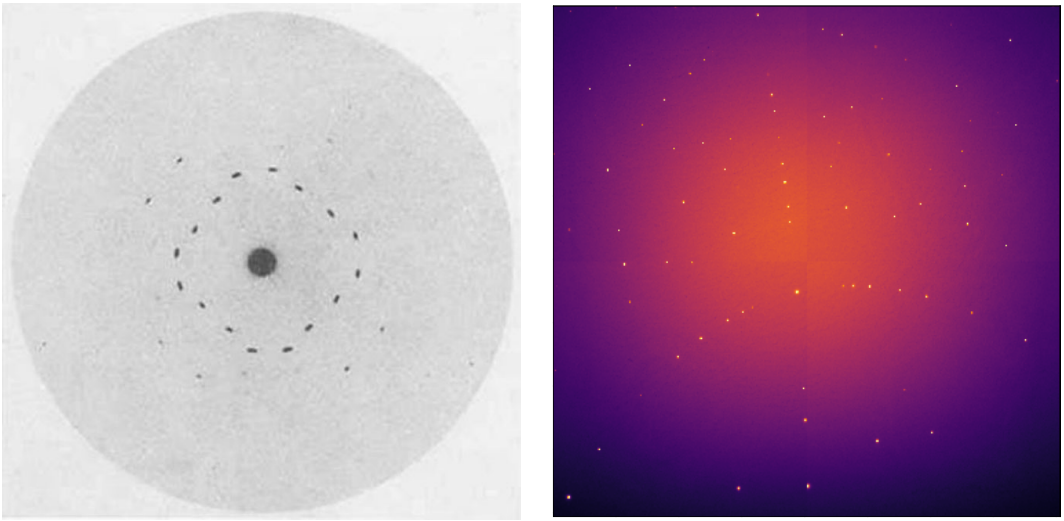


Figure A.3: (a) Laue diagram of ZnS [Friedrich et al., 1912] (b) (100) Germanium Laue diagram captured on BM32 beamline at ESRF

The µLaue provides a measurement of all the components the deviatoric strain tensor as well as the three Euler angles describing the crystal orientation without any a priori knowledge.

However, an additional hypothesis is needed to calculate the missing hydrostatic part of the strain tensor and thus the full strain tensor [Tardif et al., 2016]. The origin of the phenoma is illustrated in figure A.4. Here the stress perpendicular to the surface was considered to be null. Using Voigt notation, the $\sigma_{33}$

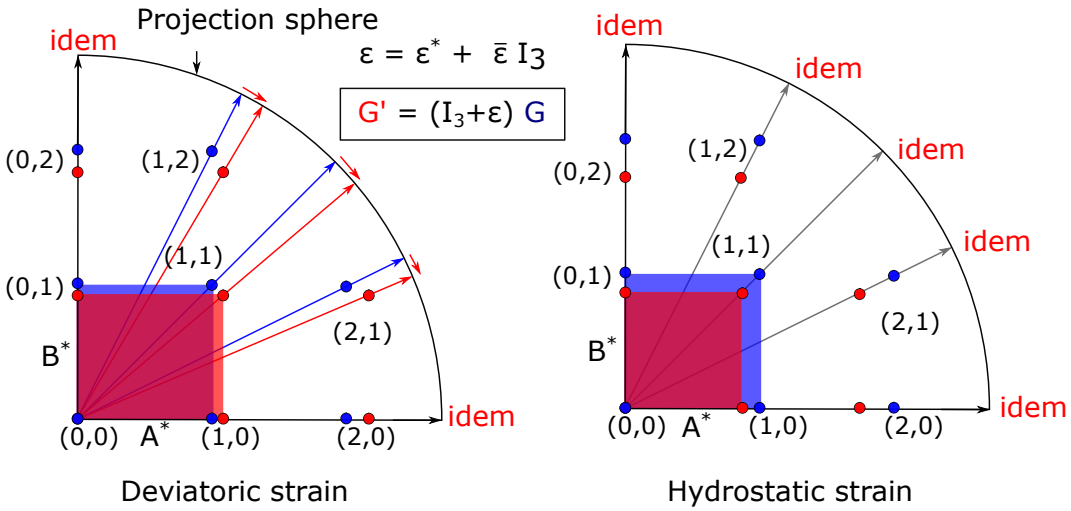


Figure A.4: Effect of deviatoric and hydrostatic strain on µLaue pattern of a crystal

component of the stress can be set to 0 in the second order generalized Hooke's law :

$$\begin{pmatrix} \sigma_{11} \\ \sigma_{22} \\ \sigma_{33}=0 \\ \sigma_{23} \\ \sigma_{13} \\ \sigma_{12} \end{pmatrix} = \begin{pmatrix} c_{11} & c_{12} & c_{12} & 0 & 0 & 0 \\ c_{12} & c_{11} & c_{12} & 0 & 0 & 0 \\ c_{12} & c_{12} & c_{11} & 0 & 0 & 0 \\ 0 & 0 & 0 & c_{44} & 0 & 0 \\ 0 & 0 & 0 & 0 & c_{44} & 0 \\ 0 & 0 & 0 & 0 & 0 & c_{44} \end{pmatrix} \begin{pmatrix} \varepsilon_{11} \\ \varepsilon_{22} \\ \varepsilon_{33} \\ 2\varepsilon_{23} \\ 2\varepsilon_{13} \\ 2\varepsilon_{12} \end{pmatrix} \tag{A.7}$$

Where $\sigma$ is the stress tensor and $\varepsilon$ the strain tensor. The subscripts 1,2 and 3 indicates the [100], [010] and [001] directions in the crystal reference frame for $\varepsilon$ and $\sigma$. $c_{11}$, $c_{12}$ and $c_{44}$ are silicon elastic constants. $c_{11}$ = 165.5 GPa, $c_{12}$ = 63.9 GPa and $c_{44}$ = 79.5 GPa [Hopcroft et al., 2010]. In particular:

$$\sigma_{33} = c_{12}(\varepsilon_{11}+\varepsilon_{22}) + c_{11}\varepsilon_{33} = 0 \tag{A.8}$$

The relation between the full strain tensor and the deviatoric strain tensor $\varepsilon'$ is

$$\varepsilon_{ij} = \varepsilon'_{ij} + \frac{\varepsilon_h}{3}\delta_{ij} \tag{A.9}$$

Where $\varepsilon_h$ is the hydrostatic strain. Thus from equation (A.8) and (A.9) it follows that

$$\varepsilon_h = 3\frac{c_{12}(\varepsilon'_{11}+\varepsilon'_{22}) + c_{11}\varepsilon'_{33}}{2c_{12}+c_{11}} \tag{A.10}$$

Thus all value of the full strain tensor could be computed using Eq. (A.9) and (A.10).

## A.3 Digital image correlation

Digital Image Correlation (DIC) is a full-field non-destructive and contact-less method that allows to determine a field of displacement and strain by comparing different images of a sample taken at different times. In this work, two dimensional DIC is used. The sample is covered is distinguishable patterns (speckles of white paint in this study). A Region Of Interest (ROI) is defined on the images. These area can either be defined as the camera full field or as smaller area as long as significant number of distinguishable patterns are visible on the chosen region. This ROI is then subdivided in smaller Zone Of Interest (ZOI). An example of an image used for DIC is presented in figure A.5. Speckles of white paint are clearly visible as well as two distinct areas that can be analyzed separately.

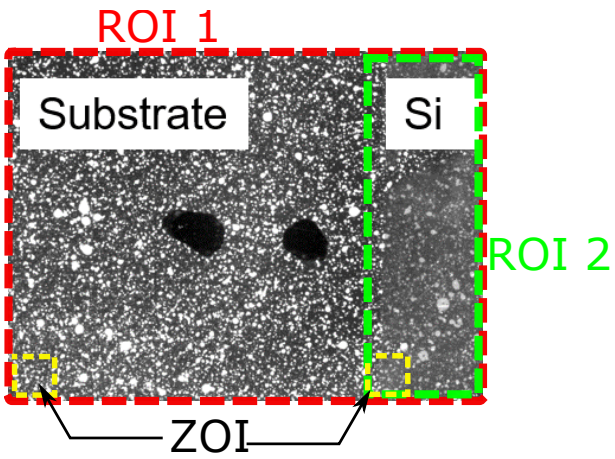


Figure A.5: Example of different ROI and ZOI in an image used for DIC

From these ZOI, a correlation is made between images taken at various steps of the analysis using the equation A.11

$$g[x + u(x)] = f(x) \tag{A.11}$$

Where x is the position in the image reference frame, u(x) the displacement field, g(x) the latest image and f(x) the initial image. The formalism used to obtain the displacement field will be described here. In this work, the calculation were made using a dedicated software: CORRELI developed under a license from LMT Cachan [Hild and Roux, 2006]. Finally the strain tensor components ($\varepsilon_{ij}$) in the studied plane can be extracted from the displacements field using equation A.12

$$\varepsilon_{ij} = \frac{1}{2}\left(\frac{\delta u_i}{\delta j} + \frac{\delta u_j}{\delta_i}\right) \tag{A.12}$$

## References

Anastassakis, E., Cantarero, A. and Cardona, M. [1990]. Piezo-Raman measurements and anharmonic parameters in silicon and diamond, *Physical Review B* **41**(11): 7529. Number: 11. III

Anastassakis, E., Pinczuk, A., Burstein, E., Pollak, F. H. and Cardona, M. [1970]. Effect of static uniaxial stress on the Raman spectrum of silicon, *solid state Communications* **8**(2): 133–138. Number: 2. III

Chandrasekhar, M., Renucci, J. B. and Cardona, M. [1978]. Effects of interband excitations on Raman phonons in heavily doped $n\ensuremath{-}\mathrm{Si}$, *Phys. Rev. B* **17**(4): 1623–1633. Number: 4 Publisher: American Physical Society.
**URL:** *https://link.aps.org/doi/10.1103/PhysRevB.17.1623* III

De Wolf, I., Maes, H. E. and Jones, S. K. [1996]. Stress measurements in silicon devices through Raman spectroscopy: Bridging the gap between theory and experiment, *Journal of Applied Physics* **79**(9): 7148–7156. Number: 9.
**URL:** *https://aip.scitation.org/doi/10.1063/1.361485* III

Friedrich, W., Knipping, P. and Laue, M. v. [1912]. *Interferenz-Erscheinungen bei Röntgenstrahlen*, Verl. der Kgl. Bayer. Akad. der Wiss., München. OCLC: 230701273. xi, IV, V

Ganesan, S., Maradudin, A. A. and Oitmaa, J. [1970]. A lattice theory of morphic effects in crystals of the diamond structure, *Annals of Physics* **56**(2): 556–594. Number: 2. II

Gassenq, A., Tardif, S., Guilloy, K., Duchemin, I., Pauc, N., Hartmann, J. M., Rouchon, D., Widiez, J., Niquet, Y. M., Milord, L., Zabel, T., Sigg, H., Faist, J., Chelnokov, A., Rieutord, F., Reboud, V. and Calvo, V. [2017].

Raman-strain relations in highly strained Ge: Uniaxial ⟨100⟩, ⟨110⟩ and biaxial (001) stress, *Journal of Applied Physics* **121**(5): 055702. Number: 5.
**URL:** *http://aip.scitation.org/doi/10.1063/1.4974202* III

Hild, F. and Roux, S. [2006]. Digital Image Correlation: from Displacement Measurement to Identification of Elastic Properties - a Review, *Strain* **42**(2): 69–80.
**URL:** *http://doi.wiley.com/10.1111/j.1475-1305.2006.00258.x* VII

Hopcroft, M. A., Nix, W. D. and Kenny, T. W. [2010]. What is the Young's Modulus of Silicon?, *Journal of Microelectromechanical Systems* **19**(2): 229–238. Number: 2. III, VI

Lockwood, D. J. and Baribeau, J.-M. [1992]. Strain-shift coefficients for phonons in ${\mathrm{Si}}_{1\mathrm{\ensuremath{-}}\mathit{x}}$${\mathrm{Ge}}_{\mathit{x}}$ epilayers on silicon, *Phys. Rev. B* **45**(15): 8565–8571. Number: 15.
**URL:** *https://link.aps.org/doi/10.1103/PhysRevB.45.8565* III

Meyer, F., Zafrany, M., Eizenberg, M., Beserman, R., Schwebel, C. and Pellet, C. [1991]. Raman scattering and stress measurements in Si $_{1-x}$ Ge $_{x}$ layers epitaxially grown on Si(100) by ion-beam sputter deposition, *Journal of Applied Physics* **70**(8): 4268–4277. Number: 8.
**URL:** *http://aip.scitation.org/doi/10.1063/1.349104* III

Peng, C.-Y., Huang, C.-F., Fu, Y.-C., Yang, Y.-H., Lai, C.-Y., Chang, S.-T. and Liu, C. W. [2009]. Comprehensive study of the Raman shifts of strained silicon and germanium, *Journal of Applied Physics* **105**(8): 083537. Number: 8.
**URL:** *http://aip.scitation.org/doi/abs/10.1063/1.3110184* III

Romain-Latu, E. [2006]. *Mesures de contraintes par spectroscopie et imagerie Raman dans des dispositifs micro-électroniques*, PhD Thesis, Institut National Polytechnique de Grenoble-INPG. III

Schmid, T. and Dariz, P. [2019]. Raman Microspectroscopic Imaging of Binder Remnants in Historical Mortars Reveals Processing Conditions, *Heritage* **2**(2): 1662–1683. Number: 2 Publisher: Multidisciplinary Digital Publishing Institute.
**URL:** *https://doi.org/10.3390/heritage2020102* xi, II

Sui, Z. and Herman, I. P. [1993]. Effect of strain on phonons in Si, Ge, and Si/Ge heterostructures, *Phys. Rev. B* **48**(24): 17938–17953. Number: 24 Publisher: American Physical Society.
**URL:** *https://link.aps.org/doi/10.1103/PhysRevB.48.17938* II

Tardif, S., Gassenq, A., Guilloy, K., Pauc, N., Dias, G. O., Hartmann, J.-M., Widiez, J., Zabel, T., Marin, E., Sigg, H., Faist, J., Chelnokov, A., Reboud, V., Calvo, V., Micha, J.-S., Robach, O. and Rieutord, F. [2016]. Lattice strain and tilt mapping in stressed Ge microstructures using X-ray Laue micro-diffraction and rainbow filtering, *Journal of Applied Crystallography* **49**(5): 1402–1411. Number: 5.
**URL:** *https://onlinelibrary.wiley.com/doi/abs/10.1107/S1600576716010347* V

Tsang, J. C., Mooney, P. M., Dacol, F. and Chu, J. O. [1994]. Measurements of alloy composition and strain in thin GexSi1-x layers, *Journal of Applied Physics* **75**(12): 8098–8108. Number: 12 Publisher: American Institute of Physics.
**URL:** *https://aip.scitation.org/doi/abs/10.1063/1.356554* III

Ureña, F., Olsen, S. H. and Raskin, J.-P. [2013]. Raman measurements of uniaxial strain in silicon nanostructures, *Journal of Applied Physics* **114**(14): 144507. Number: 14 Publisher: American Institute of Physics.
**URL:** *https://aip.scitation.org/doi/full/10.1063/1.4824291* III

Wolf, I. D. [1996]. Micro-Raman spectroscopy to study local mechanical stress in silicon integrated circuits, *Semicond. Sci. Technol.* **11**(2): 139. Number: 2.
**URL:** *http://stacks.iop.org/0268-1242/11/i=2/a=001* III